ELECTROPHORETIC DEPOSITION OF PRIMARY COAT ONTO INVESTMENT CASTING WAX PATTERNS

by
Peter James Roach (BEng.)

A dissertation submitted to the University of Birmingham for the degree of doctor of Philosophy

School of Metallurgy and Materials

College of Engineering and Physical Sciences

Abstract

The objective of the work reported in this thesis was to tailor a colloidal processing technique called electrophoretic deposition (EPD) for use within the investment casting shell formation process, where the EPD coating procedure would be used to form the primary ceramic coating on the melt-out substrate. EPD takes place due to the presence of an electric field within the suspension medium, which attracts charged particles in the suspension towards an electrode of opposite charge, onto which they are deposited.

For the complex structures created using investment casting, the die cast patterns used as the substrate for the ceramic have to be easily removed, and so substrates materials that can either be melted or dissolved out the material to leave the hollow ceramic shell used. To implement EPD into the investment casting process, this substrate needed to be conducting, and so conducting particle-filled investment casting waxes were created and analysed.

Carbon black and graphite filler were incorporated into waxes, and the conductivity and rheology of the resultant composites were studied, to gauge their suitability as an investment casting pattern material.

On the basis of both cost and for environmental reasons, the use of aqueous suspension media for EPD was preferred over the more commonly used organic systems. EPD was carried out using zircon in aqueous suspension, and the low particle concentration suspensions were stabilised through pH modification and anionic dispersant addition. The effect of suspension parameters and EPD set-up parameters on the coatings formed on compressed graphite electrodes and conductive wax electrodes were studied, through yield measurements and cross sectional analysis using scanning electron microscopy.

Acknowledgements

I would firstly, like to give my deepest and expressed thanks to my supervisor, Dr. Clive B. Ponton, as he has been truly tireless in his help and advice. I wish to extend my thanks to my co-supervisor, Dr. Sam Jones, for her help and advice regarding the investment casting aspect of my work.

I am also grateful to the EPSRC DTA Scheme, the University of Birmingham, and the Department of Metallurgy and Materials for their provision of a PhD studentship.

I would like to thank the Department of Metallurgy and Materials and the Net Shape Manufacturing Laboratory for the provision of laboratory facilities. I also extend my thanks to the members of academic and technical staff therein for their ongoing assistance in so many ways.

Other thanks go to:
Cabot, for their Vulcan carbon black powder samples
David Stonier of Dupré Minerals, for their zircon powder samples
Helmut Kreutz, for their 'Kreutzonit Super FF' Zircon powder samples
Zschimmer & Schwarz, for their Dolapix CE64 polyelectrolyte samples
Dr. Volker Hellinger of Deloro Stellite, for his help with patent searches
Steve Pilbury of Remet, UK, for wax samples and loan of high shear mixing equipment.
Dave Morson and Dave Bond of Balyson Olefines, for their information on wax melting procedures, and for samples of their waxes.

I am thankful to my friends, my family, and especially my wife, Lucia, for supporting me. I would not be where I am without them. On reading, 'Alchemy increased to 23'.

Finally, I am especially grateful to Dr. David Ford, via EICF, for the special interest shown in my PhD project and for his efforts in putting together the EICF Project Consortium to provide industrial support this project, both financially and in-kind.

TABLE OF CONTENTS

CHAPTER 1. INTRODUCTION AND AIMS OF PROJECT

1.1 Introduction

Electrophoretic deposition (EPD) is a particulate forming process. Well dispersed colloidal particles in a suspending medium gain a surface charge due to an electrochemical equilibrium state is reached with the solvent. When the suspension is incorporated as part of an electrical circuit using immersible electrodes, a direct current electric field is produced within the suspension, and the particles move in a direction determined by their charge. They are attracted towards and deposited onto the electrode of opposite charge, which is used as the deposition substrate (Tassel, 2006).

The application of colloidal processing to ceramics has been demonstrated to provide high microstructural uniformity and reliability in the products that are formed, and EPD is one such process. A number of the more well-established colloidal methods for producing complex shapes (like slip, pressure and tape-casting) require well-dispersed concentrated slips, with processing additives to improve their stability and the stability of subsequent forming operations. The EPD process is very versatile when compared with those methods, and can be modified easily for a specific application. Binder burnout is also not often required, since green coatings can contain little or no organic material. It also has the production advantages of short formation times and simplistic apparatus setup in forming complex shapes with a good surface finish.

The investment casting process involves use of an expendable pattern in the production of a metal casting. The earliest form of investment casting was known to have been carried out in Thailand around 4500 BC, with the process also being used in Ancient Mesopotamia, China and Greece for tool-making. The process was adapted for use in the

formation of jewellery and artistic products, and then for the casting of dental alloys. It was the advent of the Second World War which saw the process modified to initially develop precision aerospace components, as it could be used to manufacture heat resisting alloys. Other engineering applications followed (Clegg, 1991).

The term investment casting is derived from the distinguishing use of ceramic slurry (or investment), to form a mould with an extremely smooth surface. Precise patterns can be replicated from a design and transmitted in turn to the casting (Jones, 2003). The ceramic shell process was developed in the late 1940's and early 1950's, because it is well suited to the high tolerances required within the aerospace industry, and surpassed the use of block moulds in many applications. The use of a colloidal processing technique like EPD to form the mould shell has the potential to increase dimensional tolerances in the resultant casting, in addition to opening up intricate geometry options with a level of detail that would otherwise require the use of cores when shells are formed using investment techniques.

1.2 Project Aims

The aim of this project is to use electrophoretic deposition (EPD) within the field of investment casting, to replace the primary dip coating step with one utilising the EPD process. For the complex structures created by investment casting, the ceramic coatings need to be formed on substrates that can be easily removed. This can be done by either melting or dissolving away the substrate material to leave behind the hollow refractory ceramic shape. Specialised waxes are currently used as a substrate material for these refractory coatings. As EPD substrates need to be electrically conductive, these waxes were modified with conductive fillers in the present work, to make them suitable for use as electrophoretic deposition electrodes. By carrying out these modifications, the initial wax shaping stages presently used

could be kept in place with only minor alterations, to fit this process easily into the current investment casting methodology.

Graphite and carbon black particles are desired as a conducting phase as there are issues associated with using metal-loaded alternatives. Potential retention of any filler within the EPD ceramic face coating would ‘poison’ both the face coat and casting alloy, and the implications of having trapped metallic ions are far worse than the implications of graphite contamination. Graphite is also more suited for use within the field of aqueous media EPD, due to the effects of oxidation and metallic impurity migration when metals are used as the substrate material.

Ultimately, the goal is to use the complex shape-forming ability of EPD to create a process whereby uniform ceramic deposits can be formed on both the outside and hollow regions of complex shapes. This would thus eliminate the need for some cores (used to produce the intricate internal shapes in investment castings), with all their associated problems (including reactivity, decrease in surface quality, poor tolerance, breakage and displacement). It would also reduce the number of required steps needed in the production of ceramic shells, by taking away the core removal stage.

CHAPTER 2. INVESTMENT CASTING

2.1 Summary of Investment Casting Process

The investment casting process, as described in Section 1.1, allows for flexibility of design, and can produce castings that are intricate, with a good surface finish and excellent dimensional accuracy. Owing to the way that the ceramic shell is both formed and removed, no flash is present, and so parting line tolerances are not applicable. It can therefore be used to cast alloys that are difficult or expensive to machine. As parts are formed as part of a sprue, the investment casting process can be used to form parts in both small and large quantities, although larger quantities are needed to make it economically feasible.

The shell mould is, however, non-reusable and the number of process steps required makes investment casting an expensive and time-consuming process. It is therefore limited to casting applications where its advantages are a requirement. In addition, due to limitations in the strength/rigidity of the wax substrate and within the shell formation process itself, components formed this way cannot be too large. The investment casting process follows a number of steps that are summarised below, with reference to Figure 2.1 (Clegg, 1991):

Stage 1: A precision-engineered die is used to form an expendable pattern, which is usually made of wax. Whilst it is preferable to make the pattern from a single die-cast part, larger and more complex geometries have to be made from several sections which are then bonded together to form a multi-component die.

When the desired geometry of the investment cast metal product contains hollow internal spaces, the investment process often cannot form a shell within these sections with the required level of detail and/or mechanical strength. Such hollow channels or spaces can

instead be produced in the metal using investment casting cores. These cores are designed to match the required hollow geometry, and are typically made of a ceramic material that can be dissolved away after casting. They are often held in place using metal pins, which are pressed through the wax preform and butt up against the ceramic cores prior to shell formation. They therefore become anchored to the mould cavity wall of the investment shell, and remain in place up until the shell removal stage (Power, 1995).

Stage 2: The wax patterns are cleaned of excess material and assembled together with a gating and feeding system to form a cluster (or sprue). Using heated tools, the patterns are manually wax welded onto preformed wax gating/feeding components. Smaller, simpler patterns are often die-cast to include a complete gating system, although they still require assembly in order to produce the final sprue.

A preformed ceramic pouring cup is added to the sprue, and is used for handling purposes during the dipping and stuccoing operations. The use of a preformed cup is preferred over the use of an investment cast one as it does not tend to cast debris into the mould as the metal is poured during casting.

Stage 3: The wax pattern is covered with a ceramic coating that is built up in thickness using successive stages of dipping and stuccoing. The pattern assembly is dipped into the primary slurry and rotated to ensure complete contact between the patterns and slurry. The assembly is then withdrawn and the excess slurry is allowed to drain back into the tank. During the draining stage, the assembly is rotated in more than one orientation, to ensure that an even coating is formed. Robotic arms are often used during this stage, as strength and repeatability of motion are required. This primary coat should provide a good surface finish for the mould interior, and is formulated according to criteria set out in Section 2.2.

Stage 4: Immediately after draining, the assembly is stuccoed in either a raining cabinet or fluidised bed. Both methods are briefly described below:

a) In a raining cabinet, particles are allowed to fall onto the rotating assembly.

b) In a fluidised bed, the rotated assembly is dipped into a tank containing particles which behave like a fluid under the action of pressurised air rising from the porous base-plate of the tank.

The purpose of stuccoing is to firstly reduce drying stresses within the shell by presenting a number of stress concentration centres which reduce the magnitude of any local stresses. Stucco coats also produce a rough surface that facilitates a mechanical bond between the primary coating and the back-up or secondary investment (Jones, 2009).

The primary coat is allowed to set (i.e. air-dried until the binder gels) before the assembly is dipped in a secondary dip tank and stuccoed with coarser, dry particles, to maintain maximum mould permeability and to provide bulk to the mould. A successive number of backing coats are then applied until the coating is of a specific thickness, to give the resulting fired shell sufficient strength for subsequent processing stages. Shells are therefore dried over an extended period of time (usually 16-48 hours), before dewaxing.

Stage 5: Once the desired shell thickness has been obtained, the wax pattern can be removed. The wax expands during heating and can generate stresses that are high enough to crack the green shell. These shells are heated from the outside, which causes the surface layer of wax to melt out first, before the bulk expands under the action of heating. Molten wax either runs out of the shell or, due to permeable nature of the shell, soaks into it, to provide enough space for the expansion of the rest of the pattern wax. Two principal methods of dewaxing are implemented, and are briefly described below:

a) In flash dewaxing, the pattern and shell are inserted into a hot furnace in an inverted position. The molten wax melts and drains out, frequently burning in the process. At the high temperatures employed (1000 °C for dewaxing), shell distortion can take place.

b) In autoclave dewaxing, the use of a very rapid heating cycle means that the wax melts very quickly, and is not given the opportunity to expand as a solid to exert expansion pressure on the mould shell. The process involves the use of superheated steam at 180 °C and 600 kPa to provide the necessary rapid heating. It is a quick process, and wax can be reclaimed using this process. The equipment is, however, expensive.

Stage 6: After the dewaxing process, the hollow ceramic shell is fired to around 1000 °C, although this varies from 900 °C to 1200 °C, depending upon shell composition. This is done to burn off any residual wax inside the mould, to remove organics from the shell itself and to sinter the ceramic and preheat the mould to a temperature required for casting. Oxidising conditions are often recommended to promote the combustion of organics.

Stage 7: A metal can be cast into the ceramic shell using a number of different techniques, and a number of these a listed below:

a) Static gravity pouring is a process where the liquid metal is poured into the mould without application of any external pressure. Whilst this simple set-up is an inexpensive one, the percentage of metal cast that goes to the components (the metal yield) is low at 15 to 50%, as much of the cast weight is in the sprue and gating system (DeGarmo, 2003).

b) Counter-gravity investment casting uses a pouring technique where the mould is filled 'upside-down'. The investment shell is placed in a vacuum tight mould chamber and then lowered into a pool of liquid metal. A vacuum draws the metal up into the investment shell, and is kept in place as the metal solidifies. This technique produces higher yields (60 to 95%), fewer turbulent effects and improved grain structures (DeGarmo, 2003).

c) Vacuum pressure casting (VPC) uses a two chamber system. A crucible containing the liquid metal is situated in the upper chamber and the investment mould is housed in the lower chamber, with these chambers separated by a stopper. A pressure is applied to the liquid metal in upper chamber, whilst a vacuum is placed on the investment mould. When the stopper is removed, the large pressure differential drives the metal into the mould. This technique produces high quality castings with low porosity.

Stage 8: After cooling, the ceramic shell is broken off, either by mechanical means, through shot blasting, or through high pressure water-blasting. Leaching methods may be required where cores or intricate ceramic shells need to be removed.

Stage 9: The metal components are cut from the sprue assembly and finished before quality checks are carried out.

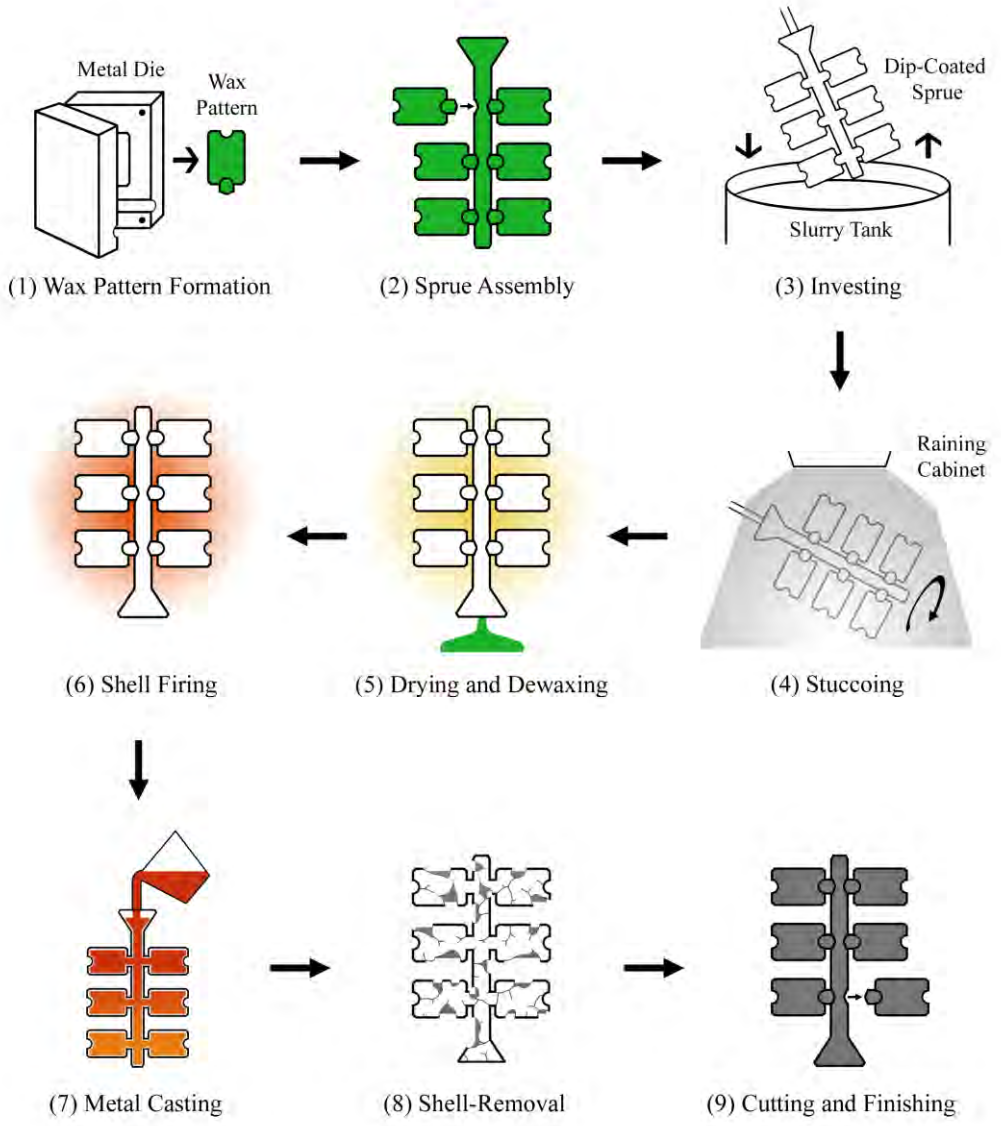

Figure 2.1 Diagram showing the investment casting process, as a step-by-step procedure. Stages (3) and (4) are carried out in order a number of times, to build up the shell thickness (adapted from a diagram by Asthana, 2006).

Several of these stages are of heightened interest within this work. The wax pattern formation, sprue assembly and investing stages require a wax with both the desired flow behaviour and mechanical properties. For the dewaxing process, both the expansion coefficient and thermal conductivity of the wax play an important role, and such demands are more closely examined in Section 5.1.

2.2 Dip Coating Process

2.2.1 Slurry Components and Preparation

The aim of this project is to compare the primary shell layer formed by EPD with that formed using dip coating techniques. The properties of the investment casting slurry are therefore of critical importance, as some of the slurry characteristics have to be replicated within the aqueous suspensions used for EPD. An investment casting slurry is a complex system containing a number of additives that tailor it for the successful dip coating of wax patterns of differing geometries. The customary components of an investment casting slurry are listed and briefly described in this section.

a) A fine refractory ceramic powder that forms the coating on the wax substrate, i.e. the pattern. These powders include silica, zircon (zirconium silicate), alumina and various aluminium silicates. The actual slurry ceramic composition depends upon the metal being cast, as each has specific temperature and non-reactivity requirements.

b) A binder that is used to hold the refractory ceramic in place as a coating on the substrate; it does so by gelling under given conditions. Colloidal silica binders gel in air, and the air being circulated has to be maintained at a controlled temperature and humidity to avoid shell cracking. Ethyl silicate binders, on the other hand, set due to a chemical reaction. Whilst this leads to improves productivity by reducing the time between coats, this is often at the expense of shell strength.

c) Wetting agents, that are confined for use in the primary coat slurry, in an amount ranging between 0.03 and 0.30 wt% of liquid. They promote wetting of the pattern by the primary coat.

d) Antifoam compounds that are commonly used in association with the wetting agent, to suppress foam formation and promote air bubble escape, especially from the pattern surface. Additions of 0.002 to 0.10 wt% of the liquid are sufficient. (Horton, 1988)

The refractory powder is added to the binder liquid, and agitation is necessary to break up any powder agglomerates and thoroughly wet and disperse the powder. A prolonged period of mixing is required to promote de-aeration and particle wetting. Slurry properties are initially regulated by close control of the initial ingredients, and viscosity measurements can be carried out throughout the homogenisation process. Viscosity measurements are supported by tests to determine the pH value, temperature, specific gravity and percentage SiO_2. Stirring must be continued after homogenisation at a reduced level, to ensure that the powder remains in suspension. Propeller mixers can be used, although rotating tanks incorporating baffles are more commonly utilised, as they ensure that no section of the slurry is allowed to settle.

2.2.2 Properties required of the Ceramic Shell

There are a number of key properties that are required of an investment casting ceramic mould or shell, and these are listed below:

1) The green (unfired) strength needs to be sufficient to withstand wax removal without failure.
2) The fired strength has to be great enough to withstand the weight of cast metal, although it must also be sufficiently weak to prevent the formation of casting defects in susceptible alloys. When very strong shells are used contraction stresses are formed

in the solidifying metal, which leads to the formation of ‘hot tears’, which are irreversible failure cracks in the semi-solid casting.

3) It must have a high thermal shock resistance to prevent cracking during metal pouring
4) It must be have a high chemical stability, and must not be affected by, or react with, the mould firing atmosphere, the dewaxing steam or any material that it may come into contact with.
5) It needs to have a low reactivity with the metals being cast to both improve the surface finish of the casting, and to avoid any detrimental effect that these reactions may have on the resultant casting.
6) The permeability and thermal conductivity of the mould must be sufficient to maintain an adequate thermal transfer through the mould wall which hence allows the metal to cool. High shell permeability is also required to allow for the removal of air that is displaced by molten metal pouring. Incomplete filling of the mould may otherwise result.
7) A low thermal expansion coefficient limits the dimensional changes within the mould wall and ultimately of the casting itself. Matched expansion coefficients in the metal casting and shell mould reduce contraction stresses (Clegg, 1991)

CHAPTER 3. ELECTROPHORETIC DEPOSITION

3.1 Introduction

The electrophoretic deposition (EPD) process can be split into two separate stages. The first, called electrophoresis, involves the movement of charged particles in suspension under the influence of an electric field. The second stage, called deposition or electro-coagulation, occurs when these particles assemble together at the electrode of opposite charge and become a deposit (Anné, 2004). The main difference between electrophoretic and electrolytic deposition relates to the nature of the moving species. The former is based on the suspension of particles in a liquid medium, whilst the latter is based on a solution containing ionic species. The principal differences between electrophoresis and electrolysis are summarised in Table 3.1. EPD from suspensions and dip coating from investment slurries have different properties and requirements, and are compared in Section 3.4.

It is important to note that electrochemical processes, electrostatic processes and electrocasting can exhibit similarities to EPD, but differ in a fundamental ways. Electrodeposition and electroplating, for example, are examples of electrochemical processes. In these methods, coatings are produced when particles and molecules migrate to the deposition electrode and are converted into an insoluble form by electrochemical reactions. In EPD, particles undergo no such reaction at the electrodes. In electrostatic processes, like electrostatic precipitation and electrostatic spraying, particles that are deposited are charged either by a high voltage injection of electrons or by tribocharging, which are processes described by Tassel et al. (2006). In EPD, the particles are charged as a result of electrochemical reactions with the suspending medium. In electrocasting, partially flocculated or gelled particles in a solvent become consolidated into a progressively dense structure under

the influence of an electric field. This process differs from EPD, as particles in EPD suspensions can move independently of one another, which is not the case in electrocasting. Additionally, particle migration in electrocasting takes place as a result of electrocapillary pumping. For EPD, on the other hand, particles in suspension move as a result of electrophoretic migration (Tassel 2006).

Table 3.1 **S**ummary of the principal differences between electrophoresis and electrolysis processes

	ELECTROPHORESIS	**ELECTROLYSIS**
Medium	suspension	solution
Moving species	particles	ions or complexes
Electrode reactions	none	electrogeneration of OH^- and neutralisation of cation species
Preferred liquid	organic solvent	mixed solvent (water-organic)
Required conductivity of liquid	low	high
Deposition rate	1-10^3 µm/min	10^{-3}-1 µm/min
Deposition thickness*	1-10^3 µm	10^{-3}-10 µm
Deposit uniformity †	limited by particle size	on nm scale
Deposit stoichiometry	Controlled by stoichiometry of powders used for deposition	Can be controlled by use of precursors

* Controlled by variation of deposition time, voltage or current density

† Controlled by electric field (Table from Zhitomirsky 2000)

3.2 Electrophoresis Stage – Theory, Principles and Mechanisms

During the electrophoresis stage, the ceramic particles first acquire an electrochemical charge from the medium into which they are dispersed due to a number of different charging modes. These include the selective adsorption or dissociation of ions between the solid and liquid phases, the adsorption or orientation of dipolar molecules on the particle surface, and the transfer of electrons due to differences between solid and liquid work functions (the work function being the minimum energy required to remove an electron from a material to a point immediately outside) (Biest 1999). The action of these mechanisms makes the colloidal particles either positively or negatively charged in nature, which determines the electrode upon which deposition occurs.

Within a polar medium like water, ions of opposite charge to the colloidal particles assemble around the particles' surface with an ion concentration greater than that of the bulk, whilst ions of like charge, which are referred to as counter-ions, are repelled away from the particles to generate an electrical double-layer. A percentage of these counter-ions move along with the particle under the influence of an electric field, and the potential at the edge of this 'captured' ion layer is termed the zeta potential (ζ), and is the effective charge of the particle in suspension. Figure 3.1 shows the double-layer in more detail.

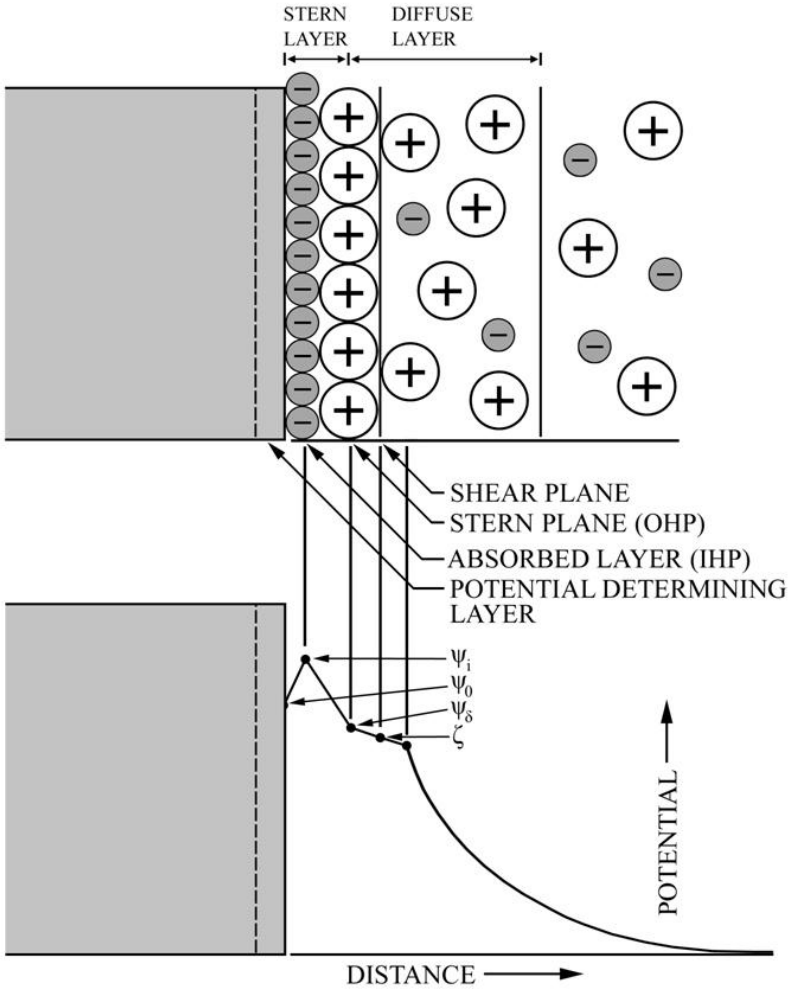

Figure 3.1 The electrical double-layer that forms around a charged particle in suspension consists of two layers, separated by the Stern plane. The inner 'Stern layer' is made up of relatively tightly bound counter-ions, whilst the 'Diffuse layer' is a region where coulombic forces and random thermal motion determine the ion distribution. The presence of the absorbed layer is explained in Section 2.2.1. On the graph of potential against distance, ψ_0 is the potential at the particle surface and ψ_i is potential at the Inner Helmholtz Plane (IHP), which is the plane cutting through the centre of the absorbed species. ψ_δ is the potential at the Outer Helmholtz plane (OHP), which is the plane cutting through the positive ions at their position of closest approach. ζ is the potential at the shear plane (known as the zeta potential) (Sennett, 1965).

The rate of particle migration under the influence of an electric field is called the electrophoretic mobility (μ_e), and is defined as the particle velocity (v) ($m.s^{-1}$) divided by the electric field strength (E) ($V.m^{-1}$), as shown in equation [3.1]. The Helmholtz-Smoluchowski equation (Henry, 1931) linked the magnitude of the spherical particles' zeta potential (ζ) with the electrophoretic mobility through the following equation [3.2]:

$$\mu_e = v / E \qquad [3.1]$$

$$\mu_e = \varepsilon \varepsilon_0 \zeta / \eta \qquad [3.2]$$

ε is the dielectric constant of the dispersion medium, ε_0 is the permittivity of free space and η is the dynamic viscosity of the dispersion medium. Equation [3.2] does not, however, take into account effect of the double-layer thickness (κ^{-1}), known as the Debye length, and is only valid when κ^{-1} is much smaller than the particle radius. The ratio of the particle radius to the double-layer thickness is given by κa (where κ is the reciprocal of the double-layer thickness and a is the particle radius), and its value is commonly used to gauge the validity of electrophoresis equation [3.2], as described below.

Within the electrical double-layer, electric field gradients and ion density gradients are present perpendicular to the particle surface, and any significant change in the ion density gradient distorts the double-layer. Equation [3.2] is based on the assumption that the double-layer is not distorted by the application of the electric field, as this has an influence the resultant particle mobility. For thin double-layers (when κa is large), the gradients in the double-layer normal to the particle surface (governed by the double-layer thickness (κ^{-1})) will be much larger than the gradients tangential to the surface (governed by the particle radius (a)). When an electric field is applied, the ions in the double-layer are set into motion by the field and move in a direction tangential to the surface. Any change in the ionic density is

small, as the ion flux due to the component of the electric field normal to the surface is balanced by the diffusive flux (O'Brian, 1981).

Gradient distortions do, however, occur when the double-layer is of increased thickness. O'Brian (1981) found that the Helmholtz-Smoluchowski equation [3.2] became invalid when κa was less than 150 (for systems when $e\zeta/kT \geq 4$, where e is the electronic charge (eV), k is the Boltzmann constant (8.617×10^{-5} $eV.K^{-1}$) and T is the temperature (K)), which corresponds to a 1 micron particle with a double-layer thickness greater than 6.7 nm. The Helmholtz-Smoluchowski model [3.2] also breaks down when large zeta potentials are involved. Even for particles with high κa, the density of counter-ions in the double-layer are so large that the ionic fluxes due to the small components of the applied electric field and fluid velocity normal to the surface become significant, and the double-layer distorts (O'Brian, 1981).

Henry developed a model in 1931 [3.3], which modified the Helmholtz-Smoluchowski equation to include terms that take into account the effects of the κa value, the relationship between the solid and liquid conductivities (K^S/K^L), and the Dukhin number (Du), which accounts for the relative contribution of surface conduction (Lyklema 2003).

$$\mu_e = \frac{2}{3}\frac{\varepsilon_0 \varepsilon \zeta}{\eta} \, f\left(\kappa a, \frac{K^S}{K^L}, Du\right) \qquad [3.3]$$

$$Du = \kappa^{\sigma} / a K^L \qquad [3.4]$$

Du is Dukhin number, K^S is the conductivity of the solid, K^L is the conductivity of the liquid, κ^{σ} is the surface conductivity of the particle, and a is the particle radius (m). One of the correction factors present, the retardation factor, f(κa), changes from 1 at low κa to 1.5 at high κa.

3.3 Deposition Stage – Theory, Principles and Mechanisms

The mechanisms of the deposition stage are far less clear than those of the electrophoresis stage considered in Section 3.2 above, and several different theories have been put forward to explain the process by which electrophoretic deposits form. The first of these was developed by Hamaker & Verwey (1940), who said that the formation of an EPD coating could be compared to the development of gravitationally formed sediment. In both these phenomena, the pressure exerted by incoming particles as they approach the substrate would enable those particles closest to the deposit to overcome interparticle repulsive forces and become part of the deposit. According to this theory, deposition would not occur from very stable suspensions, as the high interparticle repulsive forces responsible for the suspension stability would provide a barrier that inhibits all deposition at the substrate. As EPD coating have been formed experimentally from very stable suspensions, other deposition mechanisms must exist.

According to Koelmans (1955), there is an expected increase in ionic strength next to the electrode, and this ionic strength is of the same order as that required to flocculate the suspension. Flocculation can be described as process whereby stably dispersed particles are destabilised and approach one another when the interparticle repulsion forces are decreased. The presence of a high ionic concentration in solution in the region surrounding the electrode acts to reduce the thickness of the repulsing double-layer around the colloids, and this leads to the flocculation and collapsing together of the particles into a cohesive deposit. A finite amount of time would be needed for a high enough ionic concentration to build up near the electrodes, and any deposit formed before this time would not stay on the electrode when the electric field is turned off. This length of time was found to be inversely proportional to the square of the applied voltage.

For this mechanism to occur, reactions that increase ionic concentration in the vicinity of the electrodes must take place. One such example occurs in aqueous media system EPD, where water electrolysis reactions release H^+ and OH^- ions into the suspension at the electrodes. This proposed mechanism, however, cannot be the sole deposition stage mechanism, as EPD coatings have successfully been obtained from systems that experience no increase of electrolyte concentration near the electrodes. This mechanism also cannot account for how electrophoretic deposition successfully occurs on non-conducting substrates when a 'membrane method' set-up is used, as described in Section 4.5.1.2.

Sarkar and Nicholson (1996) put forward a theory that explains the deposition phenomenon without the need for increased ionic concentrations near the electrode. When the charged colloidal particle moves under the influence of an electric field, it carries with it a layer of surrounding counter-ions, and the combination of the fluid dynamics around the moving particle and the applied electric field distorts the counter-ion layer so that it becomes thinner ahead of the moving particle and thicker behind it. Ions of like charge to the colloidal particles are present in solution, and move along with the particle when an electric field is applied. They neutralise the counter-ions in the double-layer region following the charged particle, which thins the double layer 'tail'. The concentration of particles near the electrode is high, and collisions are more frequent. Van der Waals attraction dominates and leads to coagulation/increased deposit thickness when the thin leading double-layer of one particle approaches the depleted double-layer tail of another.

For the Sarkar and Nicholson mechanism to operate, sufficiently high electric field strengths are needed for double-layer distortion, and so a threshold voltage for deposition should exist. This mechanism cannot, however, explain deposition that occurs from suspensions containing high κa value particles, whose double-layers are not distorted by the applied electric field. In EPD, the ceramic particles are not involved in any form of reaction at

the electrode, and do not lose their charge upon being deposited. Sarkar and Nicholson (1996) demonstrated this through showing that a layer deposited by EPD was stripped off when the electric field was reversed. When the EPD process uses multiple stages to deposit different phases or ceramic particle compositions, it is therefore important to use similarly charged particles and similar solvent–binder–dispersant systems for gaining better control of layer thickness (Besra 2007).

3.4 Comparing Investment Slurries and EPD Suspensions

The coating mechanisms associated with dip coating (investing) and EPD coating are fundamental different. The desired properties of the investment slurry and EPD suspension differ because of this, with several important distinctions defined in this section.

The major components and desired properties of the primary slurry used for investing are described in Section 2.2.2. Investment slurry coatings consolidate on substrates primarily as a result of slip casting and liquid entrainment mechanisms (Moon, 2006). The dip coat thickness, h, can be governed by Equation [3.5]:

$$h = c_1\left(\frac{\eta U}{\rho g}\right)^{1/2} \qquad [3.5]$$

η is the liquid viscosity, ρ is the density of the liquid, U is substrate removal speed, g is the acceleration due to gravity, and c_1 is a constant of proportionality (Rahaman, 2003). Using this equation, it can be deduced that investment slurries require relatively high liquid viscosities.

EPD coatings form on substrates due to mechanisms described in Section 3.2 and 3.3. The main requirement of an EPD suspension is that it both stabilises the particles and gives them a high effective charge, which, in turn, gives them a greater mobility in an electric field. High viscosity suspensions slow the movement of charged particles in an electric field, and so low viscosity, low particle concentration suspensions are preferred (Besra 2007).

The principal component of investment slurries is a fine refractory powder, generally with a particle distribution upper diameter of 74 μm (due to the use of a 200 mesh filter). Particles with this specific distribution are chosen as a certain degree of coating permeability is required of the investment casting shell, with interparticle voids present to produce percolation channels for any escaping gas. Owing to Stokes' law of settling as described in Section 4.2.2, these particles stay in suspension due to the combined effects of high slurry viscosity and constant mechanical agitation. The role of binders, dispersants and antifoaming agents are described in Section 2.2.2.

Particles in EPD suspensions, on the other hand, tend to have sub-micron diameters, as EPD is traditionally used in applications where the required coatings are dense, with fine detail reproducibility. Larger particle size diameters cannot easily be used due to issues associated with suspended particles settling out under gravity. Mechanical stirring operations that are invariably used to inhibit this happening to investment slurries are counterproductive in the EPD process, as it readily removes the coating already formed on the deposition substrate. EPD is traditionally carried out using suspensions containing no binder, as compaction due to the presence of an electric field is often sufficient to bond the particles together within the coating. Binders can be of use, however, when larger particle diameters are used and larger coating thicknesses are required.

CHAPTER 4. EPD VARIABLES

4.1 Introduction

Besra and Liu (2007) split the factors influencing electrophoretic deposition (EPD) into two categories; those parameters related to the suspension, and those related to the process itself. The parameters related to suspension include the colloid particle size, zeta potential of the ceramic particles, dielectric constant of the suspending liquid and the conductivity, viscosity and stability of the suspension. The parameters related to the process include the effects of deposition time, the applied voltage, the solids loading (concentration of solid in suspension) and conductivity of the substrate.

4.2 Suspension parameters

4.2.1 Definition of a Colloidal Suspension

The term colloid was first used by the Scottish chemist Thomas Graham. It is defined as "an entity phase dispersed to such a degree that the surface forces become an important factor in determining its properties". Colloidal dimensions generally lie between 1 nm and 1 μm in size, and colloidal particles can be most easily recognised in the way that they cannot diffuse through membranes which otherwise grant passage to ordinary molecules and ions, through being too large in comparison.

A colloidal suspension is one where the suspended phase remains stable in the suspending medium for extended periods due to the interplay between interparticle forces. In this study, however, particles size distributions that lie outside the colloidal range are used because of the increased cost of finer grades and, in the field of EPD, the call for more

permeable coatings that can be formed when larger particles with a monomodal size distribution are used. When larger particle sizes are used, settling effects must be considered.

4.2.2 The Effect of Particle Size on Stability

Suspension stability is governed by two main factors, the particle settling rate and the suspension's tendency to either undergo or resist flocculation. The colloidal particle size therefore plays an important role with regard to the stability of the resulting suspension. The properties of the coating are also influenced by this variable, and electrophoretic deposits formed using particles with sub-micron diameters require lower sintering temperatures, shorter sintering times and can exhibit greater final product strengths (Greenwood, 2003).

For particles on the sub-micron scale, gravitational settling effects are balanced by colloidal forces, and they therefore tend to remain in suspension for long periods due to Brownian motion. Particles larger than 1 μm readily settle under the influence of gravitational forces and require constant hydrodynamic agitation to keep them from settling out. Ideally, for EPD to occur without gradients in deposition thickness, the mobility of particles under the influence of an electric field (the electrophoretic mobility (μ_e)) needs to be higher than the effects settling due to gravity, i.e. the particles need to migrate to and deposit on the deposition electrode at a rate much faster than the rate at which they settle out under gravity. With larger particles, therefore, a very strong surface charge or large double-layer thickness needs to be obtained (Besra 2007).

Stokes' law [4.1] determines the terminal settling velocity of particles in a liquid medium, taking into account buoyancy, frictional and gravitational forces at equilibrium:

$$V_s = \frac{2}{9}\frac{r^2 g(\rho_p - \rho_f)}{\eta} \qquad [4.1]$$

V_s is the particle settling rate ($m.s^{-1}$), ρ_f is the density of fluid ($kg.m^{-3}$), ρ_p is the density of particle ($kg.m^{-3}$), r is the Stokes radius of particle (m), g is the standard gravity (9.807 $m.s^{-2}$) and η is the suspension viscosity ($kg.m^{-1}s^{-1}$). As shown in Equation 4.1, a number of variables other than the particle size can influence the particle settling rate, although a number of these are fixed for a given colloidal system.

The first of these is the disparity between particle and liquid mass densities, and a large difference leads to a high rate of settling. Using zircon ($\rho_p \sim 4.6$ $kg.m^{-3}$) particles as an examples here, because zircon particle suspensions are later used in the experimental work, it can be shown that settling in acetone ($\rho_f = 0.79$ $kg.m^{-3}$) occurs at a faster rate than in water ($\rho_f = 0.998$ $kg.m^{-3}$), when other property differences are not taken into account. The second variable is suspension viscosity, and for a colloidal suspension with low levels of solids-loading, the viscosity of the suspension can correspond to that of the liquid. Zircon particles in acetone ($\eta = 0.32$ $kg.m^{-1}s^{-1}$), for example, would settle more quickly than they would do in water ($\eta = 1.005$ $kg.m^{-1}s^{-1}$). The Stokes' radius (r) corresponds to the radius of a hard sphere that diffuses at the same rate as the molecule/particle, and takes into account particle shape and the presence of a hydration sphere. So that approximations can be made, the Stokes' radius has been taken to be equal to half of the particle diameter. The effect of changing the zircon particle size on settling rate for a low-filler content aqueous suspension is given in Table 4.1 below. The final column in Table 4.1 displays the time it would take in theory for a

particle to sediment 70mm, a distance chosen because it is the approximate depth of the experimental suspensions in the present work.

Table 4.1 Theoretical particle settling data for spherical zircon particles of different diameters in low viscosity water-based suspension, according to Stokes' Law given by equation [4.1].

Suspension Media	**Particle Diameter (μm)**	**Approx Stokes' Radius (m)**	**Particle Settling Rate ($m \cdot sec^{-1}$)**	**Settling distance in 5 minutes (mm)**	**Approx Time to Sediment 70mm (time unit given)**
Water	0.1	5.0×10^{-8}	1.955×10^{-8}	0.00587	41.4 days
Water	1.0	5.0×10^{-7}	1.955×10^{-6}	0.587	9.9 hours
Water	1.5	7.5×10^{-7}	4.399×10^{-6}	1.320	4.4 hours
Water	2.0	1.0×10^{-6}	7.822×10^{-6}	2.35	2.5 hours
Water	4.0	2.0×10^{-6}	3.129×10^{-5}	9.39	37 minutes
Water	12.0	6.0×10^{-6}	2.816×10^{-4}	84.5	4.1 minutes
Water	100.0	5.0×10^{-5}	1.956×10^{-2}	5870	3.6 seconds

4.2.3 Suspension Stability and the Role of Interparticle Forces

4.2.3.1 Electrostatic Forces and Electrostatic Stabilization

A stable suspension is one where particle coagulation through flocculation is avoided. Colloidal particles are small enough to essentially avoid gravitational settling effects, and so it is important to focus upon the interplay between interparticle forces. The total interaction of potential energies (V_{tot}) is made up of the following constituent energy components [4.2]:

$$V_{tot} = V_{vdw} + V_{elect} + V_{steric} + V_{struct} \qquad [4.2]$$

V_{vdw} is the attractive potential energy due to van der Waals-interparticle attractive forces, V_{elect} is the repulsive potential energy caused by the electrostatic interaction between particles,

V_{steric} is another repulsive potential energy term, caused by the steric interactions between particle surfaces coated with adsorbed polymeric species, and V_{struct} is the potential energy caused by the presence of unadsorbed polymeric species in solution (Lewis, 2000). The first two terms that make up V_{tot} are described by Classic DLVO theory (Derjaguin, 1941) (Verwey, 1948). According to this theory, the liquid is assumed to be stationary, with collisions occurring due to Brownian translational motion.

The relationship between the van der Waals (vdW) and electrostatic force terms with interparticle distance is shown in Figure 4.1. At a distance far from the solid surface, both the van der Waals attraction potential and the electrostatic repulsion potential reduce to zero. Near the surface, a deep minimum in the potential energy produced by the van der Waals attraction exists, and particles at this separation distance tend to agglomerate together. A maximum (V_{max}), known as repulsive barrier, is located a short distance from the surface, as electrostatic repulsion at this distance dominates over van der Waals attraction. If the barrier is greater than ~10 kT, where k is the Boltzmann constant, the collision of two particles produced by Brownian motion will not overcome the barrier and agglomeration will not occur (Berg, 2009). There are a number of ways to strengthen the repulsive potential terms, and so increase the size of this barrier.

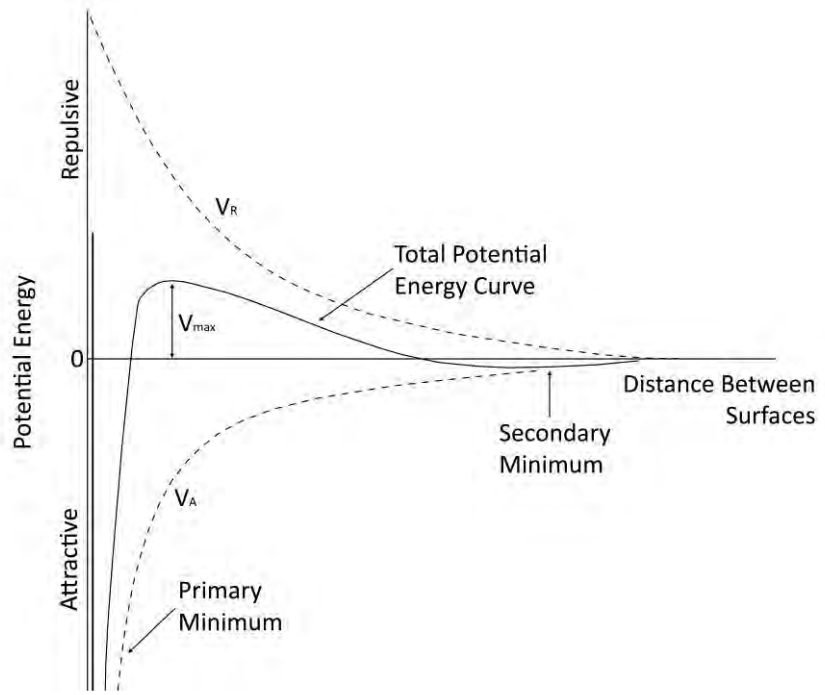

Figure 4.1 Graph showing the potential energies of the electrostatic (V_R) and van der Waals (V_A) force terms as a function of particle separation distance. The magnitude of the total interaction of potential energies is given as an unbroken curve (adapted from a diagram by Berg (2009)).

Particle interactions caused by attractive van der Waals forces have been observed over distances of several particle diameters in systems containing nanoscale particles, and the effects are particularly evident when one looks at cluster formation and growth. As a small cluster of particles increases in size, the vdW forces become dominant over a greater interaction distance, which in turn causes additional individual particles in the suspension to attach onto its surface. This particle aggregation can form weakening flaws in the final product if these aggregates persist during processing. The magnitude of the vdW interaction for a specific colloidal system is essentially independent of almost any change made to the solution, because the vdW interaction energy depends upon the surface area of the particles (Besra 2007).

The magnitude of the electrostatic repulsion term (V_{elect}) from equation [4.2] is influenced by a number of factors, as shown in Equation [4.3].

$$V_{elect} = \frac{\varepsilon a \psi_{\delta}}{2} \ln\{1 + \exp(-\kappa D)\} \qquad [4.3]$$

ε is the dielectric constant of the liquid, a is the particle radius, ψ_{δ} is the surface potential (which is often represented, i.e. approximated to, by the particle's zeta potential), κ is the reciprocal of double-layer thickness, and D is the separation distance between two interacting particles.

From Equation [4.3], one can see that a reduction in the thickness of the double-layer, κ^{-1}, lowers the value electrostatic repulsion term, and so increases the likelihood of particles agglomerating together on collision. The thickness of the double-layer is primarily influenced by the concentration of ions in solution, which can be determined by measuring the solution conductivity. Increasing the ion concentration compresses the double-layer, and therefore, for aqueous suspension stability, low solution conductivity is desired. Suspension modifications that introduce a higher concentration of ions to solution increase the suspension conductivity and destabilise particles, unless their influence is stabilising to a greater degree by either modifying the zeta potential or providing steric hindrance.

According to Equation [4.3], the value of the surface potential is proportional to the electrostatic repulsive force (V_{elect}), and so factors that influence the particle's zeta potential also affect suspension stability. As described in Section 4.2.4, the solution pH has an influence on the value of the zeta potential (ζ), and the isoelectric point (IEP) is defined as the pH when the particle's zeta potential is zero. For suspension stability, the position of the IEP is of importance, and working approximately 2 to 3 pH units away from this value in either

direction is enough to give the particles a zeta potential greater than 30 mV, which is generally accepted as being sufficient for suspension stability (Greenwood 2003).

For a particle system in suspension where the IEP is at pH 7, lowering the pH to more acidic levels or raising it to more alkaline levels stabilises the suspension by increasing the zeta potential of the particles. However, it also introduces a higher concentration of ions to the suspension, which reduces the thickness of the double layer. These stabilising and destabilising effects are conflicting, and effect of increasing the pH to either strongly acidic or alkaline conditions to increase the zeta potential for stability is counterproductive.

4.2.3.2 Steric and Electrosteric Forces

The effects of electrostatic stabilisation are often insufficient to stabilise particles at high volume fractions due to extensive double-layer overlap. When specific polymers are added to solution, certain sites on the molecule adsorb onto the colloid in suspension, to form a diffuse layer of polymer chains around the particle. As illustrated in Figure 4.2, approaching particles cannot physically achieve the proximity needed for attractive vdW forces to dominate and so cause coagulation. This stabilising effect is called the steric interaction (V_{steric}), which forms part of the total interaction of potential energies equation for colloidal stability [4.2]. Unlike with electrostatic stabilisation, as described in Section 4.2.3.1, the effects of steric stabilisation are not affected by a high concentration of ions in solution (Fritz, 2002).

Polyelectrolyte species provide electrosteric stabilisation when they are adsorbed onto a colloidal particle, which is a term used to describe the combined mechanisms of electrostatic and steric stabilisation. These species are electrostatically stabilising as they form near-surface charge complexes around the particle that increases the net surface charge density. Their addition has a dramatic effect upon both the rheological properties and the

colloidal stability. Polyelectrolytes (also known as dispersants) can be oligomeric or polymeric in nature, and their structure often consists of both dissociable and neutral side groups attached along a carbon backbone (Lewis, 2000).

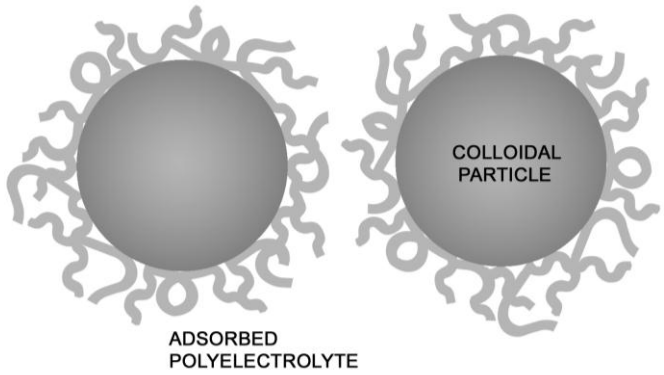

Figure 4.2 Diagram showing colloidal particles sterically stabilised by the presence of adsorbed polyelectrolyte on their surfaces.

An ‘optimum’ dispersant concentration exists for a suspension at the point when the particles’ surface area has been saturated with polyelectrolyte, to provide the colloids with a maximum level of steric hindrance. Destabilising effects occur when the dispersant concentration is below or above this concentration, as shown in Figure 4.3. Studies into dispersant-modified suspensions state that this concentration is system specific, with methods used to ascertain a value for the optimum dispersant concentration discussed in Appendix D.

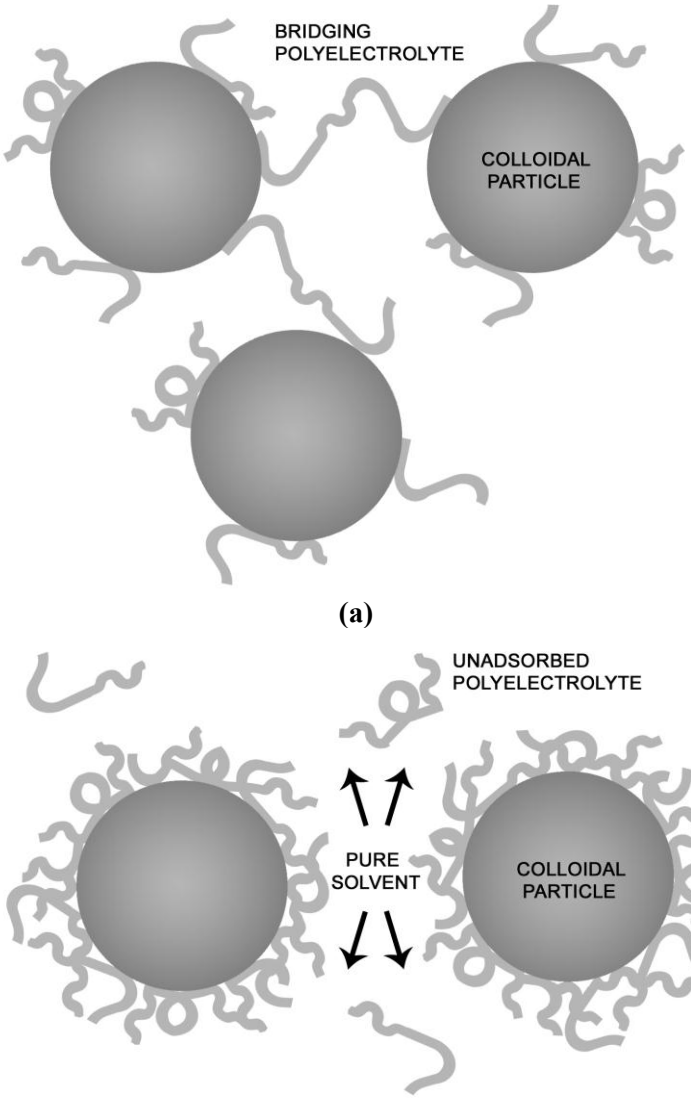

Figure 4.3 Diagrams showing the suspension destabilising mechanisms that result from dispersant addition to solution. **(a)** shows bridging flocculation destabilisation when dispersant is present at very low concentrations in suspension. The ends of the polyelectrolyte can become adsorbed onto two or more particles, which draw them together. Loose open sediments with large relative sediment heights are formed when this mechanism is in effect. **(b)** shows the effect of depletion flocculation destabilisation when dispersant is added in large quantities. The colloidal surfaces become saturated with polyelectrolyte, and any the excess remains in suspension. Depletion flocculation can occur as colloidal particles move close to one another in a polyelectrolyte-containing suspension. A polyelectrolyte-depleted region between the particles is formed (called the intercolloidal region), and a polymer concentration gradient is thus formed. Solvent between the colloidal particles diffuse out to reduce the concentration gradient, and this can cause the colloidal particles to aggregate together.

4.2.4 Factors That Influence the Particle Zeta potential

The magnitude of a particle's zeta potential in suspension varies across the pH range, and the isoelectric point (IEP) can be defined as the point when the particle zeta potential (ζ) is zero, as shown in Figure 4.4. The value of the zeta potential is influenced by a number of adsorptive and dissociative charging modes, as described in Section 3.2

An example of the adsorptive/dissociative charging mode can be described in further detail. Here, the interaction between the colloid surface sites and the liquid is controlled by suspension pH due to role of surface-charge determining (H^+/OH^-) ions. For a ceramic oxide, a percentage of the neutral M-OH sites on the particle's surface are ionised in the following reactions (where M is used to denote the oxide metal):

$$M–OH \rightarrow M–O^- + H^+ \quad [4.4]$$

$$M–OH + H^+ \rightarrow M–OH_2^+ \quad [4.5]$$

$M–O^-$ and $M–OH_2^+$ sites are formed, and the excess of one over the other determines the net surface charge (Costa, 1999). The point of zero charge (PZC) is the pH at which the concentration of both of these species is equal, which gives the particle surface a potential of zero. The surface becomes negatively charged at pH values above pH_{pzc}, and is positive at pH values below it.

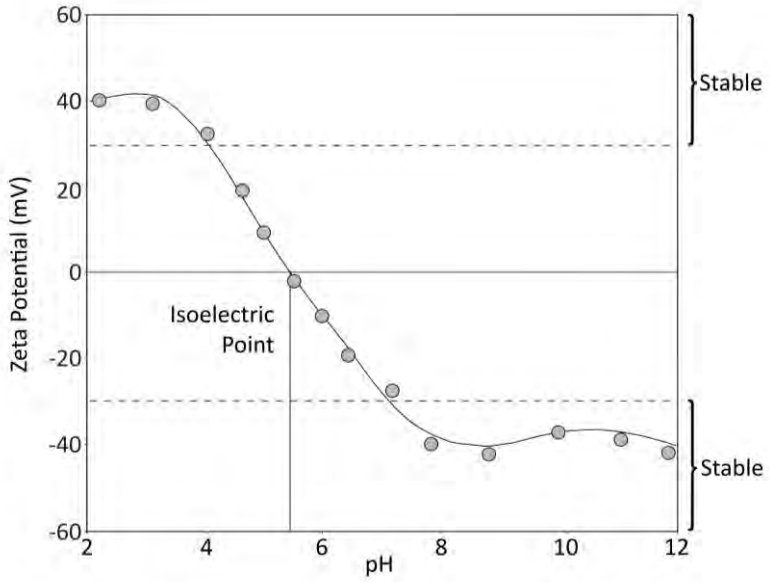

Figure 4.4 Graph of particle zeta potential against suspension pH for a nonspecific particle species, including areas denoting suspension stability (adapted from a diagram by silver-colloids (2010).

The position of the PZC in the pH range depends upon the material. The Fermi level (or Fermi energy) (EF) is defined as the highest occupied energy level of a material at absolute zero, and can define the pH of the PZC according to Mullins et al. (1998). Silica is a high Fermi energy material (EF = 5.4 eV), and has a pH_{pzc} in the acidic range (pH 2 – 3). Alpha-alumina, on the other hand, has a lower Fermi energy (EF = 3.5 eV), which gives it a more basic pH_{pzc} of 8.8 (Mullins, 1998).

It follows that a ceramic particle in suspension with no net surface charge would also not possess an electrical double-layer or zeta potential, and so there is equality between pH_{pzc} and pH_{iep} if no specific adsorption of ions takes place (Milojic, 2007). Specifically adsorbed species are ions in solution other than the surface-charge determining ions (H^+/OH^-) that display a non-coulombic affinity for the colloid surface. They form complexes with a central charge at a distance from the surface, as opposed to on the surface plane (as the case is for surface-charge determining ions) (Dobias 1993).

The effect of specific adsorption can be neglected when the suspension electrolyte is composed of monovalent ions at low concentration, and these electrolytes are often referred to as indifferent or inert (Dobias 1993). Specifically adsorbed ions in suspensions containing more highly concentrated monovalent electrolytes and multivalent species have been shown to shift the IEP and PZC in opposite pH directions (Lyklema 1984).

4.2.5 Effect Suspension Conductivity on Deposition

For aqueous suspension stability, a low level of solution conductivity is required, as the presence of ions in solution at high concentration reduce the double-layer thickness (Powers, 1975). As stated in Section 4.2.3.1, double-layer compression destabilises the suspension, as the magnitude of electrostatic repulsion term in equation [4.2] is reduced when the double-layer thickness (κ^{-1}) is decreased.

Additionally, when suspensions with high solution conductivity are used within EPD, the large number of free ions in suspension become the main current carrier when an electric field is applied. As described in Section 3.2, this reduces the electrophoretic mobility of the particles, as the solution conductivity effects the K^S/K^L term within equation [3.3].

As pH modification takes place away from the IEP, the zeta potential magnitude would increase as described in Section 4.2.4. Zeta potential increase would act to increase the particle's electrophoretic mobility in a set electric field, with the relationship displayed in equation [3.3]. As mentioned above, the introduction of ions to solution to modify the pH away from the IEP decreases the double-layer thickness, which both destabilises the particles and reduces their mobility. An optimum pH must therefore exist, where particle mobility is maximised and aggregation effects are minimised.

Low suspension conductivity does not, however, result in a suspension that can be ideally used within EPD. Ferrari and Moreno (1997) found that electrophoretic deposits would only form when the solution conductivity lay within a specific range. Linear limits for successful deposition were defined as a function of conductivity and temperature. The position and breadth of this 'deposition band' was additionally influenced by the current density. At a current density of 3.2A.m^{-2}, a deposition band was formed between 155 and 180μS.cm^{-1} (at 28°C), which then broadened to between 150 and 185μS.cm^{-1} (at 28°C) at 6.4A.cm^{-2}. Ferrari and Moreno (1997) used a 5 wt% alumina system (D_{50} = 0.5 μm) in their work, although the conductivity region is expected to be different depending upon the particle species or grade.

4.3 Experimental Techniques used to Analyse EPD Suspensions

The position of both the IEP and PZC are of importance within EPD suspension analysis for a number of reasons, as described in section 4.2.4. Comparing the position of the IEP and PZC can also be used to ascertain the effect of specifically adsorbing ions or polyelectrolytes on the particle's charging behaviour. Suspension preparation and stabilisation experiments are described in Appendix D. As the stability of the suspension is influenced by the position of both the PZC and IEP, methods in the literature used to measure PZC and IEP values are described in Appendix D.1 and D.2, respectively.

Dispersants stabilise ceramic particles in suspension as described in Section 4.2.3.2. As measurements used to ascertain the optimum polyelectrolyte concentration are often related to particle stability and agglomeration level, the techniques used in the literature are described in Appendix D.3.

4.4 Parameters Related to the EPD Set-up

4.4.1 EPD kinetics and the Hamaker Equation

Besra et al. (2007) included the effects of deposition time, applied voltage, concentration of solid in suspension and conductivity of substrate as system-based variables. The Hamaker equation [4.6] was formed by obeying the principle of conservation of mass, and can be used to show how the system variables alter the EPD coating characteristics (Hamaker 1940).

$$\frac{dY}{dt} = f.\mu.E.S.c \qquad [4.6]$$

$$\mu = \frac{v}{E} \qquad [4.7]$$

Y is the deposition yield (kg), t is the deposition time (s), μ is the electrophoretic mobility ($m^2.V^{-1}s^{-1}$), S is the surface area of the electrode (m^2), c is the concentration of solids in suspension ($kg.m^{-3}$), v is the particle velocity ($m.s^{-1}$), E is the electric field strength ($V.m^{-1}$) and f is a correction factor, taking into account the fact that not all particles brought to the electrode by electrophoresis are incorporated into the deposit (Biest 1999).

4.4.2 Role of Deposition Time

The time term (t) within the Hamaker equation is given as part of the deposition rate, and so the coating thickness will increase linearly with time if the constituent terms that make up the Hamaker equation remain constant. However, during the course of the EPD process, a number of changes can take place. Several different set-up modes can therefore be described, along with how the deposition weight changes over time for each.

According to the Hamaker equation, there is a linear relationship between the rate of deposition and the electric field strength, although this variable may not stay at a constant level over time. The electrical resistance of the EPD deposit that forms is typically larger than that of the suspension, and the growth of an insulating coating on the substrate would therefore reduce the strength of the field that can be generated for a given applied voltage. When a constant current system is used, the electric field stays constant, despite layer build-up. The difference between curves A and C in Figure 4.5 shows the effect of an increasing system resistance on deposition rate. The velocities of the charged particles in suspension are reduced by the deteriorating electric field strength, which accounts for this declining deposition rate with time.

The difference between the deposit and suspension resistances can determine the coating thickness achievable (Sarkar 1993). Using a constant voltage/constant suspension concentration set-up, they observed that it was "nearly impossible to fabricate millimetres thick samples" when ethanol was used as the suspension media for alumina, as the deposit had a far higher electrical resistivity. For alumina in an acetic acid-stabilised ethanol suspension, the resistivity of the resulting deposit was only marginally higher than that of the suspension, which resulted in thicker achievable deposits. Curves A and C should therefore be equivalent (according to Sarkar 2004) if the resistivities of the suspension and deposit are the same.

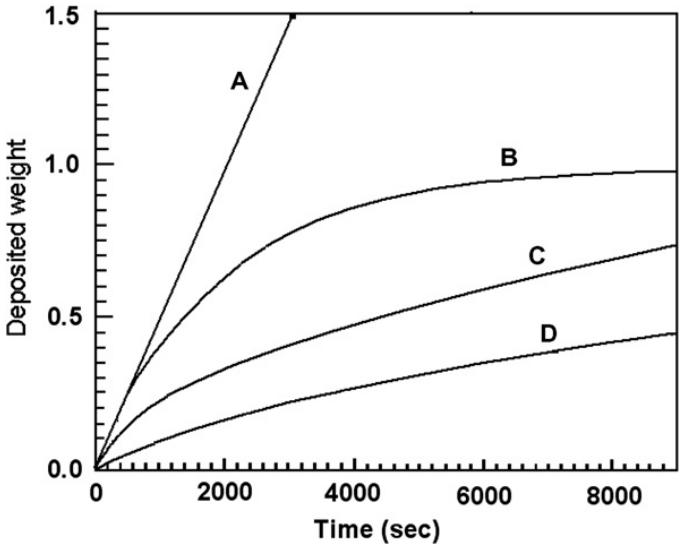

Figure 4.5 Graph showing the relationship between deposition weight and time for four different EPD systems. Curve A shows a constant-current, constant-suspension concentration set-up. Curve B shows a constant-current, decreasing suspension concentration set-up. Curve C shows a constant-voltage, constant-suspension concentration set-up. Curve D shows a constant voltage, decreasing suspension concentration set-up. (Sarkar 2004)

4.4.3 Suspension Concentration and Depletion

The concentration of particles in suspension (or solids-loading) is given by c in Equation [4.6], and there is a linear relationship between this and the deposition rate. As the EPD process brings colloids to the substrate surface over time, there will be fewer particles in suspension to increase the thickness of the electrophoretic deposit, unless the particle concentration is replenished by some mechanism. The effect of decreasing suspension concentration on rate of deposition can be seen in Figure 4.5, for both constant-current (curves A and B) and constant-voltage (curves C and D) set-ups. The formation of an EPD deposit is the principal mechanism by which the solids-loading in suspension is reduced, although the effect of particle settling due to gravity is another one that needs to be taken into consideration.

In addition to particle concentration depletion, ion concentrations also become depleted over the course of the EPD cycle. The ions that move with the charged particles in suspension are depleted at the deposition electrode, and so the conductivity of the suspension also changes over time, which affects the relationship between deposit and suspension resistances as the coating builds up (De, 1999).

To model this, Biest (1999) split the potential drops of an EPD system into terms that could be displayed as part of resistor set-up within a circuit diagram, so that the varying resistivity of a component with time could be taken into consideration. This model is more fully described in Section 4.4.5.

4.4.4 Effect of Electrode Separation Distance and Voltage

The relationship between the electric field strength (E) and applied voltage (V) for two parallel plates is shown in Equation [4.8]. In this model, there is a vacuum between the plates, and one can simplify the EPD suspension and describe it as a dielectric, so that Equation [4.9] can be used for approximations:

$$E = \frac{\sigma}{\varepsilon_0} = \frac{V}{d} \qquad [4.8]$$

$$E_{effect} = \frac{\sigma}{\varepsilon_r \varepsilon_0} = \frac{V}{\varepsilon_r d} \qquad [4.9]$$

d is the distance between the plates (m), σ is sheet charge density ($C.m^{-3}$), ε_0 is the permittivity of free space (8.85×10^{-12} $F.m^{-1}$), ε_r is the dielectric constant of the material, and E_{effect} is the effective electric field (taking into account dielectric polarisation) ($V.m^{-1}$). From these equations, for a plate electrode set-up, there is an inversely proportional relationship between

electrode separation distance and electric field strength, and a linear relationship between the applied voltage and field strength. According to the Hamaker equation [4.6], the deposition rate should therefore increase when the applied potential is raised, due to faster particle velocities achieved in suspension [4.7].

Zhitomirsky et al. (1997) monitored the effect of deposition yield against both time and voltage using a hydroxyapatite species in isopropyl alcohol. Figure 4.6 and Figure 4.7 from this work display larger resultant deposit yields when the working voltage is increased for all deposition times tested. As a constant voltage/depleting suspension concentration set-up was used, the growth of an insulating deposit decreases the intensity of the generated electric field. This is shown in the Figure 4.7, which shows a drop in current density with time (where the current density is a measure that can be approximated by the product of the electric field strength and the suspension conductivity).

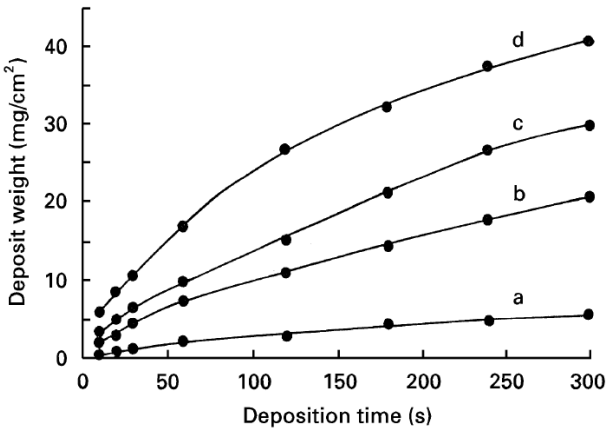

Figure 4.6 Graph from literature showing relationship between weights of deposited hydroxyapatite (on Ti_6Al_4V substrate) and time. This relationship is shown for different applied voltages: (a) 10 V (b) 50 V (c) 100V (d) 200V (Zhitomirsky 1997).

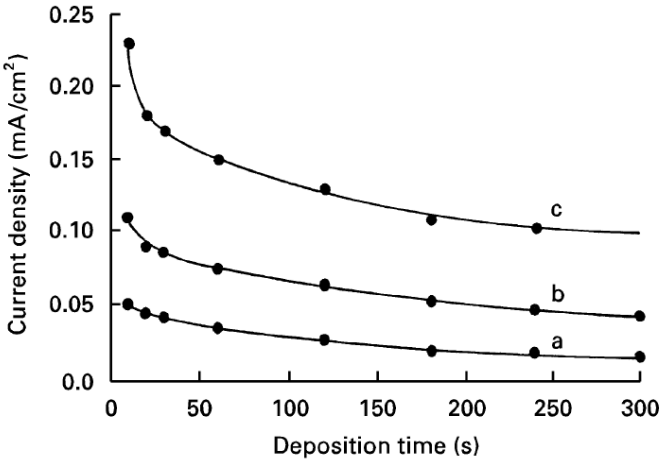

Figure 4.7 Graph from literature showing current density against deposition time for deposition of Hydroxyapatite at different applied voltages: (a) 50 V; (b) 100; (c) 200 V. (Zhitomirsky 1997).

To calculate the effect of increasing deposit thickness on the electric field, the resistance of an EPD system can be split into terms that act like resistors within an equivalent circuit (Biest, 1999). The applied potential (V) in Equation [4.10] is consumed by a potential drop at each electrode and by an ohmic potential drop over the suspension and the deposit. Figure 4.8 shows this diagrammatically.

$$V = \Delta\Phi_1 + d_1 I\rho_{dep} + (d - d_1) I\rho_{susp} + \Delta\Phi_2 \qquad [4.10]$$

$$I = \frac{V - (\Delta\Phi_1 + \Delta\Phi_2)}{[d_1\rho_{dep} + (d - d_1)\rho_{susp}]} \qquad [4.11]$$

$$E_{susp} = I\rho_{susp} \qquad [4.12]$$

d is the distance between the electrodes (m), d_1 is the thickness of the deposit (m), ρ_{dep} the resistivity of the deposit (Ω.m), ρ_{susp} the resistivity of the suspension (Ω.m), I is the current (A) and E_{susp} is the electric field strength in the suspension ($V.m^{-1}$). $\Delta\Phi_1$ and $\Delta\Phi_2$ are the potential drop terms at each electrode.

The deposition part of EPD is a kinetic phenomenon, and the rate at which particles accumulate has an influence on their packing behaviour. A strong electric field leads to a high deposition rate, although particles cannot traverse across the deposit to sit in their preferred positions and so form a close-packed structure as the higher applied potential exerts more pressure on the particles, and so restricts their movement. The presence of strong electric fields may also cause turbulence in the suspension, and the coating may become disturbed by flows in the surrounding medium, even during its deposition.

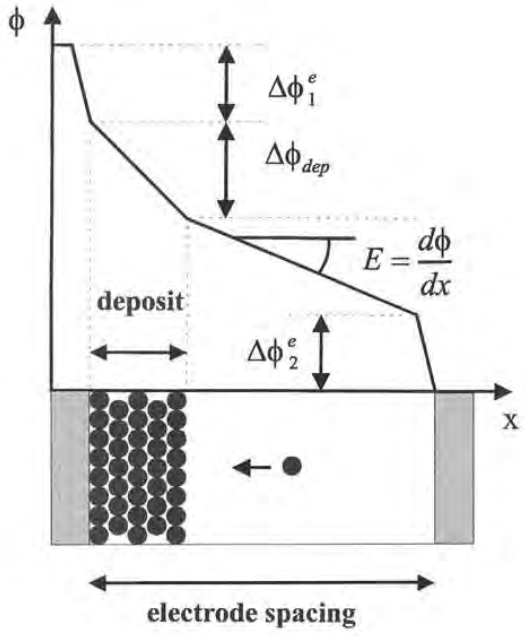

Figure 4.8 Diagram showing the evolution of the potential in an EPD set-up (Biest, 1999).

Besra et al. (2006) showed this gradient in deposit density with applied potential for an yttria-stabilised zirconia powder in an organic medium. Low EPD potentials of ~ 25V achieved dense deposits; whilst those achieved using high voltages (~ 500V) had a higher porosity.

4.4.5 Measuring Deposition Yields

The surface area of the electrode and the solids-loading of particles in suspension can be determined or calculated during the EPD process. The particle electrophoretic mobility for a given modified suspension can also be obtained using measurement techniques that also measure zeta potential, as described in Section 4.3.1. A relationship between deposit thickness and time can therefore be discerned so that deposit thickness measurements do not have to be carried out on every sample unless desired.

4.5 Additional Parameters to consider within this Application

4.5.1 Use of Aqueous Media EPD over Organic Media EPD

4.5.1.1 Advantages and Disadvantages

Both organic and aqueous systems can be used as dispersant media in EPD. Water-based systems are more environmentally friendly, require lower voltages, have faster kinetics and are cheaper as a result. It is these advantages that act at as the major drivers for research into overcoming a number of drawbacks. The main problem is related to electrochemical reactions that occur at the electrodes when a current flows. Water electrolysis occurs at voltages above 1.4 volts for pure water (Tabellion, 2004), with the following reactions occurring:

At positive electrode (anode): $2H_2O \rightarrow O_2\,(gas) + 4H^+ + 4e^-$ [4.13]

At negative anode (cathode): $4H_2O + 4e_- \rightarrow 4OH^- + 2H_2\,(gas)$ [4.14]

The action of charging mechanisms can make the colloidal particles either positive or negative in nature, and during EPD, the species would form a deposit on the cathode or anode

respectively. The gas formed at the deposition electrode can become incorporated into the forming deposit as bubbles when it fails to escape through the contact clearance that lies between the electrode and the surface of the deposit (Suzdal-tsev, 2004). Accumulated gas will eventually break through the deposited material to leave pits, blisters, or blow-holes that greatly reduce the uniformity and strength of the deposit (Moreno, 2000). Whilst a low voltage acts as a threshold for the onset of water electrolysis bubble formation, the rate of bubble production grows significantly with increasing current.

The use of metallic deposition electrodes in aqueous suspensions can lead to electrode oxidation, where metallic impurities migrate towards the surface and become retained in the deposit both as heterogeneities and residual porosity. As this can degrade the properties of the coating, it limits electrode material options, as discussed in Section 5.1.

When an electric field is applied to an aqueous EPD suspension, the liquid phase is drawn through the particle interstices in the coating being formed on the electrode substrate, in a process called water electro-osmosis. As the water migrates away from the anode and towards the cathode, its effect on anodic and cathodic EPD set-ups differ. Electro-osmosis can be a beneficial effect in anodic EPD, by accelerating the rate of drying within the coating, although it can lead to crack formation in thicker deposits if not properly controlled.

4.5.1.2 Methods for Avoiding Gas Entrapment

In an attempt to overcome the problems of associated with water electrolysis, a number of methods have been investigated, each attempting to avoid the formation of gas bubbles at the deposition surface (Suzdal'tsev 2004). A number of different techniques are highlighted in this section.

Su et al. (2001) found that the use of potentials below 4 volts led to uniform bubble-free deposits of PZT on platinum wire. Coatings greater than 5 μm in thickness, however, showed agglomeration effects on the surface due to time-related field declination. Since voltages above the threshold for water electrolysis may have to be used when thicker EPD coatings are required, this approach would not be industrially feasible for use in investment casting.

Some electrode materials can store or trap the ions formed from water electrolysis within their structure, and so inhibit gas formation. Kerkar et al. (1993) used 'hydrogen-storing' palladium as the deposition electrode in cathodic-EPD. High voltages of between 25 and 200 V could then be used, to produce 2.5 mm bubble-free coating cross-sections. Such materials possess a hydrogen storing-saturation limit, however, which would further be reduced if the material was incorporated into resins or waxes to produce a melt-out substrate.

The 'membrane method' involves the use of a porous, ion-permeable membrane that acts to separate the cathode and anode (Hamagami, 2002). A set-up devised by Tabellion et al. (2004) is shown in Figure 4.9. Ceramic particles in suspension form a deposit on the porous substrate membrane, whilst ions pass through the pores of the membrane and recombine to generate gas bubbles at the electrodes. No gas bubbles are incorporated into the deposit, as ion recombination occurs away from the where the ceramic coating is produced.
The 'membrane method' tends to produce low deposition densities (Hamagami, 2002), however, which would prevent its use in a number of ceramic coating applications.

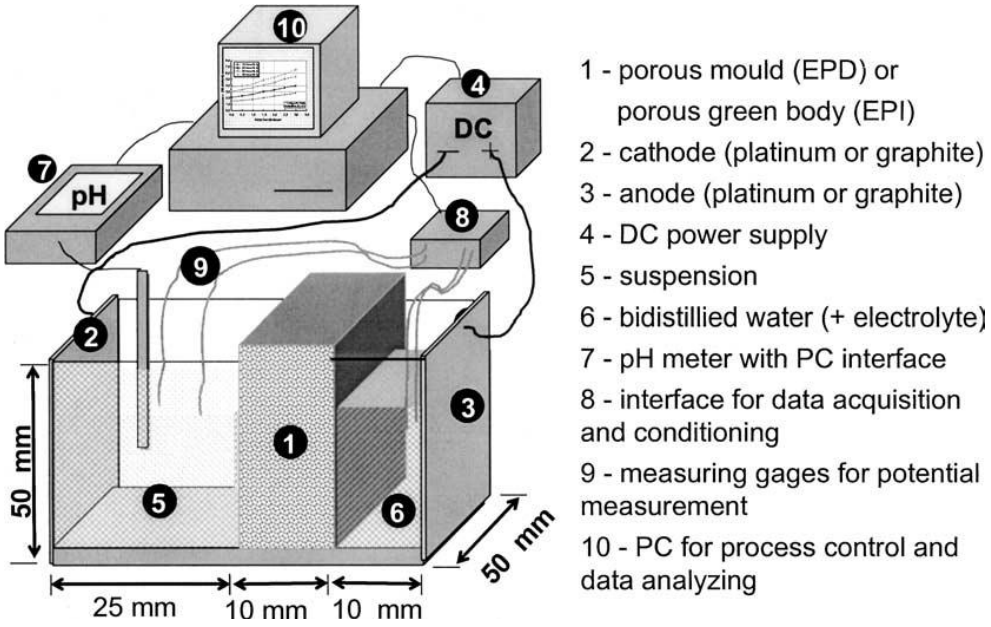

Figure 4.9 An aqueous-media EPD setup called the 'membrane method' (Tabellion 2004)

Besra et al. (2009) studied the effect of using a pulsed DC source, to give the water electrolysis gases (H_2 at the cathode and O_2 at the anode) sufficient time to escape the deposit between pulses, and so lead to bubble-free EPD coatings. In this work, a 50% duty cycle as used, and the DC pulse duration was varied from 180 seconds to 0.001 seconds.

Bubble-free deposits were achieved within a narrow band of pulse settings, as shorter pulse times led to no appreciable deposition and longer pulse times led to bubble entrapment. Additionally, pulse mode methods were more successful when cathodic EPD set-ups were used. This was attributed to the high solubility of cathodic gas, hydrogen (at 1617.6 $mg.l^{-1}$), which meant that it could easily diffuse away from the electrode surface during the pulse gaps, and thus avoid being retained in the deposit at lower pulse frequencies.

4.5.2 Effect of Substrate Conductivity

The properties of the EPD substrate strongly influence the nature of the resultant deposit. The uniformity and conductivity of the substrate is of importance as it constrains the resultant electric field strength in suspension. Chen and Liu (2001) used pressed lanthanum strontium manganite (LSM) as the EPD deposition electrode material, which has a low conductivity in its unfired state. The electrophoretic deposition of yttria-stabilised zirconia (YSZ) from suspension occurred at a slow rate, and the obtained film was non-uniform. The substrate's high electrical resistivity value was due to the presence of a binder phase, and firing the material at 700 °C removed this binder and consequently improved its electrical conductivity. Use of the more highly conductive substrate in EPD led to good quality YSZ deposits. It can be deduced that the use of a moderately conducting EPD substrate on a highly conductive tab would introduce additional terms to Equation [4.10], although there is no experimental evidence in the current literature to support this notion.

CHAPTER 5. FORMATION OF CONDUCTING DEPOSITION SUBSTRATE

5.1. Introduction – Currently Used Pattern Materials

As described in Section 2.1, the investment casting process currently uses a number of successive investment slurry coating steps to build up the ceramic shell. For the complex structures created using investment casting, the die cast patterns used as the substrate for the ceramic have to be easily removed, and this can be done by either melting or dissolving out the material to leave the hollow ceramic shape. Wax and resins are therefore commonly used, and one can look at the properties and modifications made to these materials to give an overview of the properties required of the EPD substrate.

Waxes are organic compounds of carbon, hydrogen and oxygen, as esters of fatty acids and monohydoxylic alcohols, and have a number of properties that make them suitable for use as an investment casting pattern material. Waxes have relatively low melting points (usually situated between 45 and 85°C), and form low viscosity liquids on melting. This means that the material only has to undergo a low level of heating to be die cast, and can also be melted out at temperatures far below the sintering temperature of the invested ceramic. They tend to be non-reactive with the ceramic coating and produce patterns with a good surface finish on being die cast, which is subsequently transferred to the ceramic shell.

Although an unmodified wax possesses a number of useful properties for pattern formation, it is deficient for purpose in two important areas. The first is with regard to its strength and rigidity, as the pattern needs to retain accurate dimensions both under its own weight and with the extra mass of the green ceramic coating on it. This is especially important when fragile patterns with fine structures need to be made. The second important parameter is with regard to dimensional control. The investment casting procedure is described in Section

2.1, and in the initial stage, the pattern wax is injected into a die so that it can be formed into the desired geometry. As pure wax tends to shrink by approximately 2 % (linear) on cooling from injection temperatures, surface solidification shrinkage cavitation can occur both during and after pattern injection (Clegg, 1991).

To improve the wax behaviour in these two areas, modern investment casting waxes contain numerous components, including natural hydrocarbon waxes, natural ester waxes, synthetic waxes, natural and synthetic resins, organic filler materials, and water. It is in varying these additional constituents in specific proportions that the modified wax properties such as melting point, viscosity, thermal coefficient of expansivity/contractivity and hardness can be manipulated to suit specific requirements.

Polymers are often used as additives to improve the fracture strength and fracture toughness of the wax. Polyethylene is the most commonly used polymer; other examples include ethylene vinyl acetate, ethylene vinyl acrylate, nylon, and ethyl cellulose. As they are viscous at wax processing temperatures, only small quantities should be added.

Surface cavitation, or sinking, is a manifestation of solidification shrinkage. Whilst the addition of polymers can reduce this effect, they can only be added in small quantities, and so their effect is minimal. Resins or fillers are instead used to reduce or eliminate problems associated with pattern shrinkage. Resins are liquid at wax processing temperatures, with both synthetic and natural forms being used as a wax additive. When compared to waxes, they exhibit only small volumetric changes as they are heated or cooled, and the resulting reduction in solidification shrinkage is directly proportional to the resin concentration in the wax. Fillers are generally solid at wax processing temperatures. As the filler remains solid, it does not contribute towards solidification shrinkage of the wax blend, although the reduction in the total shrinkage of the wax is directly proportional to the amount of filler added.

The choice of filler material is not only governed by its thermal expansion coefficient, because there are a number of additional factors that have to be taken into consideration before it can be successfully added to a wax. An ideal filler material has a relatively high melting point, leaves no ash on dewaxing, is non-reactive towards both the wax and all components of the shell itself and has a fine particle size, with specific gravity and thermal conductivity values that are similar to those possessed by the wax mixture. Commonly used examples include crosslinked polystyrene, isopthalic acid, terepthalic acid and water, and these meet most, if not all of the requirements stated above.

As waxes can be easily blended, many different requirements can be met. An example of this is in the creation of a wax with both a low melting point and low melt viscosity, which makes it easy to compound, inject, assemble into clusters and melt out. These properties allow for it to be injected at low temperatures and pressures, and this, combined with lack of abrasiveness, leads to lower tooling costs. Such properties would, however, come at the expense of others, like strength and thermal expansivity, and so a number of different wax grades can be used to form a single sprue according to the needs of each section. A number of wax selection criteria, with associated properties, are listed below (Clegg 1991):

1. **Injection:** Softening point, freezing range, rheological properties, ability to duplicate detail, surface and ‘set-up time’.
2. **Removal, Handling and Assembly:** Lubricity, strength, hardness rigidity, impact resistance, stability and weldability.
3. **Dimensional Control:** Thermal expansion/contraction, solidification shrinkage, cavitation tendency, distortion and stability.
4. **Mould Making:** Strength, wettability, resistance to binders and solvents.

5. **Mould Dewaxing and Burnout:** Softening point, viscosity, thermal expansion, thermal diffusivity, and ash content.
6. **Miscellaneous:** Cost, availability, ease of recycling, toxicity, environmental factors.

5.2. Possible Material Choices

As the aim of this project is to replace the primary dip coating step of investment casting with one using EPD, it is important to take note of the differences between the processes, and so come up with a substrate pattern material that can replicate what investment casting waxes do within the currently-implemented industrial process.

Electrophoretic deposition takes place due to the presence of an electric field within the suspension medium, which attracts charged particles in suspension towards an electrode of opposite charge. During the deposition stage, the particles are deposited onto this electrode to form a coating. The main modification that therefore has to be made to the pattern is to make it electrically conducting, whilst retaining or replicating the other properties of an investment casting wax. There are three main ways of carrying this out:

1. The first is to place a high electrical conductivity core within the melt-out substrate so that the whole geometry acts as the deposition substrate. The electric field formed by the coated conducting core has to be high enough to overcome the masking effect of the melt-out geometry that surrounds it. One major concern associated with this idea relates to the core design generating an electrical field that results in uneven EPD ceramic coating thicknesses on the substrate.

2. The second concept is to use an electrically conducting material which can additionally be melted or dissolved-out. The possibility of using waxes, resins or polymers containing conductive fillers is discussed in Section 5.3. The first and second concepts can be combined, as the conductive melt-out substrate could be formed with a more highly conducting electrode tab at its centre.

   Conducting polymers or conductive polymer blends could also be used to form an EPD substrate. Conjugated polymers are semiconductors due to the presence of delocalised π-molecular orbitals along their chains (Wallace, 2000), and doping processes can be used to vastly improve their electrically conductive properties. Shirakawa (1977) was the first to accomplish this, by doping a conjugated polymer called polyacetylene. Soluble derivatives of organic conductors like polythiophene (Elsenbaumer, 1986), polyaniline (Li, 1987), polyfluorene and polypyrrole have been produced, and so can be processed using a range of manufacturing techniques.

3. The third concept is to use a conductive coating that can be easily applied to the surface of the substrate before EPD is carried out. Using this method, an unmodified investment casting wax could be used to form the substrate core, which means that the investment casting stages on either side of the ceramic coating steps could be carried out with only minor alterations.

   Carbon black coatings can be deposited on non-conductive substrates, and have been used industrially for a number of applications, most notably to form an antistatic layer on cathode ray tubes (Takamiya 2000). Antistatic coatings can be painted on, or applied using thin film deposition techniques, such as electron beam deposition, chemical vapour deposition and sputtering, to produce antistatic coatings with typical thicknesses in the order of 0.1 μm (Wang 2003). For both thin film deposition

techniques and traditional painting methods, there are no perceived problems associated with increasing coating thickness so that the required electric field strengths can be produced for EPD. Achieving coating thickness uniformity on complex geometries remains an issue, however.

The in-mould coating (IMC) process involves the injection of a substance onto the surface of the moulded part while the part is still in the mould, and could be used to form conductive coatings on complex geometries without line-of-sight issues (Strauss, 2001). Cortright (2009) described the use of carbon black within an IMC, although the addition of carbon black to the IMC resin at a low loading of 2.8% is unlikely to produce the surface conductivities required for EPD. Furthermore, resin viscosity changes with carbon black addition, and it is not currently known how this relates to the coating material viscosity limit associated with the IMC process (Aramphongphun, 2007).

The Wolz process (Wolz, 2009) was created specifically for EPD applications, and involves the use of aqueous-media EPD to form alumina or zirconia coatings on a dental implant stump or abutment. An insulating stump is initially coated with a separating agent, so that it can be removed after the EPD coating operation. A hygroscopic salt like NaCl is then applied on top of this, so that the part can act as the deposition electrode. According to the author, the hygroscopic salt layer both conducts sufficiently for EPD and inhibits bubble formation from aqueous suspension (in a process described in Section 4.5.1.1), to make it a promising alternative to conductive composite substrates.

In addition to the concept of using full conducting polymer substrate electrodes, conducting polymers have been deposited onto both electrically conductive and non-conductive substrates. Hu et al. (2001) used cyclic voltammetry to form a

polyaniline (PANI) coating on graphite from a solution containing 1 M HCl and 0.2 M aniline, whilst Tüken (2006) used cyclic voltammetry to electrochemically synthesize a polypyrrole layer on stainless steel from a water-based pyrrole solution. Uchikoshi et al. (2008) formed a uniform coating of conductive polypyrrole on non-conductive glass and ceramic substrates, by chemically polymerising a water-based pyrrole solution. The potential advantage of such processes relate to the ability to coat a number of melt-out substrates from a single solution for EPD.

5.3. Filled Wax Composites

Specialised waxes are currently used as a pattern upon which the refractory material is formed, and modifying these with conducting fillers would make them into deposit electrode for EPD. The initial wax shaping stages could then be carried out with only minor alterations, which easily fits the EPD process as a whole into the investment casting process.

There are a number of materials that can be used as the conducting filler within a wax matrix. Metallic filler particles tend to have too high a density to be used as fillers within a wax, as even aluminium, with a density of 2.70 $g.cm^{-3}$ (at 25°C), would settle out quickly and produce electrically conductive inhomogeneities as cooling takes place. Even so, a patent by Kurlandsky (1955) refers to the use of finely divided silver particles as a conducting filler material within wax. One way to reduce the problem of filler settling is to develop electrically conducting filler particles with a lower density. Koenig (1978) did this by using silver-coated glass microspheres as a filler material, to form an electrically conducting thermoplastic wax.

Within aqueous-media EPD, the use of fully metallic electrodes has a number of associated problems. The main one is related to electrode oxidation that occurs when a voltage is applied, where metallic impurities migrate towards the suspension and become

retained in the deposit as heterogeneities. The presence of certain metallic compounds within the ceramic shell can have a detrimental effect on the resulting cast metal, and could be a problem if metal particle-filled wax electrodes contribute to the presence of undesirable metallic species within the face-coat of the invested ceramic shell.

In the literature, EPD is often successfully carried out on graphite electrode substrates, and so the use of carbon in a number of forms as a wax filler material can be considered. The density of electrically conductive carbon varies between 1.8 and 2.3 $g.cm^{-3}$, depending on the form of the carbon particulates, and whilst they are still likely to settle within the material as the wax solidifies, such an effect would be expected to be less pronounced than that seen in metal-filled waxes. One issue associated with their use is related to the dewaxing process, as the presence of carbon-based filler could lead to waxes with substantial ash contents. There are a number of different forms of carbon, and the structures of carbon black, graphite, carbon nanofibres and flake graphite are described in Section 5.5.

The rheology or flow behaviour of filled waxes is of great importance, and will be used to determine whether a material is suitable for industrial injection methods. The effect that the addition of filler has to a material's flow behaviour is covered in Section 6.8, which is preceded by an introduction to rheological concepts and theories in Section 6.

5.4. Composite Conductivity and Percolation Behaviour

Melt-out matrices containing conductive filler particles need to be conductive enough for EPD coating to form on the substrate's surface. Percolation is a phenomenon usually associated with the connectivity of one substance or phase within the matrix of another. The percolation threshold (P_c) is reached when this one phase is present in high enough concentration to form long-range connectivity within the random system. Whilst percolation

theory is often used to model fluid flow through porous media, the theory can be applied in the present work to the flow of electric current, as conducting particles form infinite bridges in an insulating medium. The percolation threshold here corresponds to the point where the conducting particles are at a high enough concentration to form a connecting lattice, and this is shown by a significant decrease in the sample's resistance with increasing conductor phase content (Grimmett, 1989)

There is much published information on percolation theory; and in the published work, conductor-insulator composite materials are often used to model behaviour. Simplistic models of conducting and insulating spheres in certain packing conformations give P_c bond values of 0.119 for face-centred cubic, 0.179 for body-centred cubic and 0.247 for simple cubic lattices (Zallen, 1983). These figures are only applicable when the sizes of the purely spherical conducting and insulating particles are equal in dimension, with no size distribution. Models with conductive spheres were further developed by Scarisbrick (1973), who looked at the probability of conduction occurrence within unit cubes.

R. Kusy (1977) showed that dispersions of one powder within another have properties influenced by both the particle size ratio and the volume fraction. Varying the particle size ratio $\lambda = d_i/d_c$ (where d_i is the diameter of the insulating particle and d_c is the diameter of the conducting particle) makes the mixture either random or segregated in nature, as shown in Figure 5.1. The critical volume percent (V_c) is the volume fraction required for the dispersed powder phase to become continuous, and according to this model, plotting the critical volume percent against the particle size ratio gives an exponential curve. This means that decreasing d_c within a system with a fixed insulating particle diameter results in a smaller critical volume percent. V_c and P_c are only equivalent when the dispersed powder phase is randomly distributed throughout the matrix, and so P_c values given in the literature for segregated systems have been labelled as V_c values within the present work.

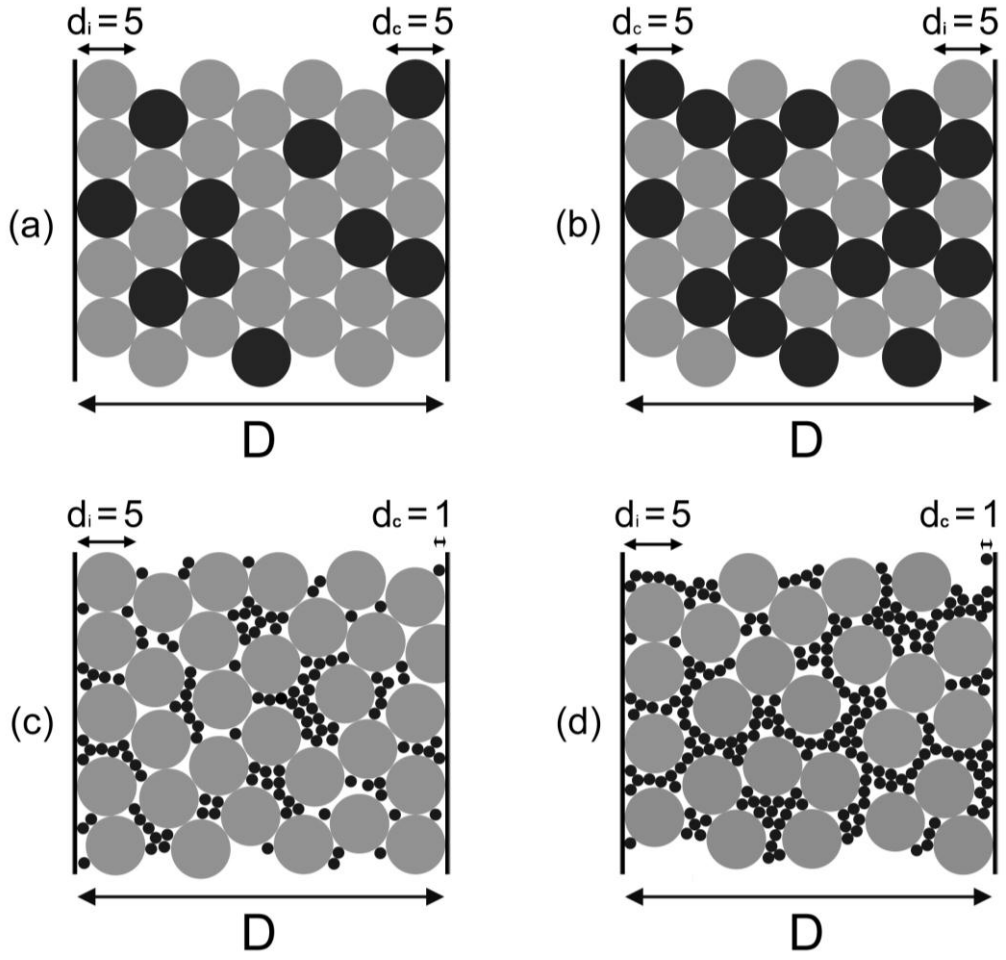

Figure 5.1 Bi-powder dispersions represented in two-dimensions, within an elementary environment, D. The dark circles represent spherical conducting particles, whilst the light circles represent spherical insulating particles.
(a) is a system where $d_i/d_c = 1$ and $V<V_c$; **(b)** is where $d_i/d_c = 1$ and $V>V_c$;
(c) is a system where $d_i/d_c = 5$ and $V<V_c$; **(d)** is where $d_i/d_c = 5$ and $V>V_c$.

A. Kusy (1977) considered the role of particle geometry on percolation, as previous models applied to either spherical or cubic particle geometries. When conducting particles with other geometries are used, the probability of a random conducting chain continuing over a distance increases. An order function ϕ is used, with $\phi = 1$ for randomly distributed spherical and cubic particles. Any decrease in the value of ϕ corresponds to an increase in the order of the conductive phase in the resistive material, which is associated with a change the conductive particle geometry and/or particle size ratio, λ.

In the work of Chiteme and McLachlan (2003), conducting graphite and carbon black powders formed onto the surface of the larger insulating wax particles to create a three-dimensional ‘‘cellular’’ structure. The V_c values obtained were approximately three times lower than those expected in the models developed by R. Kusy (1977), with a carbon black system V_c of 0.012 (1.2 vol%), and graphite system V_c of 0.035 (3.5 vol%). These differences were attributed to the combined effects of a wide particle size distribution and morphological changes on grinding and on compression.

Many systems that have been investigated do not contain a binary mixture of particles, and instead consist of conducting particles within a continuous insulating matrix. The structure of the continuous phase itself therefore has to be studied, to establish whether segregation might occur. Balberg (1987) attributed a low observed carbon black V_c values to the formation of carbon aggregates on insulating matrix grains, which is rather like the cell structure described by Chiteme (2003).

5.5. Forms of Carbon used in Conductive Filler Composites

5.5.1. Introduction

A number of conductor-insulator composite systems have been considered in the present work with the intent of using them as possible electrode materials. Carbon-based conducting fillers include graphite powder, carbon black, carbon nanofibres, carbon nanotubes and flaky graphite. The structures of carbon black and graphite, along with their use in conductive composites, are described in Sections 5.5.2 and 5.5.3, respectively, as these filler materials are focussed on within the present work.

The use of roughly spherical particles as a conductive filler material could require loadings of more than 15 - 20 wt% to give satisfactory composite conductivity values, which

may result in materials with both poor mechanical properties and a high density (G Chen 2001). Forms of carbon with higher aspect ratios have therefore been considered.

Carbon nanofibres are a form of carbon made into nanoscale cylinders. Sheets of graphene (as described in Section 5.5.3) stack on top of one another to form these cylinders in several different growth conformations, including graphene-stacking shapes resembling piles of plates, cones and cup-shapes. Nanofibres are made when specific hydrocarbons and carbon monoxide are decomposed over a hot metal surface, to produce non-continuous fibres with lengths between 5 to 100 mm, and widths between 5 and 500 nm (Rodriguez, 1995). Whilst the results for nanofibre-laden waxes are promising (Lozano, 2001) (Marken, 2001) (Dijk, 2001), the comparatively high cost of commercially grown nanofibres almost certainly makes their use in melt-out composites non-viable. The highly anisotropic nature of these fibres also has a bearing on varying conductivities within complex shapes, depending upon whether any alignment has taken place.

Carbon nanotubes are a more specific type of nanofibre, and are each composed of a graphene sheet that is wrapped into a single seamless cylinder. A multi-walled carbon nanotube (MWNT) has hollow tube geometry, where the cylinder is made up from multiple graphene cylinders of increasing diameter that are stacked coaxially around one another i.e. like a Russian doll. For their intended use, as conductive fillers within either soluble or melt-out electrodes, the use of carbon nanotubes has been discounted, as they are too expensive for purpose.

Natural Flake graphite is a form of carbon composed of layered graphite nanosheets. The structure of flake graphite differs from that of graphite powders in its morphology. Each graphite particle is made up of many randomly oriented graphite crystals; flake graphite is more distinctly plate-like, with a much larger surface area due to its structure. The layered graphene sheets of flake graphite can be separated by reactions with specific acids to create a

material called expanded graphite. Whilst the sheet-like structure remains intact, vast expansions occur in the c-direction, so that a material with a vermicular or worm-like structure is formed (Inagaki, 1989).

The properties of expanded graphite within composites showed promising results (Mills, 2006) (G Chen, 2001). One notable feature of expanded graphite relates to its formability. In a study by Mills et al. (2006), expanded graphite was compacted into a number of different shapes without the need for a binder material. Capillary forces were then used to draw the liquid wax matrix into the graphite's internal spaces. The mechanical interlocking of the expanded graphite means that this material could potentially be used to make complex shapes with high electrical conductivities. This property makes its utilisation as an EPD substrate material prospectively appealing.

5.5.2. Carbon Black

Carbon black is a form of pure elemental carbon, which exists as aciniform particulate aggregates, i.e. where particles cluster like a "bunch of grapes". Primary particles of carbon black (with diameters between 10 and 300 nm) usually tend to cluster together into primary aggregates (with diameters between 100 and 1000 nm). Industrially, carbon black is formed either through the incomplete combustion or the thermal decomposition of gaseous or liquid hydrocarbons under controlled conditions. Chemisorption occurs over the carbon black surface, to produce oxygen complexes including carboxylic and phenolic groups. These sites decrease the material's electrical conductivity, with the concentration and nature of these sites governed by the formation process and post formation operations (ICBA, 2006). Whilst the majority of manufacturers do not describe the processing steps used in the formation of

products, many advertise grades according to application, and so suitable fillers can be chosen in this manner.

The preparation routes employed by different research groups for the production of carbon black-laden wax materials often involved the addition of the conductive particles to the wax in its molten state (Chrakrabarty 1991) (Chen 1985). Specifics in the literature relating to composite formation are described in Section 8.4, whilst those associated with sample geometry for conductivity measurements are shown in Section 9.2.2. The percolation thresholds determined by a number of studies into carbon black-filled waxes and polymers are tabulated in Table 5.1. Most studies in Table 5.1 were primarily focussed either on the position of P_c, or electrical phenomena around the P_c (Chakrabarty, 1991), and so did not measure the maximum conductivity possible within their system. Chen et al. (1985) showed a more complete graph of resistance versus volume percent carbon, giving resistance values of approximately 100 Ω at 20 vol% and 1 kΩ at 15 vol%, with an apparent V_c at 10.8 vol%.

The disparity between percolation threshold values given in the literature for carbon black-filled systems can be attributed to carbon black's hierarchical structure (Chakrabarty, 1991). Both the mixing conditions and the structure of the grade specifically can govern the extent to which it forms either a random or segregated distribution within the insulating matrix.

Processing can break down the spherical or slightly angular agglomerates, and shear them into a 'mother of pearl' structure, which is a term used to describe how the particles form along the grain boundaries of the polymer or wax matrix (Brosseau, 1997). Brosseau (1997) compared the composites formed when two different carbon black grades were used to form conductive particle-filled polymers. Even though the same processing conditions were used, the different filler morphologies affected the V_c value of the resulting composite, as shown in Table 5.1. Pinto et al. (1999) found that an increased level of intermixing between

the carbon black and liquid matrix led to particle cluster break up before any shearing segregation mechanism took place. The filler distribution became more random in nature, which increased the value of the systems V_c. The presence of shear-induced conductivity channels that reduce the value of V_c would not exist if either a) the mixing process does not effectively facilitate agglomerate breakdown, or b) the carbon black powder grade does not facilitate such shear-induced deglomaration.

Table 5.1 Comparison between the V_c values of different carbon black-wax/polymer composites in the literature.

Principal Author (Date)	**Carbon Black Powder Characteristics**	**Matrix Material (Melting Point (°C))**	**V_c (vol%)**
Chakrabarty (1991)	Particle Size ~ 30 nm (~ 0.1 μm agglomerates)	Paraffin wax (63 °C)	0.76 vol%
Chen (1985)	Particle Sizes under 1 μm	White wax (58 °C)	10.8 vol%
Michels (1989)	Particle Size ~ 50 nm	Unspecified Polymer	< 1.25 vol% (< 2 wt%)
Pinto (1999)	Quimipur grade: Particle Size ~ 50 nm	Nylon-6 (225°C)	5.7 vol% (9 wt%)
Brosseau (1997)	SN2A Y50A: BET specific area 70 m^2g^{-1} Particle Size 40–60 nm	Polycondensate of Diglycidyl ether of Bisphenol F and 1,12 Diamino 4,9 dioxadodecan	0.5–0.75 vol%
Brosseau (1997)	Columbian Chem. Raven 7000: BET specific area 625 m^2g^{-1} Particle Size 20–30 nm	Polycondensate of Diglycidyl ether of Bisphenol F and 1,12 Diamino 4,9 dioxadodecan	4.5–5 vol%
Rwei (2002)	Cabot Vulcan XC72: BET specific area 254 m^2g^{-1}	Poly(dimethyl siloxane)	1–3 vol%

5.5.3. Graphite

Graphite is a form of carbon made up of layered graphene sheets, which is a term used to describe carbon with a planar hexagonal crystal lattice. These planes have a separation distance of 0.335 nm, and are held together by the combined effects of electronic delocalization and van der Waals interactions. Graphite's electrical conductivity can be attributed to the delocalization of the π-bond electrons above and below the graphene layers. These act as charge carriers, to make graphite conducting along this plane, and not in a direction perpendicular to it. Whilst a single crystal of graphite possesses highly anisotropic electrical conductivity behaviour, graphite powder consists of micro-crystals of graphite where the planes of carbon atoms are randomly orientated. Powder forms can therefore conduct electricity relatively uniformly in all directions. Graphite powders are roughly spherical agglomerates of flake-like particles, which can be formed by heating powdered petroleum coke above its graphitisation temperature.

The research of Chiteme and McLachlan (2003) enabled a direct comparison between the percolation thresholds of carbon black and ground graphite powders using the same preparation methods and matrix material. The V_c for carbon black system (1.2 vol%) was far lower than the V_c for the graphite system (3.5 vol%). This difference is associated with the way that the powder behaves within the matrix. As the carbon black particles are actually particle aggregates, they are sheared into smaller particles, which lie along the matrix's grain boundaries to form an ordered conducting network. Even though graphite powder is composed of graphite micro-crystals, on shearing, these particles do not break down in a similar fashion during the composite fabrication process. Despite this drawback, graphite's low cost and ease of use within composite formation processes justified its utilisation within the present work.

CHAPTER 6. RHEOLOGY

6.1. Introduction to Rheology

Rheology is the study of the deformation and flow of matter (Barnes, 1997), and was first defined by Bingham and Raines in 1928, deriving the term from the Greek word “rhei”, which means “to stream”. It can describe both the flow behaviour of liquids and deformation behaviour of solids, as both of these reactions are in response to the application of high shear stresses. Rheology covers all forms of shear behaviour, between that exhibited by ideal viscous (Newtonian) liquids and ideal elastic (Hookean) solids. The term viscoelastic is used to describe materials exhibiting rheological behaviour between these two extremes due to viscous and elastic properties coexisting. In order to describe and explain viscoelastic behaviour, both Newtonian and Hookean behaviour need to be described and explained.

6.2. Hookean Behaviour

Hookean elastic solids display ideal elastic behaviour, where all deformation, i.e. elastic strain, is reversed as the applied force, and hence applied stress is removed. The deformation energy is stored and subsequently recovered on relaxation. Robert Hooke developed the ‘true theory of elasticity’ in 1678, which states that “the extension of a spring is directly proportional to the load added to it”. Equation [6.1] expresses this mathematically.

$$F = -kx \qquad [6.1]$$

The displacement of the end of the spring from its equilibrium position x (m) is proportional to the applied force F (N). k is a material specific spring constant. The negative sign in Equation [5.1] relates to the fact that the restoring force (which is the force that brings the spring back toward its equilibrium length) always acts in the opposite direction of the displacement. For a Hookean solid, as shown in Figure 6.1, the application of shear stress τ (Pa) to the surface D-C results in an instantaneous deformation. Once the deformed state is reached, there is no further movement, but the deformed state persists as long as the stress is applied (Mezger 2006).

$$\tau = G\gamma \qquad [6.2]$$

The angle γ is called the strain, and is proportional to the shear stress, as shown in Equation [6.2]. G is referred to as the rigidity or shear modulus, and is a material property. These are simplistic models from an engineering standpoint, and are elaborated on in the work of Gere (2001).

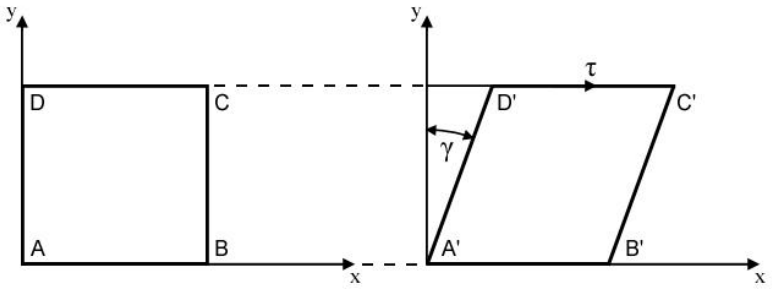

(a) **(b)**

Figure 6.1 Two-dimensional diagrams showing a block of Hookean solid; **(a)** before and **(b)** as a result on the application of shear stress τ. On the application of the stress, the material ABCD becomes A´B´C´D´.

6.3. Newtonian Behaviour

Newtonian viscous liquids, on the other hand, follow ideal viscous behaviour, where deformation causes flow which ceases when the force is removed. The deformation energy is dissipated as heat. In 1687, Isaac Newton developed the 'law for liquid', stating that "the resistance which arises from the lack of slipperiness of the parts of the liquid, other things being equal, is proportional to the velocity with which the parts of the liquid are being separated from one another". Equation [6.3] expresses this mathematically.

$$\tau = \eta\dot{\gamma} \qquad [6.3]$$

$$\dot{\gamma} = \frac{du}{dy} \qquad [6.4]$$

The shear rate $\dot{\gamma}$ (s^{-1}) is defined in Equation [6.4] as the velocity gradient perpendicular to the direction of shear, and is proportional to the applied shear stress τ (Pa). η is the viscosity (Pa.s), and is a measure of a fluid's "lack of slipperiness" or resistance to flow. Figure 6.2 illustrates this for a 2D system. The application of a shear stress τ, to the liquid (through moving the top boundary plate) results in flow. For a Newtonian liquid, the flow continues as long as the stress is applied.

When a real material is placed under shear stress, its response lies between that exhibited by a Hookean solid and Newtonian liquid. The term 'viscoelastic' is used to describe this behaviour, with further details given in Appendix B.1.2.

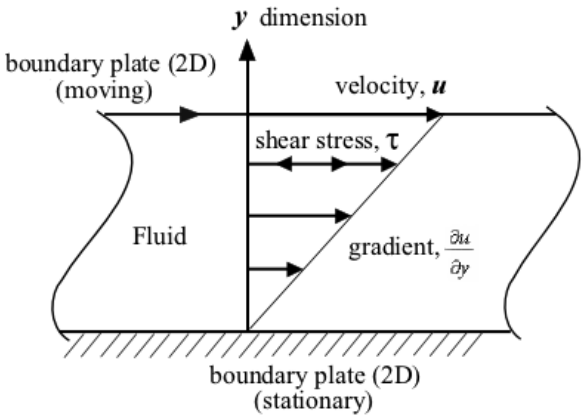

Figure 6.2 Diagram showing the 2D shear behaviour of a fluid between a stationary and moving plate. This is known as Couette flow (Munson 2008).

6.4. Viscosity Changes within Newtonian Fluids

For Newtonian fluids, certain characteristics should be observed (Barnes, 1997):

1. The only stress generated in simple shear flow is the shear stress (the two normal stress differences being zero).
2. The shear viscosity does not vary with shear rate.
3. The viscosity is constant with respect to the time of shearing and the stress in the liquid, and falls to zero immediately as the shearing is stopped. In any subsequent shearing, the viscosity is as previously measured, regardless of the resting period between measurements.
4. The viscosities measured in different types of deformation are always in simple proportion to one another (i.e. the viscosity measured in uniaxial flow extensional flow is always three times the value measured in simple shear flow for a Newtonian liquid). This proportionality is known as the Trouton ratio, *Tr*, and is equal to 3 for a Newtonian liquid. Measurements can be carried to ascertain the Trouton ratios for non-Newtonian systems, where *Tr* does not equal 3.

There are two principal variables that do alter the viscosity of a Newtonian fluid, and it is important to take these parameters into consideration when one looks at both experimental set-ups and the behaviour of non-Newtonian liquids. The first of these is temperature, and the viscosity of Newtonian liquids decreases as the temperature is increased, approximately following the exponential model shown in Equation [6.5].

$$\eta = Ae^{-B/T} \qquad [6.5]$$

A and B are material constants for the liquid and T is the absolute temperature (K). The Arrhenius-Frenkel-Eyring (AFE) formula is given in Equation [6.6], and is based on flow theories considering the potential energy that must be overcome by a molecular unit to move from one equilibrium position to the next.

$$\eta = Ce^{(E/RT)} \qquad [6.6]$$

C is a constant, E is the activation energy associated with flow and R is the ideal gas constant. Due to the presence of an activation energy term, the temperature dependence is generally stronger for Newtonian liquids with higher viscosities. The strong temperature dependence of viscosity is such that, to produce accurate results, great care needs to be taken with temperature control in viscosity experiments. This is discussed more fully in Section 7.2, which describes rheological testing.

The second variable is pressure, and the viscosity of Newtonian liquids increases exponentially with isotropic pressure (water below 30°C is the only exception to this due to the nature of its hydrogen bonding, where the viscosity first decreases before rising

exponentially). The changes are quite small for pressures differing from atmospheric pressure by about 1 kPa, and so the effect of pressure is generally ignored in viscosity experiments and most practical applications.

6.5. Deviations from the Newtonian model

6.5.1. Introduction

Newtonian behaviour is a model describing ideal viscous flow, and any liquid that shows any deviation from the above parameters can be described as being non-Newtonian. For most materials, viscosity and shear modulus are variables.

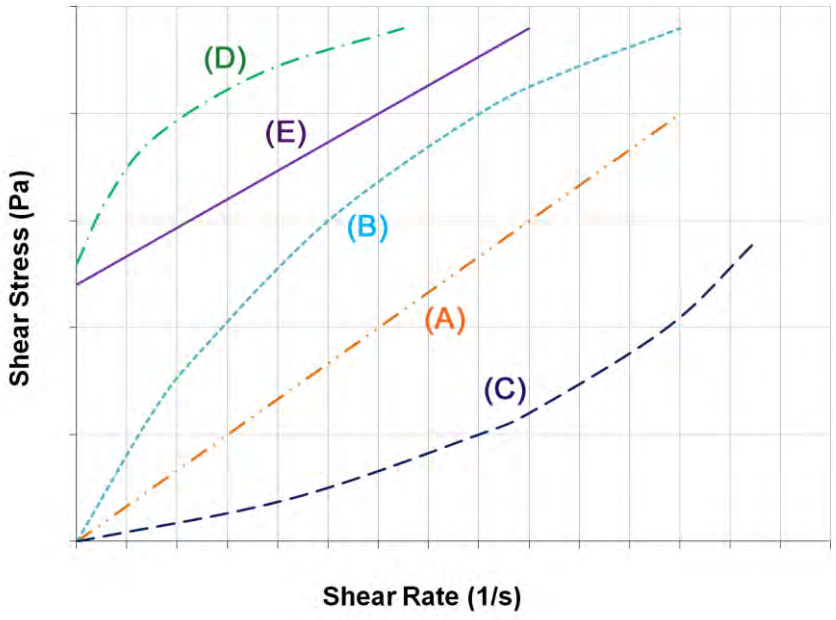

Figure 6.3 Graphs showing the relationship between shear rate and shear stress for material examples exhibiting Newtonian and non-Newtonian behaviour. **(A)** shows Newtonian behaviour (Section 6.3); **(B)** shows shear-thinning (pseudoplastic) behaviour (6.5.2); **(C)** shows shear-thickening (dilatant) behaviour (6.5.3); **(D)** shows shear-thinning behaviour with a yield point (viscoplastic) (Section 6.5.4.1); and **(E)** shows Bingham behaviour (Section 6.5.4.2).

Viscosity and shear modulus values can otherwise vary according other parameters, including the level of stress, stress duration and material history. The way that these parameters change with stress and time defines the nature of their non-linear behaviour. The models described in the following sections are affected by a change in viscosity with shear rate (and/or shear stress). The relationship between shear rate and shear stress for a number of these models is shown in Figure 6.3, where the viscosity is the curve gradient.

6.5.2. Shear Thinning Behaviour

The vast majority of non-Newtonian liquids display shear-thinning behaviour, where the viscosity decreases as the shear rate is increased. The graph in Figure 6.4 show a general curves for a shear thinning material, where the viscosity is constant at very low shear rates, called the 'zero-shear viscosity'. At high shear rates, the viscosity is again constant, but at a lower level, with a value called the 'infinite-shear' viscosity. These two extremes are referred to as the lower and upper Newtonian regions, i.e. the low and high shear rate regions, respectively (Elias, 2003). The shape of the viscosity/shear rate curve between the plateaus depends upon the changing material microstructure. Equations that predict the shape of this general flow curve needs at least four parameters, and one such model that can be used for shear thinning materials is the Cross model, as shown in Equation [6.7].

$$\frac{\eta_0 - \eta}{\eta - \eta_\infty} = (K\dot{\gamma})^m \qquad [6.7]$$

η_0 and η_∞ refer to the asymptotic values of the viscosity at very low and very high shear rates respectively, and K and m are material constants.

Filled waxes were studied within the present work, which can be modelled by looking at the rheology of suspensions. Suspension models will therefore be used to explain non-Newtonian fluid behaviour at the particle level. At rest or at low shear rates, the particles within a shear-thinning material lock up against one another, which inhibits flow. As the shear rate is increased, these particles become arranged into chains with channels between them under shear, which decreases the material viscosity. Owing to viscosity changes across the flow curve, the apparent viscosity is used, and gives the viscosity as a function of shear rate (i.e. $\eta(\dot{\gamma} = 100s^{-1}) = 0.5$).

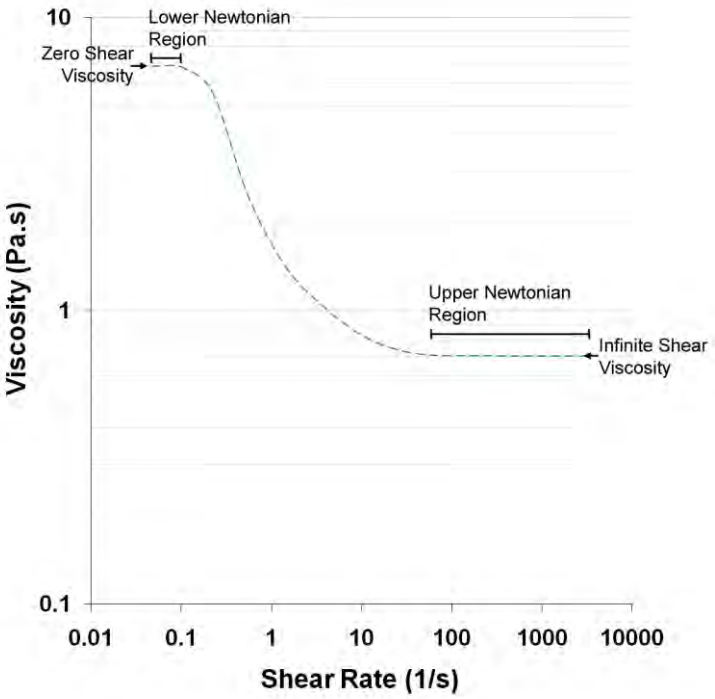

Figure 6.4 Graph showing the typical relationship between viscosity and applied shear rate for a material exhibiting shear-thinning behaviour.

6.5.3. Shear Thickening Behaviour

There are a number of cases where the viscosity of a material increases as the shear rate is increased, and the term shear-thickening is used to describe such behaviour. The act of deforming a material can cause rearrangement of its microstructure in such a way that would increase its resistance to flow with shear rate. In most shear-thickening cases, there is a region of shear-thinning at low shear rates; this is shown in Figure 6.5.

Shear-thickening is often observed in highly concentrated suspensions. At rest or at low shear rates, the liquid fully lubricates the particle surfaces and allows easy positional change, so the system behaves like a liquid. At higher shear rates, the particles wedge each other apart. The liquid no longer fills all the interstices and the material viscosity increases.

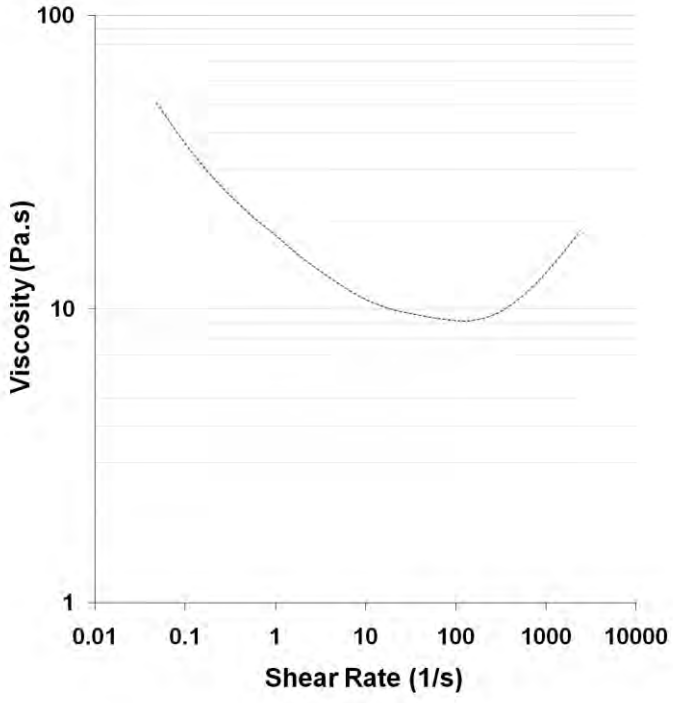

Figure 6.5 Graph showing the relationship between viscosity and applied shear rate for a material displaying behaviour often observed in highly concentrated suspensions. The shear-thinning behaviour at low shear stresses turns into shear-thickening behaviour as the particles in suspension are deformed into a conformation that resists flow to a greater degree.

6.5.4. Fluid Models with Yield Points

6.5.4.1. Shear Thinning with a Yield Point

Shear-thinning behaviour with a yield point is most commonly seen in dispersions. At rest, they build up an intermolecular or interparticle network of binding polar and van der Waals attractive forces. These forces restrict positional change of volume elements and give the substance a solid character with infinitely high viscosity. Forces acting from outside, if smaller than those forming the network, will deform the shape of this solid substance elastically. When the outside forces are sufficiently high enough to overcome the network forces, they surpass a threshold shear stress called the yield point, when the network collapses and flows. The network can now change position irreversibly and the material flows with shear-thinning (pseudoplastic) behaviour.

In addition to behaviour where the viscosity decreases above the yield point with increasing shear rate, a class of materials with shear-thickening behaviour above the yield point also exists. As before, shear-thinning effects tend to occur in concentrated suspensions after an initial reduction in viscosity with increasing shear rate.

6.5.4.2. Bingham Materials

Materials that follow Bingham behaviour possess a yield point as above, although the behaviour above this point is Newtonian. An equation used to describe the Bingham model is shown below, in Equation [6.8]:

$$\tau = \tau_b + \eta_b \dot{\gamma} \qquad [6.8]$$

τ_b is the yield stress of the material (Pa), η_a is the apparent viscosity, and $\dot{\gamma}$ is the shear rate. The Herschel-Bulkley model shown in Equation [6.9] is a modification of this, and can be used to describe the behaviour of all of the above models where the viscosity changes with shear rate.

$$\tau = \tau_b + \eta_a \dot{\gamma}^n \qquad [6.9]$$

n is an exponent called the Herschel-Bulkley index. Different values of τ_b and n can be entered into the equation to describe different Newtonian and non-Newtonian models, as shown in Table 6.1 (Mezger 2006).

Table 6.1 Newtonian and Non-Newtonian models according to Herschel-Bulkley parameters

	$\tau_b = 0$	$\tau_b > 0$
n > 1	Shear Thinning (Pseudoplastic)	Shear Thinning with Yield Point
n = 1	Newtonian	Bingham
n < 1	Shear Thickening (Dilatant)	Shear Thickening with Yield Point

6.6. Time Dependent Behaviour

6.6.1. Thixotropy and Rheopexy in Flow Curves

Thixotropic behaviour can be described as a reduction in structural strength when the material is subject to a time period under high shear. The structural changes that occur under high shear to cause this change are fully reversed during a subsequent period of rest, which makes this a completely reversible process. Thixotropy is observed in the vast majority of dispersions, encompassing suspensions, emulsions and foams; e.g. non-drip paints.

Rheopectic behaviour, on the other hand, is where there is an increase in structural strength when the material is subject to a high shear phase. During a subsequent period of rest, the material undergoes rapid and complete decomposition, where the improved structural strength reverts to its initial value. It can be described as a completely reversible process because of this. Such behaviour is observed in gypsum pastes and printer inks.

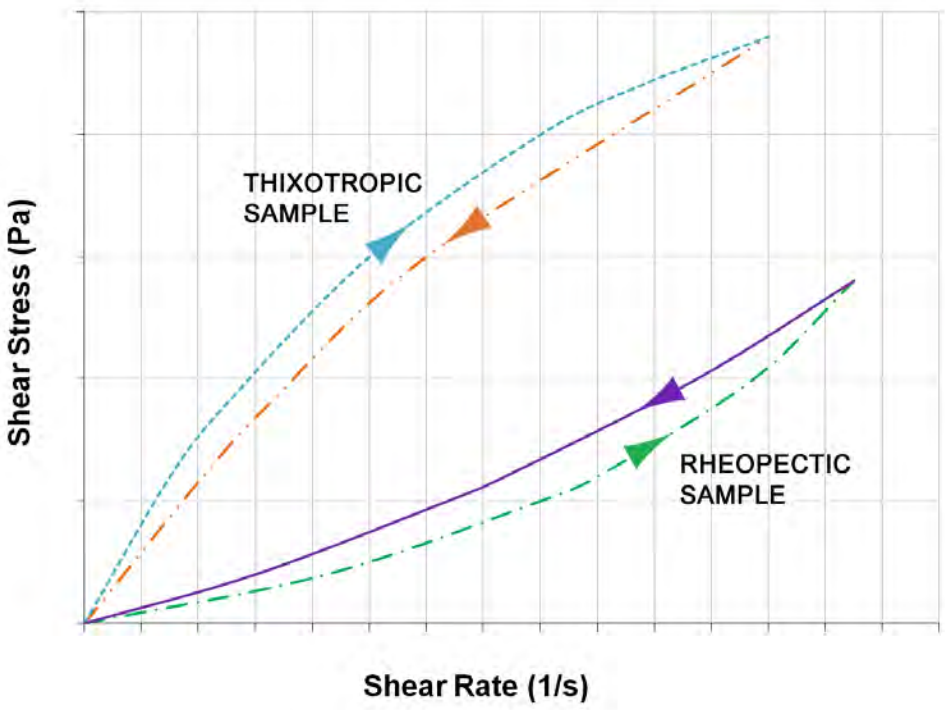

Figure 6.6 Graphs showing the relationship between shear rate and shear stress for material examples exhibiting Thixotropy or Rheopexy.

Tests are often carried out where the material is subjected to a steadily increasing shear rate (or shear stress) that reaches a finite value and then steadily decreases to zero, to form two flow curves. The one that plots shear stress values with increasing shear rate is labelled as the up curve and the one that one that plots shear stress values with decreasing shear rate is labelled as the down curve. The behaviour can be described as thixotropic when up curve shows higher shear stress values, and hence higher viscosities, than the down curve, as shown in Figure 6.6. In contrast, when the shear stress values for given shear rates on the

down curve are greater than on the up curve, the behaviour can be described as rheopectic, which is also shown in Figure 6.6.

Both thixotropic and rheopectic behaviours are associated with complex molecular or particle interactions. These are both time-dependent effects, as the material takes a period of time to revert back to its initial structural conformation after the high shear cycle. Within rheological testing, both structural decomposition and regeneration processes have to be taken into consideration for the material to be classed as having time-dependent thixotropy or rheopexy. Within testing parameters, the shear conditions for each phase must also be constant, and therefore time-related experiments involving periods of constant high shear and zero or low shear must be carried out in addition to flow curve testing (Mezger 2006). Tests associated with thixotropy are described in Section 7.2.2.

Thixotropic and rheopectic materials do not have altered rheological properties after the shear stress has been removed, and should not be confused with materials that undergo structural decomposition effects. Such behaviour is described in the Section 6.6.2.

6.6.2. Time-dependent Non-recoverable Degradation

Thixotropy and rheopexy can be described as completely reversible processes, where the structure of the material following a high shear cycle reverts to the initial conformation with its associated properties (such as strength) during a relaxation period of zero shear stress. If a material does not revert to this initial structure even after an ‘infinitely’ long period of time at rest, an irreversible, permanently remaining structural change has taken place. The material, therefore, cannot be described as being truly thixotropic or rheopectic. The structure instead undergoes ‘partial regeneration’ when shear stresses are removed, which can be expressed as a percentage of the original viscosity value.

Materials that possess a yield point (due to high solids-loading or agglomeration) or are rheopectic or partially rheopectic in nature, often flow in an inhomogeneous way, which leads to wall-slip effects. Wall-slip (also called stick-slip) occurs when sheared material experiences intermittent slipping due to lack of adhesion between the material and any surface against which it is being sheared. In materials with a yield point, it can induce motion in the material at stresses both below the yield point and above it, where it contributes to bulk shear (Coussot, 2005).

6.7. Changes in Viscosity with Voltage

Fluids whose rheological behaviour can be influenced by changes the voltage applied to them are called electro viscous fluids (EVFs) or electro rheological fluids (ERFs). They contain finely dispersed dielectric particles (e.g. aluminium silicates) in an electrically conductive liquid (e.g. water), which may be polarised in an electric field (Agafonov, 2010).

6.8. Rheology of Filled Composites

6.8.1. Introduction

The rheological characteristics of suspensions can be used to describe the behaviour of graphite and carbon black-filled wax composites. The general viscosity/shear rate curve for all suspensions is shown in Figure 6.4. A plateau of Newtonian behaviour exists at low shear rates, and is followed by the power-law shear thinning region that then flattens out to reach an upper Newtonian plateau. At some point, usually in the upper Newtonian region, there can be an increase in viscosity for suspensions of solid particles, given the appropriate conditions.

6.8.2. Suspension Rheology Models

One common employed term in the field of suspension rheology is the relative viscosity η_r. It can be used to determine the effect of filler addition on the material viscosity, and is determined using Equation [6.10]:

$$\eta_r = \frac{\eta_f}{\eta_0} \qquad [6.10]$$

η_f is the viscosity of a sample with a filler concentration 'f' (Pa.s), and η_0 is the viscosity of the substance containing no filler (Pa.s). There are a large number of models that can be used to predict the influence of filler particles on wax viscosity, and the simplest of these is the Einstein equation for hard spheres, as shown in Equation [6.11].

$$\eta_f = \eta_0\left(1+\frac{5}{2}\varphi\right) \qquad [6.11]$$

φ is the volume fraction of filler. The Einstein equation for hard spheres only applies to low filler concentrations ($\varphi < 0.1$), and this is the case due to the effect of particle interaction at higher concentrations. The Krieger-Dougherty equation, for fitting relative viscosity/filler content relationships is shown in equation [6.12].

$$\eta_f = \eta_0\left(1-\frac{\varphi}{\varphi_m}\right)^{-[\eta]\varphi_m} \qquad [6.12]$$

$[\eta]$ is the intrinsic viscosity and φ_m is maximum packing fraction (both described in Section 6.8.3). For a sphere model, the $[\eta]\varphi_m$ term is ~ 2.0 (Barnes, 1981).

6.8.3. Role of Particle Shape

Particle shape plays an important role in the rheology of suspensions, and influences the maximum packing fraction (φ_m) and intrinsic viscosity [η] parameters of Equation [6.12].

Intrinsic viscosity is a term used to describe the influence that suspended particles have on the flow behaviour of a system. Barnes (1981) provided simple empiricisms for the effect of very large axial ratio fillers on intrinsic viscosity [η].

Discs: $[\eta] = 3 \text{ (axial ratio)} / 10$

Rods: $[\eta] = 7 [(\text{axial ratio})^{5/3}] / 100$

For spherical particles with a monodisperse size distribution, φ_m lies between 0.52 and 0.74 (due to different packing arrangements, including simple cubic and face-centred cubic). For particles with non-spherical geometries, the filler particles trap a proportion of matrix on their surfaces, which contributes to a reduction in the φ_m term. This occurs because the trapped matrix is essentially immobilised and can no longer be counted as part of the continuous phase.

Clarke et al. (1967) studied the effect of particle geometry on relative viscosity over a range of filler concentrations. Barnes et al. (1997) used Clarke's experimental data to produce maximum packing fraction and intrinsic viscosity values for each system. For a system containing glass plate filler particles, an experimental φ_m of 0.38 was ascertained. Higher φ/φ_m values increase the relative viscosity of the filled material, as shown in Table 6.2. It is important to note that both graphite and carbon black powders are plate-like in nature, and such shapes trap the wax on their surfaces, which contributes to a reduction in φ_m.

Table 6.2 Tabulates the effect of particle geometry on dispersion rheology, fitting Krieger-Dougherty parameters to rheology data from a collection of studies (Barnes, 1997)

	Particle Size (μm)	**Density (g/cm^3)**	**φ_m**	**$[\eta]$**	**$[\eta]\varphi_m$**	**η_r at 10vol% using Eq. [6.12]**
Quartz Grains	53 - 76	2.58	0.271	5.8	2.15	2.691
Spheres	< 1	-	0.71	2.70	1.92	1.338
Spheres	40	-	0.61	3.28	2.00	1.431
Glass Plates	Diameter: 400 Thickness: 100 Axial Ratio = 4	2.52	0.382	9.87	3.77	3.140
Glass Rods	Diameter: 30 Max Length: 700 Axial Ratio = 23	2.01	0.382	9.25	2.48	2.123
Glass Fibres	Axial Ratio = 7	-	0.374	3.8	1.42	1.556
Glass Fibres	Axial Ratio = 14	-	0.26	5.03	1.31	1.889
Glass Fibres	Axial Ratio = 21	-	0.233	6.0	1.40	2.192

As stated previously, dispersions often exhibit shear-thinning behaviour. As the shear rate is increased, the relative viscosity decreases for each filled composition. At low shear rates (due to low shear stresses) for a non-aggregated system, the particles have to 'bounce' past one another for overall flow to occur. When higher shear rates are applied, the imposed velocity gradient gives the particles an oriented structure that lets the particles to move past one another with greater ease. When the concentration of particles in dispersion is high, shear thickening effects are also observed. The particle geometry is a contributing factor in determining the particle concentration when the transition from shear-thinning to shear-thickening occurs. For disc and rod geometries, there is a higher likelihood of dilatancy when the ratio of h-w is large.

Another issue to take into account when determining the rheology of suspensions is the effect of phase separation, which occurs because filler particles both sediment out and have a tendency to move away from interfaces. When this takes place within the rheometer, it will result in an increase in the indicated viscosity, as zones are formed within the suspension

containing a higher percentage of particles that cluster more readily and so inhibit shear. This effect is most pronounced at high solids-loadings.

6.8.4. Role of Particle Size, Distribution and Agglomeration

When the suspension concentration is above 10 vol%, both particle size and particle size distribution start to influence the rheological behaviour. Wide particle distributions increase the system's φ_m value, as smaller particles can fit between the larger ones. Smaller particle sizes have been found to increase the resultant viscosity.

The relative viscosity is also influenced by the levels of interparticle repulsion/attraction. When the interparticle repulsive forces are insufficient, particle flocculation occurs. Particle clusters are often not closely packed, and can further resist flow by enclosing and thus immobilising some of the continuous phase. By doing this, the effective particle volume in suspension is increased (Barnes, 1981).

Within carbon black-filled composites specifically, the hierarchical structure of the particles is described in Section 5.5.2. The work of Dannenberg (1977) described the effect of carbon black agglomeration on suspension rheology, and stated that shear-thinning, shear-thickening and yield point behaviour were observed within shear flow experiments, accompanied with the deformation or partial breakdown of the structures. Solid-like Viscoelastic behaviour with solid-like character was observed within oscillatory experiments. According to Kawaguchi (2001), "it is expected that one can obtain information on the flocculated structures through careful rheological experiments" using the resulting information to clarify the interactions between carbon black particles themselves. Kawaguchi also stated that carbon black-filled suspensions displayed the behaviour of materials containing highly agglomerated particles. On an observational level, the carbon black filled

waxes reached a ‘saturation’ concentration at a far lower volume% during the composite formation process. The presence of particle flocs in suspension does not negatively affect every aspect of the suspension properties; however, as shearing particle flocs can draw them out into string-like structures, which can explain the improved composite conductivities using carbon black filler.

6.8.5. Water-filled Wax

The rheology of a water-filled wax is like that of a dispersion of deformable particles in a suspension medium. The effect of liquid filler vol% on flow behaviour is not as extreme as it is when solid particles are added, and this is because the maximum phase volume is usually much higher than with solid particles, since the liquid filler droplets deform to accommodate the presence of near neighbours. In this situation, the shape of the liquid filler droplets is polyhedral and the suspension resembles foam in its structure. Maximum packing fractions of 0.90 and above are usual (Pal, 1986).

As with solid dispersions, non-Newtonian behaviour is seen to an increasing extent at higher fluids-loadings (increase in concentration). The asymptotic value of viscosity at high shear rates is generally much lower that that observed for a dispersion of solid particles at the same phase volume. This effect is ascribable to particle deformation in the emulsion. A smaller droplet size and a more monodisperse droplet size both give an increase in viscosity. Since vigorous mixing of emulsion usually gives smaller and more monodisperse particles, increasing the energy input in emulsion manufacture always increases the viscosity. Emulsion droplets at rest are spherical, but become ellipsoid in shear, which consequently increases their surface area.

CHAPTER 7. RHEOLOGICAL TESTING

7.1. Introduction to Rheometry

Rheometry is a term used to describe the study of techniques used in determining a material's rheological properties. These properties can be determined by introducing a state of shear flow, and this can be done in a number of ways. Rheometry experiments principally use one of four techniques, which are shown below (Cirre Torres, 2004):

1. Translating Parallel Plates: Flow is measured between two parallel plates, where one plate translates across a stationary plate.
2. Rotational Parallel Plates/Cone and Plate: Flow can also be measured between either two parallel plates or a cone and plate, when one rotates and the other is stationary.
3. Concentric Cylinders: Flow measured through the annular gap between two concentric cylinders. One of the two is assumed to be stationary, whilst the other rotates.
4. Capillary Tube: Capillary tube geometry describes flow through pipes, tubes or capillaries. A pressure difference between the inlet and the outlet of a capillary forces the liquid to flow. A variation of capillary flow is the flow in channels with a rectangular cross-section such as slit capillaries.

In addition to flow tests carried out as described in Section 7.2.1, oscillatory testing is carried out to define the viscoelastic properties of samples. Viscoelasticity and the uses of oscillatory rheometry are described in Appendix B.

7.2. Rheological Flow Curves

7.2.1. Flow Tests and Non-Newtonian Behaviour

As described in Section 6.6, where the concept of thixotropy and rheopexy are explained, to carry out a flow ramp test on a material sample, it is subjected to a steadily increasing shear rate (or shear stress) that reaches a finite value and then steadily decreases to zero. The purpose of carrying out flow tests is to measure the change in the material's viscosity over the shear rate (or shear stress) range, so that its flow behaviour can be defined as Newtonian or non-Newtonian, using the models described in Section 6.5.1. Additionally, the material can be shown to display either thixotropic or rheopectic behaviour if the increasing shear curve and decreasing shear curves are different, as described in Section 7.2.2.

For flow ramp tests carried out on a rotational rheometer, measurements can be produced using either a controlled shear rate (CSR) mode or a controlled shear stress (CSS) mode. The properties of the material tested can determine each technique's suitability. In CSR mode testing, the shear rate is controlled by the apparatus. CSR tests are preferred when the liquid sample is self levelling (in that it has no yield point). It is often used if the viscosity needs to be measured at a defined flow velocity, i.e. if certain process conditions need to be simulated. In CSS mode testing, the shear stress level is controlled by the apparatus. CSS tests are preferred if a material yield point needs to be ascertained, with yield points present in many dispersions, pastes or gels due to the nature of their material structures. As these tests need to accurately represent the behaviour of the material, several factors need to be taken into consideration (Mezger, 2006):

a) Flow ramp tests need to be carried out under isothermal conditions, and so anything that could alter the material's temperature during the experiments has to be controlled. The primary issue to take into consideration for rotational rheometry experiments is the effect of shear heating, as flow behaviour is also associated with a resistance to flow. The frictional force between molecules and particles as they are sheared past one another in the tested material is dissipated as thermal energy, to produce viscous heating (also known as shear heat). Temperature feedback control mechanisms are therefore put in place, to maintain a steady sample temperature over the testing period.

b) Transient effects can produce inaccuracies in flow experiments, and have a pronounced effect when a material is tested at low shear rates. Transient effects can be explained using a model based on a parallel plate system, like the one used within the present work. If one splits the sheared sample between the plates into parallel layers, during the initial time of transient flow, not all the flowing layers are shifted to the same extent against neighbouring layers. This means that the shear rate is not consistent throughout the separation gap, and results in the calculated viscosity value being transient and not steady-state as desired. It takes a certain period of time until all the other layers are also set in motion, in a process that takes longer when the shear rate is low ($< 1\ s^{-1}$). The main method of reducing such effects is to lengthen the time at each plot point.

c) Highly concentrated or highly agglomerated particles in suspension do not possess consistent rheological behaviour, as they are often subject to wall slip and phase separation effects. Wall slip is also called stick-slip, and occurs when the sample being sheared experiences intermittent slipped due to lack of adhesion between the material and any surface against which it is being sheared. Phase separation occurs when the distribution of particles in suspension becomes inhomogeneous under shear, leading to the formation of particle-rich and particle-depleted regions (possessing local viscosities

that are higher than and lower than the mean respectively). Flow ramp tests should be carried out on a number of samples from each material composition, to gauge whether time-dependent viscosity changes (as described in Section 6.6.2) are due to a consistently occurring alteration in the conformation of particles in suspension, or due to the above effects.

d) Dispersions with a high effective concentration of solid particles (either through high levels of loading or agglomeration) often possess a yield point. To determine the yield point of a material using CSS, the highest shear stress value at which the instrument measures no detectable movement was taken. If one takes this value to be the last measured point where $\dot{\gamma}$ is zero, it is clear that it would vary according to both the distance between plotted points and the shear rate resolution of the equipment. The yield point can therefore be described as test resolution limiting, and is not a material constant. Graphically, it can also be taken to be at the intersection of the flow curve on the τ axis when a linear scale is used.

7.2.2. Thixotropy and Rheopexy Measurements

Using flow ramp testing, the thixotropic or rheopectic behaviour can be observed in a material, as described in Section 6.6. The degree of thixotropy or rheopexy within a material can be measured by comparing viscosity measurements at certain shear stress values on the up flow curve (when the shear stress is increased from zero to a maximum) and down flow curve (when the shear stress is decreased from this maximum to zero shear).

Another method that can be used to gauge the level of material thixotropy or rheopexy is to measure the hysteresis area between the up and down flow curves. Taking the area under the up curve from the area under the down curve should give a positive value for

thixotropic behaviour and a negative value for rheopectic behaviour. This hysteresis area does not, however, fully define the thixotropic or rheopectic behaviour, as the period of relaxation after the test is not taken into account, when the material returns to its initial behaviour.

7.3. Variable Temperature Flow Ramps

For a Newtonian fluid, the relationship between viscosity and temperature follows the AFE relationship in Equation [6.6]. When a phase transition occurs, the temperature-related viscosity behaviour of the phase before the transition gives way to that of the one after it, and is often associated with a more sudden change in material viscosity. Within a cooling temperature flow ramp experiment, it is possible to deduce the phase transition temperature from the point where the AFE relationship is no longer observed in the sample. For a material that undergoes a series of intermediate states between solid and liquid phases, e.g. waxes, this temperature would correspond to the transition to a semi-liquid phase.

MATERIALS AND EXPERIMENTAL METHODS

CHAPTER 8. FABRICATION OF A MELT-OUT ELECTRODE

8.1 Introduction

The purpose of these experiments was to determine the viability of carbon-powder filled waxes as formable electrode materials, with the aim of creating a composite that can be used an investment casting pattern and electrophoretic deposition (EPD) electrode simultaneously. The conductivity of graphite makes it a highly suitable material for use as an electrode material.

The aim of using waxes as the matrix material allows for the deposition electrode to be melted out after the ceramic coating has been formed onto its surface. The rheology of investment casting waxes enables them to flow into and out of complex shapes, although their ability to do this is altered by the addition of a filler material. The effect of filler addition on wax rheology is more fully described in Section 6.8.

Percolation theories have been discussed in Section 5.4, and electrode samples with varying levels of filler concentration were formed to ascertain the percolation threshold (P_c) or critical volume (V_c) for each filled wax by measuring the electrical resistivity of each sample, using techniques described in Section 9.2. The relationship between filler concentration and sample conductivity can also be plotted. Rheological experiments were also carried out on molten samples, to gauge the effect of filler addition on the flow behaviour of each wax. These experiments were designed to establish whether a filled wax composite could be formed to possess both a high enough conductivity and low enough working viscosity to be used within the currently implemented wax pattern fabrication processes. Rheological testing of wax samples is described in Section 10 and Appendix B.

8.2 Matrix Waxes and Conductive Filler Particle Materials

8.2.1 Matrix Wax Grades

Within the investment casting process, waxes are invariably used to form the melt-out substrate upon which dip coating and investing can take place. In forming a conductive melt-out composite material, wax was chosen to act as the matrix for the conductive particles. Three investment casting wax grades were primarily used, and are listed below:

- Blayson Olefines A7-11 unfilled wax
- Blayson Olefines A7-7808 unfilled wax (low viscosity grade)
- Blayson Olefines A7-TC2/E filled wax (water filler content = 8 - 10 vol%)

These three wax grades were chosen for their specific properties. The A7-11 wax was chosen as it is a commonly used wax grade with properties that ideally suit it for use without any need to change current wax injection moulding parameters. The addition of filler increases the working temperature and viscosity of materials, and so the A7-7808 grade was chosen so that the increase in working viscosity could be offset against the lower initial viscosity. The A7-TC2/E wax grade was used in response to mixing difficulties associated with the presence of carbon black filler particle agglomerates. It was theorised that the use of liquid deformable filler would aid the dispersion of both graphite and carbon black within the matrix, to produce a homogenous composite with more uniform conducting characteristics. The properties of these grades according to the manufacturer, Blayson Olefines Ltd., are tabulated in Table 8.1.

Table 8.1 Wax property data from Blayson Olefines Ltd. for the three grades of wax used experimentally.

Wax Grade	Filler	Penetration (10^{-1} mm @100g)	Viscosity over Injection Range (Pa.s)	Liquid Injection Range (°C)	Congealing Point (°C)	Drop Melt Point (°C)	Fluidity
A7-11	None present	1 – 4 (hard)	0.8 – 1.3 (low)	74 – 78 °C	69 – 73 °C	73 – 76 °C	Medium
A7-7808	None Present	9 – 14 (med)	0.8 – 1.4 (low)	72 – 77 °C	62 – 67 °C	68 – 75 °C	Medium Low
A7-TC2/E	Water (6–8 %)	8 – 11 (med)	2.9 – 3.2 (high)	67 – 71 °C	63 – 67 °C	72 – 75 °C	Medium Low

8.2.2 Conducting Filler Particle Materials and Grades

Two filler powders were used to form a conductive network within the wax matrix, and were chosen as they represented graphite and carbon black particle systems, respectively:

1. Micronised Graphite Powder (Graphite Trading Company)
2. Vulcan XC605 Carbon Black (Cabot)

The micronized graphite powder is a grade of natural crystalline graphite with a high purity (99.5%). A sub-10 micron particle size distribution would reduce the degree of particle settling within the molten wax during formulation.

For many grades of carbon black, the presence of adsorbed oxygen complexes on the surface of each particle reduces their electrically conductive properties. The Vulcan XC605 grade, however, is produced specifically for electrostatic discharge (ESD) applications, and has a high conductivity as it has a high ‘chemical cleanliness’.

The powder’s size distribution, its shape and the level of particle aggregation all have a strong influence on how the particles become dispersed within the wax. These factors, in

turn, affect both the flow behaviour of the wax and its electrical conductivity. The two powder grades were therefore subjected to analyses to determine these factors.

Scanning electron microscopy (SEM), using a Philips XL30 SEM in secondary electron (SE) mode, was used primarily to characterise the geometry of the particles. Powder samples were compressed onto adhesive conductive tabs for analysis. The carbon black exhibits a larger level of clustering, whilst the graphite is more flaky and angular in nature. Both filler grades can still be described as plate-shaped according to SEM micrographs, as shown in Figure 8.1.

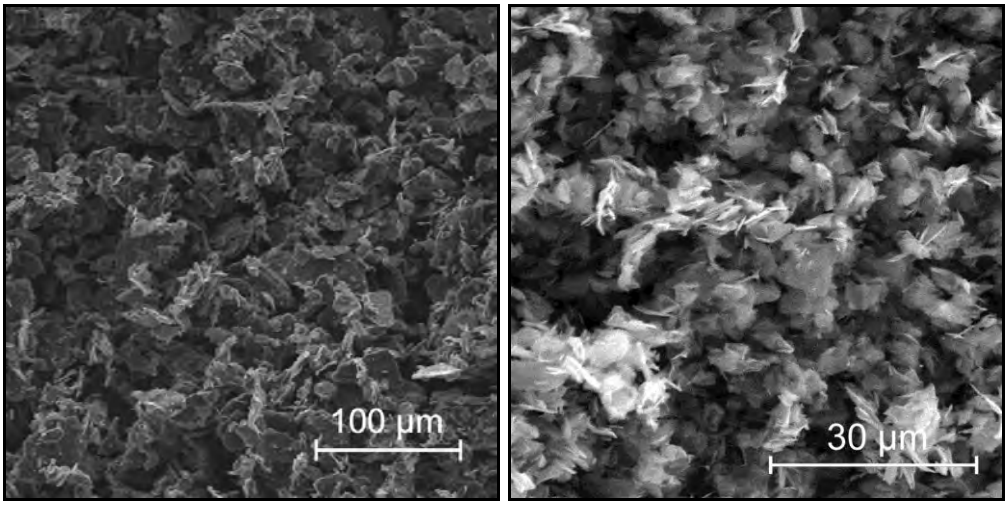

(a) **(b)**

Figure 8.1 Secondary electron (SE) Scanning electron microscopy micrographs depicting **(a)** Vulcan XC605 carbon black (Cabot) and **(b)** Micronised graphite (Graphite Trading Company) powders.

Particle size analysis for the graphite and carbon black grades are presented in Appendix A.2.1. The manufacturer information for the micronised graphite stated that the grade contained particles with diameters less than 10 µm, which was verified by analysis. The size distributions showed us that lone graphite particles with a modal diameter of ~ 1.5 µm were commonly in the form of < 10 µm clusters.

As described in Section 5.5.2, carbon black has a hierarchical structure, where 400nm primary aggregates readily agglomerate into larger clusters. When particle size analysis was carried out on the Cabot Vulcan grade, the distribution of these clusters was determined. 500 nm aggregates were present, and carbon black clusters had modal peak diameters of ~ 4 μm and ~ 20 μm. Ultrasonic processing was shown to break larger clusters ($d > 10$ μm) into smaller clusters ($d < 10$ μm) and submicron aggregates.

Powder surface area analysis was carried out using the B.E.T. method, a technique first devised by Brunauer, Emmett and Teller to measure particle surface area by determining the level of gas absorption. In this work, the isothermal adsorption of nitrogen was measured, using a multipoint method to calculate the surface area. These attributes are measured by the use of nitrogen adsorption/desorption isotherms at liquid nitrogen temperature and relative pressures (P/P_o) ranging from 0.05 - 1.0. This B.E.T. method was employed to give the Cabot Vulcan 605 carbon black a surface area of 112 m^2/g and the micronised graphite a surface area of 16 m^2/g. The carbon black surface area result is in accordance with the manufacturer's information.

8.3 Conducting Filler Particle Concentrations

For the rheology and conductivity experiments, filled waxes were made up over a range of compositions, chosen on the basis of preliminary work, which found that manual and automated stirring mechanisms could not form a homogenous composite when the graphite powder content was greater than 20 vol%. For the carbon black filled wax, this powder particle concentration upper limit was achieved at a lower level of 16 vol%. The filler particle concentrations studied, corresponding to both the conductive filler material and wax substrate, are given in Table 8.2 and Table 8.3 below, together with the primary testing criteria. For the carbon black-filled wax, rheometry results could not be successfully carried out on samples when the filler particle content was greater than 11.4 vol%, and so additional concentrations of 2.3, 4.6 and 9.2 vol% (equivalent to 4.31, 8.43 and 16.12 wt% filler) were created for analysis.

Table 8.2 Conductive graphite filler concentrations added to each of the wax grades, and their use during the electrical conductivity and rheometry experiments.

Micronised Graphite Filler (Graphite Trading Company)							
Weight% Filler	Volume% Filler *	A7-11		A7-7808		A7-TC2/E	
		Conductivity	Rheology	Conductivity	Rheology	Conductivity	Rheology
0.00	0.0	✓	✓	✓	✓	✓	✓
4.31	2.0	✓		✓		✓	
8.43	4.0	✓		✓		✓	
12.36	6.0	✓		✓	✓	✓	✓
16.12	8.0	✓		✓		✓	
19.71	10.0	✓		✓	✓	✓	✓
23.15	12.0	✓		✓		✓	
26.45	14.0	✓		✓	✓	✓	✓
29.61	16.0	✓		✓		✓	
32.65	18.0	✓		✓	✓	✓	✓

* Volume percent of graphite was calculated using a graphite bulk density of 2.2 $g.cm^{-3}$ and base wax density of 0.995 $g.cm^{-3}$.

Table 8.3 Conductive carbon black filler concentrations added to each of the wax grades, and their use during the electrical conductivity and rheometry experiments.

Vulcan XC605 Carbon Black Filler (Cabot)							
Weight% Filler	Volume% Filler *	A7-11		A7-7808		A7-TC2/E	
		Conductivity	Rheology	Conductivity	Rheology	Conductivity	Rheology
0.00	0.0	✓	✓	✓	✓	✓	✓
4.31	2.31	✓		✓	✓	✓	✓
8.43	4.61	✓		✓	✓	✓	✓
12.36	6.90	✓		✓	✓	✓	✓
16.12	9.17	✓		✓	✓	✓	✓
19.71	11.42	✓		✓	✓	✓	✓
23.15	13.66	✓		✓		✓	
26.45	15.89	✓		✓	✓	✓	✓
29.61	18.09	✓		✓		✓	
32.65	20.30	✓		✓	✓	✓	✓

* Volume percent of carbon black and graphite was calculated using an amorphous carbon density value of 1.9 $g.cm^{-3}$ and graphite bulk density of 2.2 $g.cm^{-3}$ respectively.

8.4 Composite Electrode Fabrication

Filled Wax samples were prepared using a hotplate to melt a known mass of wax within a cylindrical silicone rubber melting vessel with a 65 mm base. Chen et al. (1985) stated that working on the filled waxes at more than several degrees above the melting point could possibly result in particle segregation effects if the mixture is not constantly agitated, due to the density difference between carbon and wax (2.20 and 0.996 g/cm^3 respectively).

Although the work of Pinto et al. (1999) used Nylon-6 as a matrix for carbon black particles instead of wax, they highlighted the importance of temperature control during mixing. Like with waxes, increasing the polymer working temperature is associated with lower matrix viscosities, and according to Chan et al. (1997), this leads to a higher degree of intermixing between the carbon black and polymer particles in the interfacial regions, which

makes the conducting network less ordered. Pinto et al. (1999) found that increasing the processing temperature by 15 °C (from 208 to 223 °C) almost doubled the resistivity of the resulting 32 wt% carbon black composite.

A balance therefore must be made between using higher matrix working viscosities where composite homogeneity becomes an issue due to mixing difficulties, and lower viscosities, where the resulting conductivity is detrimentally affected. Using a thermistor, the Stuart SB160 stirrer hotplate temperature was set so that the corresponding wax temperature lay between 80 and 85°C (Clegg 1991), which was 5 – 10°C above normal wax grade working temperatures. This temperature range was chosen as the conductive particle grades studied proved difficult to intermix.

A magnetic stirring mechanism was in place to agitate the molten wax prior to powder filler incorporation, to aid homogeneity and minimise the presence of hotspots within the sample. The removal of wax hotspots was of particular importance when the water-filled A7-TC2/E wax was melted, as the water content would begin to evaporate off when the wax is held at temperatures above 85°C, which has an influence on its properties (Blayson Olefines MSDS, 2009). A 30 mm PTFE stirrer bar was present within the melting vessel, which was set to a rotation rate of approximately 200 revolutions per minute (rpm) in air. When the wax was molten, the required amount of filler material was gradually added. As the conductive filler was added, manual stirring operations were implemented to assist magnetic agitation, (which was increased to a stirring rate of 400 rpm in air), to ensure that both the filler and wax were homogenously distributed.

The final blends were poured into the heated silicone mould and the wax castings were removed when completely solidified. Unless otherwise stated, the plate in the mould would undergo a 180° flipping rotation every minute for the first ten minutes of the cooling process, to counter the effect of filler settling. For the samples used in conductivity

measurements in Section 9.2.2, two cooling regimes were used. The first used a single flipping procedure that took place shortly after the geometry was formed, as it was removed from the hotplate. The second regime involved no turning process. This was carried out so that the effect of filler particle sedimentation on localised resistivity could be measured.

The first geometry was that of a flat circular disc, with a diameter of 65 mm and thickness of 3.0 mm (±0.5 mm). This geometry was chosen so that four point probe resistance measurements could be taken from the central region of each disk without the need for significant correction factors, as discussed in Section 9.3. Each disc was formed by pouring the wax blend into an open-topped flexible silicone mould with a flat circular base and steeply inclined walls (Figure 8.6(a)). An identical heated silicone mould was then placed, male to female, into this vessel, so that the molten wax was formed into the desired shape.

The second geometry was that of a hollow hemisphere, with an inner diameter of 32mm and outer diameter of 40mm. This geometry was chosen so the EPD primary coat could be compared with the dip-formed primary coat in permeability testing, as discussed in Section 14.2. The hollow wax sphere required was formed from two hemispheres, which were bonded together after solidification. Each hemisphere was formed by injecting the heated wax into the cavity between two hemispherical silicone rubber moulds. Owing to its curved geometry, this mould was heated using an oil bath, as shown in Figure 8.6(b). A number of alternative methods to heat complex mould shapes were also used, and are discussed in Section 8.5.

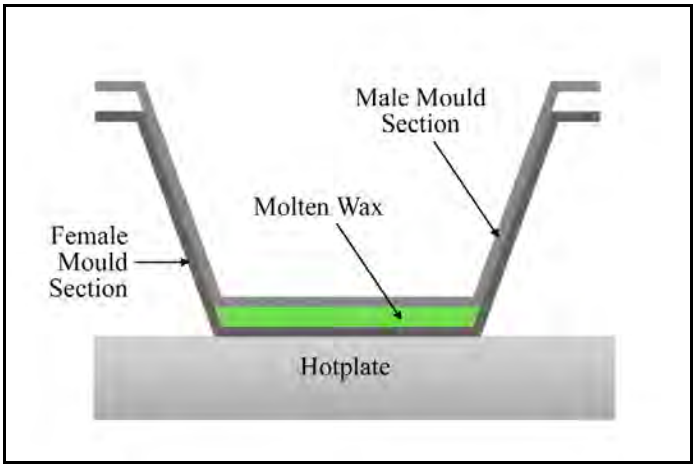

(a)

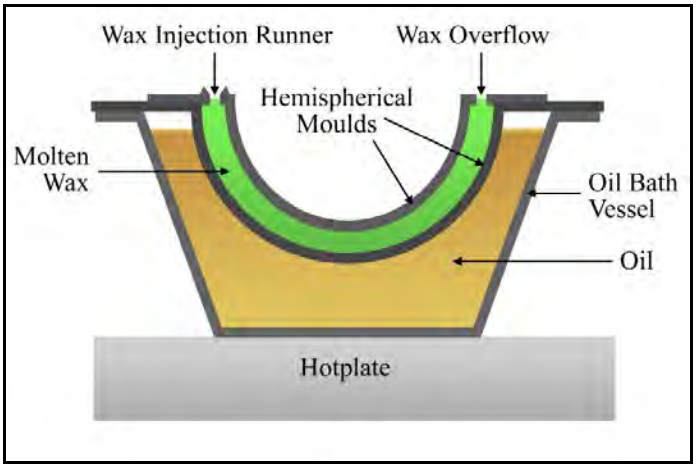

(b)

Figure 8.6 Diagrams showing **(a)** the mould used in the formation in flat circular plate wax samples; **(b)** the oil bath set-up used to heat the hemispherical mould geometry used in the formation of spherical wax samples.

The third geometry was that of a flat rectangular plate with the following dimensions; width = 25mm, length = 45mm, depth = 5mm. The process used to form this geometry was similar to the one used to form the flat circular disc. This geometry was used so that direct comparisons could be made between the compressed graphite and loaded wax deposition electrodes within EPD experiments. The formation and use of these electrodes is further described in Section 13.1.

8.5 Heating Operations and Injection Methods

The wax melting and composite fabrication processes were carried out in an open-topped vessel which was placed on a stirrer hotplate. The material temperature could be easily controlled and a number of stirring operations could be utilised within this set-up. This method of heating does, however, have a number of drawbacks, as the silicone vessel used for wax melting operation is heated from a single direction. This leads to premature wax solidification, and during the mixing stages, can result in filler content inhomogeneities.

When the silicone mould material was not held at temperatures above the wax melting point during the casting stage, premature solidification led to inferior shape reproduction and readily occurring bubble entrapment. As shown in Figure 8.6, an oil bath was initially used to preheat the more complex mould geometries, so that wax solidification could occur at a slower rate. Alternative bath materials were tested and subsequently used as they surpassed the use of oil in a practical capacity. The use of a heated mixture of wheat flour and oil was decided upon as it could be easily moulded to fit the desired shape around the mould exterior and hold this geometry during the wax pouring process.

In addition to magnetic and manual stirring mechanisms used to aid conductive filler incorporation into the molten wax, a Silverson L4RT High Shear Mixer with disintegrator shroud head was used for selected compositions. The rotating head assembly was immersed within the large molten composite volumes and kept to a rotation rate of 500 rpm as the head was moved through the mixture, to ensure that the entire volume was processed through the disintegrator head. Experiments that link the mixing temperature and shear mixing intensity to the degree of filler dispersion within the matrix are beyond the scope of the present work, although the nature of the relationship can be determined by comparing the composite flow behaviour, composite electrical conductivity and cluster-size within the etched-out matrix.

CHAPTER 9. CONDUCTIVITY MEASUREMENTS

9.1 Introduction

Resistance measurements were carried out to find the position of the percolation threshold, as well as for comparative purposes, to ascertain whether differing the processing route or material history could alter the connectivity of conductive particles within the wax matrix. A number of difference techniques are used to measure a sample's electrical conductivity. The pulse method involves applying a pulse voltage for a short duration and measuring the extent of electrical current flowing through the sample to arrive at a value for the electrical conductivity. Such a technique is most commonly applied to materials with little or no contact resistance, and so would not be suitable for use with filled composites with low to moderate conductivity (Girotto, 2002). Electrometer methods are based on electrical resistivity measurements between two points, using a technique set out in ASTM D257-99. Such a test method is not suitable for use in measuring the electrical resistivity/conductivity of moderately conductive materials, and so could not be used to compare the resistivity of filled composites over the full range of compositions.

A four-point probe technique measures the electrical resistance of conductors and semi-conductors with high accuracy, and is described in Section 9.2 as it is used within this study. One drawback of such a technique is related the required geometry of the tested sample, as a number correction factors would otherwise be needed to take into account the flow of current in a non-infinite sample volume. With a castable material like conductive particle-filled wax, such a geometry could, however, be easily made for analysis.

Two point probe techniques measure the difference in potential and the electric current that flows through the sample when a D.C. electric field is applied. This information can be turned into an electrical resistivity value by measuring the dimensions of the sample

studied. The two point probe technique can be applied to samples with a wide range of conductivities, including insulators and semi-conductors. A two point probe technique was used within the present work in Appendix C.1, and was used to confirm the conductivity / filler content relationship ascertained by four-point probe techniques.

9.2 Four-point probe measurement of resistances

9.2.1 Introduction and Theory

The resistance measurements done on carbon filled wax in the literature often used 4 point-probe methods and equipment (Chen 1985) (Chrakrabarty 1991). A four-point probe resistance measurement setup consists of four equally spaced probes positioned in a linear fashion (although square arrays are also used), with a typical separation distance of 1 mm between each. A high impedance current source is used to supply current through the outer two probes, whilst a voltmeter measures the potential difference (p.d.) across the inner two to determine the sample material resistivity, as shown in Figure 9.1.

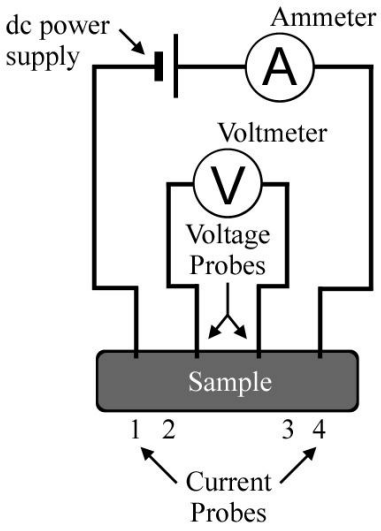

Figure 9.1 Drawing of a four-point probe resistance measurement setup (ISI).

Resistivity is a material quantity that defines a substance's resistance to current flow. The resistivity of a material can be given by the material sample resistance values when the sample geometry has been taken into account, and conversion equations exist specifically for four-point probe setups. For resistivity calculations, samples would ideally be semi-infinite in all dimensions below the testing plane. Correction factors therefore have to be implemented where this is not the case, since boundaries limit the possible paths of the electric current. According to Sakka (2004), a geometric correction factor (F) can be placed into resistivity equations as the product of three independent correction factors. These factors are related to sample thickness (F_1), lateral dimensions (F_2) and relative position of the probe on sample (F_3). Four-point probe correction tables are available for circular plate geometries (Swartzendruber 1964), and so, in the present work, the wax–carbon composite samples were formed into this shape.

In the lateral dimension, the correction factor (F_2) for a measurement taken at the centre of the sample is connected to the result given by the sample diameter (d) divided by the probe spacing (s). When a 10 mm diameter plate sample is tested with a 1 mm tip-spaced four-point probe, the correction factor is 0.9204. This becomes 0.9991 when the sample of diameter is increased to 100 mm (Topsoe 1968). One needs to have d/s ratio of at least 40 to give results that require a correction of less than a 1 % (Sakka 2004), and so the samples created in this experiment have a diameter of 65 mm. To ignore the need for complex corrections caused by F_3 issues, measurements had to be taken within 12.5 mm of the circle's centre (Topsoe 1968).

The behaviour of the four-point probe current depends upon the sample thickness (t). The thin sheet model is implemented when $t << s$, and the current in this situation is said to dissipate through the material in the form of propagating rings. The resistivity here is directly associated with sample thickness. As the specimen becomes thicker, this model for current

flow becomes less accurate. When the thickness exceeds 62.5 % of the probe spacing, the sheet resistance requires more than a 1 % correction. This would correspond to a sample thickness of over 0.625 mm when the tip separation is set at 1 mm.

The bulk model applies when the sample thickness is semi-infinite in nature (when t >> s), and the lack of nearby boundaries beneath the plane of testing means that the current is said to form spherical protrusions. As the specimen becomes thinner, the paths of current become more limited, and a correction factor of more than 1 % is required when the sample thickness is less than 5 times that of the probe spacing (t/s < 5).

Owing to the volume of material used to formation of circular wax plate geometries, the test sample thicknesses were between 2.5 and 2.8 mm. With the probe spacing fixed at 1 mm, neither of these models can be applied without the application of an F_1 correction factor. If one applies the bulk model to 2.5 and 3.33 mm thick specimen thicknesses, the correction factors would be 0.951 and 0.978 respectively (Topsoe 1968). On applying the thin sheet model, these correction factors become 0.5276 and 0.4067 (Topsoe 1968). The bulk model calculations therefore best represent the geometry of these specific circular plates. The following equation [9.1] can be used in this instance to calculate resistivity:

$$\rho = 2\pi sF.V/I \qquad [9.1]$$

ρ is volume resistivity (Ω.cm), s is the probe spacing (cm), F is the geometric correction factor, V is the voltage (V) and I is the current (A).

9.2.2 Sample Preparation and Testing using a Four-point Probe Set-up

In the literature, resistance measurements were used to ascertain the value of V_c, by comparing the resistance measurement with that of pure wax. A number of experiments cast the carbon-laden wax into either a defined rectangular plate (Chen 1985) or a circular (Chrakrabarty 1991) plate, with a thickness of 2-3mm. Resistance measurements in the present work were carried out on similar geometries, formed using procedures described in Section 8.4. To measure the effect of carbon settling out due to its relatively high density on the measured resistance (and hence conductivity), two different cooling regimes were put in place following the formation of the geometry in the mould. The first sample set was solidified with the same initial orientation, whilst the second sample set was rotated upside down for the entirety of the cooling process.

Prior to four-point probe measurements, each plate sample was lightly abraded with 120 grit SiC paper, so that the probe tips could make contact with a flat surface. Samples were then immersed in dilute ethanol for several minutes and then rinsed with deionised water to rid the surface of any debris. It should be noted that unabraded surfaces exhibit higher resistances than abraded ones, and the above process was carried out so that the effects of wax encapsulation and particle agglomeration at the top surface could be lessened. This would be a particular issue with the carbon black-laden wax samples. In addition to this, etching surface treatments are also carried out on investment casting wax patterns prior to being dip-coated, and this etching process replicates the same working surface on the conducting wax pattern prior to EPD.

The four-point probe resistance meter was set-up with a linearly positioned tip spacing of 1 mm. The probe set-up was placed on five sites with the central area of each sample, so that the linearly positioned tips were more than 20 mm from any lateral edge. One

measurement was carried out at the central point of the sample, whilst the others were taken in each of the circular plate's quadrants. This procedure was carried out on both the top and bottom plane of each sample, for reasons described in Section 8.4.

The probes were kept on the specimen surface for 2 minutes before any results were taken, to allow for the resistance measurements to stabilise. They still fluctuated over a range after this point, and so 5 randomly chosen measurements over the next 2 minute time period were chosen and averaged to give the site resistance. The maximum resistance that can be measured by this set-up is approximately 100 kΩ, which corresponds to a bulk resistivity of approximately 60 kΩ.cm for a 2.5 mm thick sample.

CHAPTER 10. WAX RHEOLOGY

10.1 Introduction

Rheology is the study of the deformation and flow behaviour of matter. An introduction to rheological concepts is given in Chapter 6. The rheological behaviour of the filled wax is of importance, since it determines what volume% of a filler material can be added to before it becomes unsuitable for use within wax pattern-forming operations.

The composite batch formation processes are described in Section 8.4, although a further casting stage was carried out to make the material suitable for rheology experiments. Each 3 mm thick cast wax plate was separated into several sectors, so that any filler content inhomogeneities in the sample due to settling would not lead to filler concentration differences from sample to sample. Each sector was then melted and cast into a new 65 mm diameter plate geometry with a thinner cross sectional thickness of 0.8 to 1.0 mm. This lower thickness meant that each sample could be easily melted on the rotational rheometer peltier hotplate prior to testing.

10.2 Rheological Techniques

10.2.1 Introduction to Rheometry Experiments

As described in Section 7.1, rheometry is the study of the techniques used to determine the rheological properties of a material. The TA Instruments Advanced Rheometer AR500 was used in the present set of experiments. This apparatus can determine the rheological properties of a fluid using a number of different testing geometries, which include cone and plate, parallel plate and concentric cylinders. Within the present work, the use of cone & plate and

parallel plate set-ups were preferred over the use of concentric cylinders, especially in rheological studies where material temperature is a variable. The cone and plate and parallel plate set-ups used a Peltier heating system, where temperature modifications could be carried out to ± 0.1°C to counteract the effect of shear heating, as described in Section 7.2.1. The equipment set-up using concentric cylinders, on the other hand, required the use of a water-bath, which would both increase the required experimental time-frame and lower the resolution and repeatability. Of the cone and plate and parallel plate set-ups, the parallel plate was used experimentally. The cone and plate set-up's separation gap of only 55 μm was deemed unsuitable for use with samples containing aggregated fillers.

10.2.2 Procedure for Using the Rotational Rheometer

Before each sample was loaded onto the AR500 rheometer, both the Peltier heated sample plate and the rotating plate were cleaned, with ethanol and then deionised water, before being dried to remove any presence of liquid. The heater plate was then brought up to operational temperature, and the distance between the parallel plates was calibrated to zero. Separation gap inaccuracies of even 10 μm can alter processing calculations and lead to significant errors in the resulting data.

After zeroing, the top plate was kept in place so that it could too be heated to the working temperature. The temperature of the moving top-plate has to be high enough to stop wax solidification as it is moved down into contact with the sample, which would otherwise hinder its approach as it attempts to reach the separation gap. This was a particular issue with the more heavily filled wax samples.

The samples used for the rheology measurements were in the form of 1mm thick sheets, as described in Section 10.1. The top plate was raised and a specified mass of the

sample was placed in the gap and allowed to fully melt before the operation gap between the two plates was set. The parallel plate separation was kept to 300 μm, as preliminary experiments with graphite filled wax composites gave inconsistent results when smaller gaps were implemented. To ensure that it was the viscosity of the wax between the parallel plates being measured, any excess wax that is pushed outside the volume between the plates is removed, as shown in Figure 10.1 (c).

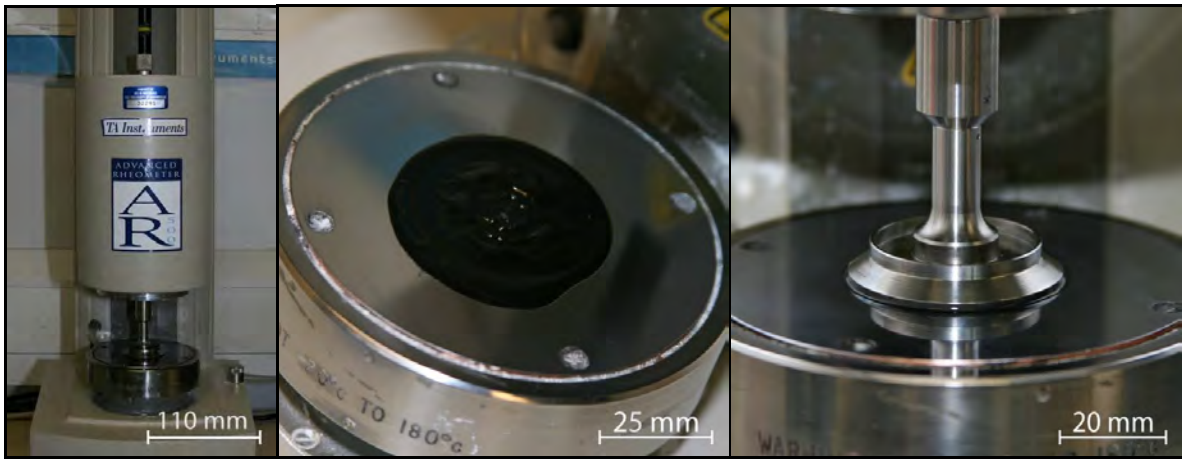

(a) **(b)** **(c)**

Figure 10.1 Photographic images showing; (a) the TA instruments AR500 rotational rheometer used; (b) a filled wax sample as it is melted on the lower fixed plate of the rheometer; (c) a wax sample as it is tested between the parallel plates. Any excess wax has been removed from the surrounding region, as it may otherwise effect viscosity measurements.

Whilst several preliminary experiments were carried out on Blayson Olefines A7-11 based composites, the lower working viscosity of the A7-7808 grade was the preferred matrix for the primary rheological studies. The shear stress values that could be produced by the TA AR500 rotational rheometer have a defined upper limit, and so the use of a base wax with a lower working viscosity led to results being obtained from samples with filler additions at higher concentrations. Samples of the micronised graphite-filled and carbon black filled waxes were formed as described in Section 8.4 at concentrations between 12.36 and

32.65 wt%, and due to particle agglomeration in the carbon black filled-wax samples, this range was extended to cover filler contents below this. Table 8.2 and 8.3 in Section 8.4 shows the range of sample compositions tested using rheological methods.

10.3 Rotational Rheometry Tests

10.3.1 Flow Curves and Viscosity Testing

Flow ramp testing is described in Section 7.2.1, and a number of terms that are used within this section are defined there. The AR500 Rheometer (TA Instruments) used within the present work produced measurements using a controlled shear stress (CSS) set-up. Many of the samples tested were solid particle suspensions in a liquid wax matrix, and a CSS mode could be used to ascertain yield point information for the more highly concentrated dispersions.

Transient effects, as described in Section 7.2.1, can be reduced by lengthening the time at each plot point within flow ramp experiments. In CSR setups, logarithmic measuring point duration can be automatically varied according to measured shear rate. In this way, results at low shear rates are given longer testing times. It was deemed that the importance of ascertaining accurate yield point values (using CSS) was of greater significance than the ability to alter measuring point duration times. A rule of thumb used by Mezger (2006) was to set the measuring point duration so that it is at least as long as the reciprocal shear rate $(1/\dot{\gamma})$; so, for samples where the minimum shear rate is 0.1 s^{-1}, the measuring point duration should ideally be greater than 10 seconds.

In the main rheological experiments, results were taken using a logarithmic preset, with 15 points plotted out per decade. In CSS mode, flow curves were plotted using data from a range of shear stress values, from 0.779 to 1500 Pa at 80°C. The experimental timeframe

was set to 480 seconds, and was the time taken for the shear stress to increase from zero to maximum and decrease to zero again. This made the measuring point duration 4 seconds, which is shorter than ideal, but was used to avoid time-related structural breakdown effects. Using the rule of thumb, samples with low shear stress viscosities of less than 3.12 Pa.s could be accurately plotted.

Dispersions with a high effective concentration of solid particles (either through high levels of loading or agglomeration) often possess a yield point, and within the present work, the value of the yield point was taken to be the point where the flow curve intersects the shear stress (τ) axis when a linear scale is used. No pre-shearing process was put in place for the initial set of flow ramp experiments. Following the results of Section 10.3.3; namely tests associated with time dependent flow behaviour, a second set of flow ramp tests were carried out on selected filled wax compositions, with the procedure modified to included a 300 second, 750 Pa pre-shear cycle.

10.3.2 Temperature Dependent Flow Behaviour

Experiments on filled waxes using a temperature ramp were carried out to see whether the addition of a thermally conducting filler material would alter the temperature of the phase transition. A temperature ramp experiment was conducted using a new sample, and tested the material at temperatures between 55 and 80 °C. An initial downward ramp (80 – 55 °C) was followed by an upward ramp (55 – 80 °C), using a heating/cooling rate of 1°C per minute (in 0.5 °C increments). CSS mode was used with constant applied shear stress values of 200, 750 and 1500 Pa.

For a sample contained within a 300 μm separation gap, this heating rate on a Peltier hotplate was deemed slow enough to ensure that there was no temperature gradient present within the sample. As the filler material is thermally conducting, the way that heat is dissipated through a wax would change with filler addition. For several material compositions, temperature ramp experiments on were also carried out using heating / cooling ramp rates of 0.5 and 2 °C per minute, to observe whether ramp rate had an effect on the viscosity curve, owing to the presence of temperature gradients in samples with differing thermally conductivities.

10.3.3 Time Dependent Flow Behaviour

In addition to observing the presence of thixotropic or rheopectic behaviour within flow ramp tests described in Section 10.3.1, tests were carried out to see whether the addition of conductive filler meant that the material possessed non-recoverable viscosity changes with time under shear, as described in Section 6.6.2.

Flow tests were carried out over a testing period of 1800 seconds (30 minutes), at a constant stress level ascertained by the results of the CSS mode flow curves. For unfilled and graphite-filled wax samples, this shear stress was set to 750 Pa, and for all samples, including carbon black filled waxes, experiments were also carried out at 1500 Pa. All tests were carried out at a constant temperature of 80.0 °C.

If significant viscosity changes were observed in samples of a filled wax, the shear stress dependent flow tests and temperature dependent flow tests were repeated using the same criteria stated in Section 10.3.1 and Section 10.3.2, all be it with a pre-shear phase in place prior to testing. This initial phase placed the sample under a shear stress of 750 Pa for 300 seconds (5 minutes), at 80.0 °C.

It should be noted that many samples that show time dependent degradation also exhibit shear thickening behaviour at high shear stresses, as they are more likely to contain a high concentration of particles (or highly agglomerated particles) in suspension. All filled wax compositions underwent three flow curve tests to gauge both sample homogeneity and test repeatability.

CHAPTER 11. ADDITIONAL WAX PROPERTIES

11.1 Ash Content Testing for Waxes

The ash content of conductive particle-filled and unfilled wax grades was determined by calculation from the mass of the residue remaining after the sample is heated in air under rigidly controlled conditions of time, sample weight and equipment specifications to a controlled temperature of (550 ± 10)°C (ASTM, 2011). The testing procedure followed the route used to test samples with small expected ash content, as both the filled and unfilled waxes were tested. A suitable open-topped crucible was used for these experiments. Using an analytical balance accurate to ±0.1 mg, the crucible was weighed first before the addition of the sample (m_1) and then with it (m_2).

The crucibles were placed in a Lenton Thermal designs 1200 °C laboratory chamber furnace at approximately 32 °C. An initial ramp rate of 5°C/minute was chosen to take the samples from ambient temperatures to 250°C, where the oven underwent a dwell time of 60 minutes. After this dwell period, the oven underwent a second temperature ramp of 10°C/minute, to take the temperature up to 550°C. A second dwell period at this temperature was set, for 60 minutes. The oven was then allowed to cool to ambient temperature before the crucibles were removed. Each crucible with its sample ash contents was then weighed (m_3). Equation [11.1] can be used to calculate the percentage ash content, A_d.

$$A_d = \frac{(m_3 - m_1)}{(m_2 - m_1)} \times 100 \times \frac{100}{100 - M_{ad}} \qquad [11.1]$$

m_1 is the mass of the empty dish (g), m_2 is the mass of the dish plus the test sample (g), m_3 is the mass of the dish plus the ash (g), and M_{ad} is the % moisture content of the test sample used for determination.

Moisture content testing was carried out on new samples from each wax composition studied. Using the same heating set-up apparatus, samples were weighed and heated at a ramp rate of 5°C/minute up to 110 °C, where the oven underwent a dwell time of 60 minutes, before the sample crucibles in the oven were allowed to cool to ambient temperature for removal. The difference in sample mass before and after testing was used to determine the moisture content.

CHAPTER 12. SUSPENSION PROPERTIES

12.1 Introduction

Both the materials and specific grades of those materials have been chosen according to criteria that would both allow EPD techniques to be introduced into the investment casting process, whilst also noting the differences and limitations of a process that is different from the currently implemented dip coat investing process. Such differences, for example, involve the use of low suspension concentrations and minimal binder usage for EPD, in contrast to the dip coat slurries, with a composition as described in Section 2.2.1 and 14.2.3.

12.2 Choice of Materials

12.2.1 The use of Aqueous Suspensions over Organic Counterparts

Due to the European Environmental policy set out in 1992 (Kiss 1993) there has been a drive towards the use of aqueous-based media within ceramic processing techniques, as processes involving organic systems are often more polluting. Aqueous-media EPD, when compared to organic-media EPD, is both a cheaper process and a more environmentally friendly one to carry out. For these reasons, the use of ceramic aqueous suspensions was chosen, even though aqueous EPD has a number of associated problems, as described in Section 4.5.1.1.

12.2.2 Zircon as a Ceramic Coating Material

Zirconium silicate ($ZrSiO_4$) is a compound widely used within the field of refractory materials, and was used within this work as it is a primary component used within the investing/stuccoing investment casting stages. This mineral is called zircon when it is formed naturally.

Five different size grades of zircon were used within this work, to both gauge the effect of particle size distribution on deposition properties and highlight any variation that may arise due to the production practices of different manufacturers. The zircon grades are listed as follows:

1) Helmut Kreutz Kreutzonit 'Super FF' zircon powder (D_{50} ~ 1 μm)
2) Helmut Kreutz Kreutzonit 'Super' zircon powder (D_{50} ~ 1.5 μm)
3) Dupré Minerals Zircon A zircon powder (D_{50} ~ 2 μm)
4) Dupré Minerals Zircon B zircon powder (D_{50} ~ 4 μm)
5) Dupré Minerals Zircon M392 zircon powder (D_{50} ~ 12 μm)

Experiments carried out to compare their particle-size distributions and their behaviour as an EPD coating material are described in Section 16.1.6 and Section 16.1.4, respectively. The two Helmut Kreutz grades were then used in the remainder of the EPD coating experiments, as they demonstrated superior deposition characteristics.

12.2.3 The use of pH Modifiers

Tetramethylammonium hydroxide (TMAH) ($C_4H_{13}NO$) and hydrochloric acid (HCl) solutions were used to alter the initial pH of the suspension prior to zircon addition. A quantity of TMAH stock solution (25 wt% in H_2O, Sigma-Aldrich) was diluted down prior to each suspension being made, to modify the suspension to a pH accuracy of ± 0.05.

A 0.51 wt% TMAH solution was formed by adding 1.0 cm^3 of concentrated TMAH (25 wt% in aqueous solution, Sigma Aldrich) to 49.0 cm^3 deionised water (10 MΩ). HCl in aqueous solution (1.0 M in H_2O, Fluka) was also diluted for this application. The 1.0 mol/dm^3 HCl solution has a mass percentage concentration 3.06 wt%. This stock solution was also diluted down before each suspension formation procedure. 5 cm^3 of the 3.06 wt% solution was added to 45 cm^3 of deionised water, to form a 0.31 wt% HCl solution for pH modification purposes.

12.2.4 Choice of Dispersant

Dolapix CE64 (Zschimmer & Schwarz) is a carbonic acid preparation – an ammonium polyacrylate that acts as an anionic dispersant, and has been used widely in the literature for stabilising colloidal systems. Dolapix CE64 is a polyelectrolyte with bivalent functional groups that completely dissociates above pH 8.5 (Gaydardzhiev, 2006). It has been used to aid the dispersal of alumina (Ferrari, 1997) (Greenwood, 2003) (Gaydardzhiev, 2006) and zirconia (Rao 2007) ceramic powders in aqueous suspension, and its successful implementation in the literature led to its use within the present work. Preliminary suspension preparation experiments related to ascertaining the optimum dispersant concentration for suspension stability are described in Appendix D.3.

12.3 Standard Suspension Preparation Procedure

To produce zircon suspensions suitable for use within EPD testing, experiments were carried out to find suspension pH values and dispersant concentrations that heralded good particle stability in suspension. These experiments are described in Appendix D.2 and Appendix D.3, respectively. For both suspension optimisation experiment and EPD experiments, a standard suspension formation procedure is laid out below. Specifics of (and exceptions to) this procedure are described in the experimental sections of Chapter 13 and Appendix D.

1) Unless otherwise stated, a suspension volume that incorporated 400 cm^3 of deionised water was used. Due to the absorption of atmospheric CO_2, the pH of the deionised water decreases gradually with time from pH ~ 7, as the following reactions take place:

$$CO_2 + H_2O \rightarrow H_2CO_3 \qquad [12.1]$$

$$H_2CO_3 \rightarrow HCO_3 + H^+ \qquad [12.2]$$

This effect would interfere with the pH measurements being taken to ascertain the difference between initial suspension pH and the pH after colloid addition. The pH of the deionised water (10 - 15 MΩ/cm) was allowed to equilibrate in the laboratory atmosphere over a 10 minute period prior to solution modification, to produce a more stable pH of 5.95 ± 0.10. For the duration of suspension preparation, the contents of the hotplate-mounted glass vessel were magnetically stirred using a PTFE-coated bar rotating at approximately 60 rpm and either heated to a temperature of 20.5°C (±2.0°C) or kept at the ambient laboratory temperature if it lay between these extremes. The pH,

temperature (°C), total dissolved solids (TDS) (ppm) and solution conductivity (μS) were measured at each step of the suspension preparation procedure.

2) A quantity of Dolapix CE64 polyelectrolyte was then added to the deionised water if required by the experiment in question. When large quantities (≥ 0.30 cm^3) were necessary, the undiluted additive (75 wt% in aqueous solution) was used. When smaller additions to suspension were required, diluted stock solutions (3 wt% and 15 wt%) of Dolapix CE64 were formed for accuracy of addition. Dispersant solutions were added to the deionised water using a 5 ml glass graduated pipette (± 0.05 ml) and fast-release pipette pump.

3) The stirring mechanism was allowed to continue for a further 2 minutes prior to pH modification. Either the dilute hydrochloric acid (HCl) solution (0.31 wt%) or the dilute tetramethylammonium hydroxide (TMAH) solution (0.51 wt%) would be used depending upon the target pH. The pH modifier was added drop-wise using a 5 ml graduated pipette (± 0.05 ml) in 0.25 cm^3 stages, and the solution was allowed to reach a stable pH between each addition. Additional suspension modifiers like NaCl conductivity solution would then be added if required.

4) When the desired stable pH was achieved, the zircon powder was then added to the modified aqueous suspension, with 40.0 g zircon added for every litre of deionised water present (which equates to a zircon concentration of 3.85 wt%) unless otherwise stated. The rate of magnetic stirring was increased from 60 rpm to 300 rpm for a ten minute time period as the zircon powder was gradually added using a spatula. The suspension was then transferred into a 500 cm^3 polymer container for a 4 hour homogenisation cycle in the roller mixer (Denley - Spiramix) before use within EPD experiments, settling experiments or zeta potential/PZC analysis.

5) During the roller mixer homogenisation cycle, suspensions were removed from the mixer and underwent two ultrasonication cycles to aid zircon dispersion, in a process more fully described in Section 13.3.3. A Jencons VCX 600 sonicator was used for these experiments, using a 13 mm solid probe tip suitable for 10 – 250 ml sample volumes. When larger volumes had to be processed, the sample volume was split up evenly and each part was sonicated separately under the same conditions.

6) The suspension's pH, solution conductivity and temperature were measured after the roll mixing cycle. TMAH was then added using a pipette, to bring the pH to a standard position for equivalent suspensions within an experiment. Suspensions with a pH_i of 8.7 were modified so that the pH_f was equal to 8.3.

CHAPTER 13. THE ELECTROPHORETIC DEPOSITION SET-UP

13.1 Electrode Substrate Material and Geometries

Compressed graphite was chosen as the initial deposition electrode material, so that the key EPD variables could be studied and benchmarked before conductive filled waxes were used as an electrode substrate material in the later experiments. Using multimeter and four-point probe measurements, the compressed graphite used was found to be highly conducting, with conductivity homogeneity in all orientations. Thus, the EPD coatings deposited on the homogenously conducting compressed graphite acted as a benchmark against which different grades of conductive particle-filled could be compared.

The compressed graphite deposition electrodes were cut from blocks of compressed graphite and shaped using abrasion techniques. Rectangular plate shape electrodes with the following dimensions were labelled as 'Type1' electrodes; width = 25 mm, length = 65 mm, depth = 8 mm. Type 1 compressed graphite electrodes were used within the EPD experiments of Section 13.3.

For EPD experiments using conductive particle-filled wax as the deposition electrode, the wax electrode fabrication procedure was the described in Section 8.4. After the conductive wax was formed and homogenised, it was cast into a rectangular silicone plate-mould to form a rectangular plate with a width of 25 mm, length of 50 mm and depth of 8 mm. This was done so that both the Type1 graphite electrode and conductive wax electrode could be immersed into the EPD suspension to a depth that gave them the same substrate geometry and surface area for EPD coating. The non-immersed volume of the wax electrode was smaller than that of the Type1 graphite electrode due to limitations in mould design.

As the conductive waxes did not possess the high electrical conductivity of pure graphite, designs implementing aluminium electrode tabs were introduced, to provide a high surface area for conductive percolation between the electrical circuit and substrate. Several designs were tested, and the one that could be most successfully inserted into the rectangular plate geometry was a flat aluminium plate, with a width of 10mm, thickness of 0.7mm and length of 70mm, of which about 40mm was inside the substrate. It was inserted into the molten conducting wax as it was cast into the rectangular plate, and it was held in place during the initial part of the cooling cycle, to making sure that its placement was equidistant between the top and bottom plate surfaces.

As with for the fabrication procedure used for the circular plate wax samples, a second heated silicone shape was placed, male to female, into the mould containing the filled wax. The cast wax underwent ten 180° flipping rotations during the cooling process, at in an attempt to avoid both filler settling effects and electrode tab displacement. Several samples were cut into cross-sections after cooling, to see whether tab displacement had taken place.

Both the compressed graphite and conductive wax deposition electrodes needed to be linked up as part of the EPD circuit. 25 Amp nickel-plated steel crocodile clips were utilised, as the pressure exerted by the spring mechanism ensured that a good electrical contact was made. This was either attached to the deposition electrode itself or to the protruding aluminium electrode tab (when present). These clips never made contact with the EPD suspension, as they were attached to the Type1 and filled-wax electrodes above their immersion lines, as described in Section 14.1.

13.2 Choice of EPD bath geometry

A cylindrical polymer vessel with a capacity of 500 cm^3 was used as the EPD bath in a number of the experiments as the geometry provided space for an encircling counter-electrode. An aluminium mesh was curved into a cylinder with a 110 mm diameter and then fitted into the vessel to follow the container's internal wall profile. This set-up was designed to accommodate suspensions with initial deionised water volumes of 400 cm^3. When the Type1 graphite deposition electrodes were used within experiments, this set-up gave electrode separation distances of 40 - 50 mm, depending upon plate orientation.

13.3 Variables Studied within EPD experiments on Compressed Graphite

13.3.1 Introduction

As described by Besra and Liu (2007), a number of variables exist that affect the properties of the resulting EPD coating. These can be split up into variables associated with the properties of the suspension itself and those relating to the EPD set-up. A number of different experiments were therefore carried out, using the suspension formation procedure featured in Section 12.3 as a common basis.

13.3.2 Voltage and Time Variables

Source voltage and deposition time parameters were varied for all EPD experiments, to see whether the deposition yields followed Hamaker-defined trends when different suspensions or set-ups were used. The EPD set-up used an EX752M power source (TTi Instruments) that was placed in controlled voltage mode. The voltage within EPD experiments was set between

0 and 40 volts, and the deposition time was set to 1, 2, 3, 5 7 or 10 minutes. For the purposes of determining whether a zircon suspension produces EPD coating with yield repeatability, a 20V set-up and 5 minute deposition time was used.

Preliminary work in the area showed that deposition yields could be improved upon if the substrate was removed from the EPD suspension when the power source was still on, as the deposition time limit was reached. Keeping the coated substrate in suspension for an extended period at zero applied voltage following deposition had a negative effect on the coating uniformity, due to effects related to water running off the coated surface.

13.3.3 Use of Sonication on Zircon Suspensions

Ultrasonication (also called sonication) is a technique that uses a high-intensity acoustic energy source to aid the dispersion of particles in suspension. A sonicator probe tip is used to direct sound waves into the liquid media, which results in alternating high-pressure and low-pressure cycles (called compression and rarefaction cycles respectively). Small vacuum bubbles or voids in the liquid are formed and grow during the low-pressure cycle, and collapse violently during a high-pressure cycle. This phenomenon is known as cavitation, and each collapse produces high local temperatures and pressures (~ 5000 K and 2000 atm.). High speed impinging liquid jets and strong hydrodynamic shear-forces that are produced as a result of bubble collapse break up any particle clusters in suspension.

The suspension formation procedure followed the description in Section 12.3, and ultrasonication steps using a Jencons VCX 600 sonicator were implemented before and during the roll mixing process. The second sonication step did not take place immediately prior to EPD, as the sonication process heats the suspension. After the secondary sonicating cycle, the suspension had to be kept within the controlled temperature conditions of the mixing lab for

approximately 1 hour, to bring the suspension temperature down to that of the laboratory environment (20.5 °C (±2.0 °C)).

To determine the effect that this process has in breaking up agglomerates that may otherwise reduce the integrity of resulting EPD coatings, the sonication cycles were carried out over a range of amplitudes, going from 0% (0 Hz) to 90% (540 Hz). For suspensions using 400 cm^3 of deionised water as the dispersing medium, the volume was split in two, so that the 13 mm solid probe tip (suitable for 10 – 250 ml sample volumes) could be effective.

As magnetic stirrer agitation could not be maintained during sonication to inhibit the settling-out of particles under gravity, A fixed cycle time of 5 minutes was chosen to limit such effects, using approximations set out in Section 4.2.2. If suspensions were left unagitated for longer periods, particle settling leads to agglomeration, as particles form clusters at higher particle densities when they collect at the bottom of the suspension. If this occurs during or after cluster break down processes (like sonication) have taken place, it can have a significant effect on the properties of the electrophoretically deposited coating. For this reason, sonication cycles were carried out twice for each suspension, both at beginning of the roll mill cycle so the surface area is maximised for dispersant interactions on the particles, and towards the end, before use within EPD experiments.

13.3.4 Effect of Particle Grades on EPD Coating Yield

In this set of experiments, the five zircon grades described in Section 12.2.2 were added to aqueous suspension at a number of concentrations, to gauge the effect of particle size distribution on deposition properties. Each suspension was formed using 400 cm^3 deionised water, which was pH modified using TMAH to reach a pH of 8.7 before zircon addition.

Each zircon grade was added to suspension at 20, 40, 60 and 80 $g.l^{-1}$ concentrations (1.93, 3.85, 5.78 and 7.70 wt%, respectively). A Dolapix dispersant concentration of 11.3 $mg.g^{-1}$ was used, and as the zircon concentration was a variable, so too was the dispersant content. The solution conductivity was therefore varied depending upon the zircon loading in suspension, and so a NaCl conductivity solution was added to bring the solution conductivity up to 250 μS/cm. Aside from the procedural variations described above, the suspension formation procedure followed that given in Section 10.2, and during homogenisation, two 50% magnitude 5 minute sonication cycles were applied to each suspension.

13.3.5 Effect of Varying Solution pH on EPD Coating Yield

The zeta-potential analysis of Dolapix CE64-modified 'Super FF' zircon and zircon 'A' suspensions was carried out as described in Appendix D.2. It was deemed that EPD would be most successful when carried out using suspensions with pH_i values between 7.5 and 11.0, where pH_i is the modified pH of the suspending medium prior to zircon addition.

Both Helmut Kreutz 'Super FF' zircon and Dupré zircon 'A' grades were tested in this experiment. Each suspension within this experiment was based on 400 cm^3 of deionised water, with a zircon concentration of 40$g.l^{-1}$. The suspension formation and processing method used followed the procedures described in Section 12.3, with several alterations described below. Two 50% magnitude 5 minute sonication cycles were applied to each suspension during the homogenisation stage, to aid particle dispersion.

Dolapix CE64 dispersant concentrations of 0.0 $mg.g^{-1}$ and 11.25 $mg.g^{-1}$ were used. As modification of pH to more alkaline levels would increase the solution conductivity beyond that of less alkaline solutions, the pH of the suspension was modified to a pH_i value

between 7.7 and 10.2, and a NaCl conductivity solution was then used to bring the solution conductivity to a constant value of ~ 255 $\mu S.cm^{-1}$.

13.3.6 Effect of Dispersant Content on EPD Coating Yield

In this set of experiments, each suspension was based on 400 cm^3 of deionised water, with a modified pH_i of 8.7. A 'Super FF' zircon concentration of 40$g.l^{-1}$ was used. The suspension formation and processing method used followed the procedures described in Section 12.3, although the ultrasonication regime used for each suspension consisted of either two 15% magnitude 5 minute sonication cycles or two 50% magnitude 5 minute sonication cycles.

The dispersant concentration optimisation experiments described in Section 12.4.2 for Dolapix CE64 dispersant modified 'Super FF' zircon suspensions showed that stability rose between dispersant concentrations of 2 $mg.g^{-1}$ (~ 0.25 $mg.m^{-2}$) and 10 $mg.g^{-1}$ (~ 1.27 $mg.m^{-2}$), and formed a plateau above this value. Preliminary EPD experiments showed that electrophoretic deposition was more successful when dispersant concentrations above this optimum value were used, and so, in these experiments, the following Dolapix CE64 dispersant concentrations were used: 0.0 $mg.g^{-1}$ (~ 0.0 $mg.m^{-2}$), 1.5 $mg.g^{-1}$ (~ 0.19 $mg.m^{-2}$), 3.75 $mg.g^{-1}$ (~ 0.47 $mg.m^{-2}$), 7.5 $mg.g^{-1}$ (~ 0.94 $mg.m^{-2}$), 11.3 $mg.g^{-1}$ (~ $mg.m^{-2}$), 15 $mg.g^{-1}$ (~ 1.88 $mg.m^{-2}$) and 19.7 $mg.g^{-1}$ (~ 2.47 $mg.m^{-2}$). After dispersant addition, dilute TMAH was used to bring the solution pH up to 8.7 for zircon addition. No NaCl conductivity solution was used to bring the suspension conductivity to a uniform value, and so the solution conductivity lay between 80 $\mu S.cm^{-1}$ and 320 $\mu S.cm^{-1}$. The results of this experiment were compared closely with those carried out in Section 13.3.7, where the effect of varying the solution conductivity with a fixed dispersant content was studied.

13.3.7 Effect of Solution Conductivity on EPD Coating Yield

In experiments gauging the effect of solution conductivity, aqueous suspensions were used with a 'Super FF' zircon concentration of 40 $g.l^{-1}$. Suspensions each used 400 cm^3 volumes of deionised water and the pH_i was set to 8.7. The suspension formation and processing method used followed procedures described in Section 12.3, using two 50% magnitude 5 minute sonication cycles for each suspension to aid cluster breakdown.

15 'Super FF' zircon suspensions were created for this experiment, each with a pH_i of 8.7 and zircon suspension concentration of 40 $g.l^{-1}$. These suspensions were divided into three categories according to the Dolapix CE64 dispersant concentration used (0.0, 7.5 and 15.0 $mg.g^{-1}$). Before conductivity solution modification, the solution conductivity of suspensions in each of these categories was 16 $\mu S.cm^{-1}$, 140 $\mu S.cm^{-1}$ and 245 $\mu S.cm^{-1}$, respectively. NaCl conductivity solution was then added to each suspension, so that the solution conductivity prior to zircon addition lay incrementally between the conductivity solution non-modified value stated above and 450 $\mu S.cm^{-1}$. This upper conductivity level was selected as a result of preliminary EPD coating experiments.

13.3.8 Effect of Particle Concentration on EPD Coating Yield

For these experiments, 400 cm^3 of deionised water was used as the basis for each pH_i 8.7 suspension, and 'Super FF' zircon concentrations of 40, 80 and 120 g/l (3.85, 7.70 and 11.55 wt%) were used. Dolapix CE64 dispersant concentration was a secondary variable within this experiment. Dispersant concentrations from 1.5 mg/g to 19.7 mg/g were used in Section 13.3.6. When more concentrated zircon suspensions were used in this experiment, the range of studied dispersant concentrations was reduced.

An increase in zircon concentration must be matched by a corresponding dispersant content increase, since dispersant concentration is measured in mg/g zircon. The effect of Dolapix CE64 addition on solution conductivity was therefore greater when more concentrated zircon suspensions were in use. The suspension formation and processing method used followed the procedures described in Section 12.3, using two 50% magnitude 5 minute sonication cycles for each suspension to aid dispersion.

13.4 Variables Studied within EPD experiments on Conducting Wax

A number of the variables described in Section 13.3 were studied when conducting wax was used as the deposition substrate. Prior to testing, a two point multimeter probe set-up was used to gauge how the resistance of rectangular plate sample compared to that of the circular disc samples used within four-point probe experiments. To mimic the wax pre-treatments carried out on the pattern waxes prior to primary dip coating, these samples were dipped in Blayson Olefines Trisol 60 Plus for 3 to 5 seconds. This is a blend of high purity aromatic hydrocarbons and biodegradable emulsifiers, used to both clean and micro-etch the wax surface. The samples were dipped in two successive vats of water, to remove and neutralise the etchant, and then allowed to dry in a controlled drying environment for several hours before EPD.

Due to the similar nature of the EPD experiments carried out on compressed graphite and conducting wax substrates, the experimental variables used are described in Section 18.2, together with the experimental results.

CHAPTER 14. EPD COATING PROPERTIES

14.1 Coating Thicknesses and Yield Measurements

The exact geometry of each Type 1 electrode was measured using a digital calliper accurate to ±0.1 mm. As each electrode substrate was sawn from a block of compressed graphite and abraded to smooth the surface. Owing to the formation procedure used, the exact geometry of each electrode was recorded. Type1 electrodes had the following ideal dimensions: width (w = 25mm), length (l = 65mm) and depth (d = 8mm). An electrode submersion depth of 40 mm was used for an ideal Type1 geometry, to give the electrode a submersed substrate surface area of 2840 mm^2 (28.4 cm^2). Type1 geometries with slightly different cross-sectional dimensions as a result of the sawing process were immersed to a depth that ensured that the deposition area of 2840 mm^2 was maintained. The designated submersion depth was marked on each sample.

All graphite substrates used for EPD coating experiments were used previously for preliminary EPD work, and were systematically cleaned by placing them in diluted acetone solution, to remove the fine layer of zircon that remained after cleaning in water. The substrates were then dipped in two successive vats of water to remove the acetone, and then dried before reuse. Viewing the cleaned substrates under SEM confirmed the fact that no zircon particles with a diameter greater than 1 μm were present on the surface. To measure EPD deposition yield, each labelled substrate was weighed both prior to the EPD coating process and afterwards, following the drying process.

Basic coating thickness measurements were carried out using the digital calliper, as half the difference between the uncoated and coated cross-sectional distances. Measurements were made in the central region of the rectangular plates at 10 mm height intervals, to see

whether a deposition gradient is present due to particle settling and run-off effects. In addition to this, the deposition thickness in the central plate regions was compared with that near the edges, to see whether the electric field intensification leads to increased deposition.

More accurate measurements were carried out on selected samples using scanning electron microscopy. For green unfired EPD samples, a tungsten carbide scribe was used to cut though the coating and score the substrate, before a manual saw was employed to make a cross section through the substrate itself. For fired ceramic coatings, a Diamant Boart TS350M saw was used to cut the coatings formed on graphite or conducting wax substrates into cross-sections for analysis. Samples were then cleaned and mounted on a specimen stub. A number of samples then underwent low vacuum gold sputter coating to make the surface electrically conducting for analysis. The scanning electron microscope used was a Philips XL-30 field emission SEM, and all micrographs were taken in secondary electron (SE) mode.

14.2 Permeability Testing of EPD primary coated Spheres

14.2.1 Introduction

Permeability is defined as the ability of a material to allow fluids to pass through it. Within the field of investment casting, the investment shell requires a certain degree of permeability, to allow for the removal of air that is rapidly displaced by the poured molten metal during casting. Insufficient shell permeability will restrict the outflow of air, and so may lead to the formation of casting defects that result from the incomplete filling of the mould. The presence of pore channels within a material increases its permeability if they interact in such a way to form a continuous path across the sample. From an investment casting standpoint, these channel need to run from the primary coat to the seal coat, and for the primary coat, particle

size, size distribution, particle packing density and temperature are key variables. Most investment shells have an open porosity minimum of 30% (Jones, 2003).

Permeability values for an investment casting shell system need to be reproducible and so industrial standards have been put in place, where the testing geometry, airflow parameters, and other variables are specified (BSI, 2003). For investment casting permeability testing, permeability is defined as the ratio of volumetric flow rate to the pressure gradient causing flow, at a given temperature. The shell permeability is of greatest importance during metal casting, and so the British standard, BS 1902-10.2: 1994 (BSI 2003) states that permeability testing is to be carried out at an elevated temperatures.

The BS 1902-10.2: 1994 permeability testing geometry is a hollow spherical ceramic geometry, which is penetrated by an impermeable hollow rod, through which the air flows. The design is shown in Figure 14.1(a). For slurry coating methods, a hollow plastic ball is used as the substrate upon which the spherical ceramic shell is formed, and an International Table Tennis Federation (I.T.T.F.) approved 3 star table tennis ball is specified. Such I.T.T.F. approved balls have a cross-sectional diameter tolerance between 37.2 and 38.2 mm, which for the purposes of testing is assumed to be 37.7 mm.

The aim of the present work was to form an EPD primary coat on permeability test piece, so that permeability of the EPD primary coat and dip coated primary coat could be compared. The EPD substrate had to be electrically conducting, however, and so the British Standard procedure could not be used without further modifications. It is stated in BS 1902-10.2: 1994 that additives in the slurry bath may attack a table tennis ball, and allows for the use of an alternative wax design. The use of a hollow spherical melt-out geometry made from a conductive particle-filled wax was therefore proposed, as shown in Figure 14.1(b).

The method used to form the hollow spherical geometry is outlined in Section 8.4 and Section 14.2.2. Since a purpose-made set of wax moulds could not be supplied with the

exact geometry of the I.T.T.F. ball, a mould design was used with a hollow sphere diameter close to that specified, so that geometric corrections could be made during permeability testing analysis. The nature of the testing procedure, along with the thickness of current EPD coatings means that further thickening/strengthening layers need to be built up using successive dip coats, for both for the EPD and dip coat primary coats.

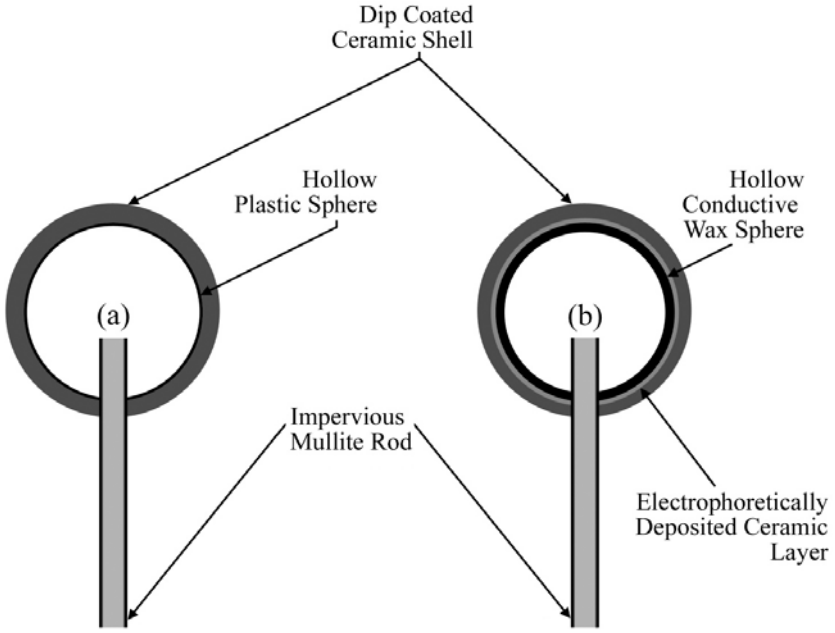

Figure 14.1 Diagram showing cross-sectional diagrams showing (a) the permeability geometry stipulated by BS 1902-10.2: 1994; and (b) a modified geometry using a conductive wax spherical substrate in place of the plastic sphere.

14.2.2 Conductive Wax Spheres for Permeability Testing

It is stated in BS 1902-10.2: 1994 that when wax spheres are used in permeability measurements, it "may prove difficult to completely drain the wax from the shell mould. If wax is used, however, it should be removed from the test piece following the normal de-waxing procedure for investment casting shell moulds and carefully inspected for cracks prior

to testing." To reduce the possibility of cracking, the wall thickness of the sphere was set to 4mm. This was both thick enough to provide a strong substrate for the ceramic coating and thin enough to avoid cracking in all fired samples.

The wax hemispheres were formed using the method described in Section 8.4. After solidification, the wax geometries were separated from the silicone moulds and any wax flash was removed using a scalpel. To form a hollow wax sphere, a heated tool was used to melt the cross-section of each hemisphere over the area where they join. Owing to the shape of each hemispherical mould, the resulting wax geometry could be described as being a hollow cylinder with a single hemispherical end, where the length of the cylindrical section is approximately 1 mm. As the process used to join the hemispheres resulted in the loss of 1 – 2 mm of material at the interface, the resulting geometry remained spherical. The hemispherical cross section diameter would have otherwise differed from that of the full sphere when measured perpendicularly to the joining plane. A soldering iron with a modified stainless steel spatula attachment was then used to smooth the edge of the sphere where the hemispheres met.

In British Standard guidelines, it is stated that the tube material should be non-porous, capable of withstanding the test temperature and possess a thermal expansion coefficient similar to that of the shell mould (BS, 2003). An impermeable mullite rod with an internal diameter of ~ 6mm was therefore used. To position the impermeable mullite rods so that they bisected the spheres and penetrated to a fixed depth of ~ 20 mm, a mark was placed on the rod. The soldering iron with a modified hollow stainless steel coring attachment was used to bore a hole into the sphere, at the interface between the wax hemispheres. To ensure that a good seal was made, a small amount of conductive wax was melted and solidified around the interface between the sphere and the rod. For some experiments, this conductive

wax was formed into a tab that ran up the length of the rod, to form an electrical contact onto which a crocodile clip could be positioned.

The wax spheres dimensions were measured using a digital calliper, with an accuracy of ±0.05mm, which was below that of the knife-edge vernier calliper suggested (accurate to 0.02mm). The results were recorded using the method in the guidelines, where four readings, taken at approximately 45° intervals around the diameter of the test piece were taken, to measure diameter uniformity. These results were averaged for calculations. The thickness of the coating test piece was calculated by taking similar measurements to those carried out on the uncoated sphere. The mean substrate sphere diameter was taken from the mean coating test piece diameter and divided by two to arrive at a coating thickness value.

14.2.3 Shell Formation and Firing

The EPD primary coating required further ceramic coating, as expected, to thicken and strengthen the mould geometry. For this, a standard slurry coating and stuccoing process was employed, and is described below. Owing to the use of zircon within the EPD primary coat, the dip system suspension was zircon/silica based, akin to that used for fabricating shells for the investment casting of steels.

The most successful EPD coatings were formed on conductive wax spherical substrates, and so this substrate type was used for tests when the EPD primary coat was and was not present within the investing cycle, as shown in Table 14.1. The cleaning/etching stage was carried out on all wax samples prior to coating, as described in Section 13.4.

The constituents of the steel primary are shown in Table 14.2. The primary stucco used to strengthen the initial dip coat was a Calcinated Zircon Sand. The secondary stucco, used after the second and third dip coats was a Molochite 30-80 grade (ECC International),

whilst that used following the remaining five dip coats was a Molochite 16-30 grade (ECC International).

For samples where an EPD primary was used, coated samples were dried in a low humidity environment at 21°C for 16 to 24 hours. A primary stucco coat could not be immediately applied to the EPD primary coat because the primary coat had to undergo a drying cycle to strengthen it due to the absence of polymeric binders, yet stuccos require a wet coat for adherence. An investment primary coat used for steel casting (composed as shown in Table 14.2) was therefore applied onto the EPD coat after drying, with the zircon sand stucco immediately applied to this.

Table 14.1 Shows the investing procedure carried out both on conductive wax permeability spheres and plates for analysis. A number of samples did not undergo Coat 0, so that primary EPD and primary slurry face coats could be compared.

Coat	Type	Slurry Code	Stucco	Drying Air Speed	Dry Time
0	EPD	Zircon EPD	n/a	(0.0 ms^{-1})	16 - 24 h
1	Dipped	'Steel' Primary	Zircon Sand	10% (0.1 ms^{-1})	19 h
2	Dipped	'Steel' Secondary	Mol 30/80	50% (3 ms^{-1})	1.5 h
3	Dipped	'Steel' Secondary	Mol 30/80	50% (3 ms^{-1})	21 h
4	Dipped	'Steel' Secondary	Mol 16/30	50% (3 ms^{-1})	1.5 h
5	Dipped	'Steel' Secondary	Mol 16/30	50% (3 ms^{-1})	1.5 h
6	Dipped	'Steel' Secondary	Mol 16/30	50% (3 ms^{-1})	1.5 h
7	Dipped	'Steel' Secondary	Mol 16/30	50% (3 ms^{-1})	1.5 h
8	Dipped	'Steel' Secondary	Mol 16/30	50% (3 ms^{-1})	n/a

The hollow wax sphere attached to the mullite rod is hereafter called the test piece, and this nomenclature is used within the rest of the text relating to permeability testing. The test piece was dipped into the primary slurry tank so that the primary slurry coated both the sphere and the portion of the tube above it by between 25 mm and 75 mm along its length. The manual coating procedure involved holding the test piece by the impermeable mullite rod

at an angle of approximately 40 - 50° from the vertical position, with the sphere at the lower end. The piece was then immersed into the slurry to the stated depth, and rotated slowly at this angle to the vertical, to ensure that a uniform thickness of slurry has coated the sphere and adjoining rod. On removal from the slurry, the test piece was rotated on a number of different planes to ensure that no area on the substrate surface became devoid of coating material as excess slurry flowed from it under gravity. The test piece was then held in the vertical position with the sphere at the upper end, for transfer to the stucco area.

For stuccoing, the required stucco, as stated in Table 14.1, is held within a polymer box. A sifting sieve is used, with a mesh diameter that lets through all singular particles of the stated stucco, and holds back agglomerated grains. The sieve would be filled with stucco and held about 200 – 300 mm above the test piece. The sieve was gently shaken, so that a stream of particles would fall onto the slurry coated test piece, which was rotated in a number of conformations so that stucco would adhere to everywhere it was required. The test piece was then hung from the top of the mullite rod within the drying room for the allocated period, as specified in Table 14.1. Further slurry coating and stuccoing stages were carried out after the formation of the primary layer, and all followed the same basic procedure.

Table 14.2 Composition and Properties of a Primary Coat used for Steel Casting.

Species Type	Specific Information	Mass (kg) Addition	System Information
Filler	200 mesh Fused Silica	11.00	Filler loading 78 %
Filler	200 mesh Zircosil	33.02	
Binding Agent	Remet LP Sol	12.55	Latex/polymer 6 %
Polymer	Adbond ADH	0.935	
Wetting Agent	Victawet 12	0.047	pH 9.4 - 9.8
Antifoam	Burst RSD-10 Antifoam	0.080	
Water	Deionised	1.98	Viscosity 100-120 B4
		Total 59.61	

14.2.4 Permeability Measurement Procedure

Following the final eighth dip coat and stucco step, the permeability spheres were dried in a controlled humidity environment for 1.5 hours, with an air flow rate of 3 $m.s^{-1}$. After this stage, the samples are removed from this environment and placed in the ambient laboratory environment, where the test piece diameters are measured using the technique applied to the uncoated spheres.

Permeability samples were then placed in a Lenton Thermal Designs 1200 °C laboratory chamber furnace for dewaxing and firing. This furnace uses two side panel heating elements to provide temperature uniformity. An initial ramp rate of 5°C/minute was chosen to take the samples from ambient temperatures to 250°C, where the oven underwent a dwell time of 60 minutes. After this dwell period, the oven underwent a second temperature ramp of 10°C/minute, to take the temperature up to 550°C. A second dwell period at this temperature was set, for 60 minutes. The oven was then allowed to cool to ambient temperature before the permeability spheres on rods were removed.

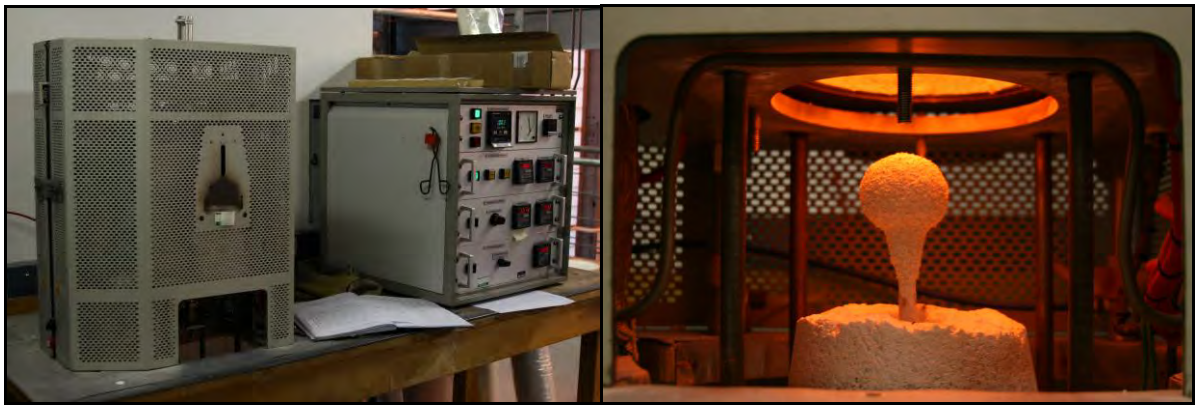

(a) **(b)**

Figure 14.2 Photographs showing the set-up used for permeability experiments. **(a)** shows both the permeability rig furnace and control unit, whilst **(b)** shows the permeability sample before it is moved up into position within the furnace for testing.

The permeability rig used for the permeability experiments was a Severn Thermal Solutions furnace with a Eurotherm 92 PID controller, as shown in Figure 14.2. From ambient laboratory temperatures, a ramp rate of 30 °C.min^{-1} was used, to bring the furnace up to a test temperature of 1000 °C, as stipulated for zircon-based coating system. Before testing, the mass flow was set to 0.0 l.min^{-1}.

The door at the base of the furnace was unscrewed and the permeability sample was placed so that the mullite rod stood vertically, attached to the air supply nozzle. The sample and door were then raised into place and screwed in position. Although this procedure was carried out as efficiently as possible, opening the door for this time lowered the furnace temperature to between 800 and 900 °C. Using a ramp rate of 30 °C.min^{-1}, the furnace temperature was increased to 1000 °C, and the sample was kept at this temperature for 5 minutes prior to any air flow permeability testing.

The control unit was used to set the mass flow to 1.00 l.min^{-1}. This value was used because it lay at the upper end of the equipment's working range, and produced pressure values in the samples that lay between 6.9 kN.m^{-2} and 34.5 kN.m^{-2}, as stipulated by BS 1902-10.2:1994. This was applied for a ten minute (600 seconds) period, with the pressure monitored and recorded at 150 second intervals. Fluctuations in the mass flow rate were also recorded during this timeframe. Using a conversion of 1.45 psi = 10 kN.m^{-2} (BS, 2003), it was possible to arrive at calculated values for the permeability μ (m^2), using Equation [14.1]:

$$\mu = \frac{\eta V_c l}{aP} \qquad [14.1]$$

η is dynamic viscosity of air at the temperature of the test (Ns.m^{-2}), V_c is the volumetric flow rate of air corrected for expansion at elevated temperatures (m^3.s^{-1}), l is the thickness of the shell mould (m), a is the inner surface area of the hollow shell mould (m^2) and P is the

pressure difference across the test piece ($N.m^{-2}$). V_c can be calculated using Charles's law, as shown in Equation [14.2]:

$$V_c = \frac{V_1 T_2}{T_1} \qquad [14.2]$$

V_1 is the volumetric flow rate at room temperature ($m^3.s^{-1}$), T_2 is the specified elevated temperature (K), and T_1 is room temperature (K). Additionally, the standard airflow capacity, (SAF) ($m^3.s^{-1}$), is calculated for experiments using Equation [14.3]:

$$SAF = \frac{P_2 V_c}{P_1} \qquad [14.3]$$

P_1 is the measured pressure ($kN.m^{-2}$) and P_2 is the standard pressure (taken to be 10 $kN.m^{-2}$). As stated in BS 1902-10.2: 1994, the area, a, in these tests is taken to be the inner surface of the mould, even though it should be calculated by integration from the inner surface of the mould shell to the outer surface of the shell (BS, 2003). According to the British Standard, this is because the primary coat is the densest and should offer the greatest resistance to air flow. A dipped primary coat is either the secondary or initial coat to be applied to substrate, for EPD coated and uncoated spheres respectively. Even though the fine particle size of the EPD coating should give the EPD primary layer an even higher resistance to air flow, and hence reduce the permeability of the shell as a whole, bubble formation due to water electrolysis may lead to the formation of air channels that bypass this layer.

ANALYSIS AND EVALUATION

CHAPTER 15. PROPERTIES OF CONDUCTIVE-FILLER MODIFIED WAX

15.1 Conductivity Measurements

15.1.1 Introduction

The principle behind carrying out conductivity experiments for filled waxes is explained in Section 5.4, and, for convenience, is summarised below. In carrying out resistance analysis of a composite material, one can find the critical volume fraction when the dispersed conductive powder phase becomes a continuous phase within the matrix. At, and above, this critical volume fraction, the composite material would be comprised of two interpenetrating continuous phase networks. Resistance analysis of the composite material also enables the relationship between conductive particle concentration and conductivity above this critical volume fraction to be determined. This critical volume fraction is called V_c, as the percolation threshold (P_c), applies to unsegregated distributions, as described in Section 5.4. Both the magnitude of V_c and the nature of the relationship between conductive particle concentration and conductivity above this critical volume fraction can be used in conjunction with rheological measurements to describe the behaviour of particles within the material. This is because both flow behaviour and conductivity are linked to the conductive particle filler concentration.

When conductive particle-filled waxes are used as melt-out EPD substrates, their conductivity can be linked to the properties of any electrophoretically deposited (EPD) coating. Experiments carried out to ascertain the resistivity of conductive particle-filled wax samples are described in Section 9. Analysis of data according to results gathered using the

four-point probe set-up is described in Section 15.1.2. Multimeter methods were also carried out to verify resistance measurement trends, with methodology and analysis shown in Appendix B.1.1 and B.1.2 respectively.

15.1.2 Four-point probe resistances

Within the present work, the resistivity of the unfilled waxes could not be experimentally verified using either four-point probe techniques or multimeter measurements, as the set-ups have operational upper limits of 100 kΩ and 10 MΩ respectively. Waxes generally possess resistivities, ρ (Ω.m), in the order of 10^{13} and 10^{17} Ω.m (NPL, 2011), where resistivity is defined in Equation [15.1]:

$$\rho = R.A/l \qquad [15.1]$$

R is the electrical resistance of the material (Ω), l is the length of the piece of material (m) and A is the cross-sectional area of the specimen (m^2). Although the V_c cannot be measured by gauging the point when the sample resistance suddenly deviates from the high resistance plateau, one can still make use of observations related to the relationship between filler content and material resistivity at higher filler concentrations.

Four-point probe measurements were carried out according to procedures described in Section 9.2. The resistivity was derived from four-point probe resistance measurements, using Equation [15.2], which is a rearrangement of Equation [9.1] in Section 9.2.1:

$$\rho = 2\pi s.T_1(t/s).V/I \qquad [15.2]$$

$$R = V/I \qquad [15.3]$$

ρ is volume resistivity (Ω.m), s is the probe tip spacing (m), V is the voltage (V), I is the current (A), R is the resistance (Ω) and $T_1(t/s)$ is the correction factor taking into account the ratio between t (the sample thickness (m)) and s (the tip spacing (m)). When four point probes with a spacing of 1 mm were used to test plate samples which were 2.5 mm thick, a correction factor of 0.951 was used (Topsoe, 1968). The relationship between average sample resistivity and filler content is displayed in Figure 15.1, for both carbon black and graphite filler within the three wax matrix grades studied.

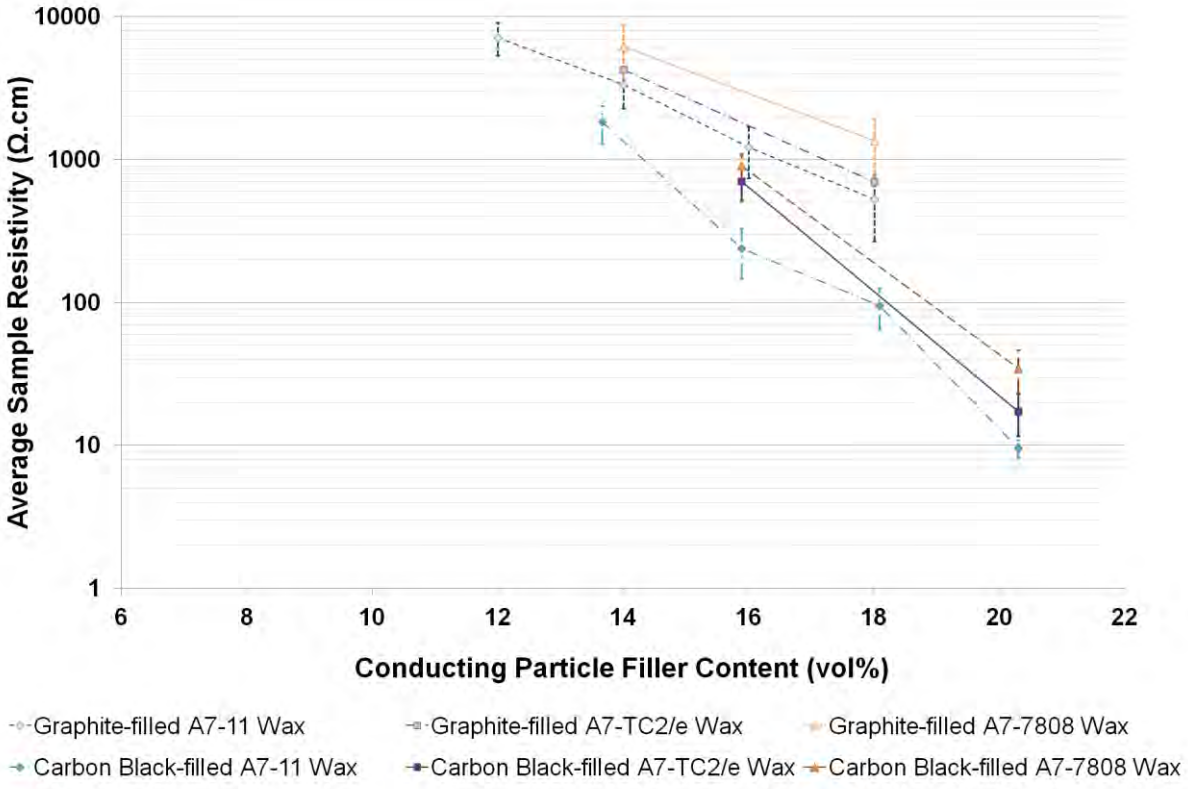

Figure 15.1 Graph showing the relationship between the material samples' electrical resistivity (Ω.cm) and the conductive filler content for three wax grades, according to four-point probe tests carried out on cast flat plates of conductive particle-filled wax.

Resistivity measurements for conductive particle-filled A7-11 wax plate samples are shown in Table 15.1 and Table 15.2, with data displayed graphically in Figure 15.1. The difference in the shape of the filled A7-11 resistivity curves featured in Figure 15.1 can be combined with observations made during sample formation, to explain the filler content-conductivity relationships.

Graphite-filled A7-11 wax samples the filler concentrations less than or equal to 10 vol% (19.7 wt%) displayed no measurable resistance values. When the graphite concentration was increased beyond 10 vol%, the sample resistivity followed a roughly exponential reduction as the filler content was increased. A finite resistivity value for a graphite-filled wax system could not be ascertained by following the exponential curve due to the limited number of plotted values. A compressed graphite plate was used to represent a 100 vol% graphite system, and possessed a four-point probe resistivity of $\sim 5 \times 10^{-3}$ Ω.cm. Such a resistivity could not, however, be reached within a filled wax composite, as filler addition is limited by its maximum packing fraction (φ_m), as described in Section 6.8.3.

Carbon black-filled A7-11 wax samples displayed similar behaviour, and samples with the filler concentrations less than or equal to 9.2 vol% (16.1 wt%) displayed no measureable resistance values. Carbon black-filled samples displayed a greater reduction in resistivity as the concentration was increased, and so exhibited lower resistivities at high loadings, averaging 9.6 Ω.cm at 20.3 vol% (32.65 wt%). The relationship between average sample resistance and filler concentration for both carbon black and graphite-filled waxes compared closely to the results of Appendix C.1.1.2.

The reason for differences in the behaviour of carbon black and graphite in wax composites can be attributed to the way that the particles are distributed as part of the composite. The graphite and carbon black both consist of plate-like particles, although the level of agglomeration in the carbon black is far more prominent. In the literature, carbon

black-filled insulator matrix composites have been formed displaying V_c values as low as 0.76 vol% (Chakrabarty 1991), as shown in Section 5.5.2. Although the V_c cannot be verified within the present work for the carbon black-filled wax systems studied due to the resistivity measurement techniques employed, it is assumed to lie between 6 and 8 vol%. When added to the molten wax grades, the Cabot Vulcan grade agglomerates must not become fully sheared out on mixing, either due to limitations in the mixing process employed or due to its structural properties (Brosseau, 1997). If this was the case, many of the particle clusters would not become fully drawn into a 'mother-of-pearl' structure, where agglomerates are sheared and segregate to the wax grain boundaries to form an ordered conductive network. When graphite-filled and carbon black-filled waxes are compared, the lower resistivities resulting from the use of carbon black can be attributed to the formation of a more segregated conductive network.

The average electrical resistivities of conductive particle-filled wax samples using different insulating wax matrix grades were also compared. The use of A7-11 wax grade as the insulating matrix led to consistently lower resistivity values for a given percentage of conductive filler, both when graphite and carbon black particles were used. This difference can be attributed to the difference in the viscosity of the wax matrix during the filler mixing and cooling stages. The mixing temperature during composite fabrication was reasonably constant (80 – 85 °C) for all wax grades, and so, as shown in the rheology experiments of Section 15.2.2, the viscosity at these temperatures is lower for the A7-7808 grade and higher for the A7-TC2/e grade at 80 °C. As described in Section 8.4, lower matrix viscosities lead to higher resultant material resistivities, as particles intermix in the interfacial regions to a greater degree, and are more likely to remain homogenously dispersed and not form conductive pathways along the matrix's grain boundaries under shear, which would otherwise reduce the resistivity of the material.

Table 15.1 Tabulating the relationship between the material samples' electrical resistivity (Ω.cm) and the conductive filler content in A7-11 wax (vol%), according to the results from a set-up where circular material plates are tested using a four-point probe apparatus.

Micronised Graphite-filled A7-11 Wax				
weight% Filler	**volume% Filler**	**Average Sample Resistance (kΩ) (2 sf)**	**Average Resistivity (Ω.cm) (2 sf)**	**Standard Deviation (Ω.cm) (2 sf)**
0	0	NR	NR	NR
8.4	4.0	NR	NR	NR
12.4	6.0	NR	NR	NR
16.1	8.0	NR	NR	NR
19.7	10.0	NR	NR	NR
23.2	12.0	12	7200	1900
26.5	14.0	5.6	3400	1100
29.6	16.0	2.1	1200	480
32.7	18.0	0.89	530	260

Table 15.2 Tabulating the relationship between the material samples' electrical resistivity (Ω.cm) and the conductive filler content in A7-11 wax (vol%), according to the results from a set-up where circular material plates are tested using a four-point probe apparatus.

Carbon Black-filled A7-11 Wax				
weight% Filler	**volume% Filler**	**Average Sample Resistance (kΩ) (2 sf)**	**Average Resistivity (Ω.cm) (2 sf)**	**Standard Deviation (Ω.cm) (2 sf)**
0	0	NR	NR	NR
8.43	4.6	NR	NR	NR
12.36	6.9	NR	NR	NR
16.11	9.2	NR	NR	NR
19.71	11.4	20	12000	3700
23.15	13.7	3.1	1800	540
26.45	15.9	0.40	240	93
29.61	18.09	0.16	95	31
32.65	20.3	0.016	9.6	1.4

In addition four-point probe measurements being carried out to determine the relationship between filler content and conductivity, work was also carried out to ascertain the effect of conductive filler settling on surface and near-surface conductivity values. The controlled thickness of the circular plate geometries enabled their use for this study. The terms ‘top surface’ and ‘bottom surface’ correspond to orientation of the samples during the cooling stage. After the powder addition and subsequent mixing stages, the samples either remained in their original orientation or were rotated during cooling so that the molten sample underside became the ‘top surface’. Each plate sample underwent a single 180° flipping rotation for cooling, unless otherwise stated; the reason being to ensure that any difference in local resistivity was due to particle settling, and not a consequence of the mixing operation.

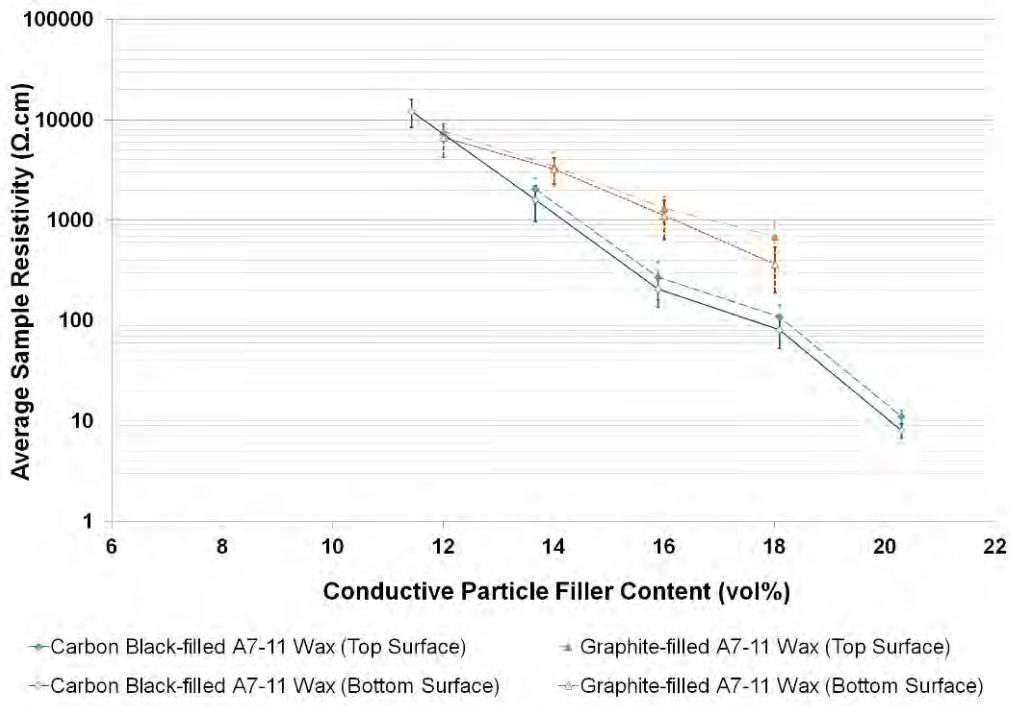

Figure 15.2 Graph showing relationship between the material samples’ electrical resistivity (Ω.cm) and the conductive filler content in A7-11 wax, according to four-point probe tests carried out on cast flat plates of conductive particle-filled wax.

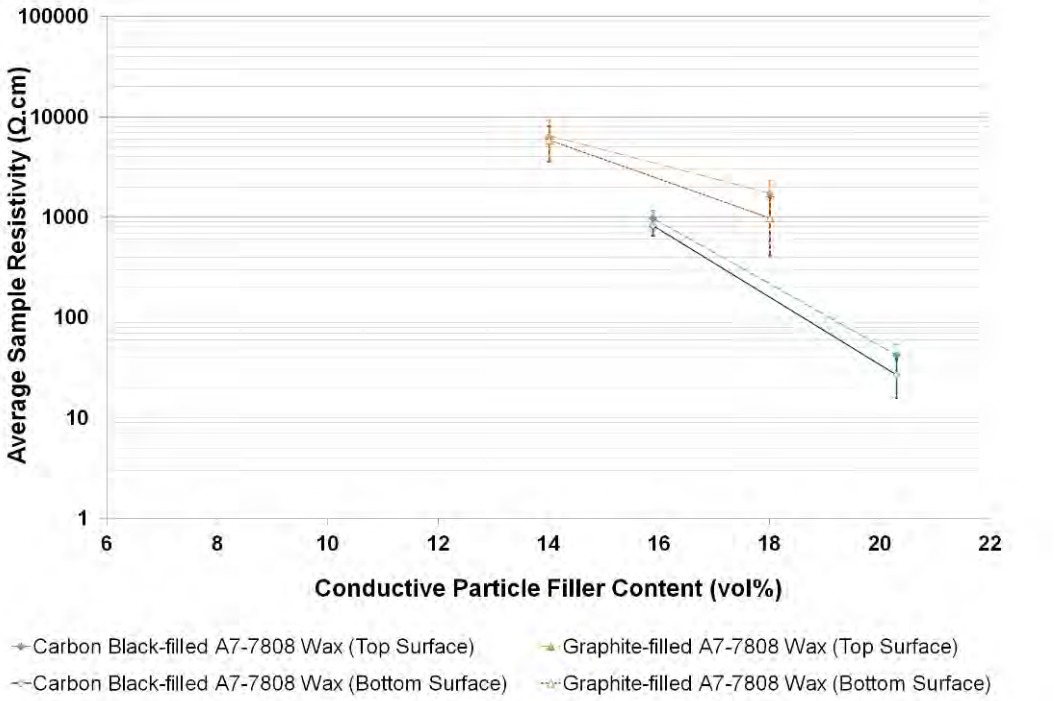

Figure 15.3 Graph showing relationship between the material samples' electrical resistivity (Ω.cm) and the conductive filler content in A7-7808 wax, according to four-point probe tests carried out on cast flat plates of conductive particle-filled wax.

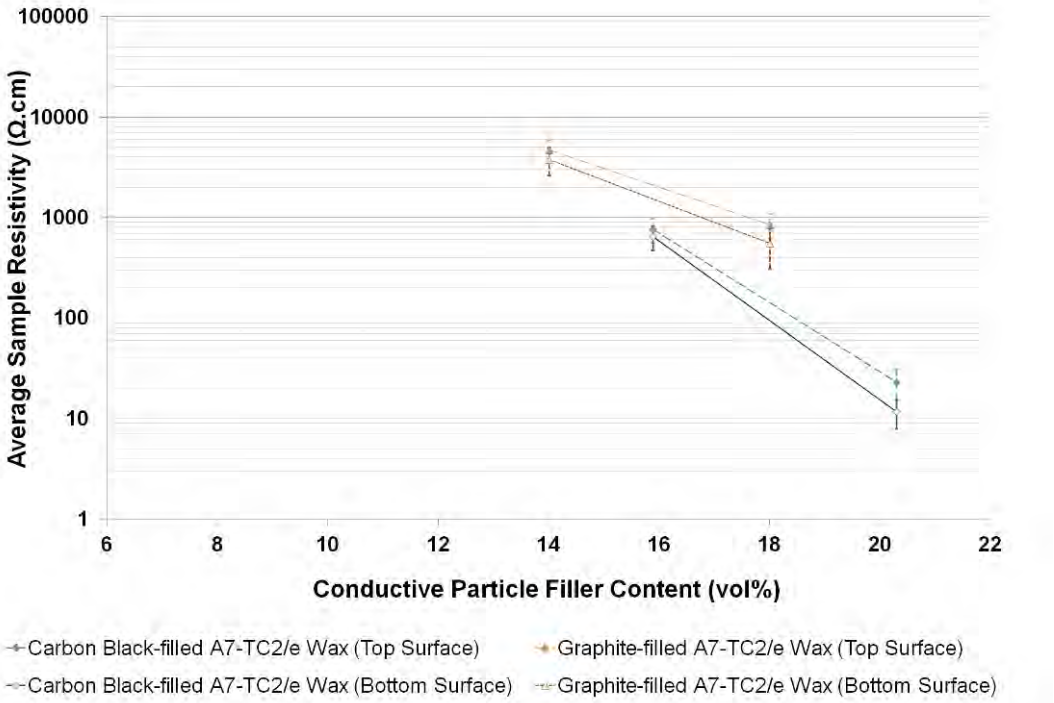

Figure 15.4 Graph showing relationship between the material samples' electrical resistivity (Ω.cm) and the conductive filler content in A7-TC2/e wax, according to four-point probe tests carried out on cast flat plates of conductive particle-filled wax.

The effect of particle settling on local sample resistivity is shown in Figure 15.2, Figure 15.3 and Figure 15.4. Surfaces that solidify as the 'top surface' consistently displayed higher resistances, and this was attributed to a carbon content gradient, for both graphite and carbon black-filled samples. Such a gradient would be formed when particles move away from the upper cooling surface due to gravitational settling. The resistivity difference was smaller when carbon black was used, and this could be attributed to a number of factors.

The density (ρ_p) of carbon black (~ 1.9 g/cm^3) is lower than that of the graphite filler (~ 2.2 g/cm^3), and so would possess a lower settling velocity according to Stokes' law [4.2]. As carbon black filler was more agglomerated within the wax, the suspension viscosity (η) at mixing temperatures, as shown in Section 15.2.2, was far greater within carbon black grades, and so this can be taken to be the greatest attributable reason for lower settling rates when carbon black filler is used. Stokes' law [4.2] would also be used to explain a greater disparity in resistivity values between the top and bottom plate surfaces when wax grades with a lower viscosity are used, although the current experimental evidence shows no significant trend.

Additional samples with filler concentrations of 14 vol% graphite and 15.9 vol% carbon black were made using A7-11 wax as the insulating matrix, and these were cooled without any rotation during cooling. These specimens displayed lower average bottom surface resistivity values compared to their rotated counterparts of the same composition. For example, the 14 vol% micronized graphite non-rotated sample had an average bottom plate resistivity of 2.15 kΩ.cm, whilst the rotated sample had a higher resistivity of 3.37 kΩ.cm. The top surface of the non-rotated samples did not produce any resistivity values, as resistance measurements were above the measureable range of the apparatus. Particle concentration gradients must exist, therefore, within the material before the cooling process takes place, which shows that the magnetic and manual stirring techniques are insufficient when it comes to producing a homogenously conducting composite.

15.2 Wax Rheology

15.2.1 Rotational Rheometry Tests

The flow and viscosity curves for waxes containing varying concentrations of conductive filler material are displayed in Section 15.2. The ordinate scale has been changed between the graphs, to accommodate the curves that are formed at one extreme (high temperature, low filler content) and the other extreme (lower temperature, high filler content). Stress-ramp flow tests were carried out at a number of temperatures, measured according to the Peltier hotplate on the rheometer. Initial experiments using the graphite-filled A7-7808 and A7-TC2/E waxes were carried out at 70 °C and 75 °C, although comparative experiments involving the use of carbon black filler at these temperatures were not reproducible. For both carbon black and graphite-filled A7-7808 and A7-TC2/e waxes, testing was carried out at 80 °C. The thixotropic behaviour of samples in CSS flow curves is described in Appendix C.2.

Wall slip effects were observed (a) when the graphite filler content within either wax was high (14 – 18 vol%), and (b) when carbon black-filled wax was loaded to a concentration above approximately 7 vol%. The material required a high stress to initiate flow, and above this stress, the shear stress versus shear rate curve was not quantitatively repeatable. For this reason, results given by carbon black filled waxes with filler additions greater than 9.2 vol% have not been included.

15.2.2 Flow Curves and Viscosity Testing

The flow properties of the unfilled A7-7808 and A7TC2/e waxes must first be analysed before the effects associated with filler particle addition are taken into account. For the low viscosity A7-7808 wax grade, shear-thinning behaviour is observed to a small extent in the

wax samples over the shear stress range of the experiment (0.1 – 1500 Pa).

For the A7-7808 wax, as shown in Figure 15.5, the viscosity initially increases at low shear rates, due to the presence of a transient viscosity peak. Such a peak is attributed to time-dependent effects, as discussed in Section 7.2.1. beyond this peak, shear thinning behaviour is observed, and for the unaged sample at 80 °C, the viscosity changes from 0.220 Pa.s at a shear rate of 2.025 s^{-1} (the position of the viscosity peak), to 0.150 Pa.s at a shear rate of about 9430 s^{-1}. The emulsified A7-TC2/e wax, as shown in Figures 15.5, displays a stronger shear-thinning relationship as the shear rate is increased. For the unaged sample at 80 °C, the viscosity changes from 1.80 Pa.s at a shear rate of 0.057 s^{-1} (the position of the transient viscosity peak), to 0.46 Pa.s at a shear rate of about 3106 s^{-1}.

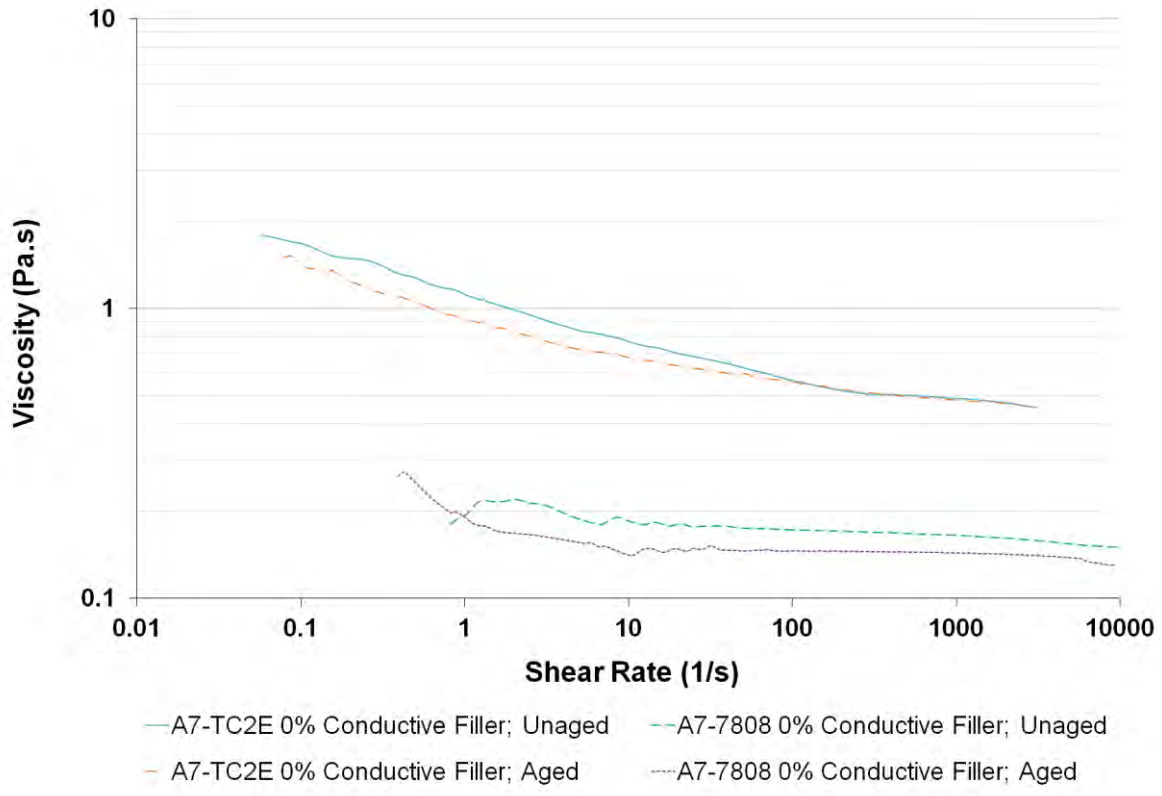

Figure 15.5 Graph showing the relationship between material viscosity and shear rate for increasing shear flow-curves. Results are for conductive particle-unfilled A7-7808 and A7-TC2/e waxes, carried out on a rotational rheometer at a temperature of 80 °C. Ageing corresponds to a 300 s, 750 Pa pre-shear cycle at 80 °C.

The effect of suspended filler particles on the material viscosity across the shear stress range can be separated from the behaviour of the base wax itself by converting the viscosity value of the filled waxes into relative viscosity (η_r) values. The unfilled wax viscosity value at each shear stress value was labelled as η_0, and compared against the filled wax viscosity at that corresponding shear stress (η_f), using Equation [6.10].

$$\eta_r = \frac{\eta_f}{\eta_0} \qquad [6.10]$$

η_f is the viscosity (Pa.s) of a sample with a filler concentration 'f', and η_0 is the viscosity (Pa.s) of the substance containing no filler. As well as influencing the absolute value of viscosity, the volume% filler concentration also has an effect on the flow behaviour, which is the relationship between shear rate and viscosity for a system, as described in Section 6.5.

If the liquid matrix is Newtonian, suspensions with a relatively low solids-loading tend to behave like Newtonian fluids, because there is little to no interaction between particles. When the filler volume fraction is increased, the free motion of particles is significantly hindered by frequent inter-particle collisions. Shear-thinning behaviour is observed, as at high shear, particles clusters are drawn out into chains which are separated by matrix channels, which promotes flow. When the system becomes even more congested at higher solids-loading, shear thickening behaviour can be observed at very high shear rates, as particle clusters 'lock up' together. The relationship between relative viscosity and shear stress for samples with different filler concentrations is shown in Figure 15.6, 15.7, 15.8 and 15.9.

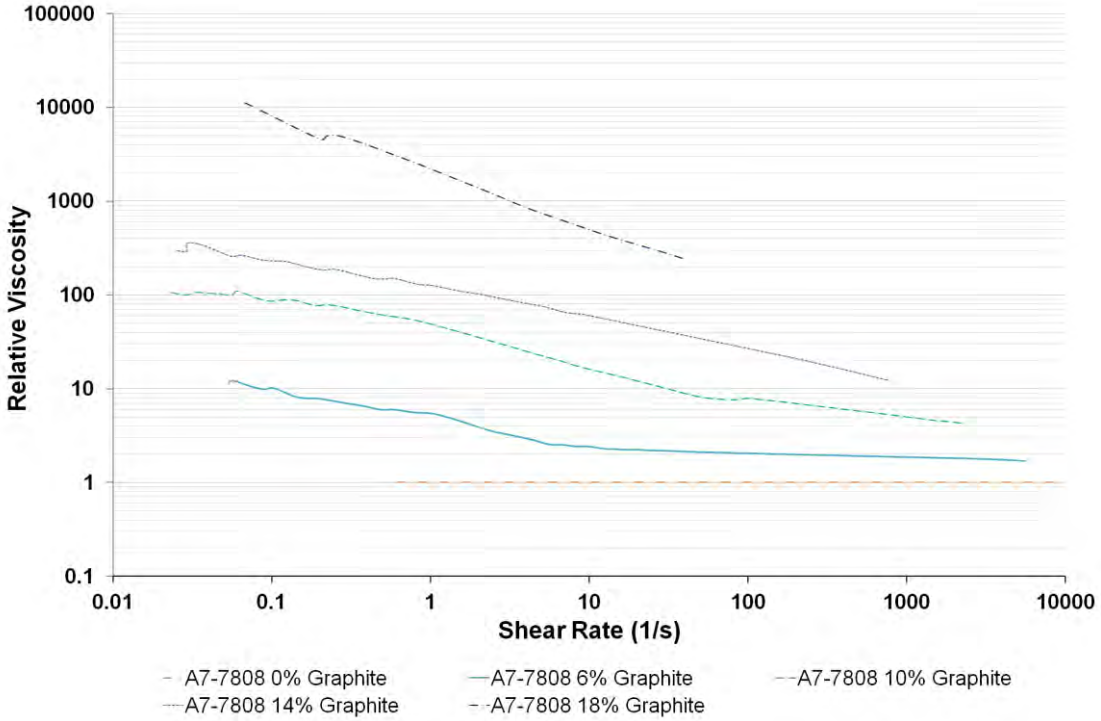

Figure 15.6 Graph showing the relationship between relative viscosity and shear rate for increasing shear-flow curves. Results are for micronised graphite-filled A7-7808 wax at different vol% loadings, carried out on a rotational rheometer at a temperature of 80 °C.

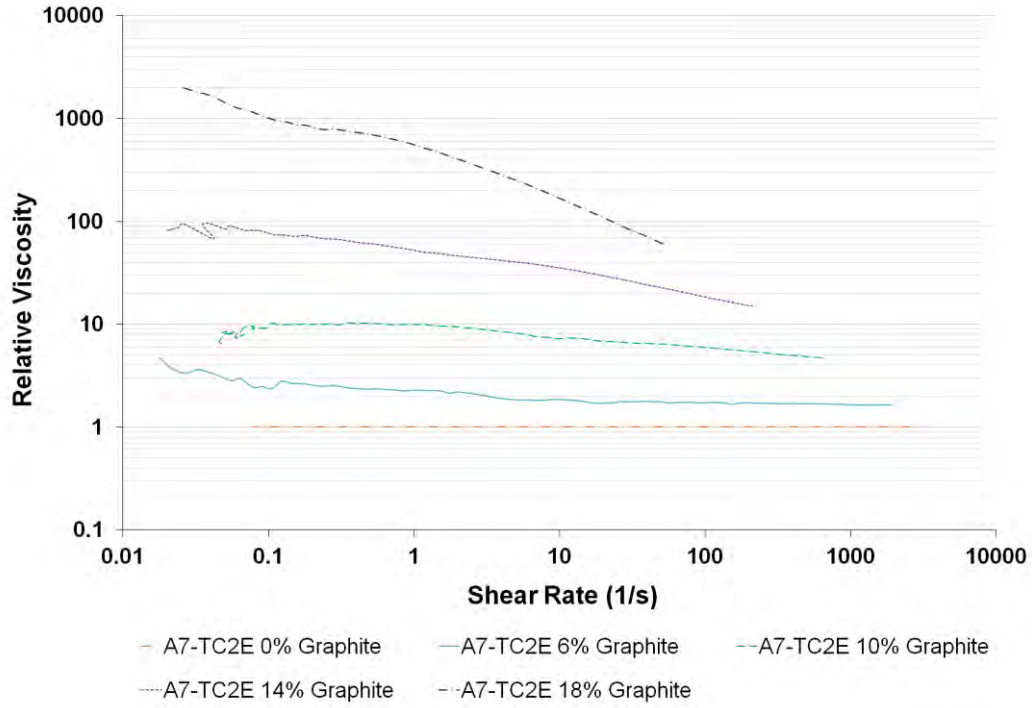

Figure 15.7 Graph showing the relationship between relative viscosity and shear rate for increasing shear-flow curves. Results are for micronised graphite-filled A7-TC2/e wax at different vol% loadings, carried out on a rotational rheometer at a temperature of 80 °C.

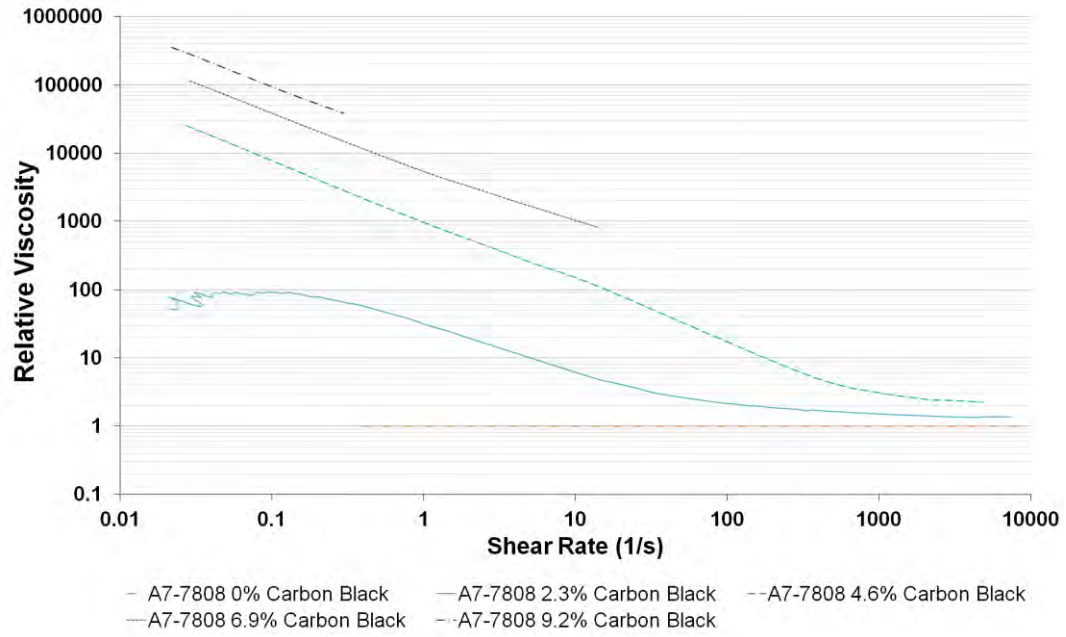

Figure 15.8 Graph showing the relationship between relative viscosity and shear rate for increasing shear-flow curves. Results are for carbon black-filled A7-7808 wax at different vol% loadings, carried out on a rotational rheometer at a temperature of 80 °C.

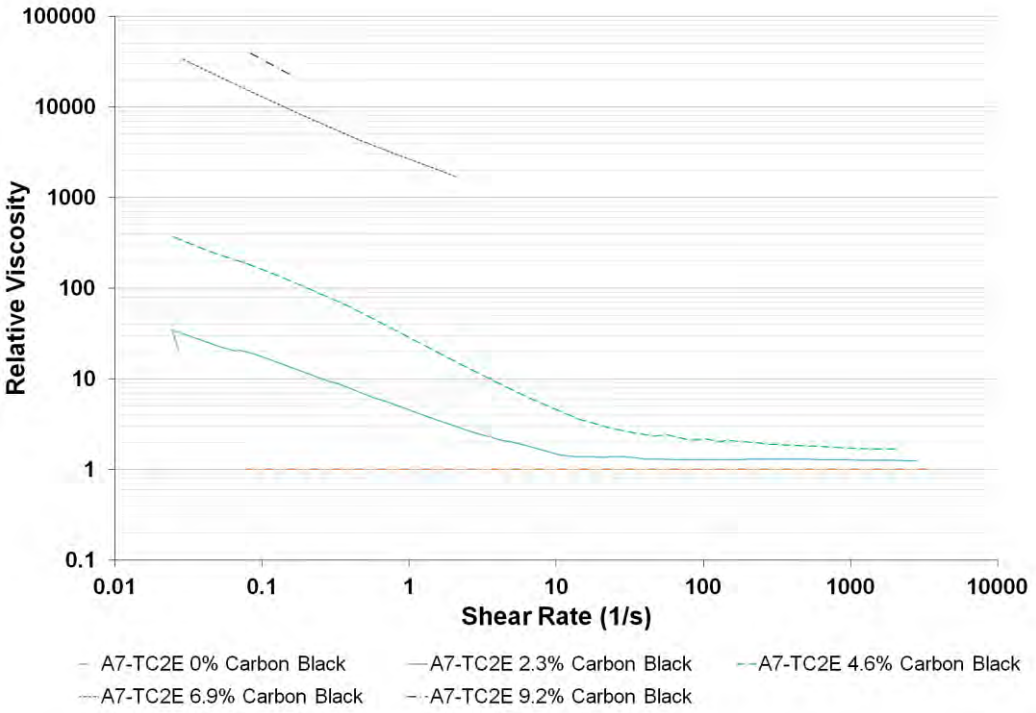

Figure 15.9 Graph showing the relationship between relative viscosity and shear rate for increasing shear-flow curves. Results are for carbon black-filled A7-TC2/e wax at different vol% loadings, carried out on a rotational rheometer at a temperature of 80 °C.

To describe shear thinning behaviour, the transition from lower Newtonian region to upper Newtonian region can be portrayed by measuring the difference between the zero-shear viscosity and infinite shear viscosity, with terms defined in Section 6.5.2. However, within the experimental range of these flow tests, no clear lower or upper Newtonian regions could be defined for any wax composition. Table 15.3 instead gives two viscosity values for each composition. The low shear viscosity of the sample corresponds to either the viscosity at the lowest measured shear rate or at the height of the transient viscosity peak (with an associated shear rate value A). The high shear viscosity corresponds to the viscosity at the highest applied shear stress value in the cycle (~ 1500 Pa), with an associated shear rate value B.

The presence of graphite filler in the A7-7808 wax, as shown in Figure 15.6, increases the shear thinning nature of the material. The presence of graphite filler in the A7-TC2/e wax had a similar effect on the shear thinning behaviour of the base wax, as shown in Figure 15.7. For the both wax grades with 0 vol% and 6 vol% graphite filler contents, the CSS flow curve gradient was steeper at low shear rates and lessened as the shear rate was increased, to approach a value for the infinite viscosity. At higher filler loadings, the gradient becomes steeper as the shear stress is increased, and does not appear to approach a finite value. When CSS flow ramp testing was carried out using higher shear stresses, to ascertain infinite shear stress viscosity values for waxes with higher filler contents, non-reproducible results were produced.

As shown in Table 15.3, samples with graphite filler contents greater than 6 vol% possessed shear thinning behaviour with a yield point, as described in Section 6.5.4.1, whose value increases as the filler content is increased. Despite the fact that A7-7808 base wax has a lower viscosity at 80 °C, the addition of graphite has a less marked effect on A7-TC2/e, when the position of the yield points and high shear viscosity values are taken into consideration.

Table 15.3 Tabulating selected results from controlled shear stress (CSS) flow tests on graphite-filled waxes. Low shear viscosity relates to the maximum measured viscosity in the up-curve, either at the lowest measured shear rate or at the transient viscosity peak, if present. Highest shear viscosity corresponds to the sample viscosity at an applied shear stress of ~ 1500 Pa.

Micronised Graphite-filled A7-7808 Wax						
weight% Filler	**volume% Filler**	**Yield Point (Pa)**	**Low Shear Viscosity (Pa.s)**	**Shear Rate A (s^{-1})**	**Highest Shear Viscosity (Pa.s)**	**Shear Rate B (s^{-1})**
0	0	n/a	0.220	2.025	0.150	9430
12.36	6.0	n/a	2.15	0.057	0.256	5590
19.71	10.0	0.45	22.6	0.023	0.643	2227
26.45	14.0	1.15	65.6	0.029	1.840	773.6
32.65	18.0	105	1840	0.068	36.6	39.4
Micronised Graphite-filled A7-TC2/e Wax						
0	0	n/a	1.80	0.057	0.456	3106
12.36	6.0	n/a	5.843	0.018	0.743	1910
19.71	10.0	n/a	11.71	0.052	2.12	687.0
26.45	14.0	1.30	78.49	0.026	6.92	209.7
32.65	18.0	27.6	1167	0.026	26.52	54.3

The presence of carbon black-filler within both A7-7808 and A7-TC2/e waxes had a more marked effect than graphite on flow behaviour, a finding that agrees with the work of King et al. (2009), in their study of graphite and carbon black in polypropylene-based resins. Although flow tests were carried out for these samples, filled samples exhibited time-related structural degradation that was not consistent for samples from the same batch, as shown in Section 15.2.4. As a result, flow tests were carried out after samples had undergone a pre-shear cycle, as described in Section 10.3.3. The relative viscosity curves shown in Figure 15.7 and 15.8 used base wax grade viscosities from samples that were also tested after a pre-shear cycle.

Table 15.4 Tabulating selected results from controlled shear stress (CSS) flow tests on carbon black-filled waxes. Low shear viscosity relates to the maximum measured viscosity in the up-curve, either at the lowest measured shear rate or at the transient viscosity peak, if present. Highest shear viscosity corresponds to the sample viscosity at an applied shear stress of ~ 1500 Pa.

Carbon Black-filled A7-7808 Wax						
weight% Filler	**volume% Filler**	**Yield Point (Pa)**	**Low Shear Viscosity (Pa.s)**	**Shear Rate A (s^{-1})**	**Highest Shear Viscosity (Pa.s)**	**Shear Rate B (s^{-1})**
0.00	0.0	n/a	0.273	0.430	0.1301	9293
4.31	2.31	0.19	13.3	0.031	0.176	7490
8.43	4.61	97	3690	0.027	0.290	1580
12.36	6.90	390	16010	0.029	105.1	14.1
16.12	9.17	930	46500	0.022	4940	0.299
Carbon Black-filled A7-TC2/e Wax						
0.00	0.0	n/a	1.497	0.078	0.453	3224
4.31	2.31	0.53	32.93	0.024	0.561	2800
8.43	4.61	5.70	253.7	0.025	0.750	2110
12.36	6.90	420	16320	0.029	761.0	2.10
16.12	9.17	1100	34100	0.040	10200	0.157

For carbon black-filled A7-7808 grades, as shown in Figure 15.8, the relationship between viscosity and shear rate shows strong shear-thinning character with a yield point, with specific values given in Table 15.4. Similar non-Newtonian behaviour is observed when the A7-TC2/e grade was used to suspend carbon black filler, as shown in Figure 15.9. Despite the fact that A7-7808 base wax had a lower viscosity at 80 °C, the addition of carbon black has a smaller effect on the rheology of A7-TC2/e when the filler concentration was low. When the filler concentration was greater than 4.6 vol%, however, the effect of carbon black on flow behaviour at high shear rates was more prominent when added to A7-TC2/e. As with in the CSS flow curve experiments involving the addition of micronised graphite filler, the

differing effect of filler particle addition on flow behaviour could be attributed to the presence of liquid filler within the A7-TC2/e matrix. However, too few filled-wax grades have been rheologically tested within the present work, and so such a conclusion cannot be made. For some of the samples with high filler contents, a viscosity increase was observed at high shear stresses (1000 to 1500 Pa). This increase was not displayed graphically, as the viscosity curves at these high shear stresses were not consistently reproducible.

Not all filled samples exhibited viscosity values when lower shear stresses were used due to the presence of limiting yield points. A shear stress parameter of 750 Pa was therefore chosen to analyse trends, as viscosity measurements were obtained under these CSS conditions for most filled wax compositions. Viscosity / filler content relationships for both new (i.e. non-aged) and aged graphite-filled wax samples are shown in Figure 15.10 and Figure 15.11 when A7-7808 and A7-TC2/e base waxes were used respectively. Viscosity / filler content relationships for carbon black-filled A7-7808 and A7-TC2/e wax samples are shown in Figure 15.12 and 15.13 respectively. The aged samples underwent a pre-shear cycle for 5 minutes at 750 Pa prior to flow ramp testing, and displayed a consistently lower viscosity when compared to the non-aged counterparts. The viscosity disparity generally grew as the filler content was increased.

The viscosity results at 750 Pa were compared against two models that have been used to describe the effect of dispersed particles on material rheology, as described in Section 6.8. The first of these is Einstein's model of hard spheres, which describes the flow of spherical non-interacting particles within dispersion (Equation [6.11]). The Einstein equation for hard spheres only applies to low filler concentrations ($\varphi < 0.1$), and this is the case due to the effect of particle interaction at higher concentrations. The Krieger-Dougherty equation is a more complex model that takes into account particle geometry and particle interactions (Equation [6.12]). For suspended spheres, the maximum packing fraction, φ_m, lies between

0.52 and 0.74. Clarke (1967) carried out rheological testing on suspensions containing glass discs with an axial ration of 4 (as described in Section 6.8.3). Both the Einstein hard sphere model curve and the experimental relationship between filler content and viscosity for Clarke's glass discs are shown in Figures 15.10 to 15.13 for comparative purposes.

When the experimental results of the present work and those of Clarke (1967) are compared, the viscosity-altering effects associated with the addition of graphite particles and glass plate particles to suspension diverge when the filler content was greater than 10 vol%, as shown in Figure 15.10 and 15.11. Above this filler content, the particle size and size distribution are known to play a greater role in the material's viscosity, and the use of smaller particles leads to higher relative viscosities (Pal, 1992). For carbon black-filled waxes, relative viscosity values deviate from Clarke's glass plate model when the filler content was greater than 4.6 vol%, as shown in Figure 15.12 and 15.13. The effect of filler agglomeration on flow behaviour within carbon black systems is believed to account for the lower divergent value, as particle agglomeration immobilises the matrix material, as described in Section 6.8.

Using the Krieger-Dougherty equation to generate a curve that follows the experimental results can produce values for the maximum packing fraction (φ_m) and the intrinsic viscosity [η], and these values could then be used to explain differences in behaviour. Sigmaplot 11.0 was used to produce values for φ_m and [η] within Equation [6.12] to fit the curve produced by experimental results. For iterative purposes, their initial values were set to those for a glass plate system ($\varphi_m = 0.382$, $[\eta] = 9.87$) (Clarke, 1967) (Barnes, 1997). Table 15.5 displays the results of the Krieger-Dougherty curve fitting.

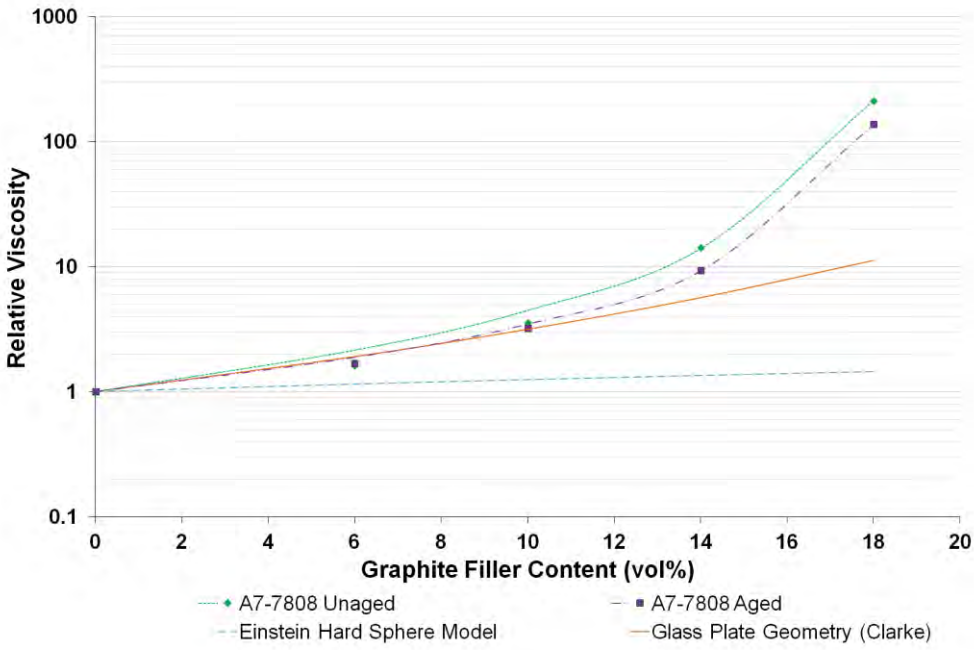

Figure 15.10 Graph showing the relationship between the rotational rheometer relative viscosity and graphite filler content for both aged and non-aged graphite-filled A7-7808 waxes (750 Pa, 80 °C). A Krieger-Dougherty curve for each data set is shown. Einstein's hard sphere model curve and an experimental curve for glass plates (Clarke 1967) are shown.

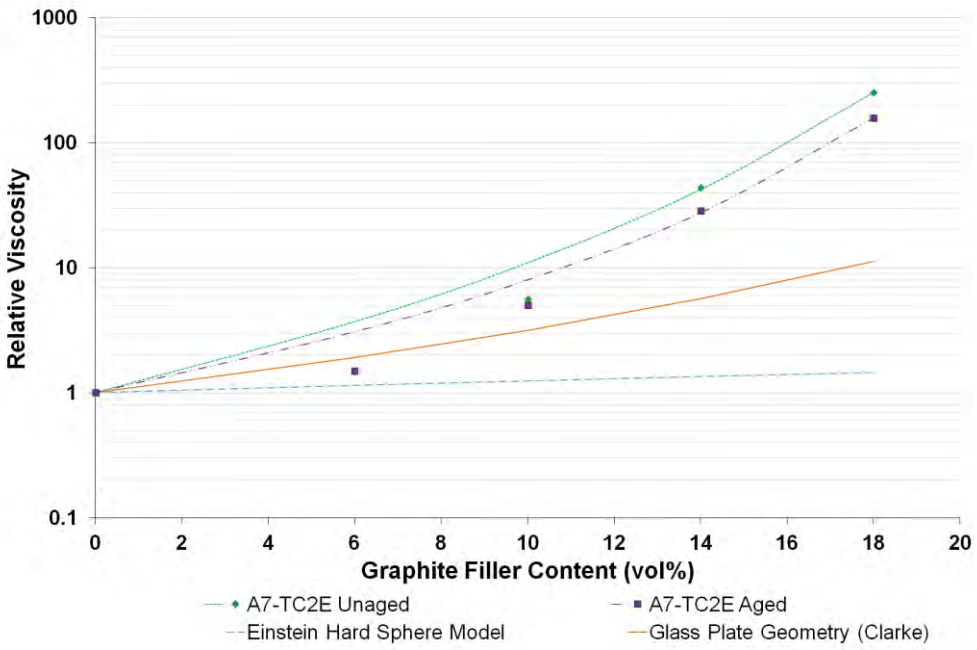

Figure 15.11 Graph showing the relationship between the rotational rheometer relative viscosity and graphite filler content for both aged and non-aged graphite-filled A7-TC2/e waxes (750 Pa, 80 °C). A Krieger-Dougherty curve for each data set is shown. Einstein's hard sphere model curve and an experimental curve for glass plates (Clarke 1967) are shown.

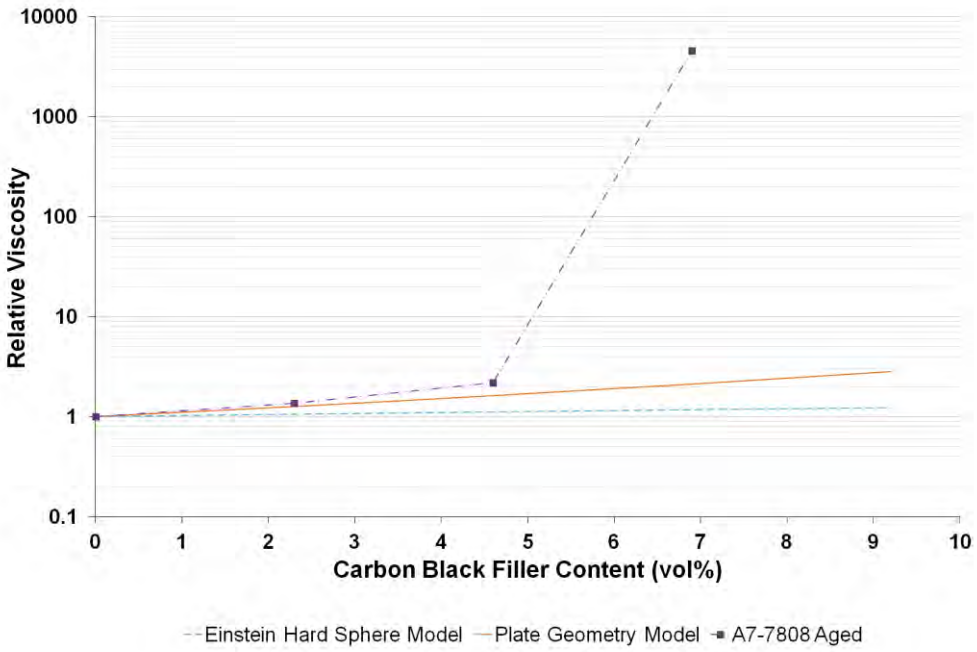

Figure 15.12 Graph showing the relationship between the rotational rheometer relative viscosity and graphite filler content for aged carbon black-filled A7-7808 waxes (750 Pa, 80°C), versus the Einstein hard sphere model and an experimental curve for glass plates (Clarke 1967).

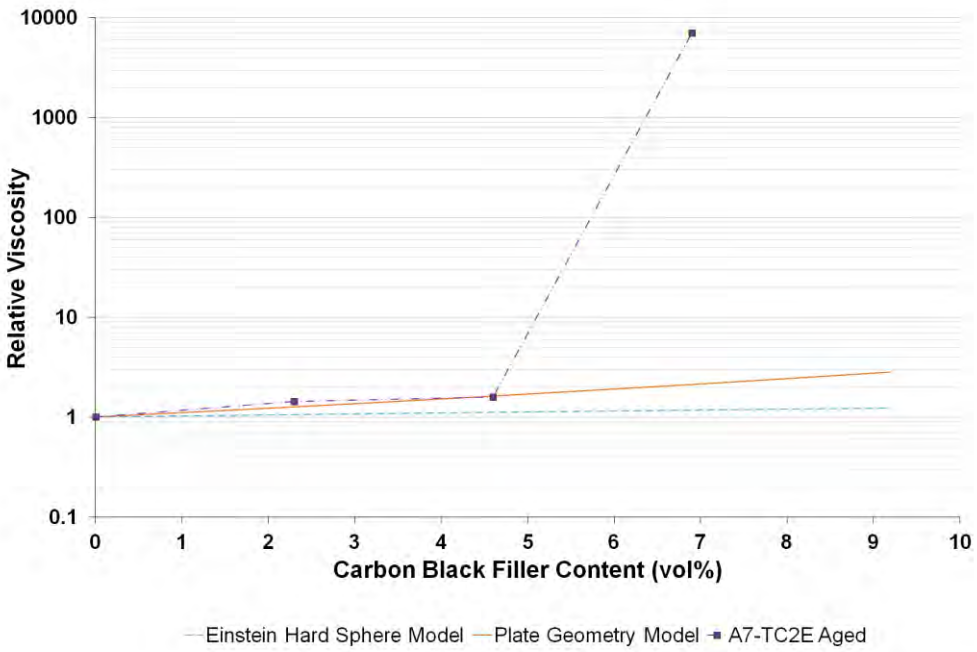

Figure 15.13 Graph showing the relationship between the rotational rheometer relative viscosity and graphite filler content for aged carbon black-filled A7-TC2/e waxes (750 Pa, 80°C), versus the Einstein hard sphere model and an experimental curve for glass plates (Clarke 1967).

Table 15.5 Values for the intrinsic viscosity [η], maximum packing fraction φ_m and goodness-of-fit parameter R^2, obtained by fitting the Krieger-Dougherty relationship against data obtained from flow curves in a rotational rheometer at varying temperatures and pre-shear states. All measurements were taken at a shear stress of ~ 750 Pa.

Base Wax	Temperature (°C)	Ageing / Pre-shear	[η]	φ_m	φ_m[η]	R^2
Micronised Graphite						
A7-7808	65	none	8.98594	0.1707	1.5339	0.9989
A7-7808	65	750 Pa, 300 s	7.32421	0.1681	1.2312	0.9987
A7-7808	70	none	9.66890	0.1791	1.7319	0.9992
A7-7808	70	750 Pa, 300 s	7.96751	0.1710	1.3624	0.9990
A7-7808	75	none	10.7291	0.1938	2.0793	1.0000
A7-7808	75	750 Pa, 300 s	9.15684	0.1900	1.7398	0.9978
A7-7808	80	none	10.6776	0.1948	2.080	1.0000
A7-7808	80	750 Pa, 300 s	8.77303	0.1899	1.666	1.0000
Micronised Graphite						
A7-TC2/e	70	none	16.89654	0.3499	5.9121	0.9958
A7-TC2/e	70	750 Pa, 300 s	-	-	-	-
A7-TC2/e	75	none	15.30119	0.2520	3.8559	0.9991
A7-TC2/e	75	750 Pa, 300 s	13.2488	0.2038	2.7001	0.9999
A7-TC2/e	80	none	19.4670	0.2852	5.5521	0.9992
A7-TC2/e	80	750 Pa, 300 s	16.4693	0.2589	4.2639	0.9993
Vulcan Carbon Black						
A7-7808	80	750 Pa, 300 s	63.4966	0.089*	5.6512	0.9998
Vulcan Carbon Black						
A7-TC2/e	80	750 Pa, 300 s	65.1056	0.089*	5.7944	0.9998

* In these results, the plots would not converge on a value for φ_m, and so the maximum value tested in that respective study was used as a minimal value.

Figure 15.10 shows the relationship between viscosity and graphite-filler content at 80 °C for both aged and non-aged graphite-filled A7-7808 waxes, along with the fitted Krieger-Dougherty curves. The corresponding value of each variable in Equation [6.12] is shown in Table 15.5, and gives values for φ_m which are only slightly above the experimental

range (φ_m = 0.1948 with no pre-shear, φ_m = 0.1899 with pre-shear). The preliminary experiments associated with graphite-filled wax composite fabrication used filler additions higher than those used here; however, the graphite particle distribution homogeneity could not be maintained. The high associated R^2 values show that this filled wax system closely follows the Krieger-Dougherty relationship.

Figure 15.11 shows the same relationship for graphite in A7-TC2/e wax for both aged and non-aged samples. Altering the Krieger-Dougherty parameters [η] and φ_m did not, however, lead to a theoretical curve shape that fitted the experimentally derived plotted points for both low and high filler contents. Relative viscosity values at 6 and 10 vol% were lower than model behaviour predictions, explaining the lower R^2 values of 0.9992 and 0.9993, respectively, at 80 °C. Figure 15.14 and Figure 15.15 show graphically the effect of temperature on flow curve-derived relative viscosity at 750 Pa when A7-7808 and A7-TC2/e waxes were used, respectively. The Krieger-Dougherty fitting should be independent of temperature, and when the A7-7808 grade wax was used as the base wax, the effect of graphite addition on relative viscosity changed little over the 15 °C temperature range studied. From the Sigmaplot data in Table 15.5, [η] increased with temperature, forming a plateau at 75 °C and above. The influence of graphite filler on the system rheology may therefore vary over the melting range. Values for the maximum packing fraction, φ_m, also increase with temperature, and go from 17 vol% at 65 °C to 19.5 vol% at 80 °C.

The relative viscosity increases with temperature, when graphite was added to A7-TC2/e at higher filler concentrations, as shown in Figure 15.15. From Table 15.5, [η] generally increases with temperature, although φ_m values show no clear temperature dependence. For carbon-black filled waxes, a temperature dependent relative viscosity at 750 Pa could not be produced due to the presence of limiting yield points when the temperature was below 80 °C.

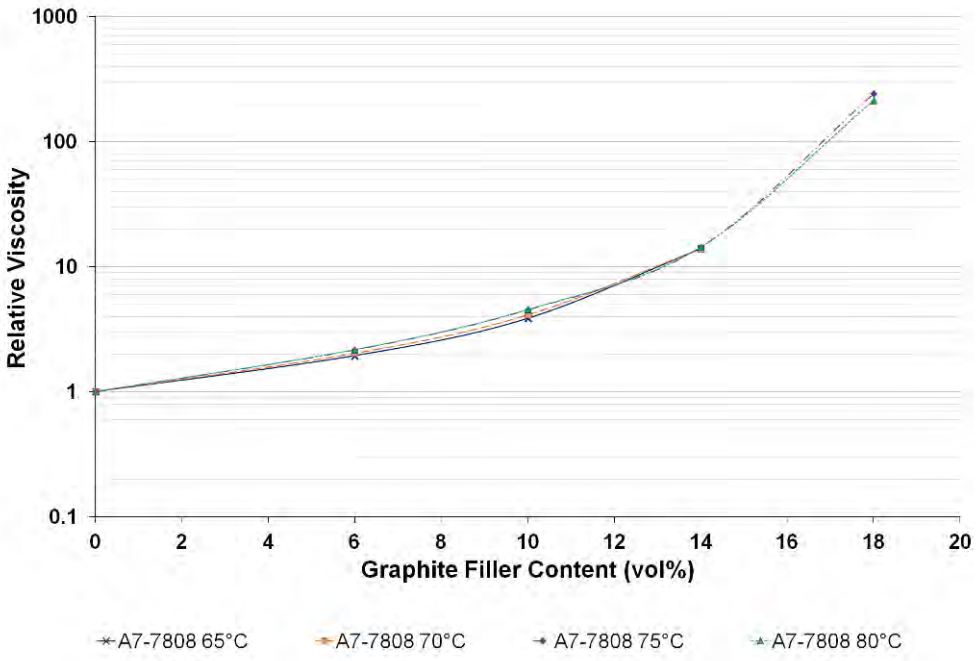

Figure 15.14 Graph showing the Krieger-Dougherty model plots showing the relationship between rotational rheometer relative viscosity and graphite filler content for non-aged graphite-filled A7-7808 waxes at differing temperatures, under a shear stress of 750 Pa at 80°C.

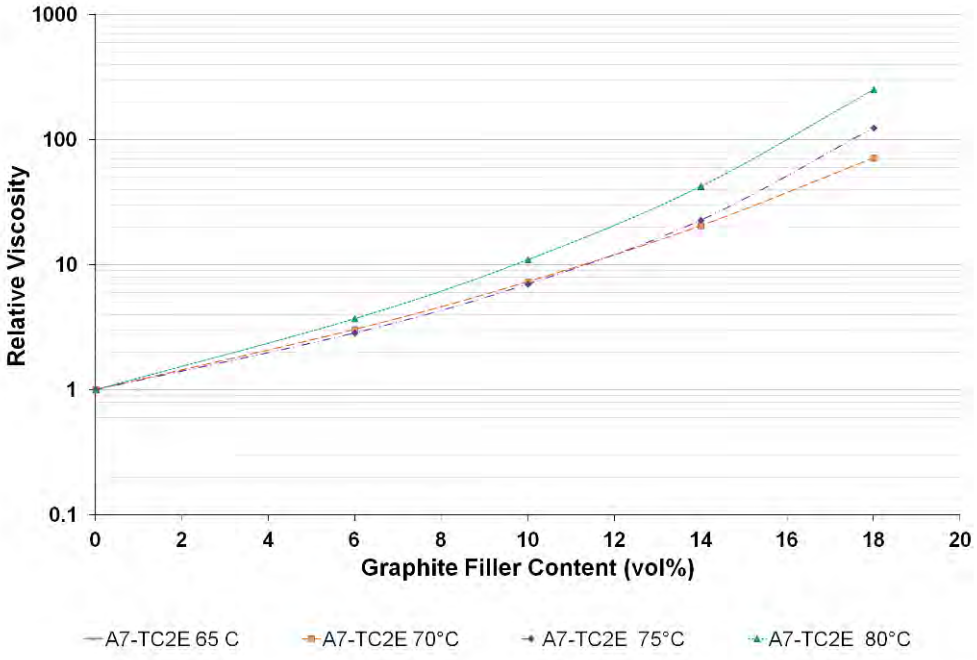

Figure 15.15 Graph showing the Krieger-Dougherty model plots showing the relationship between rotational rheometer relative viscosity and graphite filler content for non-aged graphite-filled A7-TC2/e waxes at differing temperatures, under a shear stress of 750 Pa at 80°C.

To explain the values given in Table 15.5, contributing factors that affect the variables [η] and φ_m must be considered. The value of [η] is based on the filler's contribution to the viscosity (η) of solution, and according to Einstein's model, has a value of 2.5 for solid spheres. Its value is very sensitive to the axial ratio of spheroids, and for non-spherical geometries, specific relationships have been ascertained, as shown below:

Discs: $[\eta] = 3 \text{ (axial ratio)} / 10$ [15.4]

Rods: $[\eta] = 7 \text{ (axial ratio}^{5/3}) / 100$ [15.5]

For both systems, the intrinsic viscosity can determined by measuring the reduced viscosity ($\eta_{red} = (\eta_r - 1)/c$) (where c is the mass concentration of filler in the suspension) at a number of different concentrations and then extrapolating the relationship to zero concentration, to arrive at a value for [η]. According to Mezger (2006), seven or more concentrations need to be tested to use this method, which excludes its use within this work. Within future work therefore, a greater number of filler concentrations would be studied, so that [η] could be attained using reduced viscosity methods. The differences between conductive filler grades and the effect of the wax grade could be more easily analysed.

The axial ratio of the plate-like graphite particles could be estimated from SEM micrographs, shown in Figure 15.16(b), with the estimated axial ratios used to explain any changes. The particles appear to have a fine flake-like structure, with estimated axial ratios between 4 and 10. According to the relationship in Equation [15.4], an axial ratio of 4 should lead to a [η] value of 1.2, whilst an axial ratio of 10 should lead to a [η] value of 3. The glass plates in suspension studied by Clarke et al. (1967) were stated as having an axial ratio of 4, and yet a [η] value of 9.87 was given as the Krieger-Dougherty parameter. Within the present work, similar [η] values to those obtained by Clarke were obtained when the A7-7808 wax

was used to suspend graphite, as shown in Table 15.5. However, values for [η] were roughly double this figure, when emulsified A7-TC2/e wax was used to suspend the same graphite grade. The axial ratio of the graphite particles themselves should not change in these two environments, although the base wax may have an effect on filler morphology. Interactions between filler and water in the A7-TC2/e wax may play an important role, along with wettability differences and agglomeration level.

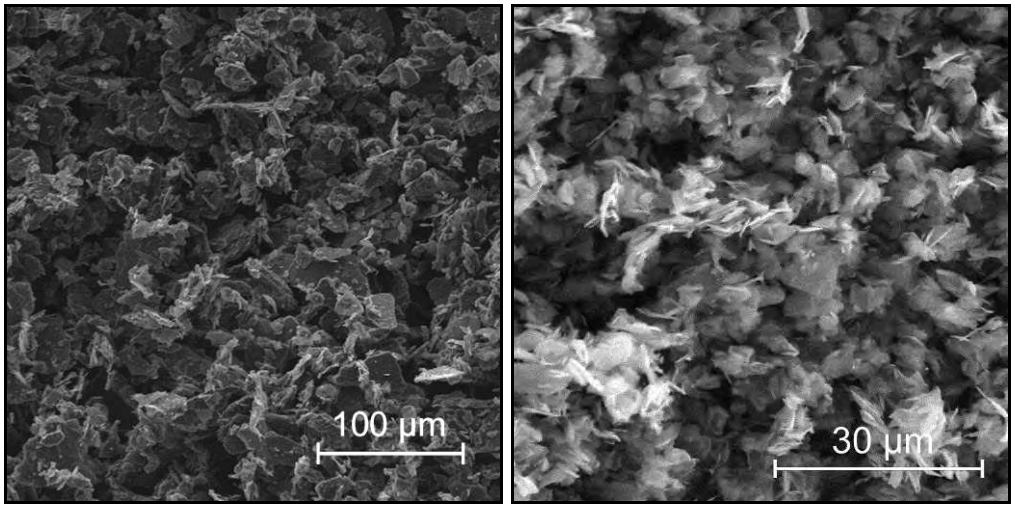

(a) **(b)**

Figure 15.16 Secondary electron (SE) Scanning electron microscopy micrographs depicting (**a)** Vulcan XC605 carbon black (Cabot) and **(b)** Micronised graphite (Graphite Trading Company) powders.

The maximum packing fraction (φ_m) represents the highest volume of particles that can be added to a suspending liquid medium. It is possible to think of this limit in terms of the free space around particles. At φ_m, there is no space for them to move, to shift past one another, and so generate flow. The particle shape, agglomeration level, size and size distribution all have an effect on this value, as described in Section 6.8. The factors listed above can be used to explain the difference between the φ_m values obtained in the present work and those given for the glass plate system studied by Clarke et al. (1967). A far higher φ_m value of 0.382 was obtained for the glass plate system, compared with ~ 0.195 for

graphite-filled A7-7808 wax and ~ 0.28 for graphite-filled A7-TC2/e wax at 80°C. Potential reasons for this disparity are discussed below.

When a grade with a finer particle size is used for a given filler volume, there would naturally be a higher number of particles present., which result in a greater number of particle-particle interactions and an increased resistance to flow. According to Pal et al. (1992), this effect becomes less marked when samples are tested at high shear, which suggests that particle-particle interactions are relatively weak and can be broken down at high shear rates. The particle size distribution of graphite in ethanol is described in Section 8.2.3.2. According to the volume% distribution, well-dispersed graphite particles had equivalent sphere diameters between 1 and 10 μm, with a modal peak at 5 μm, which is far removed from the 100 by 400 μm glass plates employed by Clarke et al. (1967). The cluster size when the graphite or carbon black is dispersed within the wax itself is unknown, and an aim of future work would be to dissolve out the matrix material to reveal the cluster distribution of filler.

15.2.3 Temperature Dependent Flow Behaviour

Above the melting temperature of the wax, it can be appreciated that the viscosity (η) follows the Arrhenius-Frenkel-Eyring (AFE) relationship, shown in Equation [6.6]. This relationship is based on the potential energy that must be overcome for a molecular unit to move from one equilibrium position to the next, which acts as the basis for flow behaviour.

$$\eta = Ce^{(E/RT)} \qquad [6.6]$$

E is the activation energy associated with flow (kJ), R is the ideal gas constant, C is a constant and T is the temperature (K). Within the present work, the behaviour of the base wax grades;

namely, the Blayson Olefines A7-7808 and A7-TC2/e waxes, are shown in Figure 15.17 and 15.18 respectively. As described in Section 10.3.2, the CSS temperature curves for each wax composition were generated at shear stresses of 200 Pa, 750 Pa and 1500 Pa. Only the results relating to the use of the 750 Pa stress parameter are presented, as the graphite-filled samples exhibited reproducible results at this stress level.

The behaviour of the base waxes must be characterised before any rheological effects related to wax modification through filler addition can be taken into account. The low-viscosity wax grade, A7-7808, displays a smooth transition from liquid to solid by slowly departing from the Arrhenius equation for the liquid at approximately 64 °C, as shown in Figure 15.17. The relationship between heating and cooling ramps is a close one. The viscosity on heating at a given temperature is greater above the melting range, although this difference becomes smaller as the temperature is increased. The wax displayed viscosity measurements down to the minimum tested temperature of 55 °C, where both the heating and cooling viscosity behaviour was similar.

As shown in Figure 15.18, the solidification range for the A7-TC2/e is more defined, and occurs below 69 °C on the cooling ramp, with a 100-fold increase in viscosity (at 750 Pa) observed over a 4 °C temperature range. Both the heating and cooling curves show similar behaviour for the unfilled wax. Between 62 and 64 °C, a region exists where the viscosity-temperature relationship is reversed within both the heating and cooling curves. There is no attributed single reason for this behaviour, owing to the complexity of the wax system.

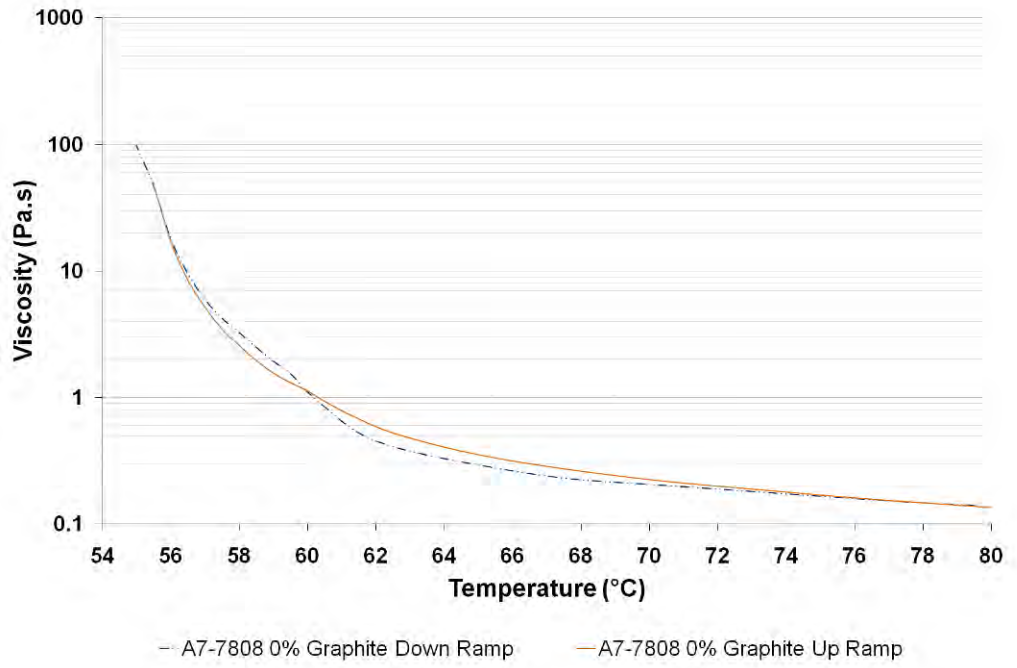

Figure 15.17 Graph showing the relationship between viscosity and sample temperature for unfilled A7-7808 wax in a rotational rheometer under a shear stress of 750 Pa.

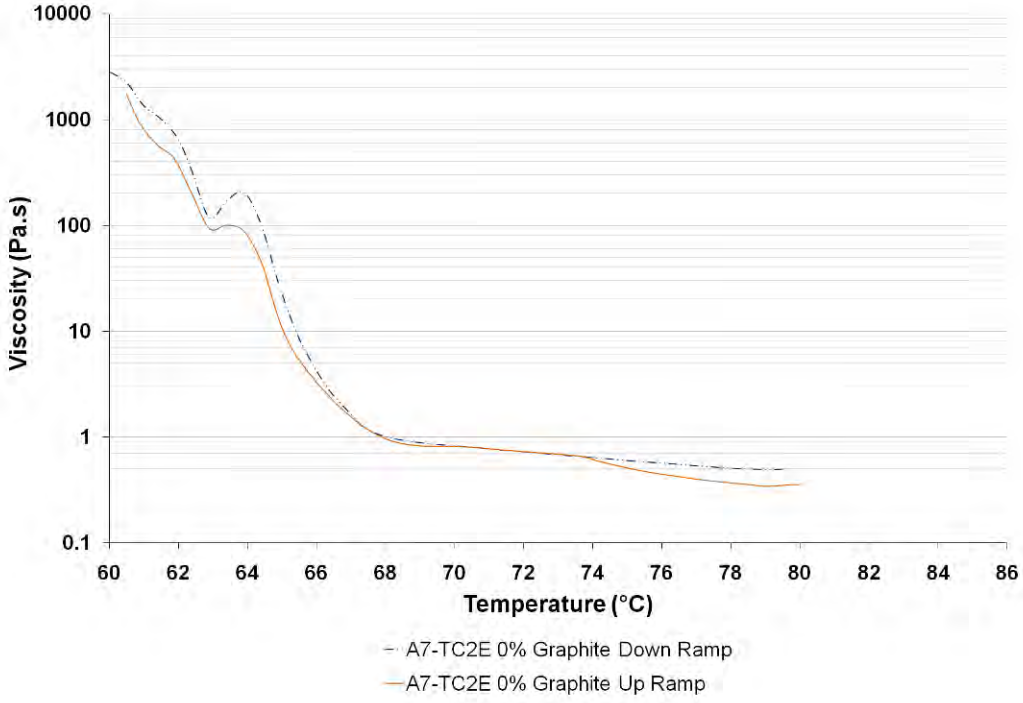

Figure 15.18 Graph showing the relationship between viscosity and sample temperature for unfilled A7-TC2/e wax in a rotational rheometer under a shear stress of 750 Pa.

The temperature ramp results were fitted against an Arrhenius equation plot for each test using Sigmaplot 11.0. It was possible to arrive at a temperature range for each composition where liquid-phase AFE behaviour was observed in the decreasing temperature and increasing temperature ramps, as shown in Table 15.6.

Table 15.6 Temperature range for each graphite-filled A7-7808 and A7-TC2/e wax composition where Sigmaplot-derived AFE behaviour is observed in the liquid. Results from each decreasing temperature ramp and increasing temperature ramp are shown.

A7-7808 Wax	vol% micronised graphite filler				
	0.0	6.0	10.0	14.0	18.0
Cooling Curve AFE behaviour	80 – 63 °C	80 – 63 °C	80 – 63 °C	80 – 63 °C	-
Heating Curve AFE behaviour	64 – 80 °C	64 – 80 °C	64 – 80 °C	64 – 80 °C	-
A7-TC2/e Wax	vol% micronised graphite filler				
	0.0	6.0	10.0	14.0	18.0
Cooling Curve AFE behaviour	80 – 68 °C	80 – 67 °C	80 – 67.5 °C	80 – 68 °C	-
Heating Curve AFE behaviour	68.5 – 80 °C	70.5 – 80 °C	71.5 – 80 °C	73 – 80 °C	-

Table 15.7 Temperature range for each carbon black-filled A7-7808 and A7-TC2/e wax composition where Sigmaplot-derived AFE behaviour is observed in the liquid. Results from each decreasing temperature ramp and increasing temperature ramp are shown.

A7-7808 Wax	vol% Vulcan XC605 carbon black filler				
	0.0	2.3	4.6	6.9	9.2
Cooling Curve AFE behaviour	80 – 63 °C	80 – 63 °C	80 – 63 °C	80 – 63 °C	-
Heating Curve AFE behaviour	64 – 80 °C	64 – 80 °C	64 – 80 °C	64 – 80 °C	-
A7-TC2/e Wax	vol% Vulcan XC605 carbon black filler				
	0.0	2.3	4.6	6.9	9.2
Cooling Curve AFE behaviour	80 – 68 °C	80 – 68.5 °C	80 – 68.5 °C	80 – 69 °C	-
Heating Curve AFE behaviour	68.5 – 80 °C	74.5 – 80 °C	75.5 – 80 °C	76.5 – 80 °C	-

Controlled shear stress (CSS) temperature ramps for graphite-filled A7-7808 waxes are shown in Figure 15.19. As displayed in Table 15.6, all samples start to obey the AFE relationship for the liquid phase at a similar temperature. The addition of 6 vol% graphite has little effect on the shape of the flow curves. As the filler loading is further increased, the up and down temperature curves become more distinct, with the up-curve displaying lower viscosities when the sample is liquid. The reason for this can be attributed to the time-related degradation of filler clusters under shear, which reduces the sample viscosity. As shown in Section 15.2.4, ageing has a greater effect in samples with higher filler concentrations. Additionally, wax is ejected from the region between parallel plates during the course of each testing cycle, which may reduce the sample's resistance to flow.

The changing characteristics of the A7-TC2/e temperature curves with micronised graphite addition are shown in Figures 15.20. All the down curves in Figure 15.20(a) depart from AFE behaviour at approximately 68°C, although the addition of graphite increases the gradient of the viscosity curve in the solid-liquid transition region. The shape of the up curve is altered by the addition of filler, as shown in Figure 15.28(b). The point when the filled material starts to obey the AFE relationship in the up curve is shifted to higher temperatures, as shown in Table 15.6. The gradient of curves in the solid-liquid transition region increase as the filler content is increased, as it does in the decreasing temperature curves. The solid-liquid transition in the up curve therefore occurs over a shorter temperature range when samples contain higher filler concentrations.

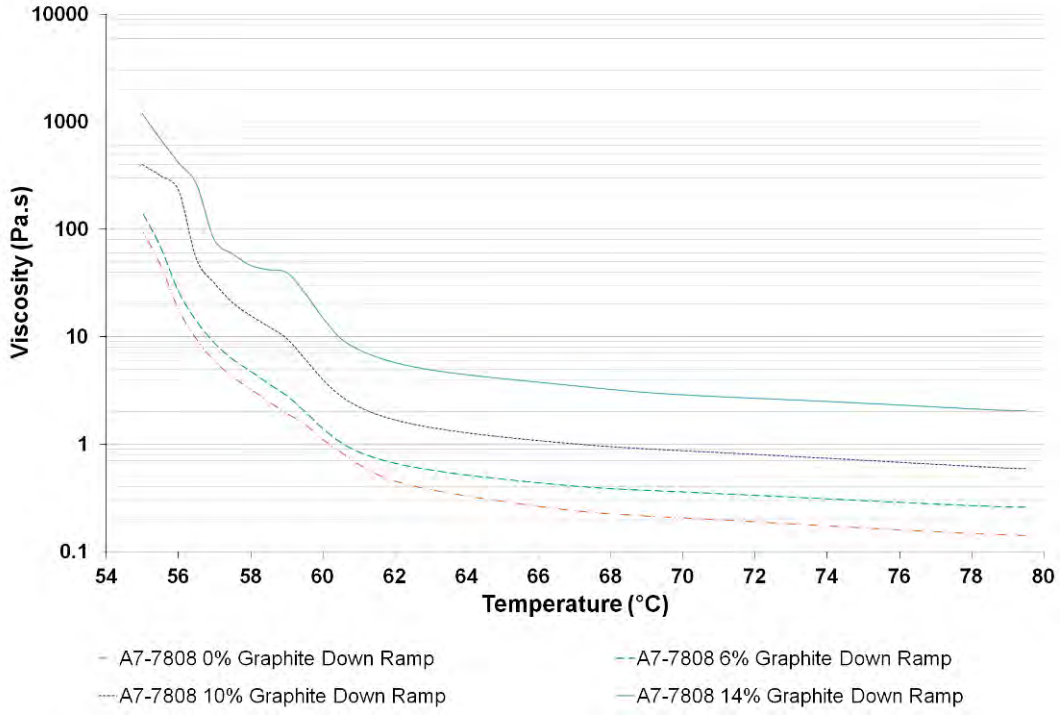

(a)

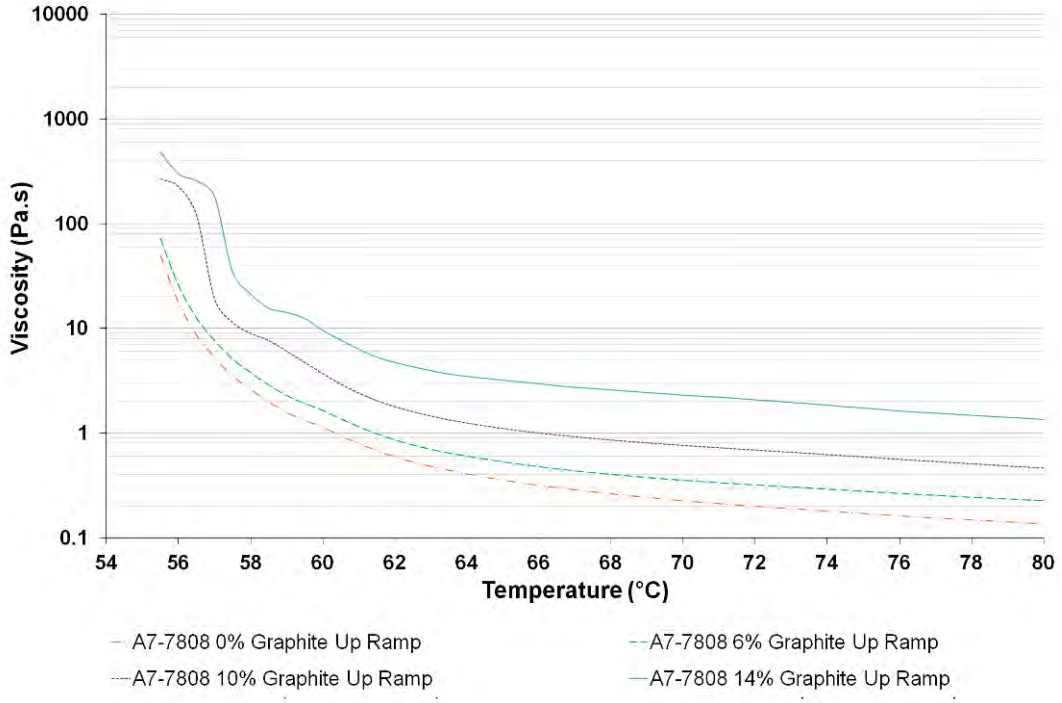

(b)

Figure 15.19 Graph showing the relationship between viscosity and sample temperature for graphite-filled A7-7808 wax samples in a rotational rheometer under a shear stress of 750 Pa. Graph **(a)** shows the cooling curves, whilst graph **(b)** shows the heating curves.

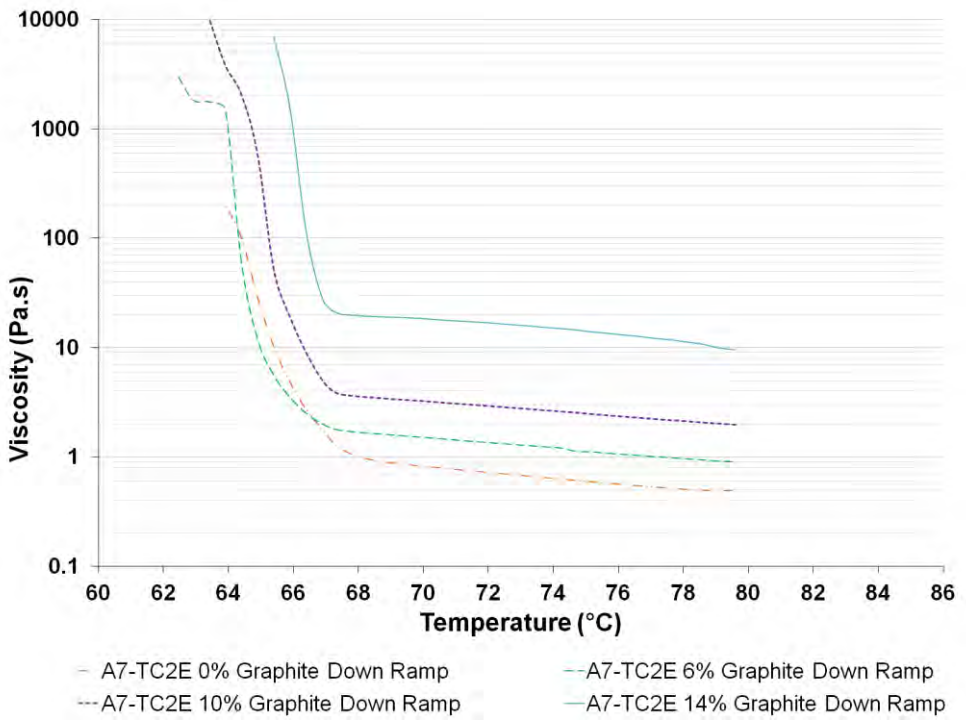

(a)

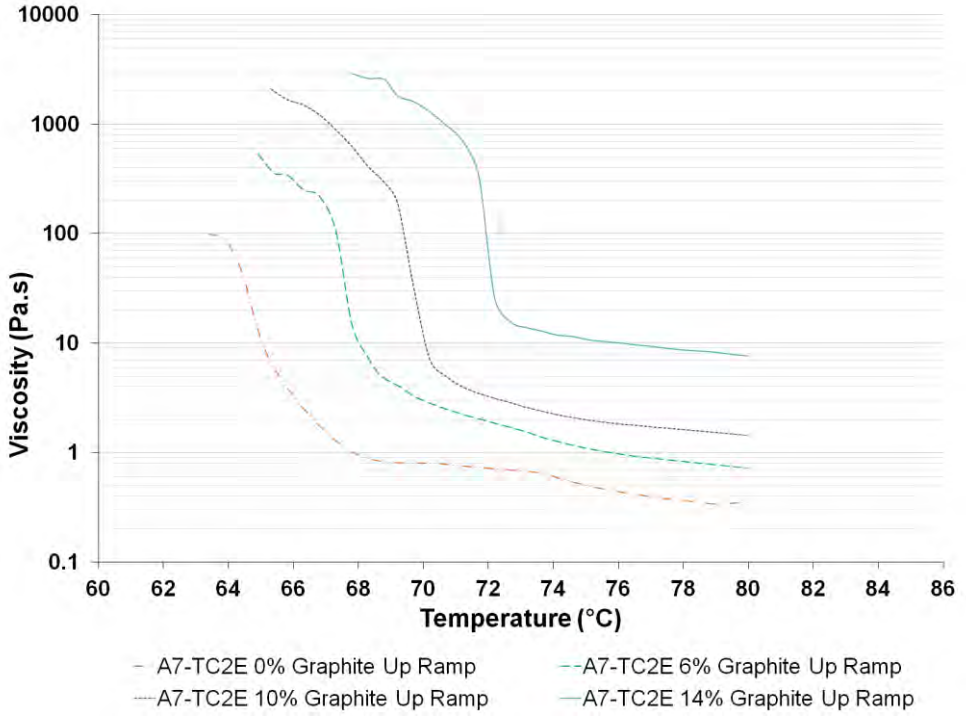

(b)

Figure 15.20 Graph showing the relationship between viscosity and sample temperature for graphite-filled A7-TC2/e wax samples in a rotational rheometer under a shear stress of 750 Pa. Graph **(a)** shows the cooling curves, whilst graph **(b)** shows the heating curves.

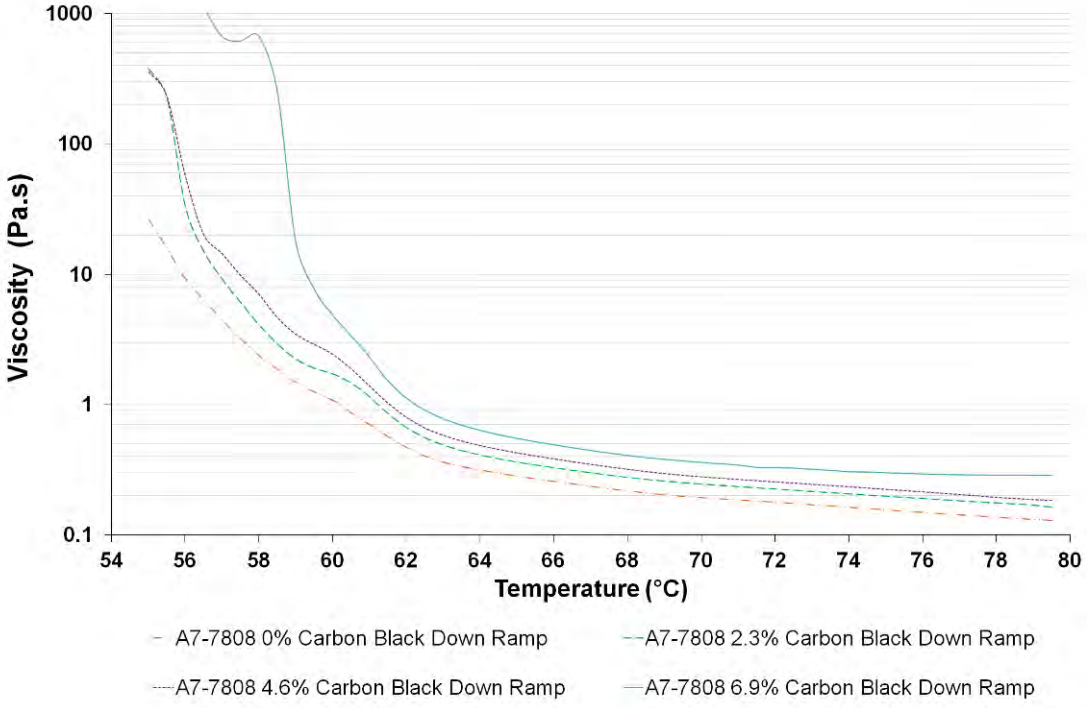

(a)

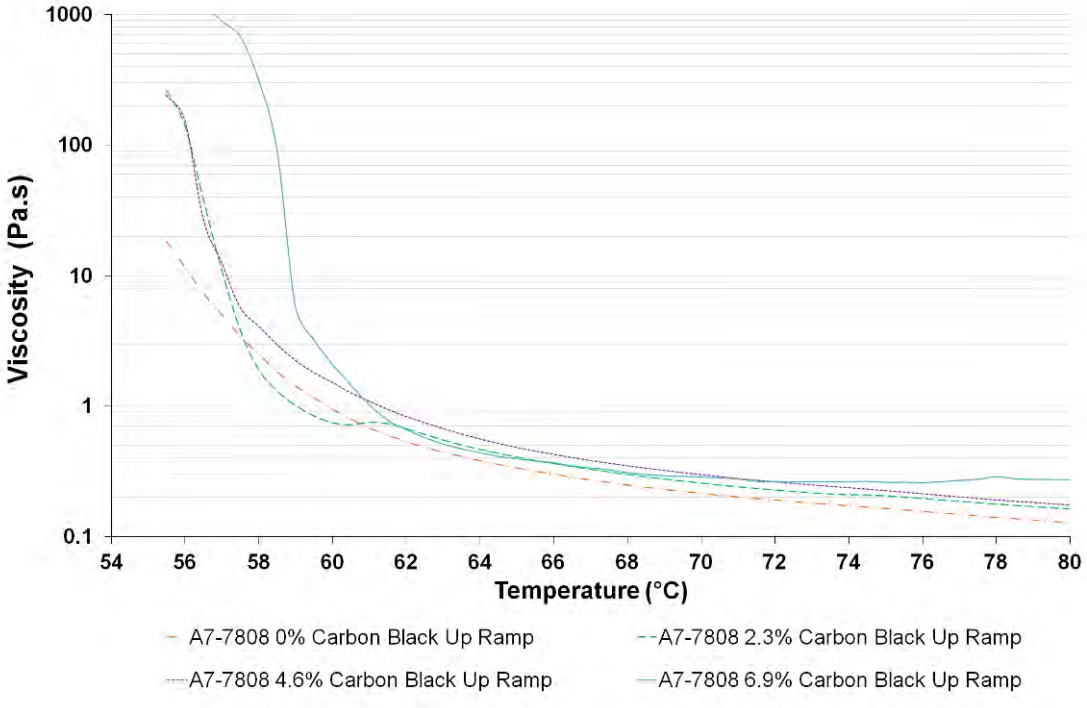

(b)

Figure 15.21 Graph showing the relationship between viscosity and sample temperature for carbon black-filled A7-7808 wax samples in a rotational rheometer under a shear stress of 750 Pa. Graph **(a)** shows the cooling curves, whilst graph **(b)** shows the heating curves.

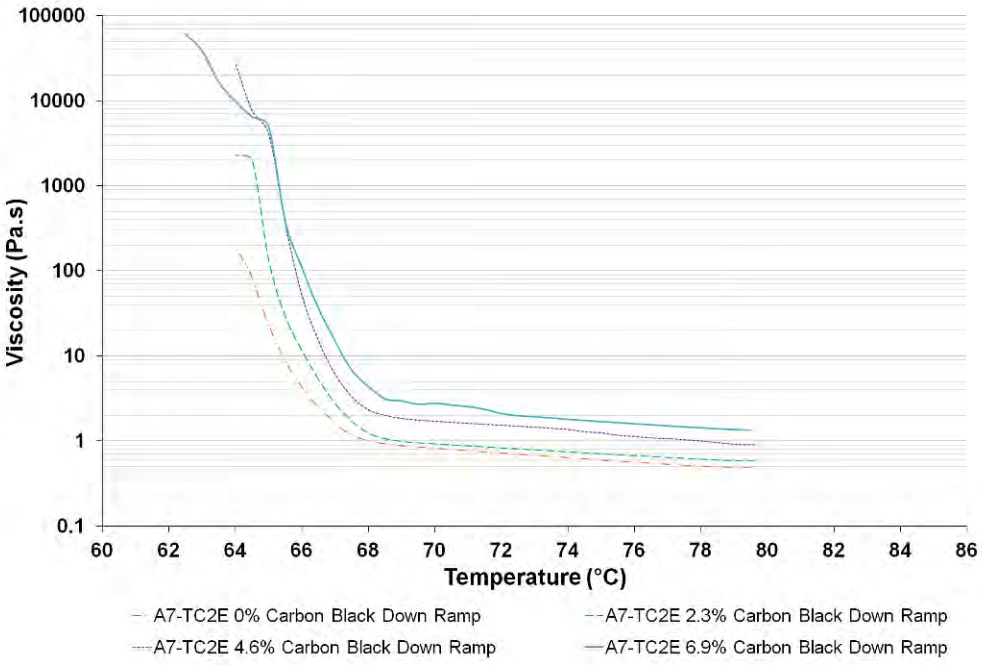

(a)

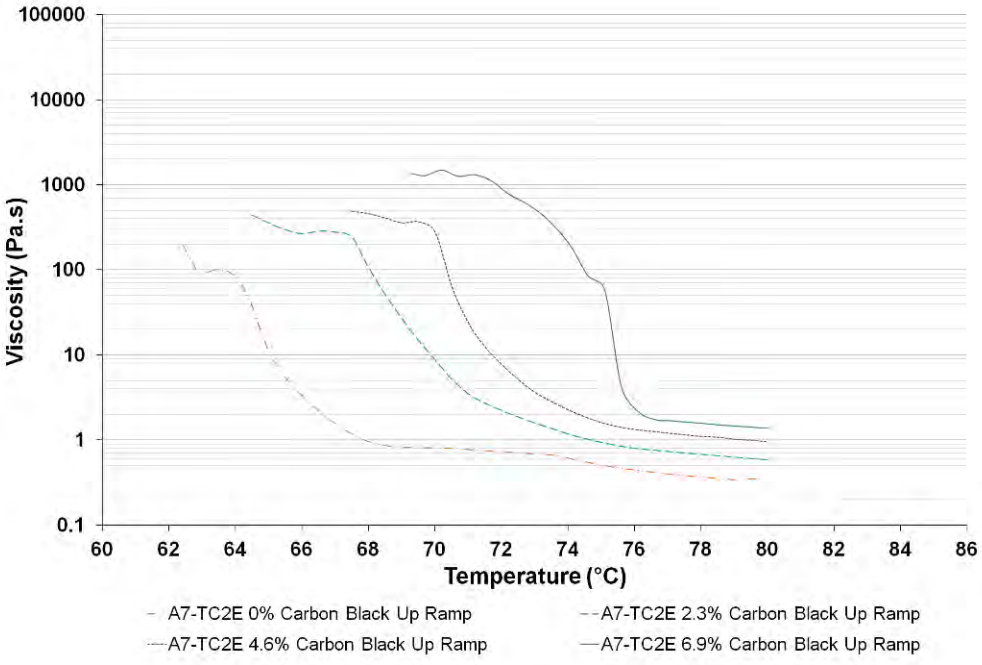

(b)

Figure 15.22 Graph showing the relationship between viscosity and sample temperature for carbon black-filled A7-TC2/e wax samples in a rotational rheometer under a shear stress of 750 Pa. Graph **(a)** shows the cooling curves, whilst graph **(b)** shows the heating curves.

When carbon black was used as the conductive filler in the samples for the temperature ramp experiments, pre-shear cycles were put in place, as the effect of cluster breakdown under shear would lead to sizeable curve changes during the initial stages of each experiment. The influence of carbon black filler addition to the A7-7808 temperature ramps is shown in Figure 15.21. Within the down curves, the temperature at which samples depart from AFE behaviour is unaffected by filler content, as shown in Table 15.7, although the gradient of the curve below 64 °C (i.e. over the solid-liquid transition temperatures) increases with it. The position of each up curve within the liquid region follows a similar line to the down curve, which could partially be attributed to the use of pre-shear cycles. The effect of carbon black addition to A7-TC2/e is shown in Figures 15.22. Like in the A7-7808 experiments, the temperature when the samples depart from AFE behaviour in the down curve is unaffected by carbon black filler addition. The gradient of the curve at temperatures below 69 °C increases as the filler concentration is increased. The shape of the up curve for each composition, however, departs that of the down curve when filler is added. Within the carbon black-filled A7-TC2/e up curves, AFE behaviour is only observed at increasingly high temperatures, as shown in Table 15.7, with the gradient of the transition region steepening as the filler content is increased.

When micronised graphite and carbon black are used as filler materials within the A7-TC2/e wax grade, the solid–liquid transition region is shifted to higher temperatures in the up-curve compared with the down-curve. No change is observed, however, when the A7-7808 grade is used; the reason for this cannot be fully determined without compositional information on each wax grade, which is an unknown. On heating, the presence of filler within the A7-TC2/e appears to inhibit the flow of the base wax to a greater degree. The lower viscosity of the unfilled A7-7808 wax may have an influential effect, since as the temperature is increased in the heating (up) ramp, the viscosity decreases, and so an increase

in shear rate would enable better intermixing. This intermixing would reduce the temperature inhomogeneity within the sample, and so lead to a heating curve that more closely follows the cooling curve. It would therefore be the material's viscosity at the lowest point on the cooling ramp that has an effect on the heating curve. Additionally, when CSS temperature ramps were carried out on fresh cycles, using a temperature ramp rate of 0.5 °C per minute instead of the 1 °C per minute previously used, no significant changes were observed.

15.2.4 Time Dependent Flow Behaviour

Any change in viscosity behaviour using a set shear stress over a constant time period could be used to indicate any breakdown or rearrangement in particle agglomerates under constant high shear. The graphs in Figures 15.23 to 15.26 show the relationship between viscosity and time under shear for samples under the constant shear stress cycle of 750 Pa at 80 °C, which is the same stress parameter used for pre-shear procedures featured in Section 10.3.3, albeit with an extended cycle time of 1600 seconds (as opposed to 300 seconds for pre-shear). When a constant shear stress parameter of 750 Pa was used, the conductive-filler unmodified A7-7808 wax and A7-TC2/e wax displayed little variation in viscosity with time. The viscosity values for the other samples were converted in relative viscosity values, so that the effect of filler addition to different base wax grades could be compared.

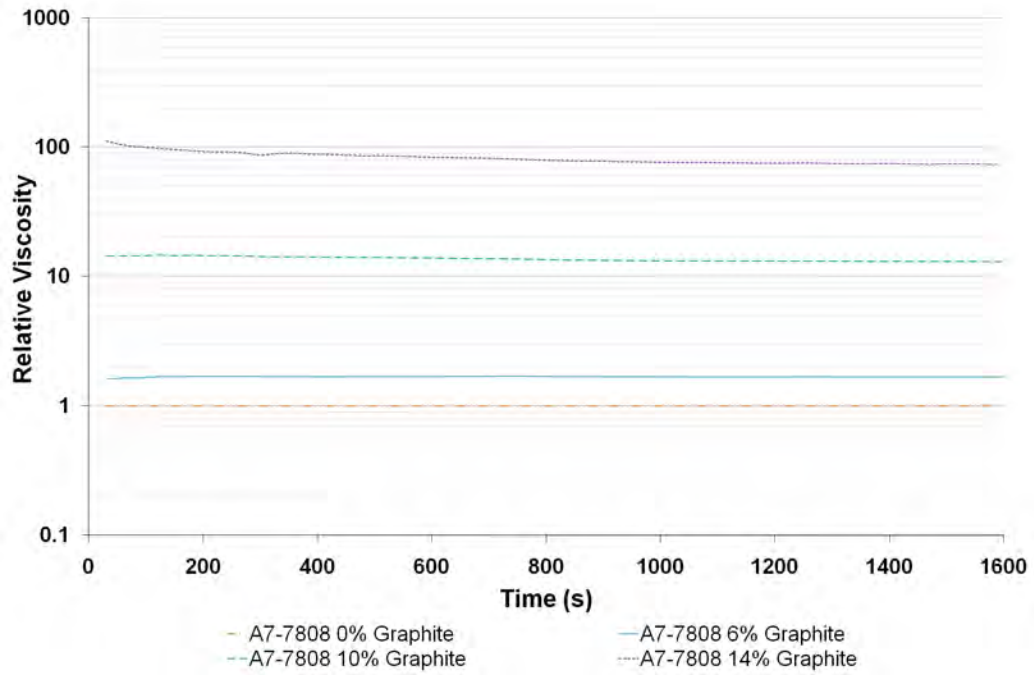

Figure 15.23 Graph showing the relationship between relative viscosity and time under shear for micronised graphite-filled A7-7808 wax in a rotational rheometer under a shear stress of 750 Pa at 80 °C.

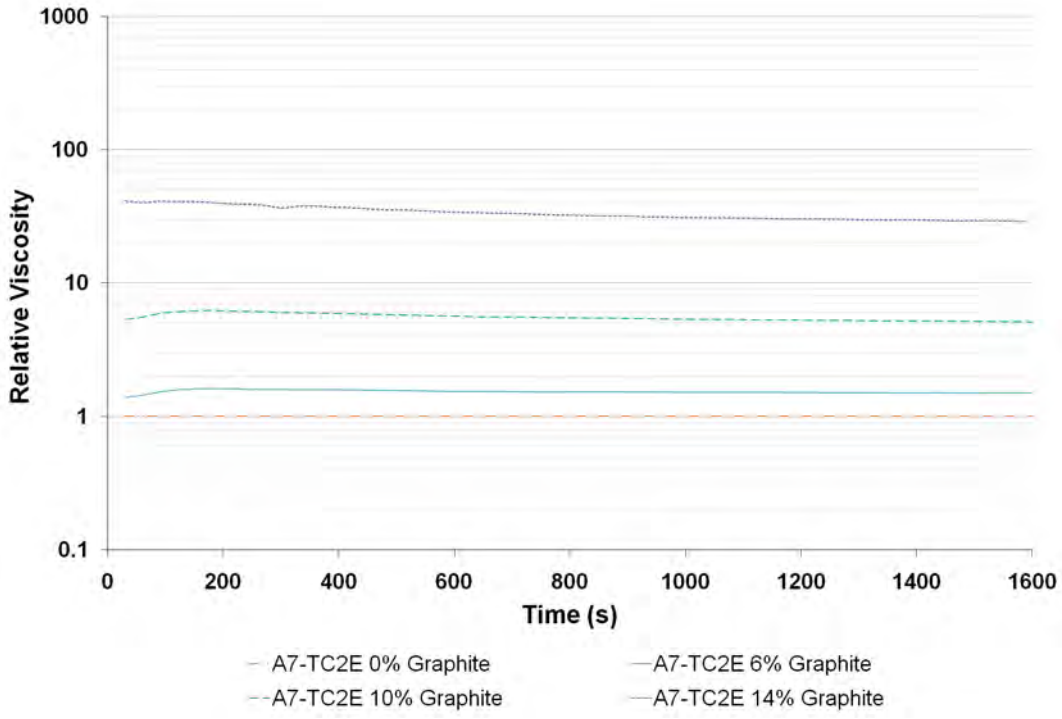

Figure 15.24 Graph showing the relationship between relative viscosity and time under shear for micronised graphite-filled A7-TC2/e wax in a rotational rheometer under a shear stress of 750 Pa at 80 °C.

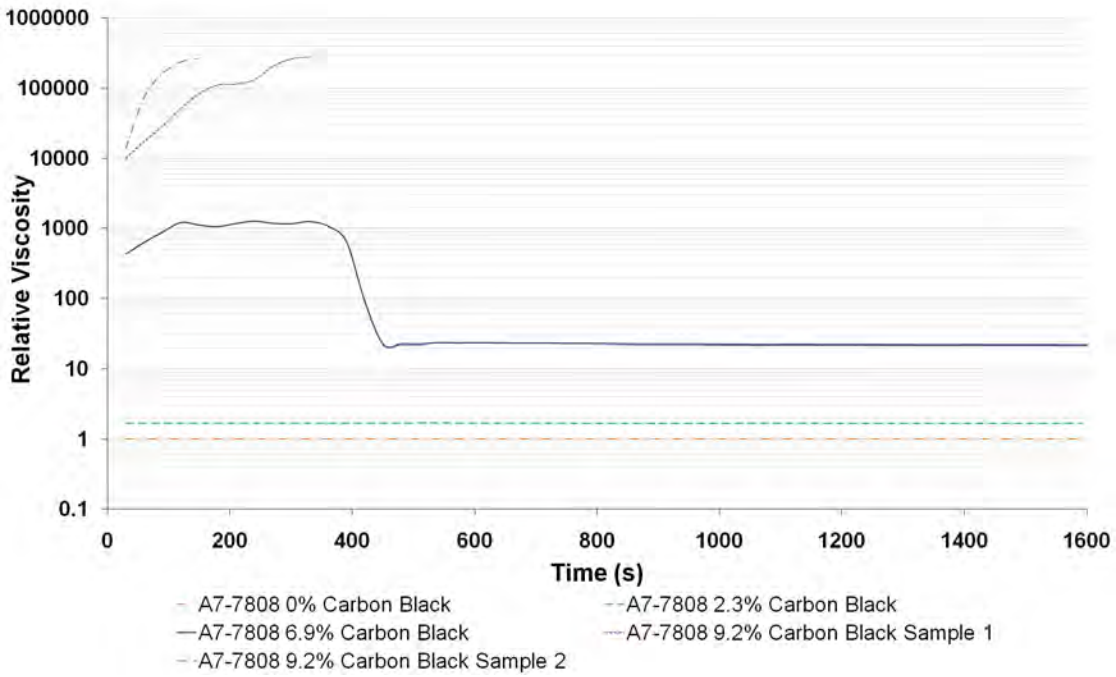

Figure 15.25 Graph showing the relationship between relative viscosity and time under shear for carbon black-filled A7-7808 wax in a rotational rheometer under a shear stress of 750 Pa at 80 °C.

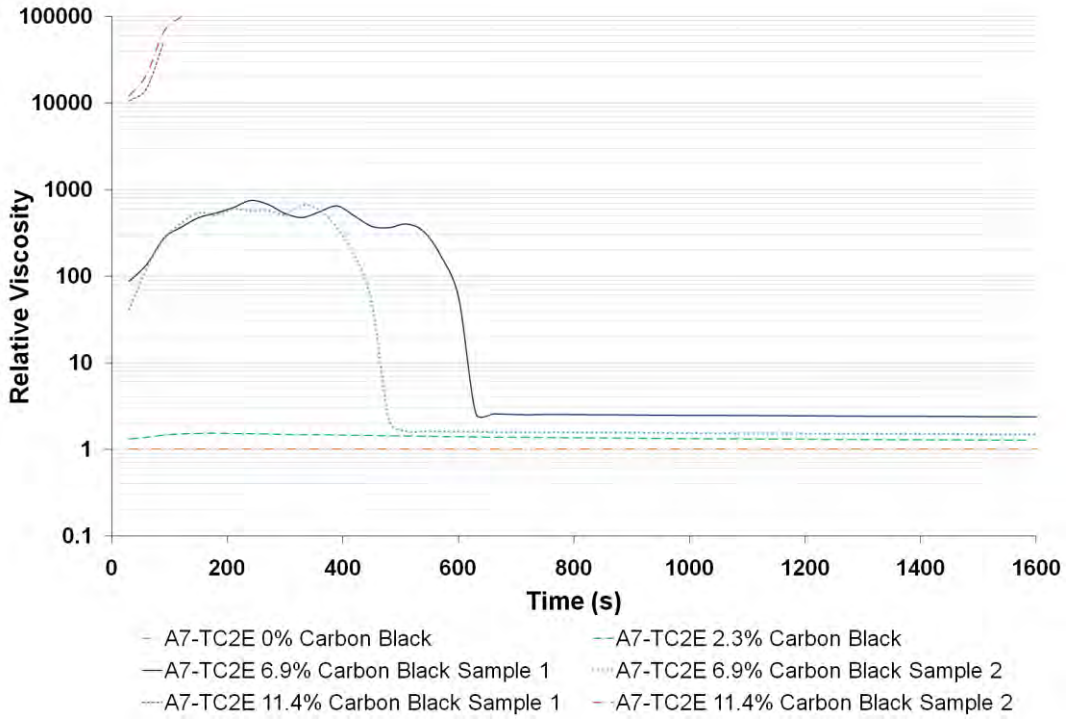

Figure 15.26 Graph showing the relationship between relative viscosity and time under shear for carbon black-filled A7-TC2/e wax in a rotational rheometer under a shear stress of 750 Pa at 80 °C.

When graphite filler is added to either A7-7808 or A7-TC2/e grades, as shown in Figures 15.23 and 15.24, respectively, the viscosity values decrease slightly with time. As both unfilled wax grades show no significant variation in viscosity when tested under the same conditions, and so viscosity changes that would result from material being ejected from the testing gap can be disregarded. As the curve gradient increases as the graphite concentration is increased, time-dependent change in the material under shear can be linked to the presence of filler particles, and more specifically, interparticle interactions. As the time under shear is increased, any particle clusters would be gradually broken up, and the filler material would move into a conformation under shear that resists flow to a lessened extent.

The behaviour of both A7-7808 and A7-TC2/e base waxes changes more significantly with carbon black filler addition, as shown in Figures 15.25 and 15.26. When the filler addition was below 6.9 vol%, the material behaved like the graphite-filled samples within the present experiments, and displayed a slight reduction in viscosity with time under constant shear stress. For the 6.9 vol% carbon black-filled A7-7808 and A7-TC2/e wax samples, the viscosity increased over the first 200 seconds to reach a high viscosity plateau region. The time period over which the samples remained at this relatively stable viscosity was not constant, and for samples tested, a sudden reduction in the viscosity occurred from 400 to 600 seconds into the testing cycle. After this, a relatively stable lower viscosity was reached. The carbon black filler was more agglomerated than the graphite, and so would increase the viscosity of the resultant wax to a greater extent, as described in Section 15.2.2. The formation of the high viscosity plateau existed due to interactions between particle clusters, which form clustered agglomerates that more effectively inhibit flow. For carbon black-filled samples when the filler content was greater than 4.6 vol%, removal of the top plate after the experiment procedure revealed that material between parallel plates contained particle clusters that were non-homogenously distributed.

From these experiments, it would appear that the 300 second pre-shear cycle used for temperature ramps and flow ramp experiments would not be sufficient to overcome the initially high viscosity values. However, it is uncertain as to whether the viscosity values exhibited in the lower viscosity region truly represent that of the carbon black-filled material. Any sudden change from initial high viscosity values is suspected to be as a consequence of phase separation and wall slip effects, which are described in Section 7.2.1. This is especially likely as the final viscosity values are variable between samples with the same composition.

When the carbon black content was above 6.9 vol% the A7-7808 wax and 9.2 vol% in the A7-TC2/e wax, the viscosity increased to approach a high plateau region, as it did in the samples with lower filler concentrations. A sudden decrease in viscosity was not however observed, and the viscosity increased to the point where no detectable shear rate measurements were produced for the remainder of the tested time period. The movement of carbon black particle clusters under shear, to bring together multiple agglomerates, must occur as it did for lower concentrations of carbon black-filled wax. Instead of simply depleting certain areas of filler, which would lead to wall slip effects and an associated drop in viscosity between parallel plates, the agglomerates would reach dimensions where they bridge the top and bottom plates to greatly resist shear. Such clusters were visibly present within the sample following the experimental process, after the upper parallel plate was removed. An avenue for future work would analyse the relationship between the mixing procedure during composite formation and the time-dependent viscosity behaviour, to see whether high-shear mixed samples still exhibit cluster ‘lock-up’ at a given filler loading.

15.3 Ash Content Tests

Ash content testing was carried out on both base waxes and conductive particle-filled wax samples, according to procedures set out in Section 11.1. Using Equation [11.1], the ash content (A_d) of each sample could be calculated as a percentage. The raw data for equation [11.1] and the calculated ash contents are tabulated in Table 15.8.

The manufacturer states the graphite's ash content as being < 0.5%, with a moisture content of less than < 0.2 %. The ash content of the carbon black grade is unspecified, and the powder is stated to have a moisture content of < 1.0 %. For each wax composition tested, separate samples of each filled wax grade were used carried out to ascertain the moisture content, using a procedure described in Section 11.1.

The ash contents of the filled waxes, shown in Table 15.8, may be below the real values because although the alumina crucible used to contain the wax sample had steep sides, a lid was not used to contain the contents. In the dewaxing oven which used an air circulation unit, some of the ash could have been carried away on the flow of air, and so lowered the final measured ash content. Although accuracy levels are of importance, the significant issue raised by these ash content test results relates to the presence of ash at concentrations greater than 0.1% in any wax containing either conductive filler type. Ash concentrations greater than 0.1% in the wax are described as being undesirable in Section 5.1.

The main problem associated with the use of wax with high ash content relates to ash being left in the mould after dewaxing, which would then become incorporated into the metal and leads to the formation of inclusions defects in the casting. These high ash contents make the conductive waxes undesirable for use within investment casting, as shown in Section 16.3, although the use of alternative synthetic graphite filler grades with controlled ash contents should avoid these problems. The use of such conductive fillers is a possibility in future work.

Table 15.8 Calculated ash content data for A7-7808 and A7-TC2/e waxes, as a function of carbon black and micronized graphite filler content

A7-7808 Wax	**Micronised graphite**			**Carbon black**		
Volume% Filler	**0.0**	**10.0**	**14.0**	**0.0**	**6.9**	**11.4**
Weight% Filler	**0.0**	**19.7**	**26.5**	**0.0**	**12.4**	**19.7**
Initial wax mass ($m_2 - m_1$) (g)	1.127	1.204	1.131	1.127	1.268	1.114
Post-dewaxing mass ($m_3 - m_1$) (g)	0.002	0.196	0.282	0.002	0.078	0.124
Moisture content (M_{ad}) (%)	0.12	0.13	0.20	0.12	0.09	0.14
Calculated ash Content (A_d) (%)	0.18	16.30	24.98	0.18	6.17	11.15
A7-TC2/e Wax	**Micronised graphite**			**Carbon black**		
Initial wax mass ($m_2 - m_1$) (g)	1.108	1.086	1.147	1.108	1.230	1.162
Post-dewaxing mass ($m_3 - m_1$) (g)	0.001	0.147	0.266	0.001	0.100	0.136
Moisture content (M_{ad}) (%)	6.0	5.7	5.3	6.0	5.2	5.3
Calculated ash content (A_d) (%)	0.10	14.35	24.49	0.10	8.57	12.36

15.4 Permeability Testing

As described in Section 13.3, EPD suspension properties were tailored to enable EPD on conductive wax substrates. Zircon EPD coating operations were carried out on graphite-filled wax rectangular plate sections, and achieved thickness uniformity with tolerances of ~ 20 μm on flat plate surfaces. However, the uniformity of coating thicknesses achieved on the plate geometry substrates could not be replicated on the spherical conductive wax substrates required for the investment shell permeability experiments for the reasons discussed later in Section 16.2.1.

Permeability testing is, therefore, considered here under wax properties rather than under EPD behaviour, as the suitability of filled waxes as investment shell coating substrates was nonetheless assessed. Permeability spheres were formed using the procedures set out in Sections 8.4 and 14.2.2; two sample types were made: (a) unfilled A7-7808 wax hollow spheres and (b) 14 vol% micronised graphite-filled A7-7808 wax hollow spheres.

Since an EPD primary coat could not be successfully formed on the conductive wax spheres, the full investment cycle was implemented on both filled and unfilled wax spheres, as specified in Section 14.2.2. Figure 15.27 displays images of a selection of the successive coating steps on a hollow wax sphere substrate. In addition to the investment process being carried out on wax spheres, it was also concurrently carried out on EPD coatings formed on compressed graphite plates, as they had the thickness, uniformity and strength to allow dipping to take place without structural breakdown of the EPD layer taking place. This is shown in Figure 15.27(d) and (e), and was carried out to strengthen the EPD primary, so that SEM analysis of the fired EPD primary coating could take place. This analysis is shown in Section 16.2.2.

Following dewaxing, the permeability spheres formed using A7-7808 wax and 14 vol% graphite-filled A7-7808 wax substrates were tested on the permeability rig. Results from these tests are shown in Table 15.9 and Table 15.10, along with permeability values, μ, for each sample, derived using Equations [14.1], [14.2] and [14.3] from Section 14.2.4. Even though the permeability shells formed on the unfilled and filled wax spheres were of the same composition, the permeability values were lower when 14 vol% graphite-filled A7-7808 was used. One possible reason for this could be related to the surface texture of the wax. According to BS 1902-10.2: 1994, which covers permeability testing, the primary coat is the densest layer, and therefore has the greatest effect on permeability measurements.

Table 15.9 Permeability test sphere dimensions and permeability test results. Pressure and Flow rate values were taken during a dwell period, 5 minutes into the air-flow cycle.

For 14vol% graphite-filled A7-7808 wax permeability spheres						
	Dynamic Viscosity of Air at 1273K	Volumetric Flow Rate of Air at 1273K	Room Temperature	Testing Temperature	Pressure	Pressure difference across piece
Sample	η (Ns/m^2)	V_c (N/m^2)	T_1 (K)	T_2 (K)	(N/m^2)	P (N/m^2)
1	0.00004152	0.0000675	293	1273	40681	40681
2	0.00004152	0.0000665	293	1273	46817	46817
3	0.00004152	0.0000663	293	1273	40198	40198
	Av. Internal diameter of shell mould	Av. External diameter of shell mould	Av. Thickness of shell mould	Inner surface area of the shell mould	SAF at 10 kN/m^2	Permeability
Sample	(mm)	(mm)	l (m)	a (m^2)	$\times 10^{-5}$ m^3/s	μ ($\times 10^{-13}$ m^2)
1	39.00	52.35	0.00668	0.00470	1.66	0.978
2	39.28	52.55	0.00663	0.00477	1.42	0.820
3	39.20	51.50	0.00615	0.00475	1.65	0.887

Table 15.10 Permeability test sphere dimensions and permeability test results. Pressure and Flow rate values were taken during a dwell period, 5 minutes into the air-flow cycle.

For unfilled A7-7808 wax permeability spheres						
	Dynamic Viscosity of Air at 1273K	Volumetric Flow Rate of Air at 1273K	Room Temperature	Testing Temperature	Pressure	Pressure difference across piece
Sample	η (Ns/m^2)	V_c (N/m^2)	T_1 (K)	T_2 (K)	(N/m^2)	P (N/m^2)
4	0.00004152	0.0000697	293	1273	29166	29166
5	0.00004152	0.0000669	293	1273	25718	25718
6	0.00004152	0.0000665	293	1273	29717	29717
	Av. Internal diameter of shell mould	Av. External diameter of shell mould	Av. Thickness of shell mould	Inner surface area of the shell mould	SAF at 10 kN/m^2	Permeability
Sample	(m)	(m)	l (m)	a (m^2)	$\times 10^{-5}$ m^3/s	μ ($\times 10^{-13}$ m^2)
4	39.40	51.40	0.00600	0.00480	2.39	1.24
5	39.63	52.05	0.00621	0.00485	2.60	1.38
6	38.90	52.35	0.00673	0.00468	2.24	1.34

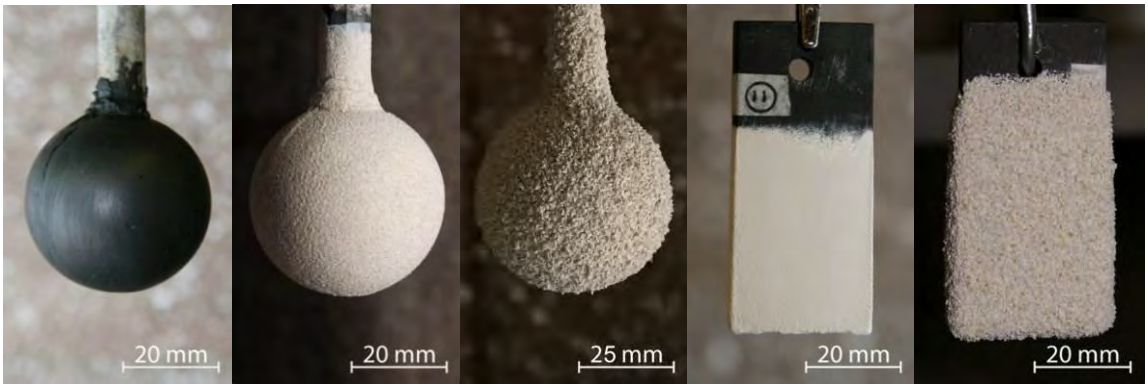

(a) **(b)** **(c)** **(d)** **(e)**

Figure 15.27 Photographs showing three stages of the dip coating procedure for 14 vol% graphite-filled A7-7808 wax permeability sphere within **(a), (b)** and **(c)**, and a EPD zircon coated compressed graphite substrate, **(d)** prior to, and **(e)** after, strengthening slurry dip and stucco coats.

If the graphite-filled wax allowed this coat to bind more strongly and uniformly than on the unfilled alternative, such a difference could be produced. However, it was found that after the permeability measurements on the graphite-filled wax substrate shells had been done, ash from inside the spheres could be agitated out through the spheres' inserted mullite tube. A cross-section was made into Sample 2, as shown in Figure 15.28 (a); a significant coating of ash is present on the interior surface. Sample 2 is also shown in Figure 15.28 (b), after the ash interior coating had been rinsed away using deionised water. On inspection, no ash particles were embedded within the ceramic shell.

This coating should account for the decreased permeability of the investment shells formed on the graphite-filled wax hollow sphere substrates. To test this, a water spray was used to remove ash from the interior surface of each shell, before drying. Samples 3 and 5 then underwent a second permeability test, with the results shown in Table 15.11. From this, it is possible to attribute the decreased permeability to the ash coating, since the permeability values of the unfilled and filled wax substrate samples were brought more closely in line with one another.

Table 15.11 Displays the data derived from permeability sphere sample measurements and permeability testing. Pressure and Flow rate values were taken 5 minutes into the air flow cycle at elevated temperatures.

For 14vol% graphite-filled A7-7808 wax permeability spheres						
	Dynamic Viscosity of Air at 1273K	Volumetric Flow Rate of Air at 1273K	Room Temperature	Testing Temperature	Pressure	Pressure difference across piece
Sample	η (Ns/m^2)	V_c (N/m^2)	T_1 (K)	T_2 (K)	(N/m^2)	P (N/m^2)
5clean	0.00004152	0.0000695	293	1273	25408	25408
3clean	0.00004152	0.0000694	293	1273	24201	24201
	Av. Internal diameter of shell mould	Av. External diameter of shell mould	Av. Thickness of shell mould	Inner surface area of the shell mould	SAF at 10 kN/m^2	Permeability
Sample	(mm)	(mm)	l (m)	a (m^2)	$\times 10^{-5}$ m^3/s	μ ($\times 10^{-13}$ m^2)
5clean	39.63	52.05	0.00621	0.00470	2.74	1.50
3clean	39.20	51.50	0.00615	0.00475	2.87	1.69

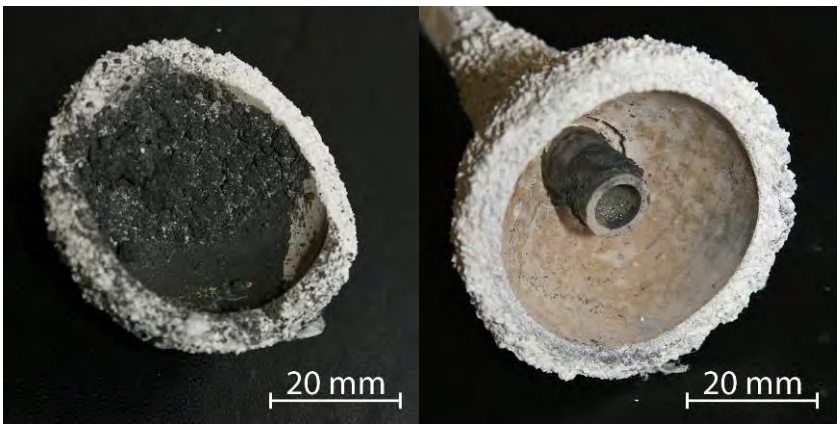

(a) **(b)**

Figure 15.28 Photographs showing a cross-section cut from permeability sphere Sample 2 after permeability testing. Image **(a)** shows the ash coating the shell interior that accounts for the lower than expected measured permeability values. Image **(b)** shows the Sample 2 hemisphere cross-section bisected by the mullite rod, following cleaned using water.

CHAPTER 16. EPD EXPERIMENTS

16.1 Deposition on Compressed Graphite Planar Substrates

16.1.1 Introduction

Initial work relating to EPD was focussed on optimising the suspension and deposition set-up parameters for a system where limited substrate conductivity was not an issue. As described in Section 13.1, compressed graphite substrates with rectangular plate geometry were chosen, as they had an easy to calculate surface area, with 90° edges that could be used to demonstrate the effect of focussed electric field strength on localised deposition behaviour. This geometry could also be easily replicated in conductive or non-conductive wax, by casting the material into a mould with these dimensions. Direct comparisons could therefore be made between substrates with differing conductivities.

A number of different EPD variables were investigated experimentally, and the experimental results are described, discussed and analysed in the following sections. The observed differences between the electrophoretic deposition behaviour on compressed graphite and on conductive wax substrates are discussed in Section 16.2. All experiments were carried out using a controlled voltage set-up, as described in Section 13.3.2. The Helmut Kreutz 'Super FF' zircon grade was used in EPD suspensions, at a suspension concentration of 40 $g.l^{-1}$, unless otherwise stated.

Each yield measurement is given as mass values on the plate substrate, with an immersed surface area of 28.4 cm^2. This value was not converted into a surface area-related value, as it would not represent average deposition on a flat surface. This was due to both the increased deposition thickness at substrate edges and the increased coating thickness at the base of the plate substrate due to suspension depletion.

16.1.2 Applied voltage as an EPD variable

The applied voltage corresponds to the value set on the TTi Instruments EX752M power source, as no resistor elements other than the EPD cell itself existed within the circuit diagram. The voltage and current value given by the power source display were compared with the corresponding readings given by a Fluke 83 multimeter, which measured values between contacts on the substrate electrode and aluminium counter-electrode. Such comparisons were of particular significance when a low conductivity electrode substrate was in place. When an EPD coating was formed on the compressed graphite, mass measurement was carried out, to give a total deposition yield value and average surface area-related yield value. In addition to measuring deposition yield, optical photographs were taken in order to give an impression of coating uniformity and surface void formation on a millimetre scale. These images were used to identify and record coating run-off, coating non-uniformity and surface pit-formation, as the deposition yield values can often be similar, whether in the presence or absence of such features.

As described in Section 14.1, selected samples were firstly scored along cutting lines using a tungsten carbide scribe to cut through the coating, before a manual saw was employed to make a cross-section sample of the underlying substrate. Deposition thickness measurements involved using secondary electron (SE) scanning electron microscope (SEM) micrographs.

Figure 16.1 shows the average deposition yields as a function of applied EPD cell voltage from a number of identically prepared suspensions, with each suspension being used to coat four to five graphite substrates using a range of applied voltages. A number of key suspension and set-up parameters are listed on the graph and in the figure caption. Subsequent sections describe how these variables affect the deposition yield and behaviour. It should also

be noted that the counter electrode had the geometry of a surrounding cylinder, with an electrode separation distance of 40 to 50 mm. Both the counter-electrode shape and electrode separation distance affect the strength of the resultant electric field.

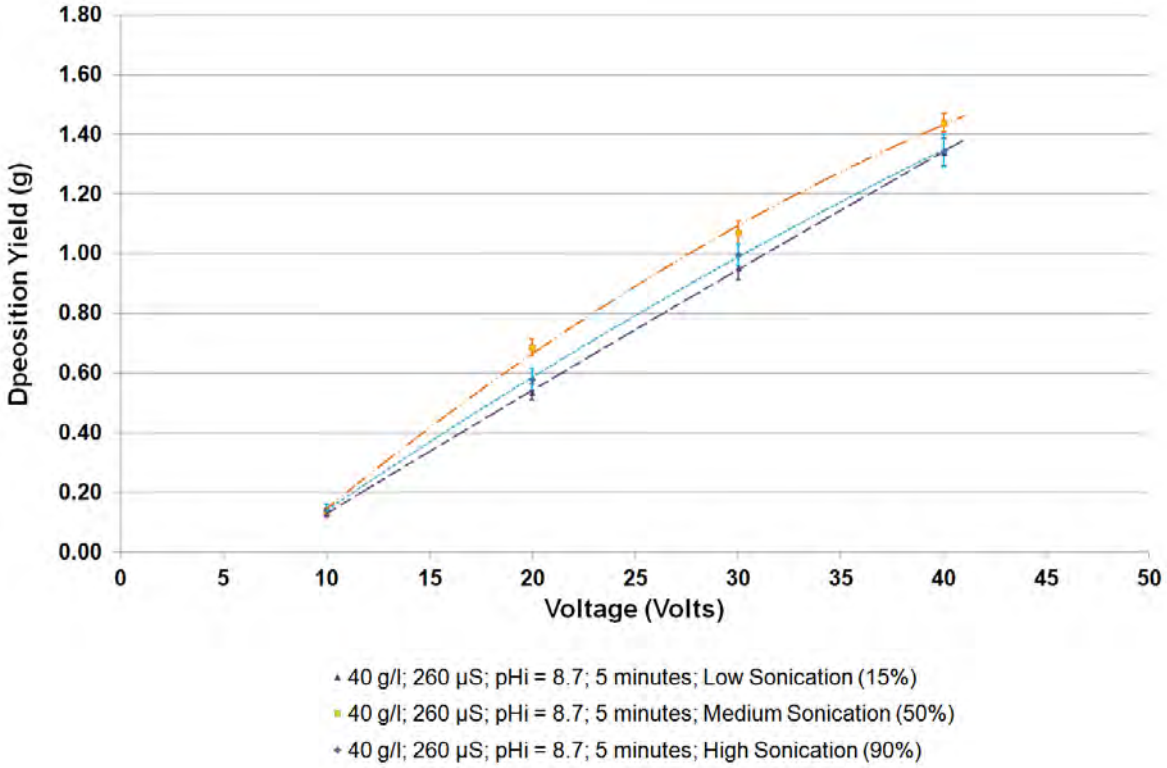

Figure 16.1 EPD deposition yield versus applied EPD cell voltage, as a function of sonication intensity level over a 5 minute period. Although the sonication levels of 0%, 15%, 30%, 50% and 90% of the operational maximum were used, this graph shows the three most frequently used levels. Each sonication time period was set to 5 minutes (300 seconds), with period 1 implemented shortly after the zircon powder addition and period 2 implemented during the 4 hour homogenisation process, as described in Section 13.3.3.

For this experiment, the ultrasonication power level used for the suspension preparation sonication cycles was a further variable to be considered. A Jencons VCX 600 sonicator was used for all the sonication cycles, operated as described in Section 13.3.3, with the effect of sonication on zircon particle size distribution analysed in Appendix A.2.2. For both 300 second (5 minute) suspension sonication periods, the equipment had its power level

set to 0%, 15%, 30%, 50% or 90%. As the operational maximum of the device was 600 watts, this corresponds to power outputs of 0, 90, 180, 300 and 540 watts, respectively.

From Figure 16.1, between 10 and 40 volts, there is a roughly linear relationship between the deposition yield and the applied EPD cell voltage when the suspension parameters were set as described. On the basis of the data trend line, there would be zero deposition yield when the EPD voltage is below ~ 6 V. Preliminary work with other suspensions showed that a thin layer of zircon was deposited when the potential difference was set to 5 volts, with no adherent coatings being formed at lower EPD potential.

Deposition from suspensions subjected to different sonication levels could be compared when the applied EPD voltage was set to 20 V or higher because the level of coating run-off would not significantly affect yield. The coating deposition yield reached a peak when the sonication power level was set to 50% (300 watts). The reason for this is the observed coating uniformity achieved from suspensions subject to this sonication level; images of the zircon coated graphite substrates are shown in Figure 16.2.

The effect of increasing EPD cell voltage is not only linked to a roughly linear rise in coating yield. As seen in the digital SLR photographs in Figure 16.2, the amount of coating run-off, which is most easily observed from the extent to which the coating is pulled down from the top of the deposition area, lessens at higher voltages. As stated in Section 4.5.1.2, a low applied EPD voltage of 4.1 V acted as the threshold for the onset of water-electrolysis bubble formation, and the rate of bubble production grew significantly with increasing current (Su, 2001). Within the present work set-up, increasing the applied EPD voltage led to an associated increase in EPD circuit current.

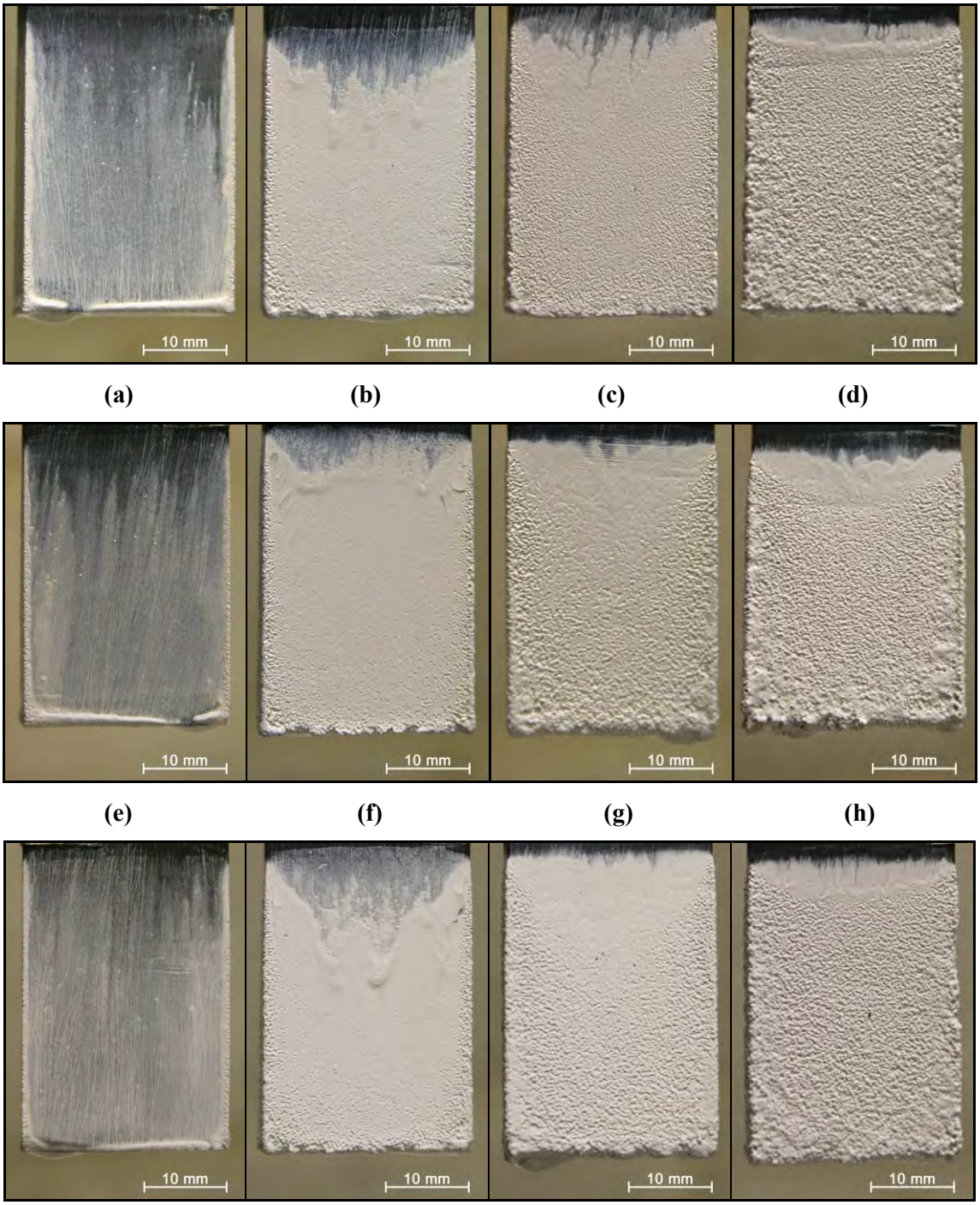

Figure 16.2 Digital SLR images showing examples of zircon EPD coatings on compressed graphite substrates. **(a) to (d)** are images of coatings from suspensions subjected to two 15% magnitude sonication periods; **(e) to (h)** are from suspensions subjected to two 50% magnitude sonication periods, and **(i) to (l)** are from suspensions subjected to two 90% magnitude sonication periods. The following EPD voltages were applied for 5 minutes: **(a) (e) (i)** 10 volts; **(b) (f) (j)** 20 volts; **(c) (g) (k)** 30 volts; **(d) (h) (l)** 40 volts. The sonication procedure used is described in Section 13.3.3.

The EPD coatings formed from suspensions subjected to the three different sonication pre-treatments are shown in Figure 16.2. For all three suspension categories, an increased level of pore and pit retention was observed in the coatings as the voltage was increased from 10 volts to 40 volts. The degree of pit formation due to gas formation was consistent for the three different sonication pre-treatments. The use of the 50% magnitude sonication pre-treatment led to coatings with the lowest level of coating run-off, which consequently led to higher deposition yields.

The EPD zircon coatings on the substrates increased in thickness as the applied EPD potential, i.e. voltage was increased. In addition to this, the coatings on the edges of the samples were thicker than on the samples' planar surfaces; this was most noticeably the case for the intermediate applied EPD voltages (10 and 20 V). As described by Van der Biest (2004), high current density areas are produced around the deposition electrode edges, which lead to increased coating thickness in these areas. The effect of increased binding strength on the plate edges is most notably observed in Figure 16.2 (images (a), (e) and (i)), where the coating on the central area of the plate is itself pulled off by the suspension as it runs off due to gravity, to leave an adherent coating zone 1 to 2 mm wide running around the substrate edges.

As shown in Figure 16.2 (images (a), (b), (c) and (d)), the thickness disparity between the flat substrate surface and edge became less pronounced when the EPD voltage (and therefore electric field strength surrounding the substrate as a whole) was increased, Coating run-off on the substrate plate surface was limited to a greater extent during the drying stage when higher potentials were applied, and accounts for this trend.

In addition to taking mass measurements to determine deposition yield values and optical photographs to give information on coating uniformity, scanning electron microscopy (SEM) micrographs were taken of selected prepared samples, in order to evaluate the surface

topography (see Figure 16.3 to Figure 16.6) and determine the cross-sectional thicknesses of coatings in their green (unfired) state. This information from the SEM micrographs enabled the relationship between the applied EPD voltage and the deposited coating characteristics (thickness and void inclusion) to be ascertained.

Figure 16.3 shows that whilst the number of cracks within a given surface area appears to be constant for the 20 volts and 30 volts EPD samples, the severity of cracking appears to increase with applied EPD voltage. This, however, could be attributed to the increasing thickness of the coating, as opposed to the growing effects of bubble entrapment through water electrolysis.

Cross-sections of the zircon coatings on their supporting graphite substrates were made as described in Section 14.1. All cross-sections in the horizontal plane (with the substrate in the orientation for EPD coating) were carried out at a distance halfway up the coated area. Such cross-sections were made to both measure the deposition thickness at different points on the sample and observe the degree of void formation that would otherwise go undetected by micrographs of the deposition surface. By carefully scraping off the zircon coating on one of the flat plate surfaces, it was possible to measure the deposition thickness at a 90° angle i.e. perpendicular substrate edge, to see how the deposition thickness varied with substrate immersion depth in the suspension used for EPD.

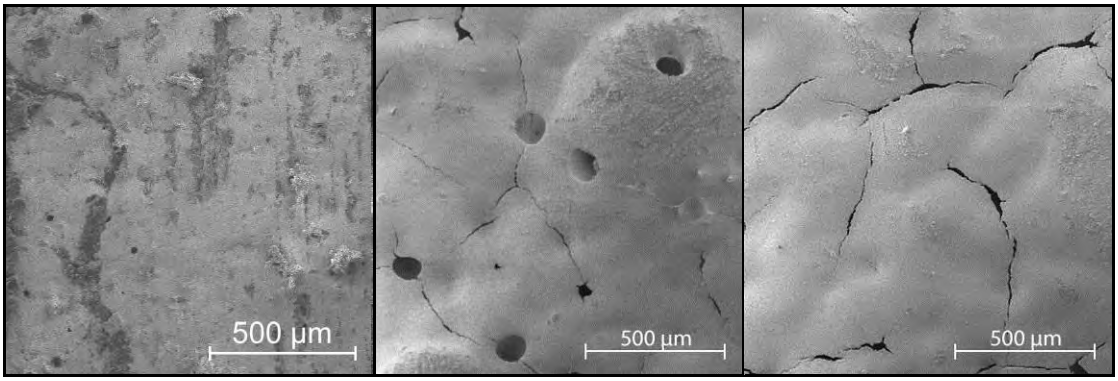

(a) **(b)** **(c)**

Figure 16.3 SEI micrographs (SE mode) showing the as-deposited surfaces of dried green zircon coatings formed using aqueous EPD for 5 minutes at the following voltages: **(a)** 10 volts; **(b)** 20 volts; **(c)** 30 volts.

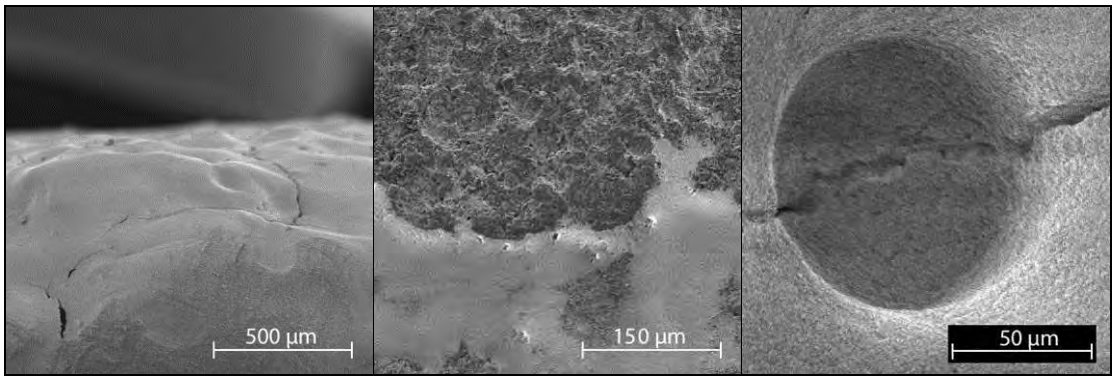

(a) **(b)** **(c)**

Figure 16.4 SEI micrographs (SE mode) showing the as-deposited surfaces of dried green zircon coatings formed using aqueous EPD for 5 minutes at the following voltages: **(a)** 30 volts, with the surface at an angle, highlighting its uneven nature; **(b)** 20 volts, showing an area where coating run-off has occurred; **(c)** 20 volts, showing a close up of a surface pit.

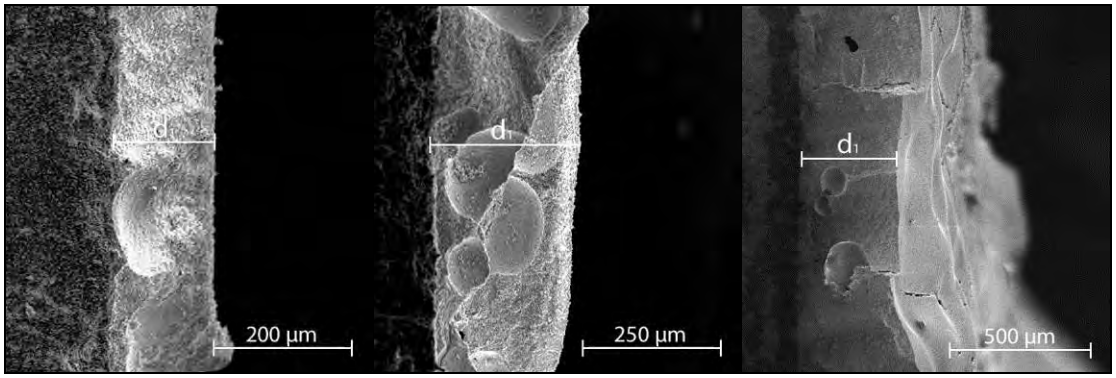

(a) **(b)** **(c)**

Figure 16.5 SEI micrographs (SE mode) showing through-thickness cross-sections of the green deposited zircon coatings on the plate surface, formed using aqueous EPD for 5 minutes at the following voltages: **(a)** 15 volts (d_1 ~ 150 µm); **(b)** 20 volts (d_1 ~ 250 µm); **(c)** 30 volts (d_1 ~ 350 – 400 µm).

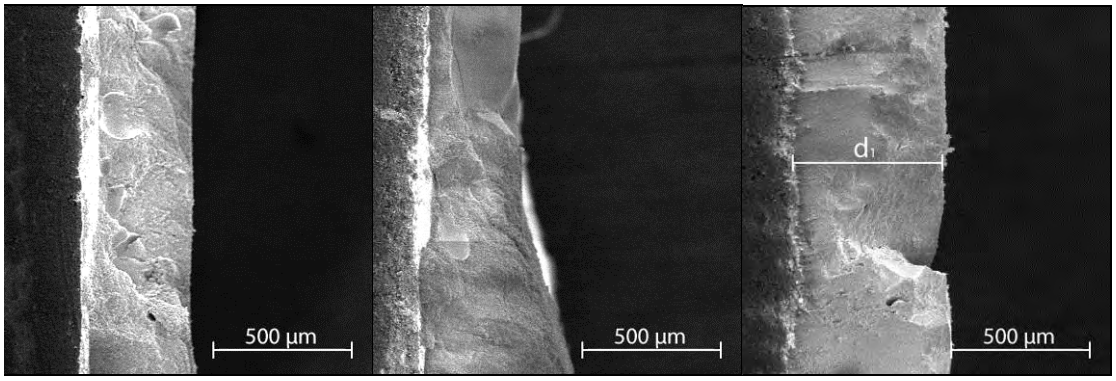

(a) **(b)** **(c)**

Figure 16.6 SEI micrographs (SE mode) showing through-thickness cross-sections of the green deposited zircon coatings on the plate surface, formed using aqueous EPD at 30 volts for 5minutes: **(a)** is from a section on the central plate surface (d_1 ~ 350 to 400 µm); **(b)** is from a section near the substrate corner (d_1 ~ 350 to 500 µm); **(c)** is from a section running along the substrate edge (d_1 ~ 500 µm).

The zircon coating as-deposited dried EPD coating through-thickness section in Figure 16.6(a) was taken from a central area on the electrode surface, some distance from the substrate edges. An increase in coating thickness is observed with increasing applied voltage; the relationship is shown graphically in Figure 16.7. Thickening at the substrate corners can be observed in Figure 16.6(b); the deposit thickness increased by about 150 microns (140%) at the corners when 30 V 5 minute set-ups were applied.

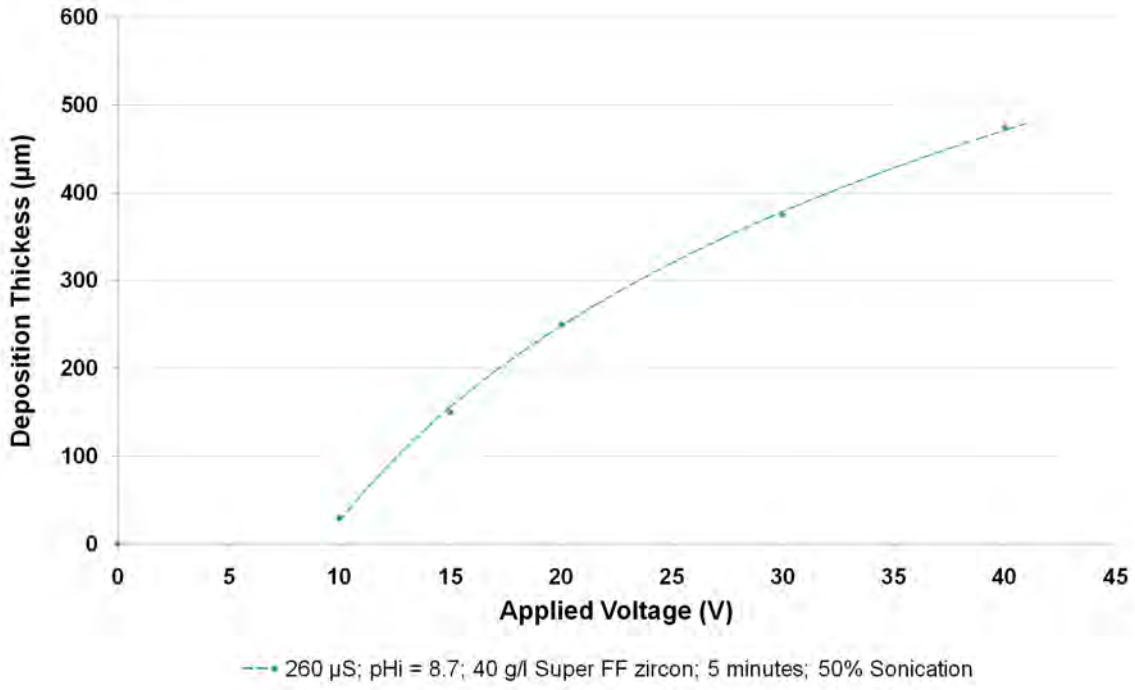

Figure 16.7 Graph showing the green deposit thickness as a function of applied voltage for electrophoretic deposition of Helmut Kreutz 'Super FF' zircon powder in aqueous medium on graphite substrates (using the suspension parameters given in Figure 18.2 (e to h)). The deposition thickness data were acquired from SEI micrographs of transverse cross-sections of EPD zircon coated substrates. The deposition thickness value at 10 V was determined at a region where coating runoff was minimal on the plate surface, whereas the other deposition thickness values are averaged values (as coating run-off was less of an issue when applied voltages above 10 V were used).

The Hamaker equation (Hamaker 1940) variables in Equation [4.6] describe the theoretical relationship between the EPD set-up parameters and the EPD deposition yield. Equation [4.6] shows that the deposition yield is linearly proportional to the EPD electric field strength when all the other parameters are constant. From current measurements using a multimeter connected to the EPD cell deposition-electrode and counter-electrode, no current ran through the EPD suspension from the counter-electrode to the deposition-electrode when the applied voltage was below approximately 4.1 volts. The deposition yield versus applied EPD voltage trend lines in Figure 16.1 can be extrapolated to zero deposition yield at an

applied voltage between about 4 and 7 volts, depending upon the suspension preparation method.

All suspensions that could be used to form adherent EPD coatings exhibited a threshold voltage level, below which negligible coating deposition occurred. The relationship between the EPD deposition yield and the applied EPD voltage at voltages above this threshold level was either a linearly proportional one or one where the deposition yield increase declined as the voltage was increased. This decline follows trends seen in the literature, as shown in Section 4.4, where the formation of an electrically resisting EPD coating reduces the strength of the electric field for a constant voltage EPD system.

The reason for the linear relationship seen in a number of EPD experiments can be attributed to an increase in value of the correction factor, f (Equation [4.6] in Section 4.4.1). The degree of coating run-off, which reduces the value of f, is inhibited by the stronger binding forces brought about by increased electric field strength generated by an increased applied EPD voltage. Agglomerated particles in suspension have a negative effect on deposition, as the loosely formed particle clusters may not be fully bound into an adherent coating as they are deposited onto either the bare deposition-electrode surface or on an already deposited EPD coating. These particle agglomerates are either pulled off as the coated substrate is removed from suspension due to the surface tension or by the excess water present in the coating that drains away due to gravity as the coating is dried. Agglomerates are more commonly present within unsonicated suspensions, as shown within Appendix A.2.2, and so well sonicated suspensions that contain a minimal amount of particle clustering did not generate the corresponding increase in f that was seen in suspensions where the resulting EPD coatings exhibit moderate levels of coating run-off.

16.1.3 Time as an EPD Variable

The two experiments described and discussed in Section 16.1.2 used applied voltage as an EPD variable. In this section, the effect of sonication level and PVA binder content on deposition was again studied, although deposition time was set as the principal variable. Experiments were carried out using the same preparation procedures and parameters as those described in Section 16.1.2.

Figure 16.10 shows the relationship between EPD deposition yield and EPD deposition time for suspensions subjected to different sonication periods during their preparation. As with the results in Section 16.1.2, where EPD from these suspensions was carried out at a number of different voltages, the use of two 50% (300 Watt) 5 minute periods produced the highest deposition yields from among the sonication procedures tried, as shown in Figure 16.10. The images of Figure 16.11 show that using 50% magnitude sonication cycles during pre-processing lead to improved coating uniformity at longer deposition times. The reason for this is explained in Section 16.1.2, and correlates with the improvement in deposition yield. Using an applied voltage of 20 V, the deposition rate was either constant, or decreased slightly with time. The trend line through the non-zero deposition time data extrapolates roughly back through the origin; thus, EPD can be seen to form adherent coatings almost immediately after the potential difference (i.e. constant voltage) was applied, at least according to the minute timescale employed.

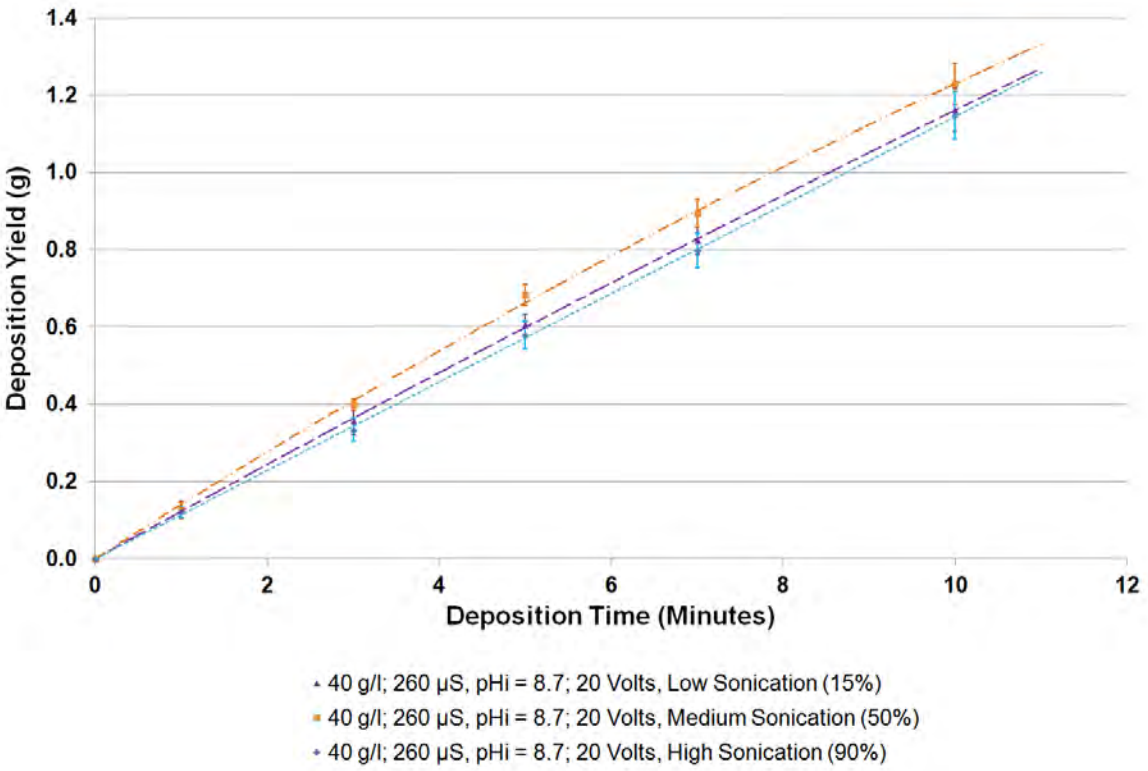

Figure 16.8 EPD deposition yield as a function of applied EPD deposition time and sonication intensity, from suspensions subjected to sonication at a given intensity for two 5 minutes periods. The sonication stage of the suspension formation procedure was altered to gauge its effect on both deposition yield and uniformity. Although the sonication levels of 0%, 15%, 30%, 50% and 90% of the operational maximum were used, this graph shows the three most frequently used levels. Sonication procedures were carried out on suspensions as described in Section 13.3.3.

The shapes of the curves in Figure 16.8 deviate from linear deposition yield versus deposition time behaviour due to a number of factors. The Hamaker equation [4.6] is a rate equation, and so any deviation from linear behaviour can be attributed to changes in one of the stated variables, or to physical changes in the suspension.

Section 3.2 looks at the electrophoresis stage of EPD, and gives a number of models that can be used to work out the particle mobility from the particle's zeta potential, with Equation [3.2] being the most simplified example.

$$\mu_e = \varepsilon \, \varepsilon_0 \, \zeta / \eta \qquad [3.2]$$

The dielectric constant of the dispersion medium (ε), dynamic viscosity of the dispersion medium (η) and zeta-potential (ζ) are expected to change only by a small amount, if at all, over the experimental timeframe, and so the mobility (μ or μ_e) can be taken to be a constant within the Hamaker equation [4.6]. The effective surface area of the electrode (S) can be thought of as increasing with time, most notably when greater coating thicknesses are produced on sharply angled substrates. Assuming uniformity of deposition, the formation of a 500 μm thick EPD coating on a Type 1 electrode substrate increases the EPD surface area from 28.4 cm^2 to 30.8 cm^2, which acts as a multiplication factor of 1.00024 within the Hamaker equation [4.6].

Such a change is, however, small compared to other changes; the most notable of these being the change in the electric field strength (E) in a constant voltage system. The electrical resistance of the EPD deposit that forms is typically higher than that of the suspension, and the growth of an insulating coating on the substrate would therefore reduce the strength of the electric field that can be generated by a given applied voltage. The concentration of solids in suspension (c) is known to deplete as particles both settle under gravity and become part of the EPD coating.

Use of the EPD deposition rate (based on final EPD deposition mass measurements) to describe the relationship between the EPD deposition yield and the EPD deposition time, is not fully accurate when applied to these experiments. It does not take into account those particles that do not become incorporated into the final weighed deposit. Particles were lost from the coated substrate as the electrode substrate was removed from suspension, due to surface tension. As the water content of the coating was driven off on drying, particles would be dragged from the surface by water, with such run-off effects described in Section 16.1.2.

The mass of these ‘lost’ particles could not be weighed and hence could not be factored in. At a constant voltage, it is possible for the correction factor, f, to change with time due to a number of different factors. The growth of an insulating coating reduces the strength of the electric field generated during EPD (at constant applied voltage) as time passes, and this would lead to the outer coating being less well bound to the underlying EPD layer. However, areas of reduced deposition or areas where suspension run-off has pulled particles from the coating are more prominent when the deposition time is lower, as shown in Figure 16.9(b) and (f). In this experiment, lower levels of coating run-off were observed as the deposition time was increased (for the time parameters tested).

In Section 16.1.5, non-optimised suspensions were studied, and the use of 10 minute deposition times led to lower yields than expected when Hamaker equation variables (excluding f) were taken into account. Stable dried coatings were formed when 5 minute deposition times were used, yet coating run-off was observed when longer deposition times were used. The change in the value of f with time can be attributed to two possible factors. The coating may have been pulled off due to the presence of more weakly adhering particles deposited the latter stages of the deposition period. Another reason can be related to the mechanical integrity of the deposit as its mass increased, as the deposited coating may become too large (in thickness and extent) to support itself on the substrate, when both subject to its own weight and the weight of the residual suspension retained by the coating as it was removed from the EPD suspension.

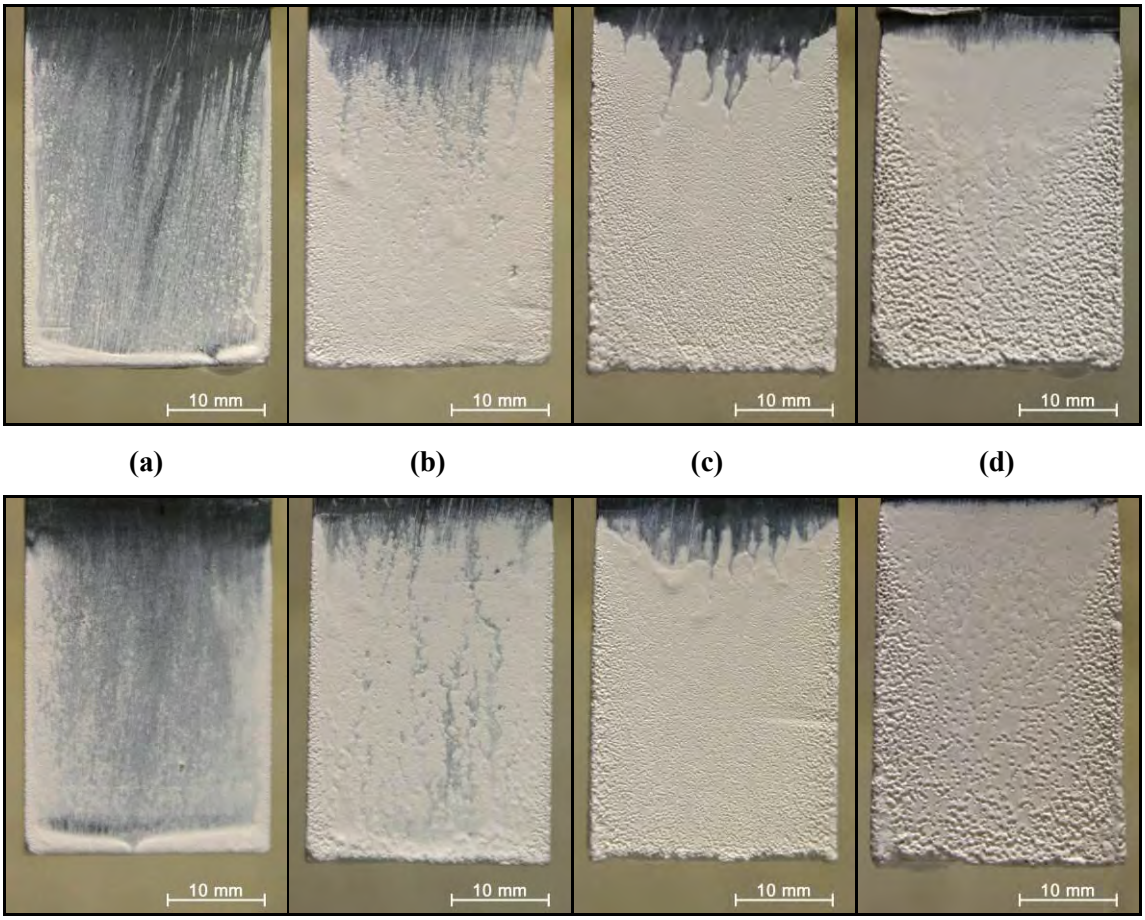

(a) **(b)** **(c)** **(d)**

(e) **(f)** **(g)** **(h)**

Figure 16.9 Digital SLR images showing examples of zircon EPD coatings on compressed graphite substrates. **(a) to (d)** are images of coatings from suspensions subjected to 15% magnitude sonication periods, whilst **(e) to (h)** are images of coatings from suspensions subjected to two 50% magnitude sonication periods. The following 20 volts EPD deposition times were applied: **(a) (e)** 1 minute; **(b) (f)** 3 minutes; **(c) (g)** 5 minutes; **(d) (h)** 10 minutes. Sonication procedures were carried out on suspensions as described in Section 13.3.3.

16.1.4 Use of Different Particle Grades

The grades of zircon used within this experiment are named in Section 12.2.2, and consist of two zircon grades produced by Helmut Kreutz and three grades produced by Dupré Minerals, all with differing particle size distributions. The suspension preparation followed a standard procedure, with the specifics given in Section 12.3. Two suspensions were tested for each zircon grade at their respective suspension concentrations.

The Helmut Kreutz 'Super FF' zircon powder showed the thickest deposition characteristics when the applied voltage was set to 20 V, as shown in Figure 16.10. This was the case when zircon concentrations of 60 $g.l^{-1}$ and 80 $g.l^{-1}$ were used, and there was a negligible deposition yield difference between the Helmut Kreutz 'Super' and 'Super FF' zircon grades at 20 $g.l^{-1}$ and 40 $g.l^{-1}$. Figure 16.10 also shows the significant difference in the deposition behaviour of Helmut Kreutz zircon powders versus the Dupré zircon powders, over the range of zircon suspension concentrations used in this study.

The EPD deposition yield did not increase linearly as the suspension concentration was increased for the Helmut Kreutz grades. The principal reason for this gradient reduction at higher concentrations can be attributed to the effect of weakening electric field strength with deposit growth, as described in Section 16.1.3. Whilst the EPD deposition time was a constant in these experiments, the use of higher suspension concentrations results in greater initial deposition rates according to equation [4.6]. Insulating coatings that significantly inhibit further deposition are therefore formed within the 5 minute deposition timeframe, leading to deposition mass values that 'tail-off' when higher solid-loadings are used because of the greater initial deposition rates.

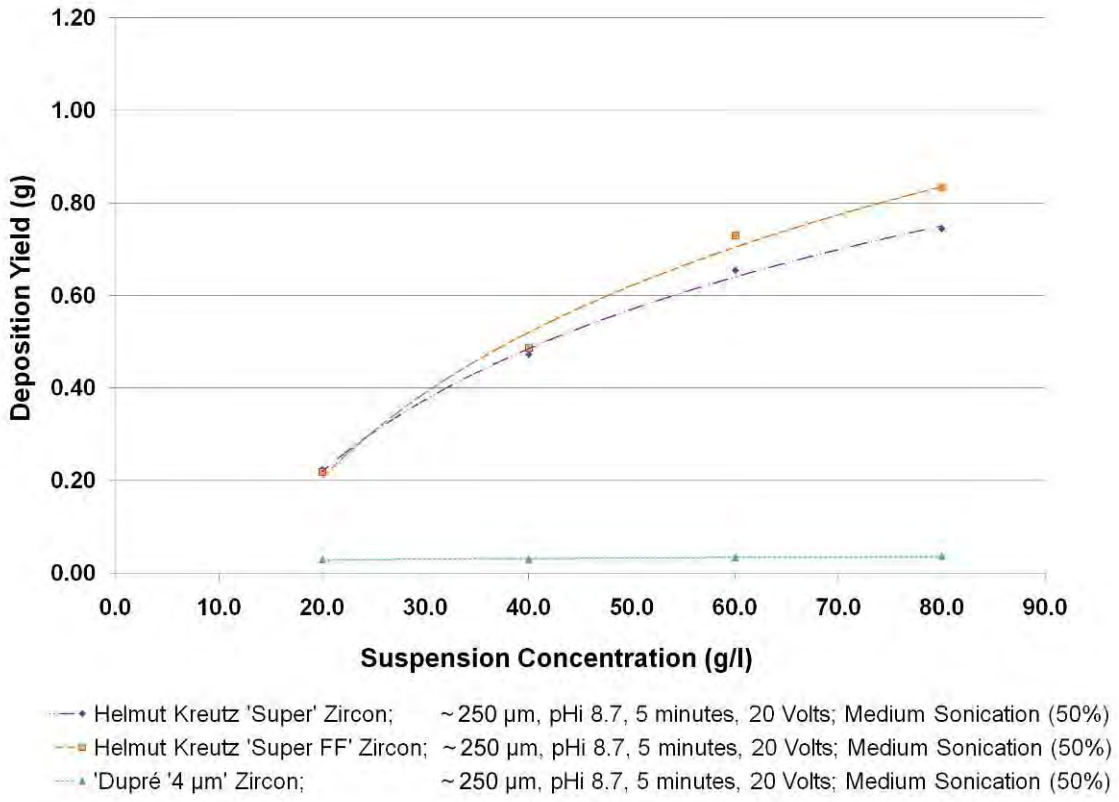

Figure 16.10 EPD deposition yield versus zircon suspension concentration, as a function of zircon powder grade. EPD was carried out on compressed graphite substrates at 20 volts, with a 5 minute deposition time. Although the Dupré 'A' (2 µm) and 'C' (12 µm) grades were also tested, they displayed similar yields to that achieved by the Dupré 'B' (4 µm) grade, and are therefore not shown on the graph.

As shown in Figure 16.10, when the Dupré Minerals zircon powder grades were suspended in aqueous solution for use within this set of EPD experiments (20 V applied EPD voltage, 5 minute EPD deposition time), average deposition yields were low and constant as the zircon concentration in suspension was increased. To see whether the yields achieved through dipping were comparable to the Dupré Minerals zircon EPD yields, graphite substrates were immersed into the zircon suspensions for a 5 minute time period with no EPD potential applied. All the sample substrates exhibited a negligible zircon coating mass, and so this suggests that the thin, weakly adhering Dupré Minerals zircon deposits were formed as a result of an EPD process.

From these experiments, the Dupré Minerals zircon EPD yield seems to be independent of zircon concentration, which suggests that the zircon coating thickness is limited for some reason. The Dupré coating could be highly insulating, and this would cause the deposition rate to quickly tail off to a very low level after a short deposition time. Alternatively, there may be limited inter-particle cohesion and particle-substrate adhesion in the coating, which limits its stability on the substrate. The latter reason is more viable, because the Dupré coatings were non-adherent. Particle clusters would fall back into the suspension as deposition substrates were removed from the liquid.

The presence of large particles or clusters in the Dupré grades may inhibit EPD coating cohesion and adhesion. Particle size analysis was therefore carried out on the zircon grades in Appendix A.2.2, to see whether the distributions were markedly different. As shown in Section 16.1.2 and Section 16.1.3, Helmut Kreutz zircon suspensions that were subjected to higher power ultrasonication during homogenisation produced higher EPD coating yields. Within particle sizing experiments, the use of higher sonication intensities led to a small shift in the distribution peaks towards smaller diameters. The use of smaller, unagglomerated particles therefore improves the uniformity and adherence of the resultant EPD coatings, under the testing conditions used.

The presence of larger agglomerated particles in the Zircon ‘B’ and ‘C’ grades would go to explain the poor performance of the Dupré zircon powders in EPD experiments. The size distribution of the Dupré Zircon ‘A’ (2 μm) grade, however, was very similar to the distribution of the Helmut Kreutz ‘Super’ grade, and so the poor performance of Zircon ‘A’ during EPD cannot be explained on the basis of its particle size distribution alone.

Another aspect that may have a bearing on coating stability relates to the charge and stability of the zircon particles in suspension. Zeta potential analysis was carried out on the Dupré ‘A’ grade and Helmut Kreutz ‘Super FF’ grade in Appendix D.2, for both Dolapix

CE64 dispersant free and dispersant-modified suspensions across the pH range. Zeta potential differences between zircon grades could account for discrepancies in EPD coating mass. Over the pH range used within EPD experiments (pH_i 7.5 – 10), the 'Super FF' grade zircon exhibited higher zeta potential magnitudes than the Dupré 'A' zircon grade. This difference is small, however, and for dispersant-free suspensions, the zeta potential of Dupré 'A' zircon at pH_i 9.5 was close to the zeta potential of Helmut Kreutz 'Super FF' zircon at pH_i 8.0.

In Section 16.1.5, adherent deposition was achieved from dispersant-modified 'Super FF' zircon suspensions across the alkaline pH range. No substantial EPD coating were produced by Dupré grade suspensions at any tested pH, even though dispersant-modified Dupré zircon 'A' suspensions at pH_i 9.5 and Helmut Kreutz 'Super FF' zircon suspensions at pH_i 7.8 possessed particles with similar zeta potentials. The Dupré grade's coating adherence issue cannot, therefore, be attributed to zeta potential differences between zircon grades.

The experimentally derived positions of the apparent PZC and isoelectric point (IEP) were compared in Section D.2. The IEP / PZC disparity was similar for both Dupré and Helmut Kreutz zircon grades, which means that the purity is similar. This tends to suggest that the explanation for the poor EPD performance of the Zircon 'A' powder lies in the particle surface chemistry, and perhaps even particle morphology, which may affect packing behaviour in the EPD coating.

16.1.5 Effect of varying pH

From zeta-potential analysis featured in Appendix D.2, it was deemed that cathodic EPD using Dolapix CE64-modified 'Super FF' and zircon 'A' suspensions would be most successful when suspensions possessed pH_i values between 7.5 and 11.0. Within the experiments of this section, the pH is defined as the pH value of dispersant-modified aqueous solution measured prior to the addition of zircon, which is known within the present work as

pH_i. The suspension formation procedure used is described in section 12.3 and 13.3.5. As modification of the pH to more alkaline levels would increase the solution conductivity beyond that of less alkaline solutions, a set dispersant concentration of 11.25 $mg.g^{-1}$ was used. Using the standard suspension formation procedure, the pH of the suspension was modified to the specific pH_i value, and then the inert conductivity solution was used to bring the solution conductivity to a value between 250 and 260 $\mu S.cm^{-1}$.

Figure 16.11 shows the change in EPD deposition yield with suspension pH_i for Dolapix CE64-modified 'Super FF' suspensions, where several different EPD set-up parameters were used. Although Dupré zircon 'A' was also tested, no strongly adherent deposits were formed from suspensions using this grade, regardless of pH_i. The EPD coatings and deposition yields that resulted from the zircon suspensions without polyelectrolyte addition are also not depicted, as no substantial deposits were formed during these experiments. The reason for this is discussed in Section 16.1.6. In addition to the graphical relationship presented here, photographic images of the most significant coatings achieved by polyelectrolyte-modified zircon suspensions at different pH_i values are displayed in Figure 16.12.

For the 5 minute period at 20 V, improved average deposition yields were evident as the suspension pH_i value was increased. Additionally, as shown in Figure 16.12 (a to d), an improvement in deposition characteristics can also be observed as the pH becomes more alkaline. For the 40 V EPD set-ups, the uniformity of the coating shows no improvement as the pH was increased from 8.7 to 10.2, as shown in Figure 16.12 (e to h), which was accompanied by an associated plateauing in the EPD deposition mass yield when suspensions with higher pH_i values were used.

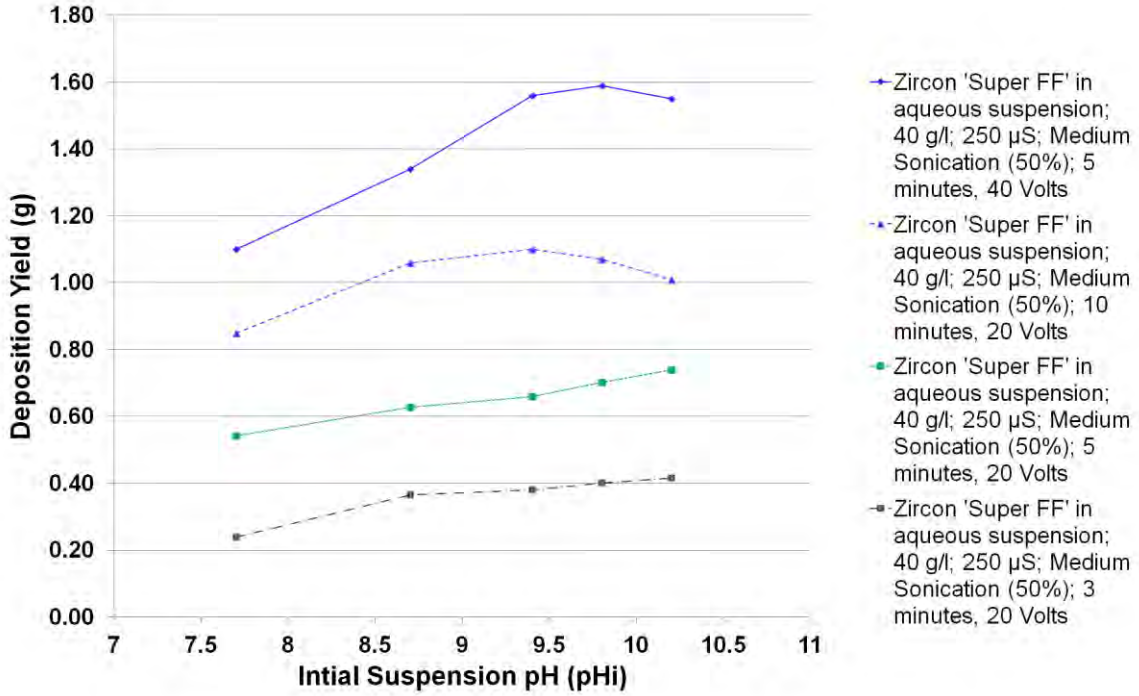

Figure 16.11 EPD deposition yield versus EPD suspension pH_i, as a function of EPD applied voltage and deposition period, for Dolapix CE64-modified 'Super FF' zircon suspensions with solution conductivities of 250 $\mu S.cm^{-1}$. Sonication periods at 50% magnitude for 5 minutes were used during homogenisation, as described in Section 13.3.3.

For suspensions with different pH_i values, the effect of deposition time on yield for 20 volt set-ups was also studied, and an example zircon coating from each set-up is shown in Figure 16.13. In Figure 16.11, it can be seen that there is a steady increase in deposition yield with pH_i for both the 20 V 5 minute and 20 V 3 minute EPD set-ups. Visual inspection of samples indicated that both thicker and more uniform deposition results from using suspensions with a higher pH_i; although, for the 3 minute deposition period, coating run-off was a yield-reducing problem throughout. For the 20 Volt 10 minute setting, however, there appears to be a peak in deposition yield at pH_i 9.4, and this is combined with a slight reduction in uniformity on visual inspection.

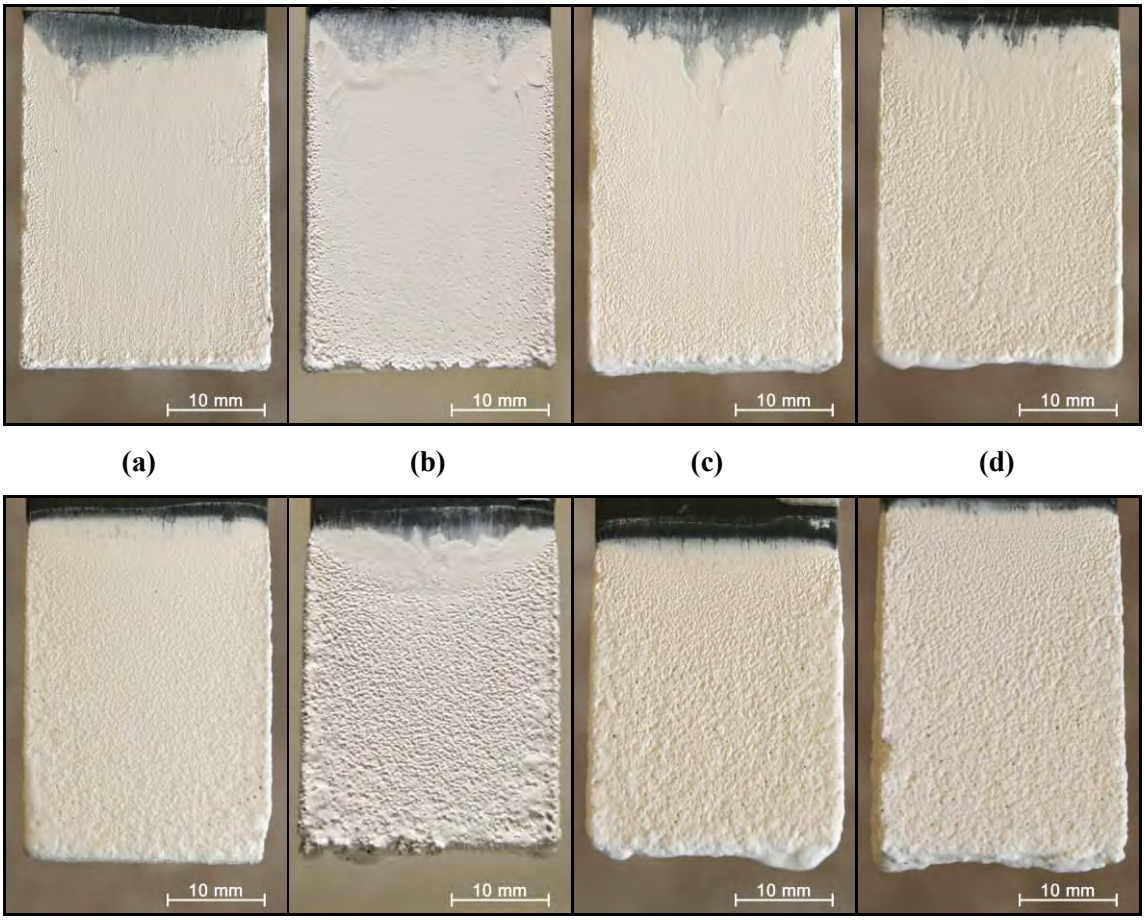

Figure 16.12 Digital SLR images showing examples of zircon EPD coatings on compressed graphite substrates. **(a) to (d)** show coatings from suspensions subjected to a 20 V, 5 minute EPD period, whilst **(e) to (h)** show coatings from suspensions subjected to a 40 V, 5 minute EPD period. All suspensions had a suspension conductivity of 250 $\mu S.cm^{-1}$ and a zircon concentration of 40 $g.l^{-1}$. The suspension pH_i values were: **(a) and (e)** pH_i = 7.8; **(b) and (f)** pH_i = 8.7; **(c) and (g)** pH_i = 9.6; **(d) and (h)** pH_i = 10.2.

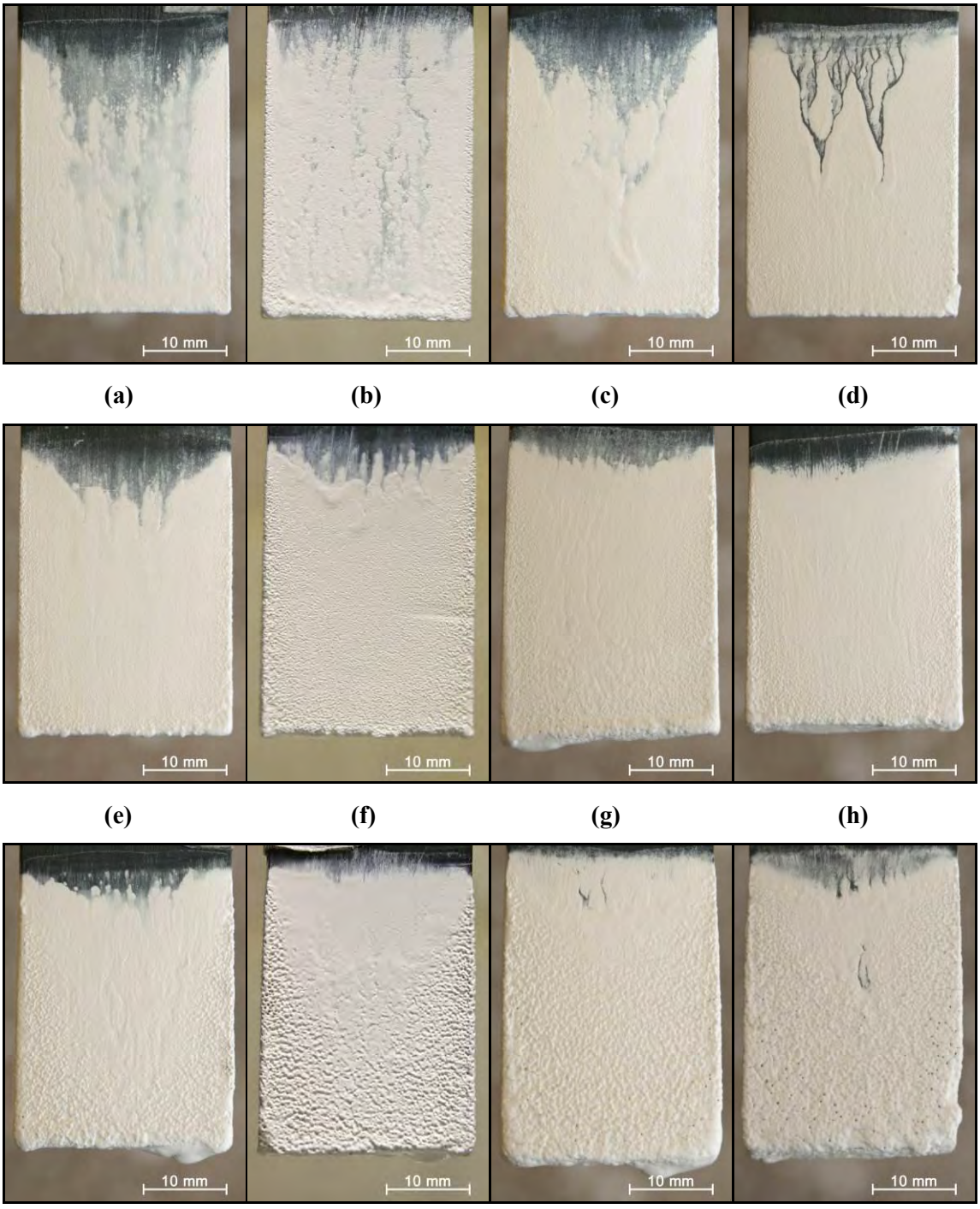

Figure 16.13 Digital SLR images showing examples of zircon EPD coatings on compressed graphite substrates. **(a) to (d)** show coatings from suspensions subjected to a 20 V, 3 minute EPD period, **(e) to (h)** show coatings from suspensions subjected to a 20 V, 5 minute EPD period, and **(i) to (l)** show coatings from suspensions subjected to a 20 V, 10 minute EPD period . All suspensions had a conductivity of 250 $\mu S.cm^{-1}$ and zircon concentration of 40 $g.l^{-1}$. The suspension pH_i values were: **(a), (e) and (i)** pH_i = 7.8; **(b), (f) and (j)** pH_i = 8.7; **(c), (g) and (k)** pH_i = 9.6; **(d), (h) and (l)** pH_i = 10.2.

Modifying the suspension pH alters the colloidal suspension in two principal ways. As stated in Appendix D.2.3. The zeta potential changes from a high positive value at a low pH, becomes zero at the IEP and changes to a large negative value at a high pH, and for the anodic electrophoretic deposition experiments studied here, we are concerned with the value of the zeta potential as it becomes more negative above the IEP. For dispersant modified suspensions, the particle's zeta potential values increase by a small degree as the pH is increased, as shown in the analysis of Appendix D.2.3. Higher particle zeta potentials lead to both better particle dispersion and increased particle mobility under the influence of an electric field. Additionally, as described in Section 4.2.5, modification to raise the pH to more alkaline levels also introduces a higher concentration of ions to the suspension, which reduces the thickness of the double layer (the Debye length (κ^{-1})). For this experiment however, the solution conductivity was kept constant for all suspensions, through the addition of NaCl inert conductivity solution.

For the 20 V, 10 minute EPD setups (and to a lesser extent, the 40 V, 5 minute setups) the use of high pH_i value suspensions led to a reduction in deposit binding strength, as discussed in section 16.1.3. The action of the TMAH base and the NaCl conductivity solution on the double-layer may, however, differ; and hence, each may compress the layer thickness and so destabilise the suspensions by differing degrees. If this is the case, and if TMAH in large concentration negatively affects the suspension dispersion stability, then counteracting influences of increased zeta potential and reduced stability with increasing pH must lead to optimised conditions occurring at moderate pH values within the studied pH range. Although only a small number of different pH_i value suspensions were studied in the alkaline pH region for this experiment, the best EPD deposition properties for the polyelectrolyte-modified zircon system occurred when the pH_i lay between 8.7 and 9.5.

16.1.6 Effect of Dispersant Content

The optimal concentration of Dolapix CE64 dispersant for 'Super FF' zircon suspension stability was obtained by carrying out sedimentation studies, as shown in Appendix D.3, and gave an optimal value between 5 and 10 $mg.g^{-1}$. In the suspension formation process for 40g/l zircon suspensions with a pH_i value of 8.7, the use of a these dispersant concentrations led to suspensions with solution conductivities between 90 and 170 $\mu S.cm^{-1}$. Within preliminary work, however, the use of higher dispersant concentrations led to better deposition characteristics, which can either be linked to improvements based on increasing the solution conductivity, or to additional effects that the dispersant may have on either the suspension or the resulting coating.

Within this experiment, using the method set out in Section 13.3.6, Dolapix CE64 dispersant modified 40 $g.l^{-1}$ 'Super FF' zircon suspensions were focussed upon, using dispersant concentrations between 0 and 22.5 $mg.g^{-1}$ (corresponding to solution conductivity values between 15 and 320 $\mu S.cm^{-1}$). Figure 16.14 shows the relationship between dispersant concentration and yield for the suspensions studied in this section. No deposition yields are shown when the suspension's dispersant concentration was less than ~ 4.5 $mg.g^{-1}$, as the coatings were not sufficiently bound to the substrate, and were pulled off by suspension surface tension as they were removed from the EPD bath.

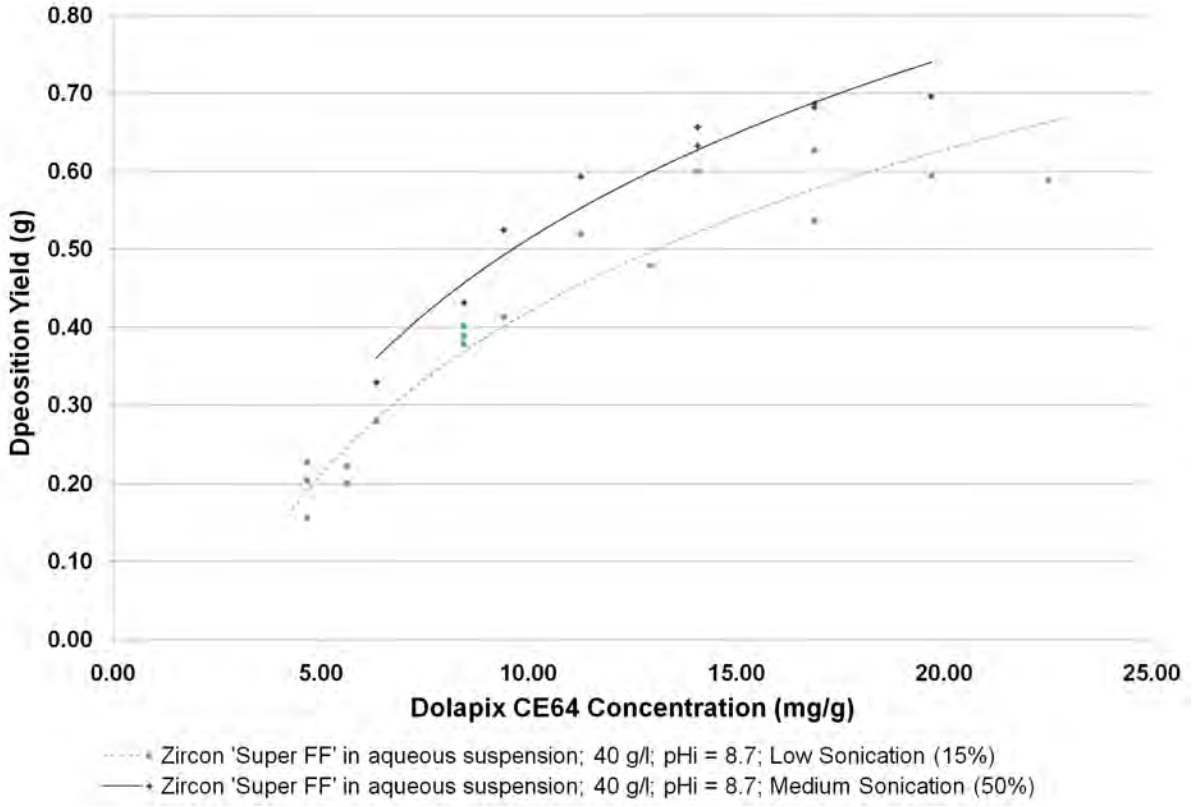

Figure 16.14 EPD deposition yield versus Dolapix CE64 concentration, as a function of sonication intensity during suspension homogenisation. All Dolapix CE64-modified suspensions used a 'Super FF' zircon concentration of 40 $g.l^{-1}$ at pH_i 8.7. The sonication procedure is described in Section 13.3.3.

From zeta potential analysis in Appendix D.2.3, the zeta potential of 'Super FF' zircon suspensions at a pH_i of 8.6 displayed an increase from 37 mV to 54 mV when the dispersant content is increased from 0 $mg.g^{-1}$ to 20 $mg.g^{-1}$. Using this information, it can be supposed that a threshold dispersant content exists in increasing the zeta potential to a high enough value to both stabilise the suspension and give the particles sufficient 'throwing power' to become part of an adherent coating.

The sole effect of increasing the zeta potential through dispersant addition would not be enough to explain deposition differences. According to Appendix D.2.3, a zeta potential magnitude of 50 – 55 mV was obtained for dispersant-free suspensions at pH_i 10.3 and dispersant modified suspensions at pH_i 8.6. In the work of Section 16.1.5, dispersant-free

zircon suspensions with pH_i values greater than 10 were studied alongside Dolapix CE64 dispersant modified zircon suspensions. For both suspension sets, a constant solution conductivity of 250 $\mu S.cm^{-1}$ was used, although no adherent deposition resulted from any of the dispersant-free suspensions.

The presence of Dolapix CE64 dispersant must therefore change the behaviour of zircon particles in a way beyond simply increasing its zeta potential magnitude through specific adsorption processes. In carrying out EPD experiments, it is clear that the transition between non-adherent deposition and adherent deposition is not governed solely by the magnitude of the particles' zeta potentials. The stability of particles in suspension is improved as a result of dispersant addition, as shown in Appendix D.3, when the settled depth and opacity gradient in unagitated dispersant modified and dispersant-free suspensions were compared. This could explain the lack of binding deposits in samples with low dispersant concentrations, as the presence of bridging flocculation, and hence particle clusters in the deposit, could reduce the coating stability.

As shown in Figure 16.14, the yield increases linearly with CE64 addition when the dispersant concentration is increased from 4 $mg.g^{-1}$ to 10 $mg.g^{-1}$. Above this level, the yield increases but at a reduced rate until a yield plateau region is reached at about 20 $mg.g^{-1}$. Examples of the zircon deposits achieved within this experiment are shown in Figure 16.15. Low levels of dispersant addition (5 $mg.g^{-1}$ to 8 $mg.g^{-1}$) resulted in medium levels of deposition build-up with noticeably thicker deposition in the 0.5 mm regions along plate edges.

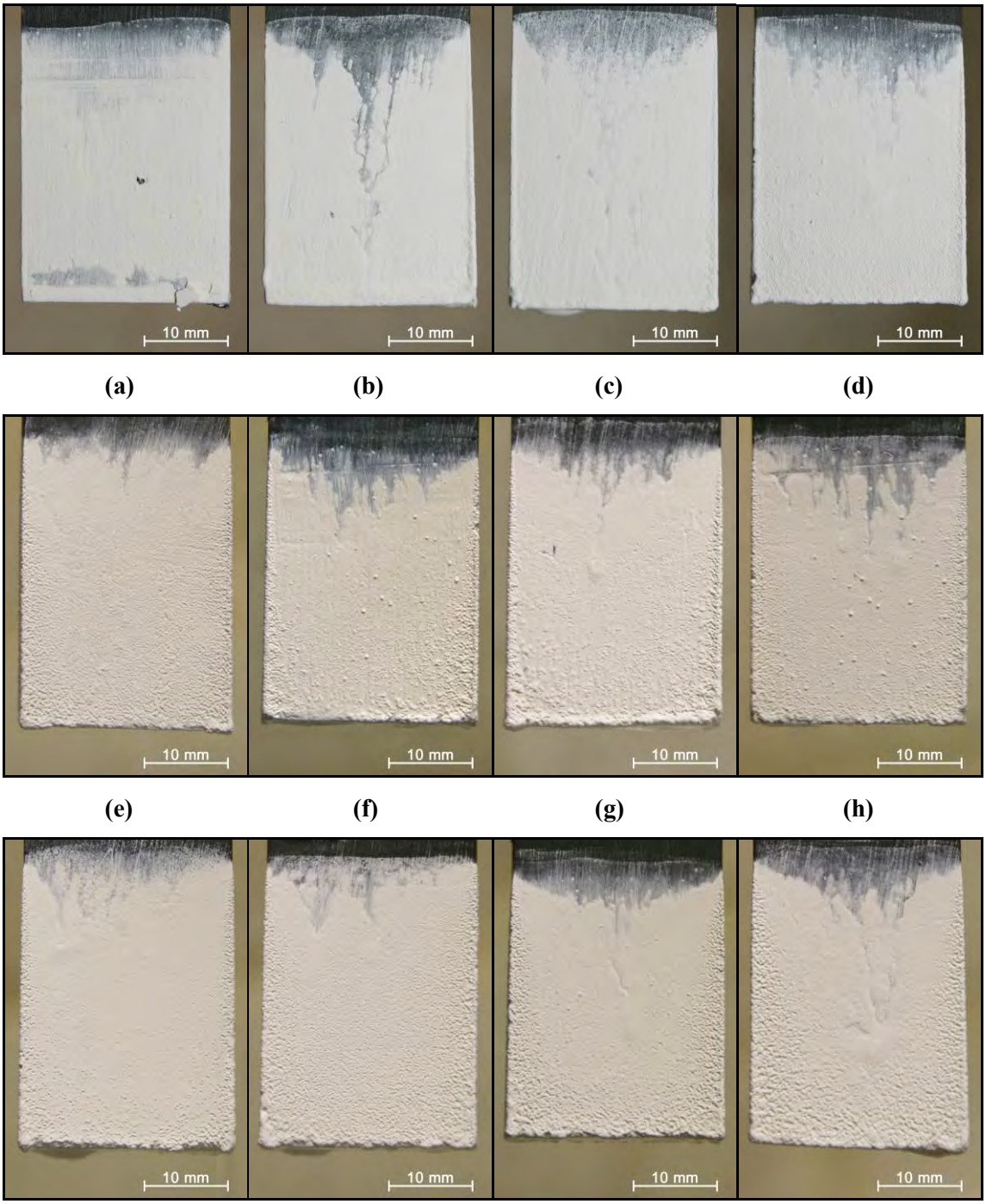

Figure 16.15 Digital SLR images showing examples of 'Super FF' zircon EPD on compressed graphite substrates. All suspensions had a zircon concentration of 40 $g.l^{-1}$ and pH_i of 8.7, and the EPD process used a 20 Volt, 5 minute set-up. Deposits where formed from suspensions with the following Dolapix CE64 dispersant concentrations; **(a)** 5.0 $mg.g^{-1}$ (85 $\mu S.cm^{-1}$), **(b)** 5.6 $mg.g^{-1}$ (95 $\mu S.cm^{-1}$), **(c)** 6.5 $mg.g^{-1}$ (120 $\mu S.cm^{-1}$), **(d)** 8.4 $mg.g^{-1}$ (150 $\mu S.cm^{-1}$), **(e)** 8.4 $mg.g^{-1}$ (150 $\mu S.cm^{-1}$), **(f)** 9.4 $mg.g^{-1}$ (165 $\mu S.cm^{-1}$), **(g)** 11.3 $mg.g^{-1}$ (180 $\mu S.cm^{-1}$), **(h)** 12.9 $mg.g^{-1}$ (205 $\mu S.cm^{-1}$), **(i)** 14.1 $mg.g^{-1}$ (240 $\mu S.cm^{-1}$), **(j)** 16.9 $mg.g^{-1}$ (270 $\mu S.cm^{-1}$), **(k)** 19.6 $mg.g^{-1}$ (290 $\mu S.cm^{-1}$), **(l)** 22.5 $mg.g^{-1}$ (320 $\mu S.cm^{-1}$).

At higher dispersant levels (8 $mg.g^{-1}$ to 13 $mg.g^{-1}$), the edge thickening effect became less distinct as the coating on the plate surfaces become more uniform, due to a reduction in coating run-off effects. The most uniform coatings resulted from suspensions with dispersant contents between 14 and 17 $mg.g^{-1}$, the level of run-off was minimised due to increased binding strengths. When the dispersant level was increased beyond this, deposition run-off again became a problem, as an increased rate of gas formation was observed during the EPD cycle, which either weakened the coating being formed or led to problems as the coated substrate was removed from suspension. Reasons for this are discussed in Section 16.1.7.

16.1.7 Effect of Suspension Conductivity

As described in Section 16.1.6, the zircon coating yield increases with dispersant concentration until a plateau region is formed when the Dolapix CE64 concentration reaches 19.6 $mg.g^{-1}$ (which corresponds to a solution conductivity of 290 $\mu S.cm^{-1}$ within those experiments). The experiments of this section were carried out to see whether this increase was due to the presence of increased dispersant levels, or was as a result of increased solution conductivity. The compositions of the suspensions used within these experiments are set out in Section 13.3.7.

The relationship between deposition yield and the solution conductivity is shown in Figure 16.16, and the EPD yields from dispersant modified suspensions are not improved by an increase in solution conductivity beyond that already imparted by the Dolapix CE64 and TMAH pH modifier. For both CE64 concentrations tested, a yield plateau region was formed when the conductivity is increased, although coating degradation began to occur when suspensions were used with solution conductivities above 350 $\mu S.cm^{-1}$. This was shown by a reduction in yield values in Figure 16.16, and in the photographs of deposition shown in

Figure 16.17, a reduction in coating uniformity could be observed when dispersant-modified suspensions with solution conductivities greater than 250 - 330 $\mu S.cm^{-1}$ were used. For these samples, coating pull-off occurred as the substrates were removed from suspension.

For the Dolapix CE64 dispersant-free suspensions shown in Figure 16.17(g – i), no yield improvement was observed as the solution conductivity of the suspensions was increased, although slight improvements were observed when the coated substrate is slowly removed from the EPD bath, as shown in Figure 16.17(g).

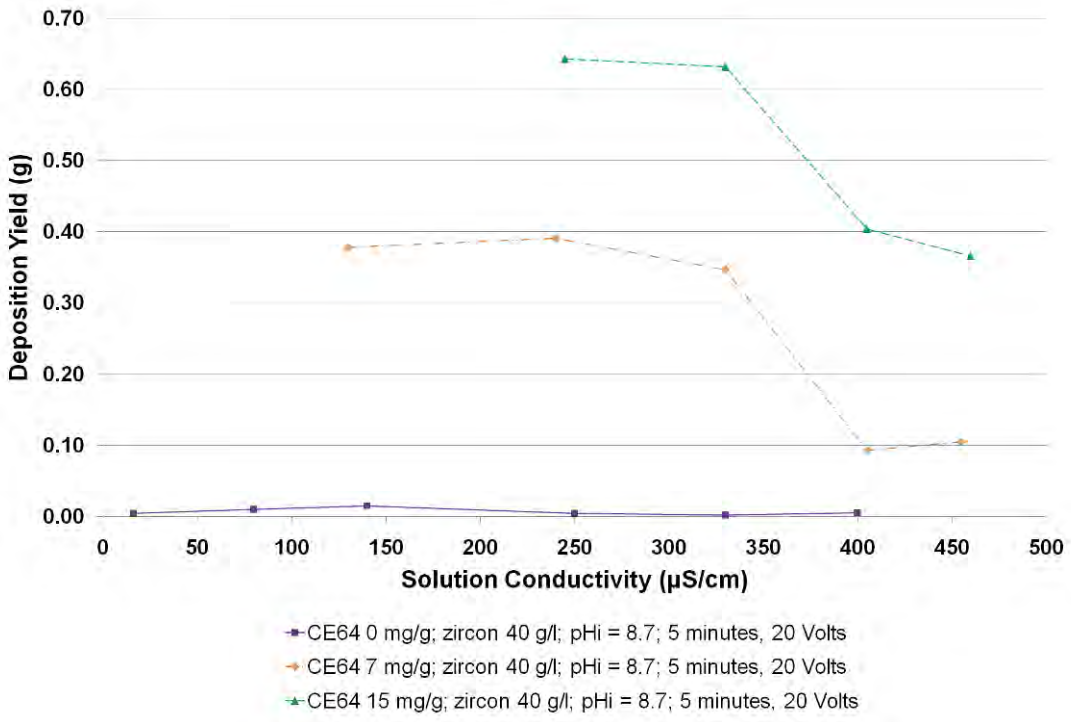

Figure 16.16 The relationship between solution conductivity and deposition yield for three Dolapix CE64 concentrations. All suspensions used a 'Super FF' zircon concentration of 40 $g.l^{-1}$ at pH_i 8.7. All samples underwent 20 V, 5 minute EPD cycles.

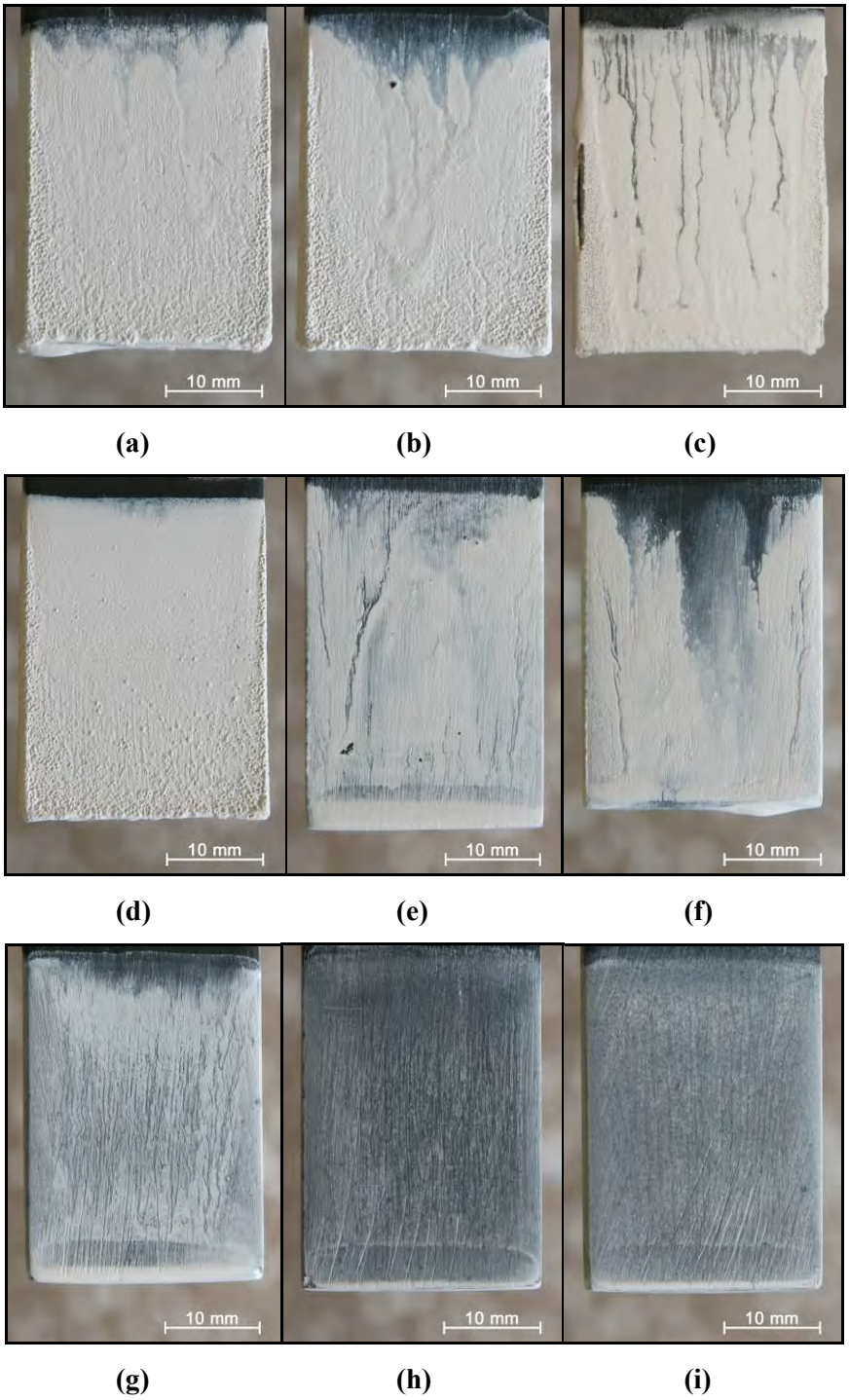

Figure 16.17 Digital SLR Images showing examples of 'Super FF' zircon EPD coatings on compressed graphite substrates. All suspensions had a zircon concentration of 40 $g.l^{-1}$ and pH_i of 8.7, and the EPD process used a 20 Volt, 5 minute set-up. Deposits where formed from suspensions with the following Dolapix CE64 dispersant concentrations; **(a)(b)(c)** 15.0 $mg.g^{-1}$; **(d)(e)(f)** 7.5 $mg.g^{-1}$; **(g)(h)(i)** 0.0 $mg.g^{-1}$. Suspensions were also augmented to possess the following solution conductivities; **(a)** 245 $\mu S.cm^{-1}$, **(b)** 330 $\mu S.cm^{-1}$, **(c)** 405 $\mu S.cm^{-1}$, **(d)** 240 $\mu S.cm^{-1}$, **(e)** 405 $\mu S.cm^{-1}$, **(f)** 455 $\mu S.cm^{-1}$, **(g)** 140 $\mu S.cm^{-1}$, **(h)** 250 $\mu S.cm^{-1}$, **(i)** 400 $\mu S.cm^{-1}$.

According to Section 4.2.5, the solution conductivity must lie within a band of values for EPD to successfully occur. For suspension stability, the conductivity needs to be low, as otherwise, the large number of solution ions present in solution compress the double layer of each particle, which leads to agglomeration and an open deposited structure. Within EPD set-ups specifically, the large number of free ions in solution (indicated by high solution conductivity values) act as the main current carrier when an electric field is applied, which reduces the electrophoretic mobility of the particles. The reduced 'throwing power' of the particles, in addition to the increased likelihood of particle cluster formation, would lead to an EPD coating that is more unstable, and therefore prone to run-off effects. The action of these mechanisms is confirmed by the experimental findings, both in the current section and in section 16.1.6.

Ferrari and Moreno (1997) described how EPD would only successfully occur for an aqueous alumina system when the solution conductivity lay within a specific range. In the present work, a solution conductivity upper band is observed, although the presence of a lower band cannot be ascertained as deposition would not successfully occur without the presence of an anionic dispersant, which itself increases the solution conductivity. The solution conductivity band for dispersant-free suspensions, does not, however exist for the grades of zircon studied in the alkaline pH range.

Increased EPD coating yields were achieved when the dispersant content was increased beyond the optimum level of 5 – 10 mg/g, and this can be attributed to the effect of the Dolapix CE64 dispersant itself, as solely increasing the solution conductivity led to no discernable yield improvement. There are a number of possible reasons for this behaviour.

The optimum dispersant concentration used was based on the results of sedimentation experiments. As described in Appendix D.3.1, methods that derive the

optimum dispersant concentration from stability measurements take into account both the polyelectrolyte's steric and electrostatic stabilising mechanisms. More accurate measurements would need to be carried out, to obtain a more accurate figure for the optimum dispersant concentration in suspension.

The presence of excess dispersant in solution may work as a polymeric binder that acts to improve the strength and uniformity of the zircon coating on the substrate. Increasing the presence of 'excess' dispersant is solution would improve deposition characteristics until destabilisation occurs due to the negative effects associated with high solution conductivities, as described in 4.2.5. This supposition can be confirmed by carrying out additional zeta potential experiments to gain a value for the optimum dispersant content that is related solely to the electrostatic stabilising mechanisms, by assessing when the zircon zeta-potential improvement with dispersant addition reaches a plateau. If this correlates to value given in improved settling experiments, then the presence of excess dispersant in solution must have a beneficial effect on the coating yield.

16.1.8 Use of Different Suspension Concentrations

The use of different suspension concentrations was additionally glimpsed upon in the experiments of Section 16.1.4, when different zircon grades were used within EPD. Most of the EPD experiments in this Chapter use zircon suspension concentrations of 40 g/l. EPD coating thicknesses comparable to those achieved by investment casting slurry primary coats were achieved on compressed graphite plates using 40 V 5 minute cycle parameters.

For substrates with lower electrical conductivities, such as carbon black-filled waxes and graphite-filled waxes, these suspensions and set-up criteria would not lead to coatings that bind to the substrate with sufficient strength to support their own weight. According to the

Hamaker equation [4.6], several suspension and set-up parameters can be altered to counter the effect of low substrate conductivity.

The suspension concentration (c) is one such parameter, although in increasing this value, the concentration of Dolapix CE64 dispersant must too increase. This anionic dispersant has the strongest solution conductivity modifying effect of all solution additives within this study, and so an extra variable is created. The solution therefore, was to create suspensions with increased particle concentration with a range of Dolapix CE64 dispersant concentrations and solution conductivity values. In this way, the effect of zircon concentration can be assessed, by taking into consideration both parameters. The experimental method used within this section follows the procedure set out in Section 13.3.8.

Figure 16.18 shows the effect of Dolapix Ce64 concentration on deposition yield for suspensions with zircon concentrations of 40, 80 and 120 $g.l^{-1}$ (3.85, 7.70 and 11.55 wt%). The dispersant content range for each suspension concentration differs as non-uniform anomalous coating yields resulted when parameters outside those shown were used. Increasing the dispersant concentration to beyond ~ 15 $mg.g^{-1}$ for the 80 $g.l^{-1}$ zircon suspensions and ~ 10 $mg.g^{-1}$ for the 120 $g.l^{-1}$ zircon suspensions increased the solution conductivity to a level when 'frothing' gas formation at the deposition electrode destabilised any coating there. For the samples where the zircon concentration was set to 40 $g.l^{-1}$, there was insufficient binding strength to produce adherent coatings when the dispersant concentration was less than ~ 7.5 $mg.g^{-1}$, which corresponds to a solution conductivity of 100 $\mu S.cm^{-1}$. When the EPD voltage is set to 20 V and to 40 V, all suspension concentrations display increased yields as the dispersant concentration is increased, within the experimental range of each.

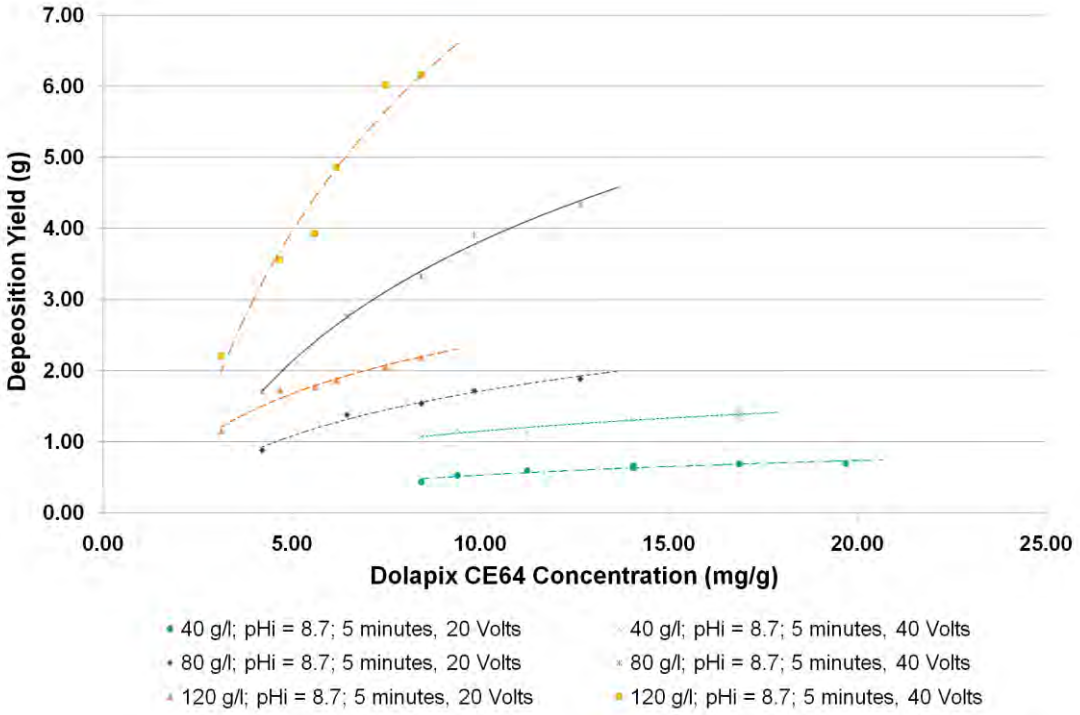

Figure 16.18 EPD deposition yield versus Dolapix CE64 concentration, as a function of zircon concentration in suspension or applied voltage. All 'Super FF' zircon suspensions had a pH_i of 8.7, and underwent 50% magnitude sonication cycles during homogenisation, as described in Section 13.3.3.

Figure 16.19 shows the same data displayed in Figure 16.18, but measures deposition yield against solution conductivity. When the dispersant concentration is too low, EPD coatings do not form with adequate strength and uniformity to maintain their integrity on removal from suspension. As the modifiers that contribute to conductivity in this experiment are TMAH (pH modifier) and Dolapix CE64 (dispersant), solutions that produce uniform coatings have to possess a certain level of conductivity. As described above and in Section 16.1.7, when solution conductivity levels were too high, coating stability also became an issue, and here, problems began when the solution conductivity was greater than 400 $\mu S.cm^{-1}$.

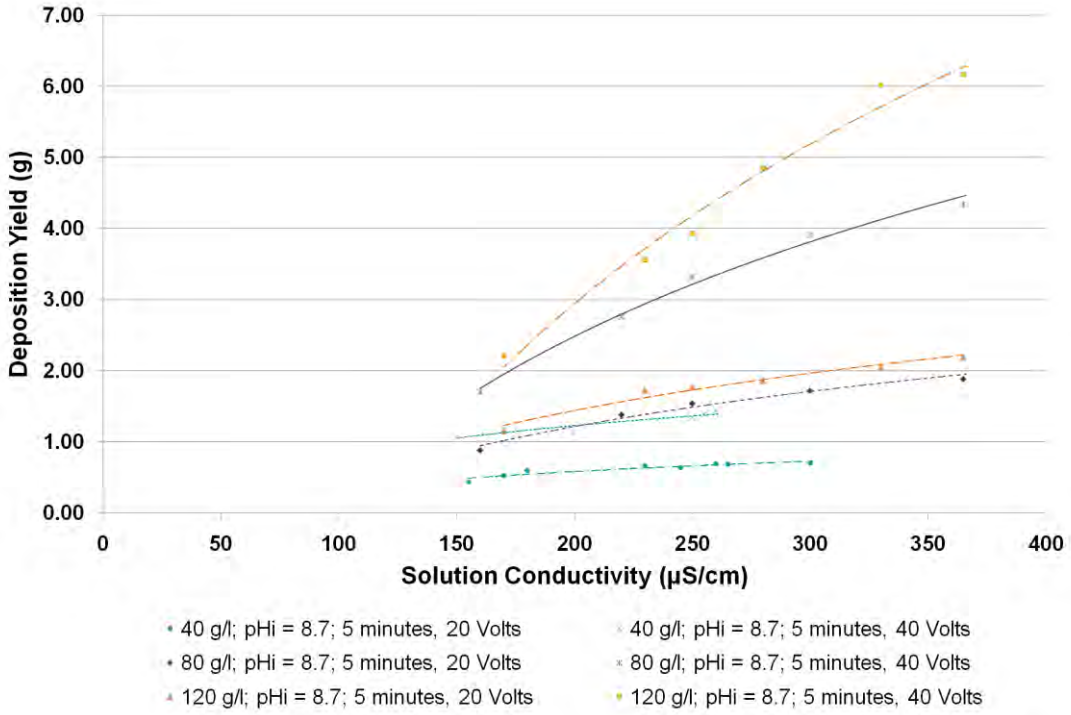

Figure 16.19 EPD deposition yield versus Dolapix CE64 augmented solution conductivity, as a function of zircon concentration in suspension or applied voltage. All 'Super FF' zircon suspensions had a pH_i of 8.7, and underwent 50% magnitude sonication cycles during homogenisation, as described in Section 13.3.3.

Using this data, it is possible to see the relationship between zircon concentration in suspension (c) and deposition yield when the conductivity is fixed (with variable dispersant concentration) and when the dispersant concentration is fixed (with variable conductivity). Figure 16.20 shows the change in deposition yield on compressed graphite plate electrodes at 20 V and 40 V for variable zircon content suspensions with a fixed Dolapix CE64 dispersant concentration of 8.4 $mg.g^{-1}$. In Figure 16.21, the relationship between zircon suspension concentration and yield is plotted for suspensions with a fixed a fixed conductivity of 250 $\mu S.cm^{-1}$. In addition to sample yields being plotted, additional points were marked out in each graph, which correspond to expected yield values, given by best-fit curves in Figure 16.18 and Figure 16.19 respectively.

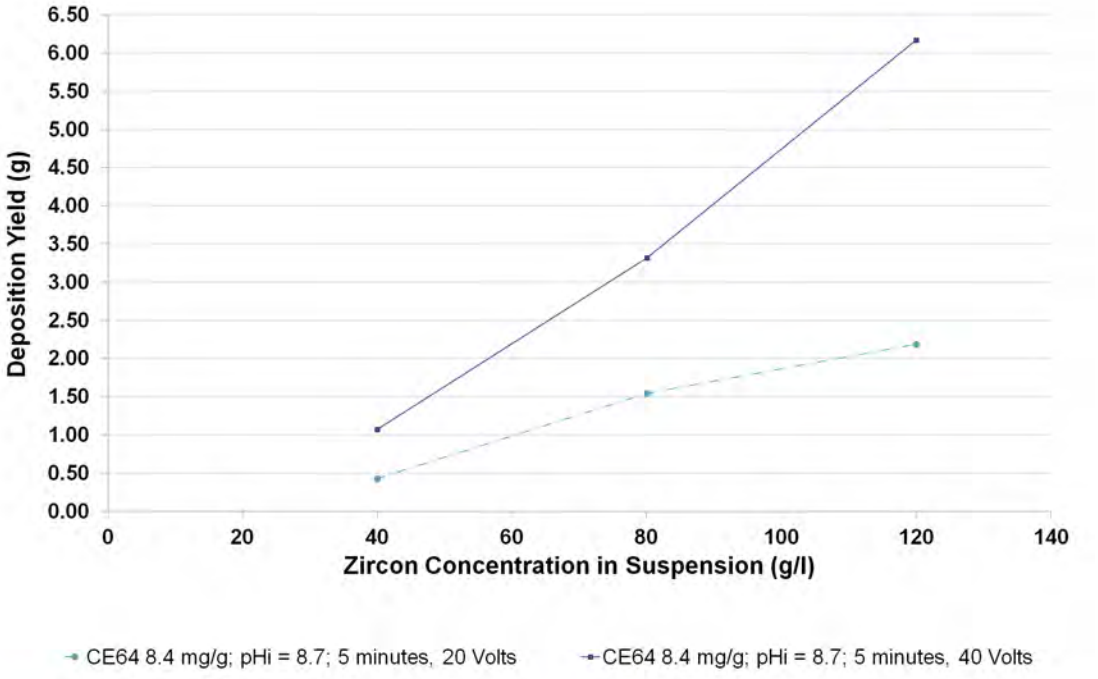

Figure 16.20 EPD deposition yield versus zircon concentration in suspension, as a function of applied voltage. All 'Super FF' zircon suspensions had a pH_i of 8.7, Dolapix CE64 concentration of 8.4 mg/g and underwent 50% magnitude sonication cycles during homogenisation, as described in Section 13.3.3.

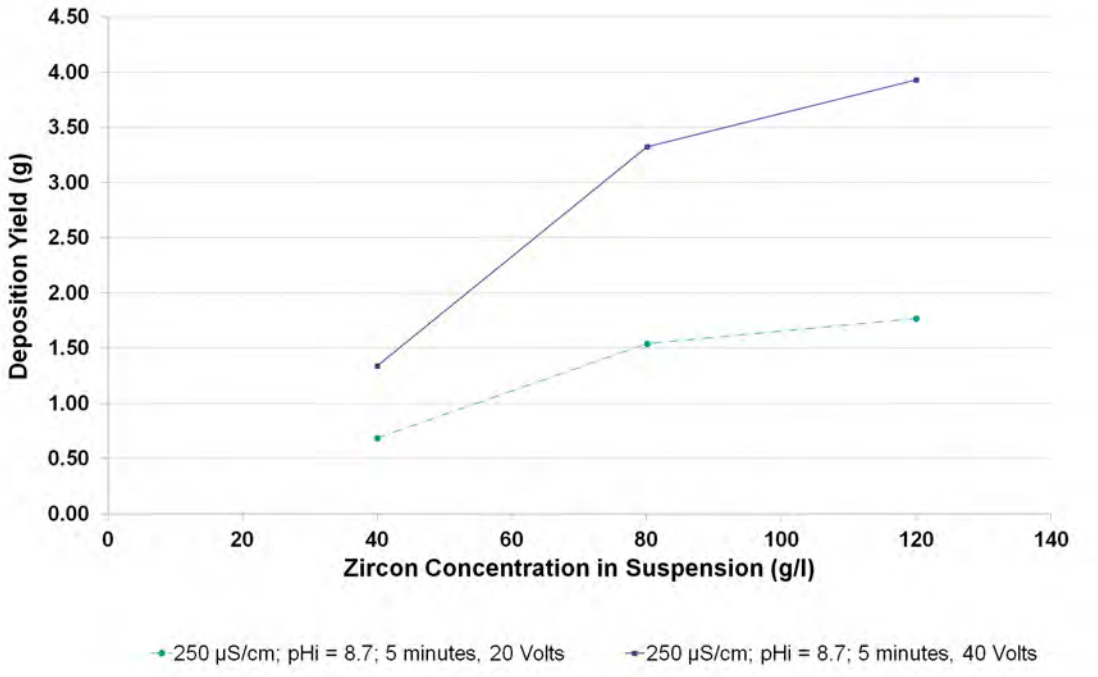

Figure 16.21 EPD deposition yield versus zircon concentration in suspension, as a function of applied voltage. All 'Super FF' zircon suspensions had a pH_i of 8.7, solution conductivity of 250 $\mu S.cm^{-1}$ and underwent 50% magnitude sonication cycles during homogenisation, as described in Section 13.3.3.

For both 20V and 40V set-up parameters, one can see that increasing zircon content leads to an increase in deposition yield, although this relationship is more linear in Figure 16.20 than in Figure 16.21. The reason for this can be explained by looking at how conductivity and dispersant convention variables change within each graph.

As described in Section 16.1.7, increasing the solution conductivity using a non-dispersing species (like an inert polyelectrolyte) had a negligible effect on yield up to the point where the solution conductivity was too high for EPD. The yield improvement associated with increasing the conductivity using the Dolapix CE64 dispersant is far clearer, as shown in Section 16.1.6. Within Figure 16.21, the Dolapix CE64 dispersant concentration in suspension decreases from 16.4 $mg.g^{-1}$ to 5.6 $mg.g^{-1}$ as the zircon content is increased. For the experimental range shown, reducing the dispersant concentration leads to lower yields, and the effect of keeping the solution conductivity constant has no substantial yield improving effect. In Figure 16.20, the solution conductivity increases from 155 to 365 $\mu S.cm^{-1}$ when the zircon content is increased. The effect of increasing the solution conductivity and the effect of keeping the dispersant concentration constant have no beneficial or detrimental effect on yield, which accounts for the curves' constant gradient.

In the Hamaker equation [6.4], the relationship between zircon concentration (c) and deposition rate is a linear one, and so, for a fixed deposition time, the yield should linearly increase if all other variables are constant. When an applied voltage of 20 V is used, a non-linear relationship is observed both in Figure 16.20 and in Figure 16.21. This is primarily due to the changing rate at which the electric field strength in solution is weakened, as described in Sections 16.1.2 and 16.1.3. The EPD deposition rate would initially be higher when suspensions with higher zircon contents are used. The formation of a thicker insulating coating decreases the electric field strength (and therefore deposition rate) to a greater degree for the remainder of the fixed deposition time.

Figure 16.22 visually shows the effect of dispersant concentration on EPD deposition behaviour from 120 $g.l^{-1}$ zircon suspensions, for deposition using 20 V and 40 V EPD set-ups. For the samples that were used in a 20 volt set-up specifically, increasing the dispersant concentration increases the deposition thickness on the central plate regions, which is indicative of increased binding strength. This may account for the improved yields shown in Figure 16.18.

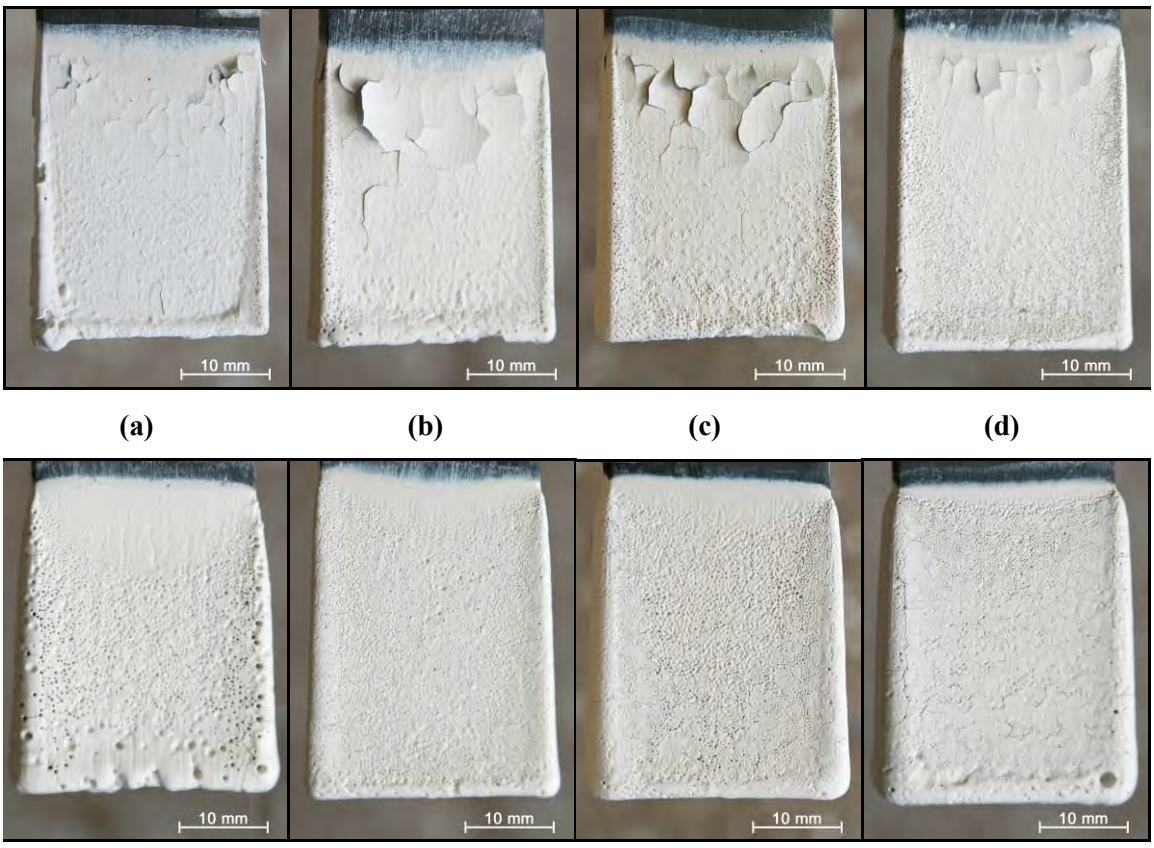

Figure 16.22 Digital SLR images showing examples of zircon EPD coatings on compressed graphite substrates. Images **(a)** and **(e)** are from suspensions with a dispersant concentration of 3.1 $mg.g^{-1}$ (170 $\mu S.cm^{-1}$), **(b)** and **(f)** are from suspensions with a dispersant concentration of 4.7 $mg.g^{-1}$ (230 $\mu S.cm^{-1}$), **(c)** and **(g)** are from suspensions with a dispersant concentration of 6.2 $mg.g^{-1}$ (280 $\mu S.cm^{-1}$), **(d)** and **(h)** are from suspensions with a dispersant concentration of 7.5 $mg.g^{-1}$ (330 $\mu S.cm^{-1}$). All suspensions had a zircon suspension concentration of 120 $g.l^{-1}$ and pH_i of 8.7. The following EPD set-up parameters applied: **(a - d)** 20 Volts, 5 minutes; **(e - h)** 40 Volts, 5 minutes.

Deposition cracking was, however, an issue for many of the samples formed from high concentration zircon suspensions due to the presence of drying stresses. For the 40 volt samples, high porosity was observed when the dispersant content was low, as shown in Figure 16.22(e), for reasons that cannot be verified without further study. For the other samples, coating growth, and especially thickness uniformity in the vertical plane, increases with dispersant content. Figure 16.23 shows examples of deposition from 40 $g.l^{-1}$ and 80 $g.l^{-1}$ zircon suspensions, and shows how the deposition yield increases with zircon concentration. The suspensions had a fixed solution conductivity of 250 $\mu S.cm^{-1}$, and show us that, although the coating thicknesses increases, the characteristics (void formation etc.) remain comparable.

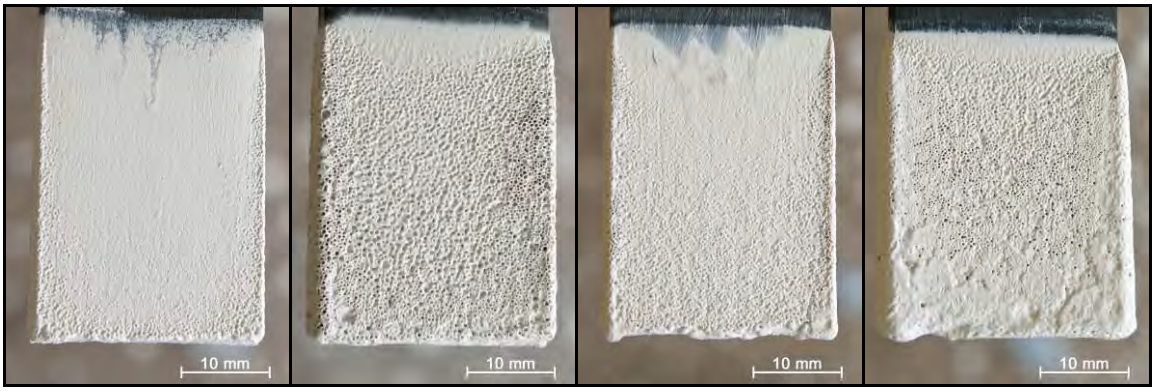

(a) **(b)** **(c)** **(d)**

Figure 16.23 Digital SLR images showing examples of zircon EPD coatings on compressed graphite substrates. Images **(a – b)** are from suspensions with 40$g.l^{-1}$ zircon concentration, whilst **(c – d)** are from suspensions with 80$g.l^{-1}$ zircon concentration. All suspensions had a suspension conductivity of 250 $\mu S.cm^{-1}$ and pH_i of 8.7. The following EPD set-up parameters apply: **(a) and (c)** 20 Volts, 5 minutes; **(b) and (d)** 40 Volts, 5 minutes.

16.2 Variables Studied within EPD experiments on Conducting Wax

16.2.1 Deposition Behaviour on Conductive Wax Electrode Substrates

Information corresponding to the optimisation of suspensions and EPD set-ups for deposition on compressed graphite electrode substrates was used to tailor the same suspensions for use with conductive wax substrate electrodes. There are a number of principal differences between these two classes of deposition electrode material. As the conductivity of the substrate is lower, the electric field produced is far weaker for a given applied voltage. This is similar in nature to the masking effect observed within the EPD work on compressed graphite in Section 16.1.3 and 16.1.8, when the growth of an insulating coating reduces the electric field strength, which in turn lowers the deposition rate. For moderately conducting substrates, the electric field strength is reduced at t = 0, and so for a given voltage and suspension type, the maximum achievable coating thickness would be is lower.

Another issue to take into account is the effect of conductivity variability within electrode substrates. Compressed graphite has a low resistivity, which was measured to be uniform in all orientations. In a composite system where particles form conductive pathways through an insulating matrix, local changes in conductivity are likely, and may result in uneven levels of deposition before complicating factors like electric field intensification at substrate edges are taken into account. The standard deviation of measurements within the four-point probe experiments of Section 15.1.2 helps to illustrate the range of conductivities found within ‘homogenous’ composite samples. The surface texture of the material is an additional factor that may affect the binding strength of the coating on the substrate. Compressed graphite electrodes were abraded and cleaned prior to being used within EPD experiments, whilst the conductive wax surfaces were treated with Trisol 60 Plus to etch and create a surface texture suitable for investment primary dip coating.

Two specific melt-out compositions were chosen for use in EPD experiments, and were chosen as a compromise had to be made between conductivity and formability. 16 vol% graphite-filled A7-7808 and 15.9 vol% carbon black-filled A7-7808 waxes were used, and according to four point probe measurements, had resistivities of ~ 3 kΩ.cm and ~ 0.9 kΩ.cm respectively. An aluminium electrode tab was immersed into a number of conductive wax plate substrates, as described in Section 13.1, to see whether the presence of an electrode tab would improve deposition on the conductive wax substrates, by increasing the strength of the electric field produced.

A 40 $g.l^{-1}$ 'Super FF' zircon suspension, containing 15 $mg.g^{-1}$ Dolapix CE64 dispersant with a solution conductivity of 250 $\mu S.cm^{-1}$ and a pH_i of 8.7, was a representative suspension used within EPD coating optimisation experiments on compressed graphite. When conductive wax electrodes were coated using a 20 V 5 minute EPD set-up, both the zircon coating thickness and its uniformity were poor. Several variables present in the Hamaker Equation [4.6] therefore had to be altered to improve the deposition rate on melt-out electrodes. In raising the applied voltage from 20 V to 40 V, the electric field strength was increased. Examples of deposition on graphite and carbon black-filled substrates are shown in Figure 16.24, and compared with the coatings formed on compressed graphite substrates using a equivalent zircon suspension. Despite the voltage increase, the use of conductive wax substrates led to poor zircon coatings, from the point of view of both uniformity and thickness. Within work involving compressed graphite substrates, the level of electrolysis gas production was large, and as shown in Figure 16.24(e), led to coatings that contained a high density of voids and pits. Although the uniformity of zircon coatings on conducting wax substrates was poor using these suspension parameters, gas bubble formation was only observed in coatings formed on carbon black wax samples that contained an aluminium electrode tab, for reasons given later on in the Section.

To improve deposition behaviour on conducting waxes, one possible option was to increase the applied voltage of the system so that the resultant electric field matched the one formed when a 20 V compressed graphite substrate set-up was used. However, the effect of substrate conductivity inhomogeneity due to the particle-matrix composition would lead to an exemplification of coating irregularities seen in Figure 16.24(d).

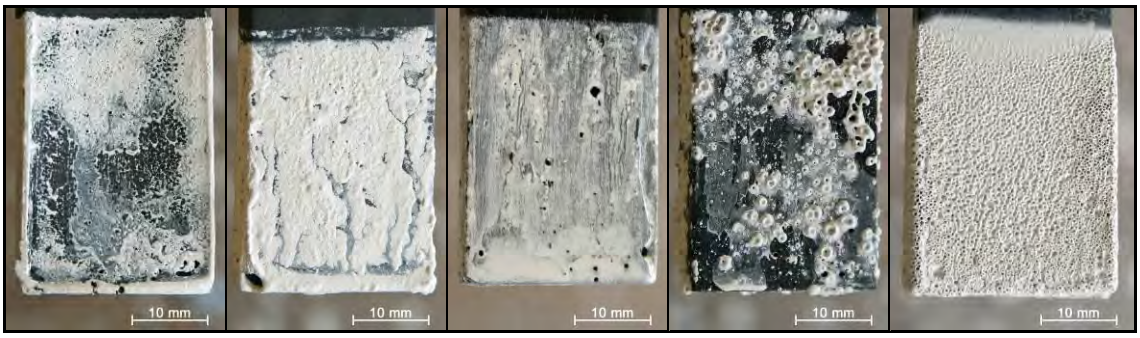

(a) **(b)** **(c)** **(d)** **(e)**

Figure 16.24 Digital SLR images showing examples of zircon EPD coatings on differing substrates. All suspensions had a 'Super FF' zircon concentration of 40 $g.l^{-1}$, pH_i of 8.7 and solution conductivity of 260 $\mu S.cm^{-1}$. The EPD process used a 40 Volt, 5 minute set-up. The following substrates were used: **(a)** 16 vol% (29.6 wt%) graphite-filled A7-7808 wax, with no interior electrode tab, **(b)** 16 vol% (29.6 wt%) graphite-filled A7-7808 wax, with an interior aluminium electrode tab, **(c)** 15.9 vol% (26.5 wt%) carbon black-filled A7-7808 wax, with no interior electrode tab, **(d)** 15.9 vol% (26.5 wt%) carbon black-filled A7-7808 wax, with an interior aluminium electrode tab, **(e)** compressed graphite Type1 substrate.

An alternative route would be to keep the voltage at 40 V and increase the concentration of zircon particles in suspension (c) to enhance the deposition rate. On compressed graphite electrodes, concentrations of 80 $g.l^{-1}$ and 120 $g.l^{-1}$ were used, and led to successful coating formation, as shown in Section 16.1.8. On observation, both coating cracking and bubble entrapment were common EPD coating features when these suspensions were used to form coatings on compressed graphite, due to the rapid deposition rate. Examples of zircon deposition from 80 $g.l^{-1}$ suspensions on graphite-filled wax, carbon black-

filled wax and compressed graphite substrates are shown in Figure 16.25. Although coating uniformity was not achieved on either of the filled-wax grades at 80 $g.l^{-1}$, a improvement in deposition characteristics can be observed when Figure 16.24(a) and (c) and Figure 16.25(a) and (b) are compared.

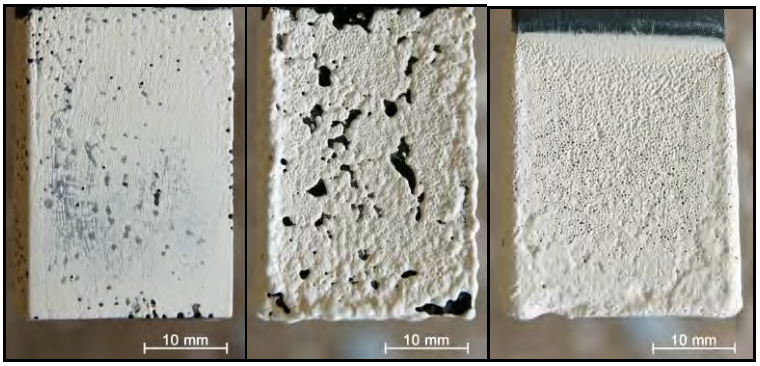

(a) **(b)** **(c)**

Figure 16.25 Digital SLR images showing examples of zircon EPD coatings on differing substrates. All suspensions had a 'Super FF' zircon concentration of 80 $g.l^{-1}$, pH_i of 8.7 and solution conductivity of 250 $\mu S.cm^{-1}$ (8.4 $mg.g^{-1}$ dispersant). The EPD process used a 40 Volt, 5 minute set-up. The following substrates were used: **(a)** 16 vol% (29.6 wt%) graphite-filled A7-7808 wax, with no interior electrode tab, **(b)** 15.9 vol% (26.5 wt%) carbon black-filled A7-7808 wax, with no interior electrode tab, **(c)** compressed graphite Type1 substrate.

Better deposition characteristics were achieved on both carbon black and graphite-filled wax substrates when the zircon suspension concentration was set to 120 $g.l^{-1}$, as shown in Figure 16.26 and Figure 16.27. Zircon deposition yields on graphite-filled wax substrates that did not contain an aluminium electrode tab displayed reproducibility when the set-up parameters used on the substrate in Figure 16.26(b) were used. As a result, 120 $g.l^{-1}$ suspensions with a range of dispersant concentrations were created to see whether this variable had an effect on yield for conductive wax substrates, as it did for deposition on compressed graphite substrates in Section 16.1.6 and Section 16.1.8. A graph comparing yields for the three substrate types using 120 $g.l^{-1}$ suspensions is shown in Figure 16.28.

Due to the limited number of wax substrates, only one substrate of each type could be tested for each suspension in dispersant concentration tests, and so trends could not be declared unless they were clearly defined. For the tab-less graphite wax substrates, there is little variation in the deposition yield as both the dispersant content and solution conductivity are increased, although the highest yield occurred when the dispersant content was 4.7 $mg.g^{-1}$ (250 $\mu S.cm^{-1}$). In observations, the most uniform coating was formed under these conditions, as shown in Figure 16.26(b). The relationship between dispersant concentration and yield for tab-less carbon black-filled wax substrates was far more variable due to the irregular coatings formed on these substrates, as shown in Figure 16.27(c). Greater deposition yields are generally achieved for carbon-black filled samples as they processed higher substrate conductivities, although a higher level of thickness variability is also observed across the sample, due to the combined effects of bubble entrapment and conductivity variations due to the presence of particle clustering in the wax.

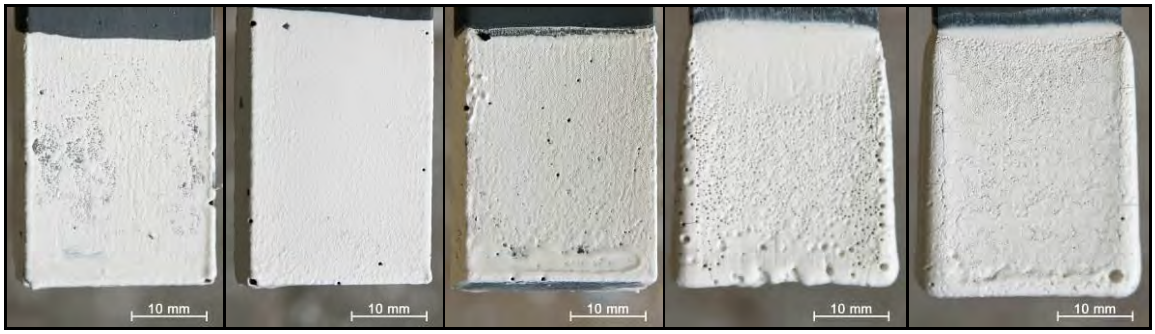

(a) **(b)** **(c)** **(d)** **(e)**

Figure 16.26 Digital SLR images showing examples of zircon EPD coatings on differing substrates. All suspensions had a zircon concentration of 120 $g.l^{-1}$ and pH_i of 8.7. The EPD process used a 40 Volt, 5 minute set-up. In **(a – c)**, 16 vol% (29.6 wt%) graphite-filled A7-7808 wax substrates, with no interior electrode tab, were used. In **(d – e)**, compressed graphite Type1 substrates were used. The suspensions had the following dispersant concentrations; **(a)** and **(d)** 3.1 $mg.g^{-1}$ (170 $\mu S.cm^{-1}$); **(b)** 4.7 $mg.g^{-1}$ (230 $\mu S.cm^{-1}$); **(c)** and **(e)** 7.5 $mg.g^{-1}$ (330 $\mu S.cm^{-1}$).

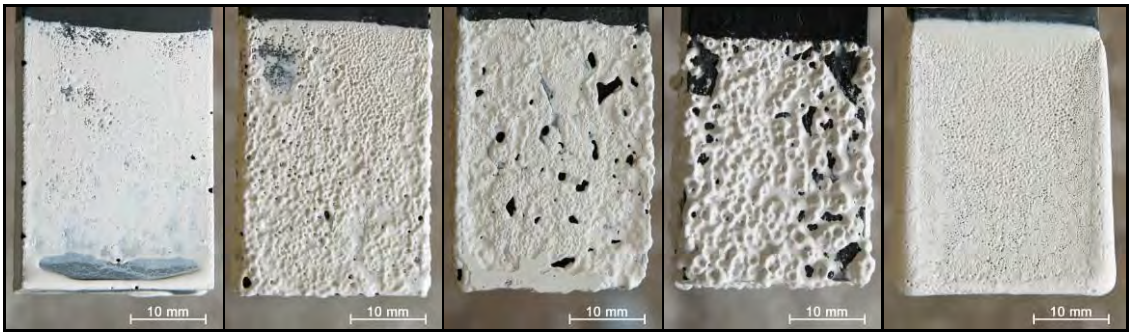

(a) **(b)** **(c)** **(d)** **(e)**

Figure 16.27 Digital SLR images showing examples of zircon EPD coatings on differing substrates. All suspensions had a zircon concentration of 120 $g.l^{-1}$, pH_i of 8.7 and dispersant concentration of ~ 5.6 $mg.g^{-1}$ (250 $\mu S.cm^{-1}$). The EPD process used a 40 Volt, 5 minute set-up. The following substrates were used: **(a)** 16 vol% (29.6 wt%) graphite-filled A7-7808 wax, with no interior electrode tab, **(b)** 16 vol% (29.6 wt%) graphite-filled A7-7808 wax, with an interior aluminium electrode tab, **(c)** 15.9 vol% (26.5 wt%) carbon black-filled A7-7808 wax, with no interior electrode tab, **(d)** 15.9 vol% (26.5 wt%) carbon black-filled A7-7808 wax, with an interior aluminium electrode tab, **(e)** compressed graphite Type1 substrate.

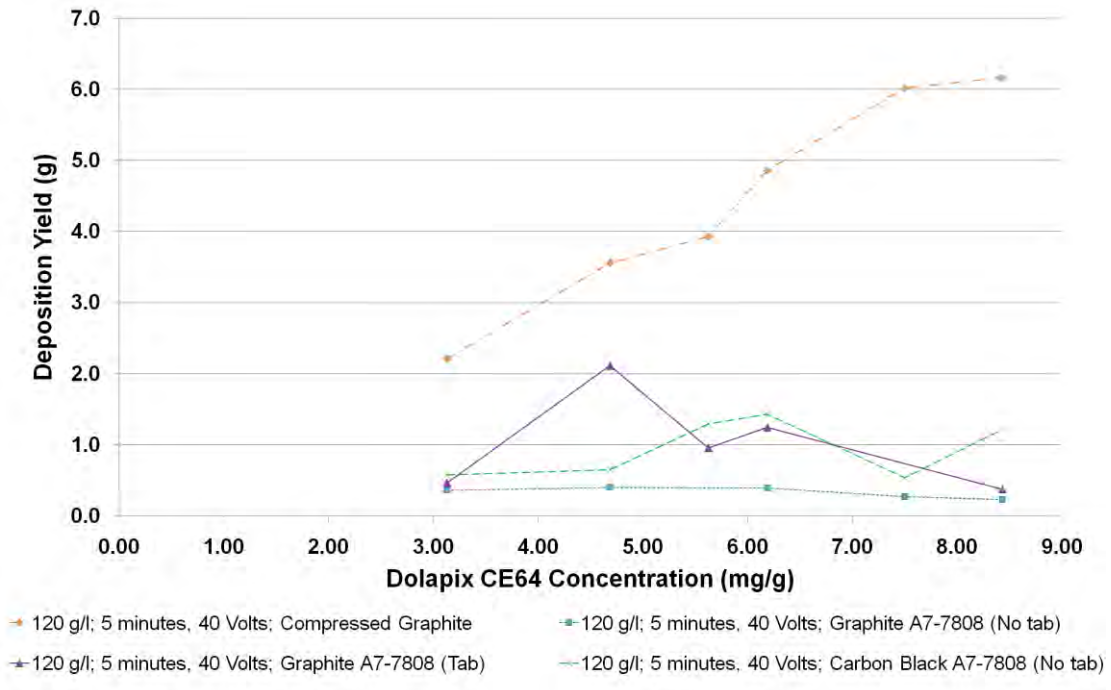

Figure 16.28 EPD deposition yield versus Dolapix CE64 concentration, as a function of substrate electrode material. All 'Super FF' zircon suspensions had a concentration of 120 $g.l^{-1}$, pH_i of 8.7, and underwent 50% magnitude sonication cycles during homogenisation, as described in Section 13.3.3. All samples underwent 40 V, 5 minute EPD.

When an aluminium tab was present within either graphite or carbon black-filled wax substrates, the coating displays an increased thickness in places, but with greater thickness variation across flat plate surfaces where the electric field should be more uniform. This non-uniformity is also demonstrated in Figure 16.28, as inconsistent yield masses are caused by the run-off effects that may or may not occur depending upon the distribution the coating on the substrate. The thickness variation, which is more accentuated when carbon black-filled wax substrates are used, can be attributed to the agglomerated distribution of conductive particles within the wax. When a cluster size approaches the distance between the tab and substrate surface, areas of relative high conductivity are formed. The local electric field strength in these areas is greater, and the local zircon coating behaviour begins to approach that seen on compressed graphite substrates. Other areas conversely have a lower filler particle concentration, and exhibit a lower conductivity, to lead to either thin or non-adherent localised coatings.

As shown in Figure 16.28, relatively uniform deposition resulted from suspensions when the Dolapix CE64 concentration was set to ~ 6 $mg.g^{-1}$. The EPD coating yield using different substrates were plotted in Figure 16.29, as a function of substrate conductivity. Since very few samples were coated using the specific suspension conditions described in Figure 16.29, the relationship cannot be defined unless a range of conductive wax compositions with varying conductivities were created and tested in the same way. An aim of future work would be to define the relationship between deposition yield and substrate conductivity, by create EPD substrate with a range of conductive particle-filled wax compositions.

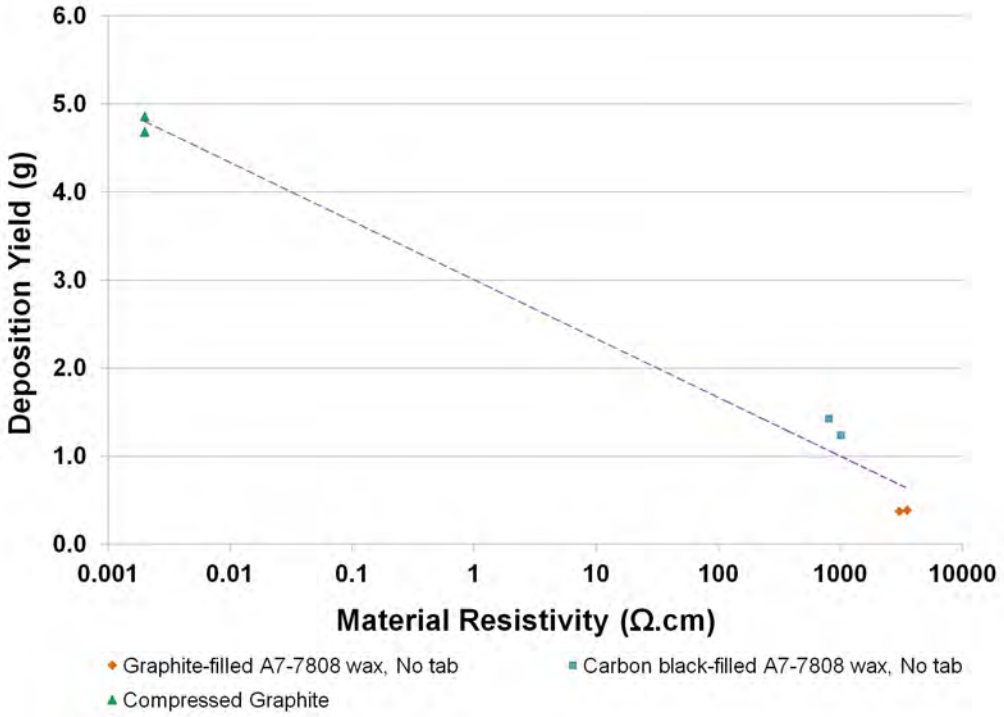

Figure 16.29 EPD deposition yield versus substrate material resistivity for EPD using 'Super FF' zircon suspensions with a concentration of 120 g/l, Dolapix CE64 concentration of 6.2 mg/g, solution conductivity of 280 µS/cm and a pH_i of 8.7. All suspensions underwent 50% magnitude sonication cycles during homogenisation, as described in Section 13.3.3.

16.2.2 EPD Coating Properties for Conductive Wax Substrates

Within this Section, the characteristics of 'green' (unfired) EPD zircon coatings formed on graphite-filled wax substrates are compared with those formed on compressed graphite. Additionally, the differences between fired shell surfaces and cross-sections of dipped and EPD primaries are compared.

The unfired surface of EPD coatings formed from zircon aqueous suspensions, with a 'Super FF' zircon concentration of 120 $g.l^{-1}$ at pH_i 8.7, are shown in Figure 16.30. The higher deposition yield on compressed graphite substrates is accompanied by both the formation of

pits with average diameters of ~ 100 µm and the presence of undulating surface texture that is indicative of the presence of voids beneath the coating surface. Cracking is also present to a large degree. When the 15.9 vol% carbon black-filled A7-7080 wax substrate was used, the surface was composed of regions of uniform deposition, as shown in Figure 16.30(c), and those which were of variable thickness, as shown in Figure 16.31(b). The uniform areas contain voids and pitting, although their occurrence on the surface is less frequent. The surface of the coated 16 vol% graphite-filled A7-7808 wax substrate was smooth a devoid of visible pitting on the plate surface.

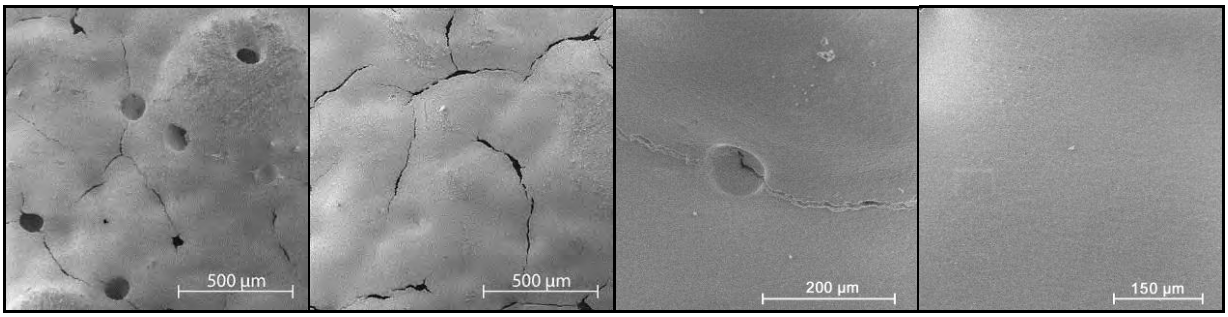

Figure 16.30 SEI micrographs (SE mode) showing unfired EPD coatings surfaces using a 'Super FF' zircon suspension with 120 $g.l^{-1}$ loading at pH_i 8.7, with a dispersant concentration ~ 4.7 $mg.g^{-1}$ (230 $\mu S.cm^{-1}$). The EPD process used a 40 Volt, 5 minute set-up. The following substrates were used; **(a) and (b)** compressed graphite; **(c)** 15.9 vol% carbon black-filled A7-7080 wax; and **(d)** 16 vol% graphite-filled A7-7808 wax.

Deposition cross sections from the same EPD coatings are shown in Figure 16.31, and all cross sections were taken at a immersion depth midpoint, to ensure that thickness values were not influenced by the effects of coating run-off, as in addition to deposition gradients being formed on the substrate, extra material was drawn towards the base of the plate electrode as the substrate is removed from suspension. Within Section 16.1.8, this 'zircon slurry' was observed to obscure void formation at the bottom of the plate electrodes.

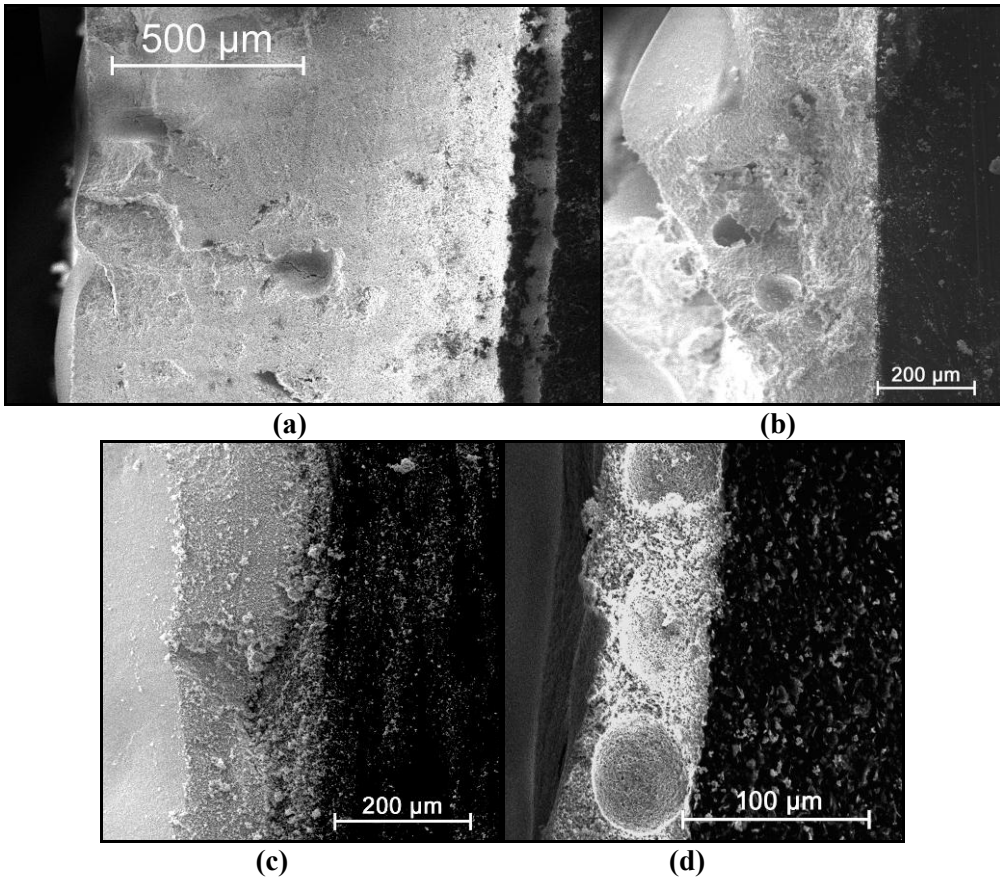

Figure 16.31 SEI micrographs (SE mode) showing unfired EPD coating perpendicular cross sections using a 'Super FF' zircon suspension with 120 $g.l^{-1}$ loading at pH_i 8.7, with a dispersant concentration ~ 4.7 $mg.g^{-1}$ (230 $\mu S.cm^{-1}$). 40 Volt, 5 minute EPD set-up. The following substrates were used; **(a)** compressed graphite; **(b)** 15.9 vol% carbon black-filled A7-7080 wax; and **(c) and (d)** 16 vol% graphite-filled A7-7808 wax, for substrate edge and plate surface respectively.

The use of compressed graphite substrates leads to deposition thicknesses of approximately 1200 µm on the substrate edges and 1000 µm on the plate surface. Such uniformity was not achieved when carbon black-filled A7-7080 wax substrates were used, although on the plate surface, the deposition thickness varies between 50 and 500 µm, as shown in the peaks and troughs of Figure 16.31(b). The coating uniformity for graphite-filled A7-7808 wax substrates was far greater, and thickness values of 200 µm on the substrate edges and 75 µm on the plate surface can be given. Even though pitting is not observed on the substrate surface, 50 µm voids are present, as shown in Figure 16.31(d).

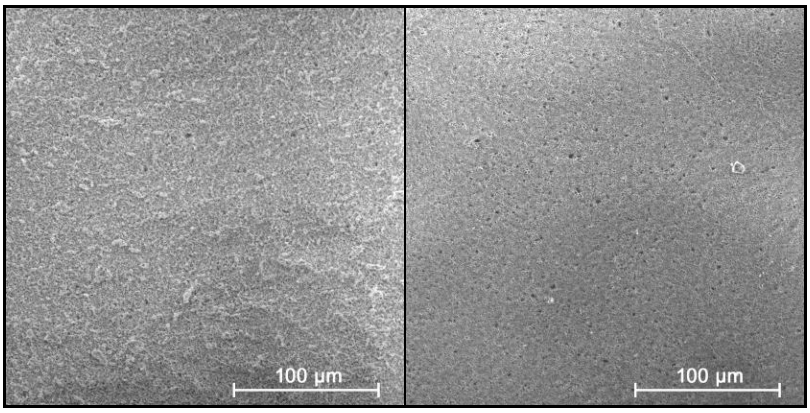

(a) **(b)**

Figure 16.32 SEI micrographs (SE mode) showing unfired internal surfaces of EPD coatings using a 'Super FF' zircon suspension with 120 $g.l^{-1}$ loading at pH_i 8.7, with a dispersant concentration ~ 4.7 $mg.g^{-1}$ (230 $\mu S.cm^{-1}$). 40 Volt, 5 minute EPD set-up. The following substrates were used; **(a)** compressed graphite; **(b)** 16 vol% graphite-filled A7-7808 wax.

In Figure 16.32, green EPD coating surfaces that would form the interior mould wall are shown. When compressed graphite and graphite-filled wax are used as substrates, the interior surfaces formed are uniform, dense, and contain no visible pitting that may result from gas being trapped at the interface between coating and substrate surface. The surface texture differs, although this is due to the differing nature of the substrate surfaces. The cast wax was smoother than the abraded compressed graphite, and this is shown in the rougher surface of Figure 16.32(a).

Compared to EPD cross sections within Section 16.1.2, for set-up parameters that lead to similar deposition thicknesses on compressed graphite (20 $g.l^{-1}$ zircon, 7 $mg.g^{-1}$ dispersant, 50% power sonication, 20 V, 5 minute cycle), the uniformity is higher and level of void formation, lower, when deposition takes place on graphite-filled wax substrates. Thicknesses achieved on these wax substrates would be insufficient for use as primary coats, although further increases in zircon suspension concentration should herald increased thicknesses if particle stability in suspension remains when such an increase is carried out.

After the permeability experiments of Section 15.4 were carried out, the fired spherical shells used for permeability studies were prepared to make the samples suitable for analysis using a scanning electron microscopy. In addition to the dip coated wax substrate spheres formed, EPD was carried out on compressed graphite plates, and these underwent the same dip coating cycle, to strengthen the EPD primary so that it could be fired. In Figure 16.33, the shell surfaces that face into the mould interior region are shown.

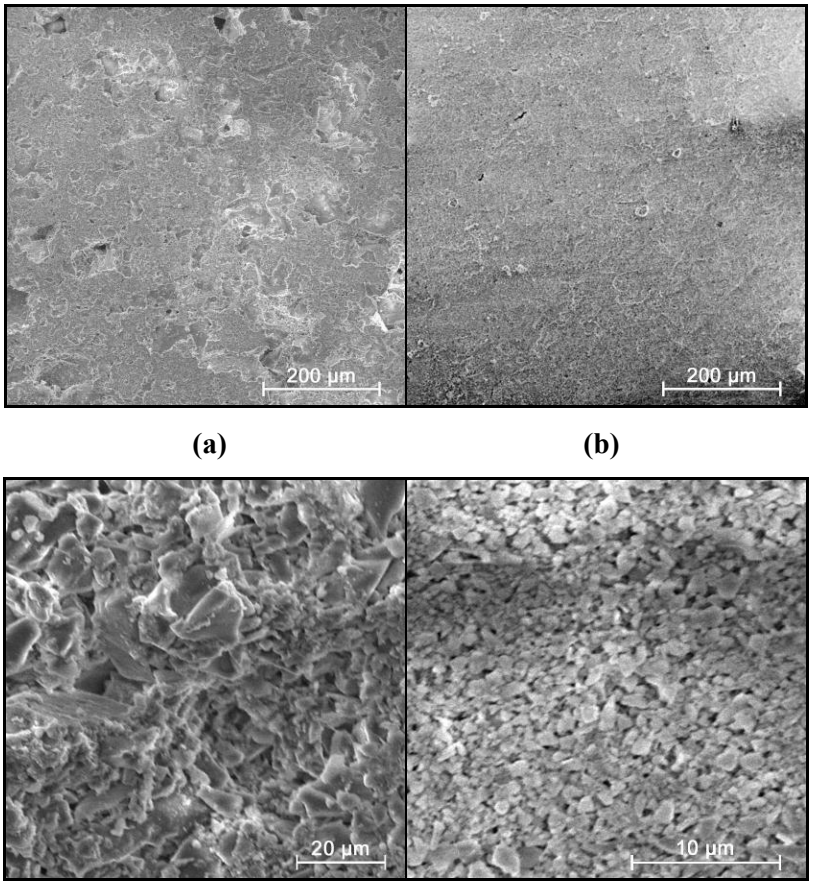

Figure 16.33 SEI micrographs (SE mode) showing fired internal surfaces of EPD and dip coated primary coats. **(a) and (c)** show the surface of the dip primary coat, containing embedded 100 µm primary stucco particles. **(b) and (d)** show the surface of the fired EPD primary coat.

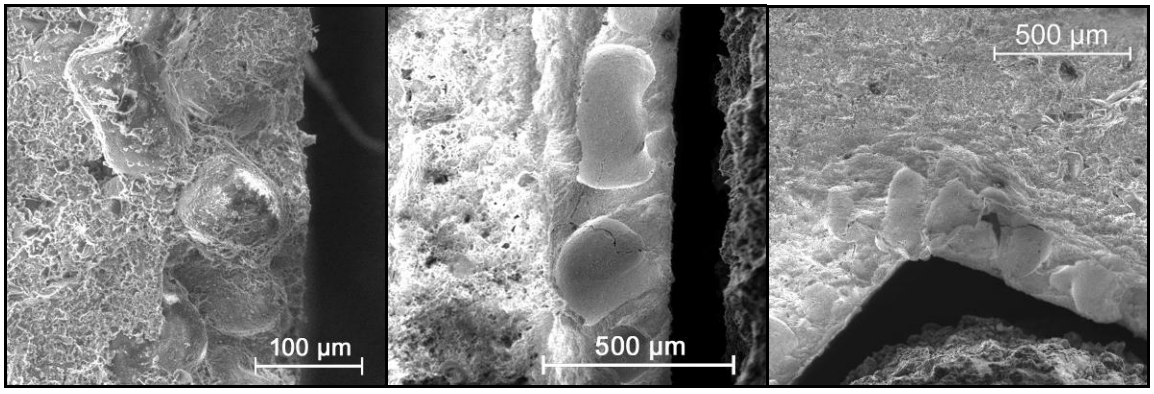

(a) **(b)** **(c)**

Figure 16.34 SEI micrographs (SE mode) showing fired perpendicular cross-sections of EPD and dip coated primary coats. **(a)** shows the cross section of the primary coat, containing embedded 100 µm primary stucco particles. **(b)** shows the fired EPD primary coat with dip coated primary to the left. **(c)** shows the EPD primary at a substrate corner section.

The interior surface textures of the EPD and dip coated primaries differ in a number of ways. As the EPD had to undergo a drying cycle prior to the dip primary and stucco being added, the stucco rests on top of the EPD primary layer, and so does not penetrate into the primary, as otherwise shown in Figure 16.33(a). On closer magnification, the particles in the dip coated sample had variable geometries, and particle diameters between 2 and 40 µm were visible on the surface. The narrow distribution of near-spherical 0.5 – 2 µm particles present in the EPD primary is in agreement with the particle size analysis of the 'Super FF' grade. In Figure 16.34, the coating cross sections can be compared. In agreement with the observations on the mould interior surface, the stucco particles become fully embedded within the dip primary, but rest on top of the EPD coating. The EPD and further dip coats shown in Figure 16.34(b) and (c) is separated by a distinct visual transition, as dense particle packing containing large 200 µm voids gives way to a less dense dip coat containing larger, more irregular particles. The lack of stucco integration can be attributed to observations made during the shell build-up process, when the dry EPD primary drew moisture away from the dip primary, to inhibit the adherence of stucco particles.

CHAPTER 17. CONCLUSIONS AND FURTHER WORK

17.1 Conclusions

The aim of this project was to tailor a colloidal processing technique called electrophoretic deposition (EPD) for use within the investment casting shell formation process, where the EPD coating procedure would be used to form the primary ceramic coating on the melt-out substrate.

EPD was initially carried out on compressed graphite substrates, using aqueous suspensions of zircon at low concentrations (1.9 – 11.6 weight %). Adherent deposition would not occur unless the zircon particles were stabilised using an anionic dispersant (Dolapix CE64). Zeta-potential analysis showed that dispersant-free and dispersant-modified zircon particles in suspension could possess similar zeta-potentials through pH modification within the alkaline region, and so deposition differences were attributed to improvements in suspension stability.

Deposition yields were improved when the dispersant concentration was increased beyond the optimum concentration, as defined by sedimentation experiments. It can be deduced that excess dispersant in solution may work as a polymeric binder, which would influence the integrity of the EPD coating and/or its adherence to the substrate. Further study is warranted, as ideally, a number of anionic dispersants need to be compared, to find the species that most effectively stabilises and binds the zircon into an EPD coating. For this research, the optimum dispersant concentration for each system would be determined using a combination of methods.

The success of EPD coating formation was zircon grade specific. Zeta-potential analysis and particle size analysis could not differentiate between successful and unsuccessful grades, and so deposition disparity was attributed to chemical differences on the zircon

surface, undetected by the analysis techniques of this study. Further studies are needed to isolate these differences, by looking more closely at the relationship between zircon stability in suspension and EPD coating adherence.

Water electrolysis is associated with the use of aqueous suspension media. Within the present work, all EPD zircon coatings on compressed graphite exhibited voids and pitting within coating cross sections, with a pore frequency that increased with deposition rate. Future work would adapt methods that have been used in the literature to inhibit gas bubble entrapment. The use of a pulsed d.c. power source was more successfully implemented using a cathodic EPD set-up in the literature, and so zircon suspension modifications would have to be carried out to stabilise the system in the acidic region.

Permeability measurements for the EPD primary coat could not be successfully carried out, as coating uniformity on conductive wax permeability spheres was insufficient for analysis. Scanning electron microscopy was used to analyse the zircon EPD coatings, and high green densities were present in the regions where water-electrolysis voids and pits were absent. Several options can be carried out to increase the permeability of the resultant EPD coatings.

It is possible to modify the surface of a particle species using a process called heterocoagulation, where one particle species is coated with another particle species due to differences in their electrostatic potential. Heterocoagulation studies would be carried out using zircon particle-coated fine polystyrene spheres, where both species are deposited onto a substrate using EPD. These spheres would be volatilised during firing, and the resultant coating would have both a controlled pore size and uniform face-coat surface. Another possible method is to use Pickering emulsions, where charged particles surrounding emulsified droplets, and are deposited using EPD to similar effect.

Conductive particle-filled investment casting wax grades were tested, to assess their viability as conductive melt-out substrate materials. The use of a low viscosity wax grade (Blayson Olefines A7-7808) improved the dispersion characteristics of filler in the composite at a set working temperature. In conductivity testing, these composites exhibited consistently higher resistivities across the range of filler concentrations. From this, it can be deduced that particles are less likely to segregate to grain boundaries during cooling when the matrix has a low viscosity. Lower sample conductivities would result as particles are not ordered within the percolation network.

Resistivities of 1200 kΩ.cm and 240 kΩ.cm were attained for 16 volume% graphite-filled and carbon black-filled wax samples respectively. The higher conductivity values associated with the use of carbon black filler was attributed to its high surface area and hierarchical agglomerated structure, as rheological analysis showed that it was not broken down into sheared-out structure during mixing. Rheologically, the addition of graphite filler to waxes followed the Krieger-Dougherty relationship for agglomerated plate-shaped particle suspensions.

The behaviour of graphite and carbon black particles within the wax with regard to clustering and segregation could not be easily analysed using optical or SEM microscopy. By carrying out filler incorporation procedures over a range of temperatures, the relationship between mixing regime and resistivity could be produced for a given composite composition. An etchable or dissolvable matrix material would additionally be used, so that percolation structures could be compared.

As a melt-out EPD substrate material, the use of graphite-filled waxes was preferred. Thin but structurally uniform zircon coatings were produced, and this was attributed to conductivity consistency within the samples. The deposition behaviour on more complex conductive wax substrate geometries was poor, although future work which is focussed on

tailoring suspensions for use with moderately conducting substrates would overcome these problems.

Ash content testing carried out revealed that both the carbon black and natural graphite filler grades left ash after de-waxing. This is of importance as the presence of ash in the mould leads to inclusions in the resulting cast metal. In future work, conductive waxes could be formed using synthetic graphite particle grades, which have very low ash contents.

Appendix A – Particle Size Analysis

A.1 Theory and Procedures

A.1.1 Introduction to Particle Sizing

The aim of particle sizing is to provide particle size distribution data that accurately reflects the true particle size distribution. Each particle in the distribution is given a single value that is indicative of the particle's size, although most particles are non-spherical and therefore possess non-equiaxed dimensions, i.e. an aspect ratio ≠ 1. Many particle sizing techniques assume that the particles being studied are spherical, and therefore equate a particle's response to the technique's sizing parameter to that of particle spheres of specific size. For a non-spherical particle, the size value given therefore corresponds to that of an 'equivalent sphere', which varies according to the analysis technique used. For the laser diffraction methods used within this study, the reported sphere diameter corresponds to one that would yield an equivalent light scattering pattern to the measured particle. This approximation corresponds to the sphere of equivalent average cross-sectional area.

Once the particle size has been calculated for the measured sample, the distribution of particle sizes within the sample can be displayed in a number of ways. Within the present work, two graphs are present for each particle grade, and depict particle size distribution according to (1) volume% - where the intensity each plotted point is tied to the volume fraction of suspended particles occupying that size range; and (2) number% - where intensity is linked to the number fraction of particles occupying that size range. The volume distribution also corresponds to the mass distribution if the particle density is the same for all sizes, although it must be noted that agglomerates have a lower density due to the packing space present between particles.

A.1.2 Analysis Procedure

A.1.2.1 Introduction to Procedures

The particle size distributions for both the conductive filler grades and zircon grades were obtained using a Beckman Coulter LS320 laser diffraction particle size analyser. These powders, most notably the graphite and carbon black, tend to agglomerate in suspension due to intermolecular interactions.

One method that can be used to break up these clusters, and so provide a size distribution closer to that of the dry powder, is ultrasonication. Additionally, the change in the shape of the distributions with ultrasonication can provide information on the presence and size of clusters. In ultrasonication, a probe is used to transmit sonic waves into the suspension. Micro-bubbles form as a result and break up these particle clusters when they collapse, in a process more fully described in Section 13.3.3. A Jencons VCX 600 ultrasonic processor was used for these experiments, using the 13 mm solid probe tip (suitable for use with both aqueous and ethanol-based suspensions with 10 to 250 ml sample volumes). The ultrasonication settings used for the conductive filler grades and zircon grades are described in Sections A.1.2.2 and A.1.2.3, respectively.

Beckman Coulter LS320 laser diffraction particle size analyser was utilised in the present work, using a small volume module set-up to hold the samples. The LS320 uses reverse Fourier lens optics incorporated in a patented binocular lens system, which allows the apparatus to optimize light scattering across the widest dynamic range in a single scan (Beckman Coulter 2009). Laser diffraction analysers require samples with a low particle concentration in suspension, and so samples were diluted prior to testing, as described in Sections A.1.2.2 and A.1.2.3.

Before each sample was added for analysis, a variable speed circulation pump was activated at 50 rpm, as it would act to both remove gas bubbles from the testing liquid and circulate the particles through the sample cell to help keep them dispersed. Both the suspension medium and the desired distribution for data analysis were entered into the software as both of these factors influenced calculations. The liquid present within the apparatus was flushed out through the drain nozzle and replaced by the liquid used to suspend the sample. PIDS (Polarization Intensity Differential Scattering) settings were put in place, so that the size distribution of particles with sub-micron diameters could be more accurately measured (Beckman Coulter 2009).

The apparatus underwent calibration procedures before the new sample was added. The diluted sample was then added drop-wise to the small volume module through the sample port using a pipette. This was done so that machine would not become saturated with the sample suspension, and sample drops were added until the detector displayed obscuration values between 8 and 12%, and PIDS values between 45 and 55%. A 0.375 μm to 2000 μm sweep range was used for each run, and the particle size by volume%, surface% and number% in differential or cumulative (greater than or less than) distributions were logged.

A.1.2.2 Test Procedure for Conductive Filler Grades

The conductive filler grades used within the present work are described in Section 8.2.2. Owing to the immiscibility of both carbon black and graphite powders in water, reagent-grade ethanol was used as the suspending medium. For each suspension made up for particle size distribution analysis, the powder was added to the suspending medium at a concentration of 5.0 weight% (wt%), using 4.0 g of dry powder in 76.0 g (96 cm^3) of ethanol.

Half of the suspension samples underwent ultrasonication prior to dilution, after the homogenisation period on the rolling mill. The ultrasonication cycle time was set to 10 minutes at 300 Watts (50% of the operational maximum), as suspension heating led to significant levels ethanol evaporation when intensities and cycles times above these were used. The suspension was vigorously mixed and allowed to homogenise by placing it on a rolling mill for 10 minutes prior to further dilution.

For each prepared suspension, a 0.5 cm^3 volume was taken from the suspension using a pipette, and this was added to 4.5 cm^3 of ethanol (reagent-grade 99%) in a specimen container. This dilution reduced the particle concentration to a level suitable for analysis. The suspension fluid was described as being ethanolic for the purposes of software calculations, and Mie theory was used to analyse the particle sizing data, as alternative Fraunhofer approximations are not suited for use with particle size distributions containing non-spherical material less than 2 μm in size, which is the case here. For each diluted suspension tested, three samples were analysed, and an average of these was taken to form a particle size distribution curve if no anomalous behaviour was observed.

A.1.2.3 Test Procedure for Zircon Grades

The zircon powder grades used within the present work are described in Section 12.2.2. The zircon suspensions used for particle size analysis were formed using the basic procedure set out in Section 10.2, with a number of specifics described below. For each zircon grade, a 400 cm^3 volume of deionised water was used to form the suspending medium. Before the zircon powder was added at a concentration of 40 g/l, Dolapix CE64 dispersant was added at a concentration of 11.3 mg/g zircon, and the suspension was modified to pH_i 8.7. After zircon addition, each suspension was split into two equal volumes.

During a 4 hour roller mixer homogenisation cycle, the first suspension underwent two 5 minute sonication cycles at 90 Watts (15% of the operational maximum), and the second suspension underwent two 5 minute sonication cycles at 300 Watts (50% of the operational maximum).

After homogenisation, a small quantity of each suspension was removed for particle size analysis. Samples taken from the 40 g/l zircon suspensions were diluted in deionised water prior to analysis, to form samples with a zircon concentration of ~ 5 g/l. The suspension fluid was described as being aqueous for the purposes of software calculations, and deionised water was used to flush tested samples through the drain nozzle. Mie theory was used to analyse the particle sizing data, as particle sizes less than 2 μm were present. For each diluted suspension tested, three samples were analysed, and an average of these was taken to form a particle size distribution curve if no anomalous behaviour was observed.

A.2 Results and Analysis

A.2.1 Conductive Filler Size Distributions

Particle size distribution graphs for graphite particles in ethanol are shown in Figure A.1 and Figure A.2, whilst those for carbon black suspensions are shown in Figure A.3 and Figure A.4. For each of these graphs, two size distributions are shown, and correspond to results from the each of the suspension preparation routes.

The manufacturer information stated that the micronised graphite contained particles with diameters less than 10μm, and this is shown in both the vol% and number% distributions. In the vol% graph shown in Figure A.1, one main distribution peak is shown with a mode of 6 μm (which shifts to 5 μm when the ultrasonication processing step was in place). In the number% graph shown in Figure A.2, two main peaks are present, with modes

of 1.9 μm and 4.2 μm (which shift to 1.7 μm and 3.3 μm, respectively, under ultrasonication). Under ultrasonication, the intensity of the 3.3 μm peak was reduced, and the intensity of newly present 500 nm and 1.7 μm peaks increased. This shift suggests that graphite particles represented within the 1.5 μm diameter peak are commonly in the form of < 10 μm clusters. The ultrasonication cycle used does not appear to break up all clusters, and instead breaks singular particles from the agglomerates, to reduce their diameter.

The particle size distributions for carbon black are displayed in Figure A.3 and Figure A.4, relating to volume% and number%, respectively. As described in Section 5.5.2, carbon black has a hierarchical structure, where primary particles of carbon black tend to be in the form of 400nm primary aggregates which cannot be broken down with conventional shear forces. These aggregates can themselves readily agglomerate into clusters that can be between 1 and 1000 μm in diameter.

In the carbon black vol% size distributions in Figure A.3, two particle size distribution peaks exist with modes of 3.8 μm and 22 μm. The magnitude of the peak at larger diameters is significantly reduced when carbon black suspensions are ultrasonicated, and leads to a heightened peak at 4 μm, as well as greater intensities at the sub-micron level. The number% distribution in Figure A.4 shows that the presence of a large number of sub-micron particles due to ultrasonication in turn reduces the peak height of particles in the 1 – 10 μm size range, even though the volume% distribution shows that the volume% of particles within this size range increases. Ultrasonication is therefore shown to breaks clusters greater than 10 μm in size into submicron aggregates and clusters less than 10 μm in diameter.

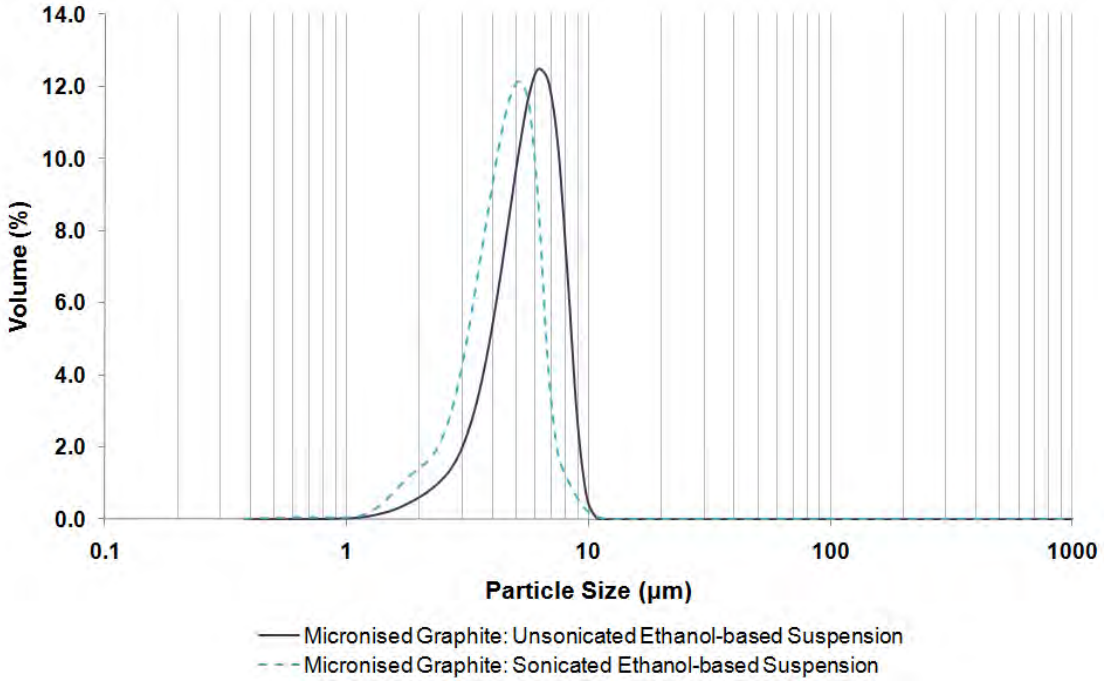

Figure A.1 Laser diffraction particle size analysis of the micronised graphite powder, using reagent grade (99.8+%) ethanol as the suspending medium. The graph displays peak intensity according to volume% of the particles. Displays lower channel diameters, analysed using Mie theory.

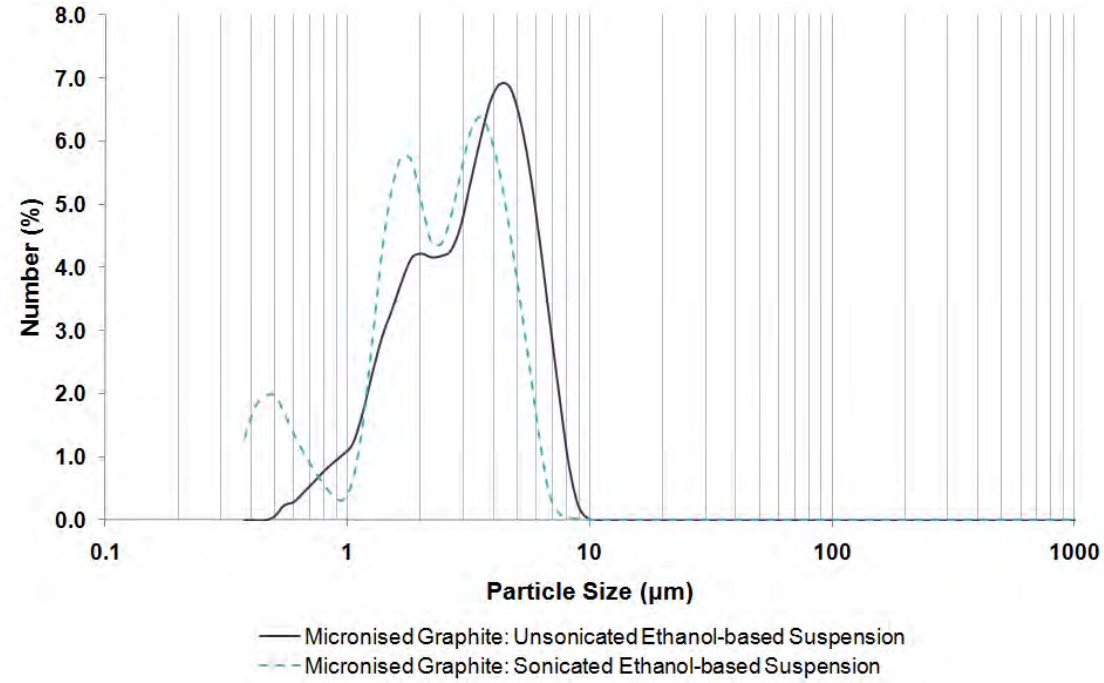

Figure A.2 Laser diffraction particle size analysis of the micronised graphite powder, using reagent grade (99.8+%) ethanol as the suspending medium. The graph displays peak intensity according to number% of the particles. Displays lower channel diameters, analysed using Mie theory.

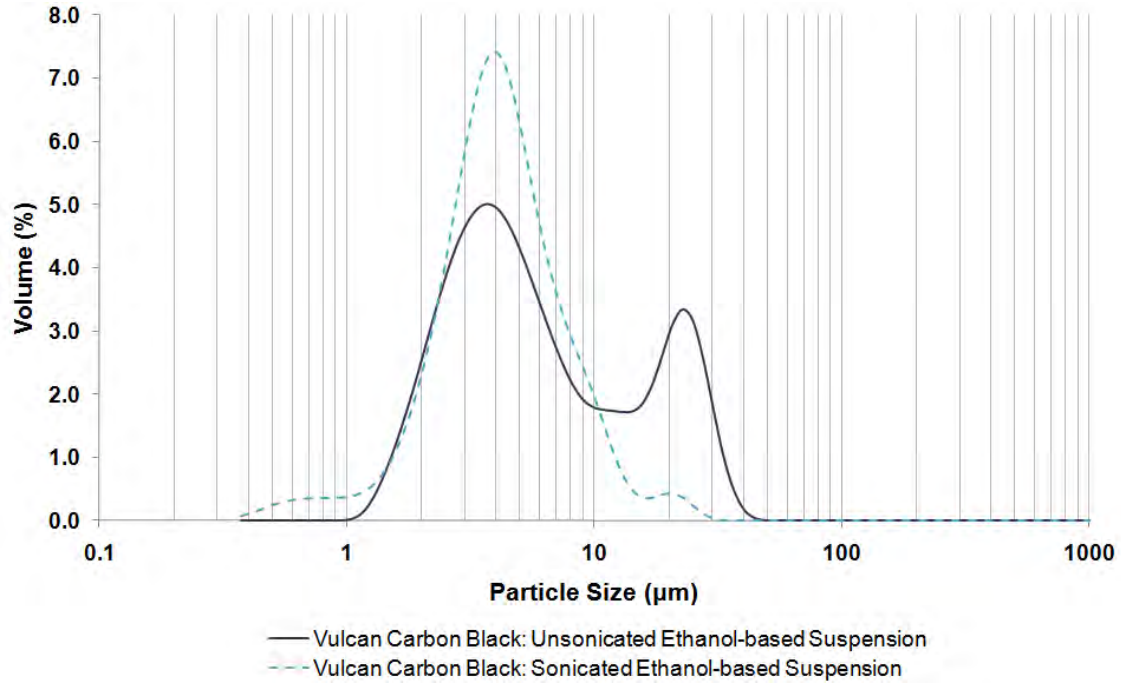

Figure A.3 Laser diffraction particle size analysis of the Vulcan carbon black powder, using reagent grade (99.8+%) ethanol as the suspending medium. The graph displays peak intensity according to volume% of the particles. Displays lower channel diameters, analysed using Mie theory.

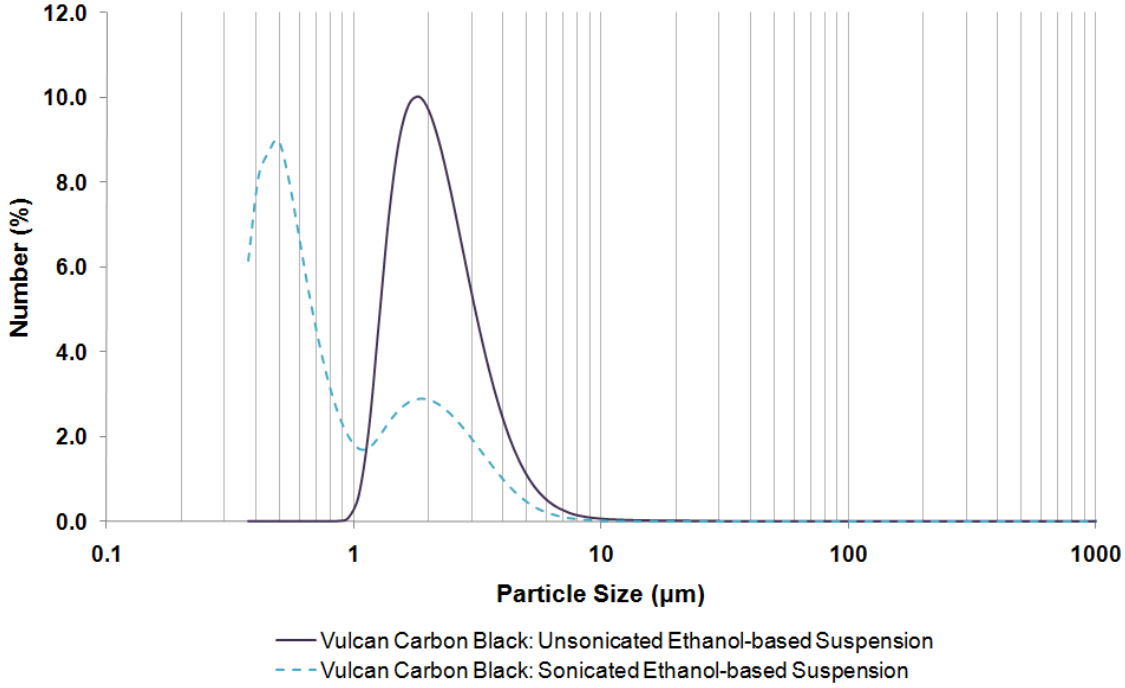

Figure A.4 Laser diffraction particle size analysis of the Vulcan carbon black powder, using reagent grade (99.8+%) ethanol as the suspending medium. The graph displays peak intensity according to number% of the particles. Displays lower channel diameters, analysed using Mie theory.

It is important to note that particles with diameters of less than 375 nm cannot be detected using the LS320 laser diffraction analyser, as obtaining the size distribution of primary aggregates were beyond the capabilities of this apparatus. The laser diffraction particle size distribution data shows the full distribution of agglomerates, but cannot display all submicron aggregates, which could instead be analysed by a Beckman Coulter Delsa™Nano submicron particle size analyzer, and is an aim of future work.

A.2.2 Zircon Grade Size Distributions

The zircon grades analysed within this section are tested according to the procedure in Section A.1.2.3. Two graphs are presented for each grade, and depict the particle size distribution according to (1) the volume % (vol%) of particles in each channel diameter; and (2) the number fraction (number %) of particles in each channel diameter. The particle sizing data for the Dupré zircon grades are shown in Figures A.5 to A.10, and those for Helmut Kreutz grades are shown in Figures A.11 to A.14.

Two differing levels of ultrasonication were used to see whether this pre-processing step acted differently both on different particle size distributions and on different manufacturer zircon powder grades. The presence of agglomerates can be assessed by noting the relative changes in the particle size distribution for the two different levels of ultrasonication. Comparing the size distribution with volume and number percent distribution data can also be of use, because the number % data tend to be biased by the presence of many smaller particles/particle agglomerates, while the volume% data tend to biased by the presence of a relatively small number of larger particles and particle agglomerates.

For the Dupré Zircon ‘A’ (2 μm) volume% (vol%) distributions shown in Figure A.5, the low ultrasonication level sample exhibited peaks at 700 nm and 3 μm, whilst these

peaks are shifted to 550 nm and 2.2 μm when samples underwent a higher power ultrasonication cycle. For the Dupré Zircon 'B' (4 μm) vol% graph in Figure A.7, peaks exist at 700 nm, 3.3 μm and 8 μm, and although the 8 μm peak is reduced in intensity when a higher sonication intensity is used, the lower diameter peaks are almost unchanged in position. The vol% size distribution for Dupré Zircon 'C' (12 μm), as displayed in Figure A.9, shows peaks at 750 nm, 4 μm, 9 μm and 15 μm. When a higher sonication intensity is used, the two larger diameter peaks reduce in intensity, although the peak positions are shifted to slightly larger sizes. The peaks at smaller 'equivalent sphere' diameters increase in size with sonication. For all the Dupré grades, the shift in peak intensity with increased sonication intensity how clusters of small particles are broken down during a period of more intense sonication.

Helmut Kreutz 'Super FF' and 'Super' zircon grade volume% distributions are shown in Figure A.11 and Figure A.13, respectively. The 'Super FF' grade displays peaks at 550 nm and 2.3 μm, which are shifted to the 520 nm and 2.1 μm positions, respectively, when the sonication intensity is increased. The 'Super' grade, on the other hand, displays peaks at 650 nm and 3.1 μm, which are shifted to 610 nm and 2.8 μm positions, respectively, when the sonication intensity is increased.

In the number% distributions for the Zircon 'A' (2 μm), 'Super FF' and 'Super' zircon grades, as shown in Figure A.6, A.12 and A.14, respectively. The 550 to 700 nm peaks change when the sonication level is increased, and becomes skewed towards smaller sizes. The change is not, however, clear in the number% distributions for the Zircon 'B' (4 μm) and Zircon 'C' (12 μm) grades, given in Figure A.8 and A.10 respectively, suggesting that particles in the 2 to 5 μm size range in the larger nominal particle size zircon grades are distinct and not an agglomeration of smaller particles, as the case may be for the Zircon 'A' powder grade.

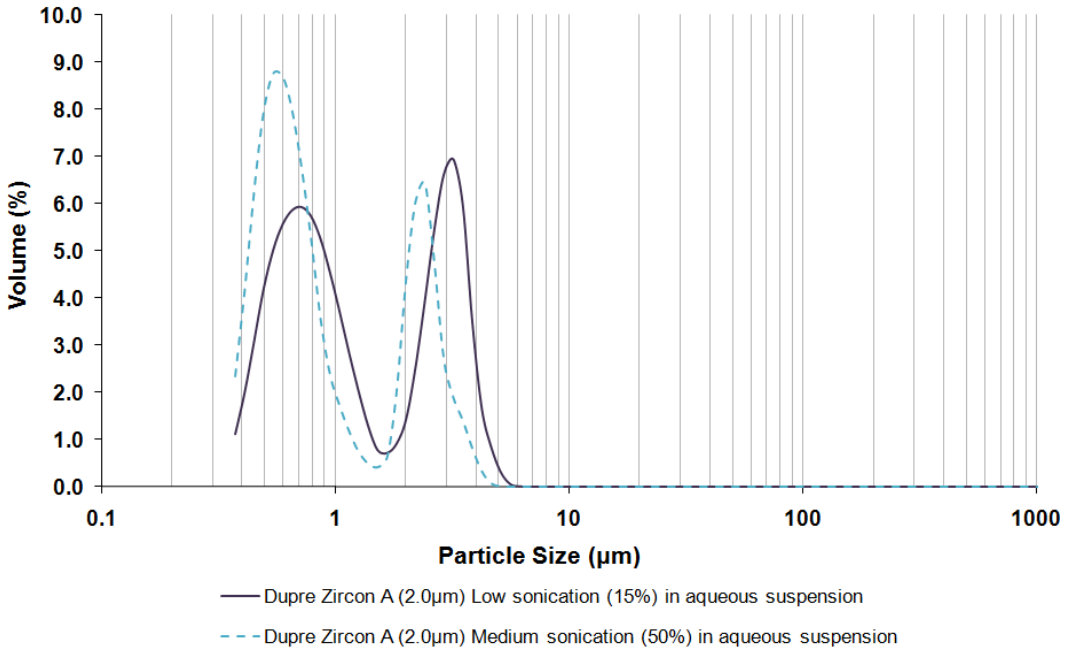

Figure A.5 Laser diffraction particle size analysis of the Dupré Zircon 'A' (2 µm) grade zircon powder, using deionised water as the suspending medium. The graph displays peak intensity according to volume% of the particles against particle size. Displays lower channel diameters, analysed using Mie theory.

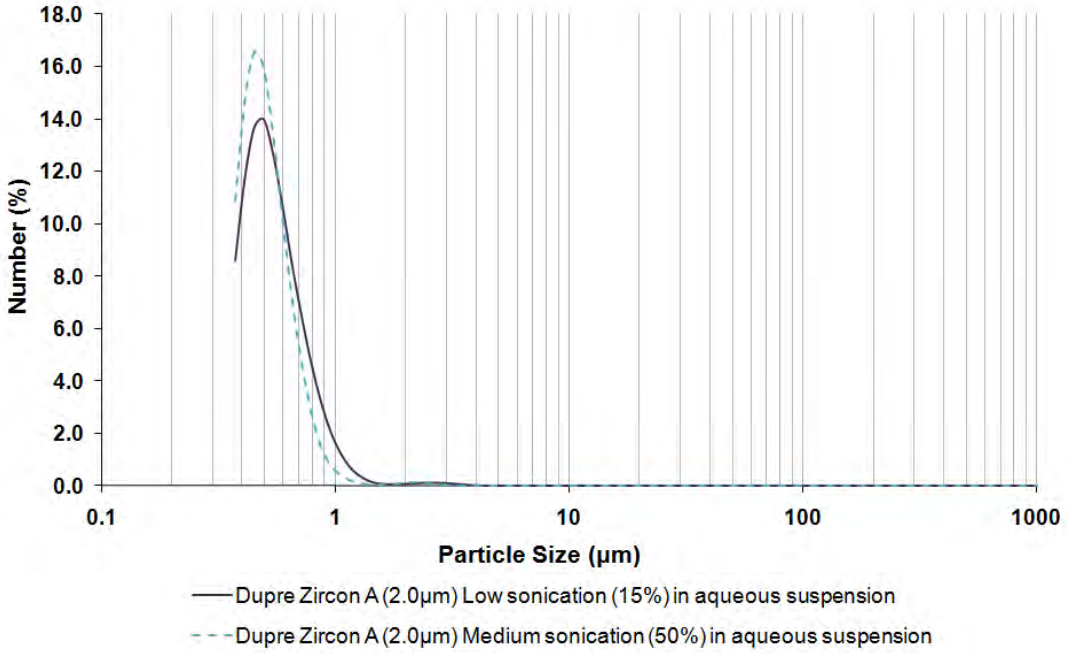

Figure A.6 Laser diffraction particle size analysis of the Dupré Zircon 'A' (2 µm) grade zircon powder, using deionised water as the suspending medium. The graph displays peak intensity according to number% of the particles against particle size. Displays lower channel diameters, analysed using Mie theory.

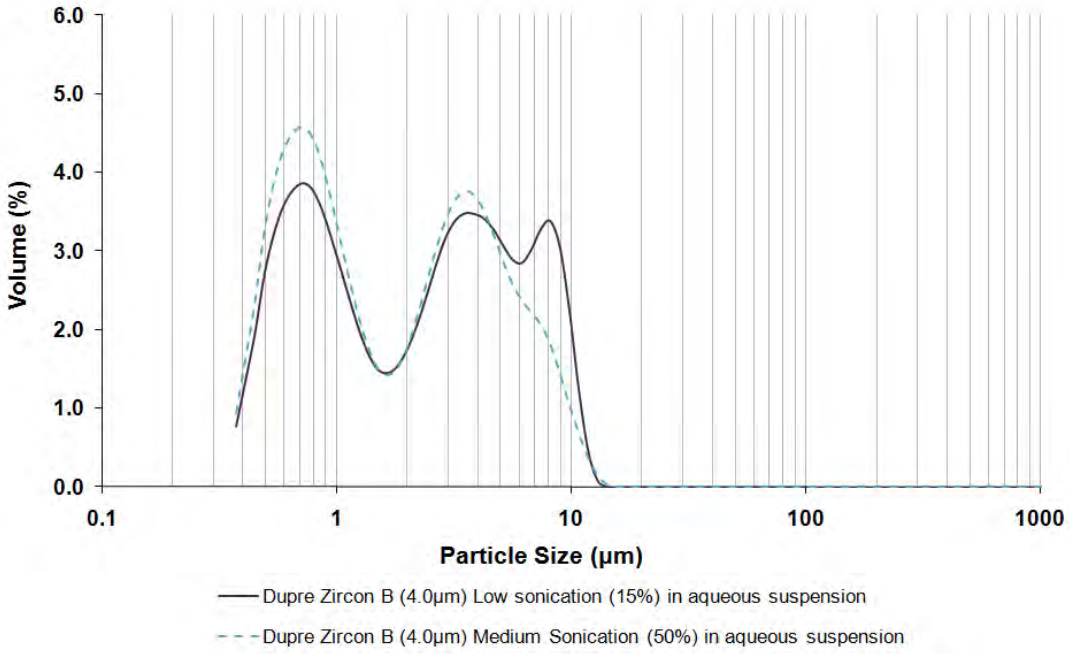

Figure A.7 Laser diffraction particle size analysis of the Dupré Zircon 'B' (4 µm) grade zircon powder, using deionised water as the suspending medium. The graph displays peak intensity according to volume% of the particles against particle size. Displays lower channel diameters, analysed using Mie theory.

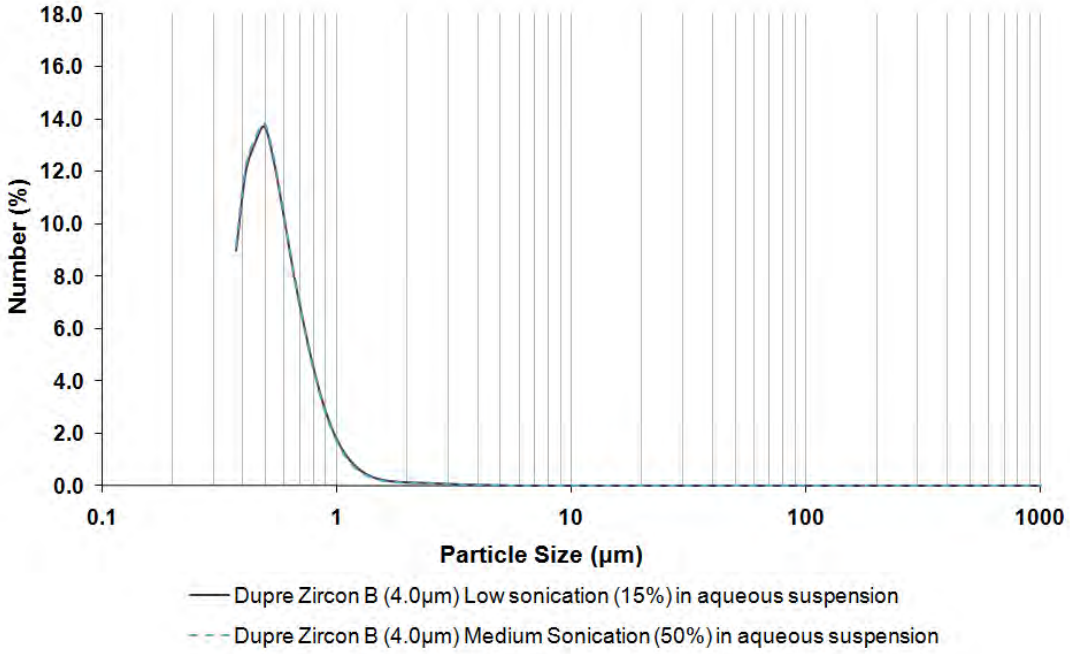

Figure A.8 Laser diffraction particle size analysis of the Dupré Zircon 'B' (4 µm) grade zircon powder, using deionised water as the suspending medium. The graph displays peak intensity according to number% of the particles against particle size. Displays lower channel diameters, analysed using Mie theory.

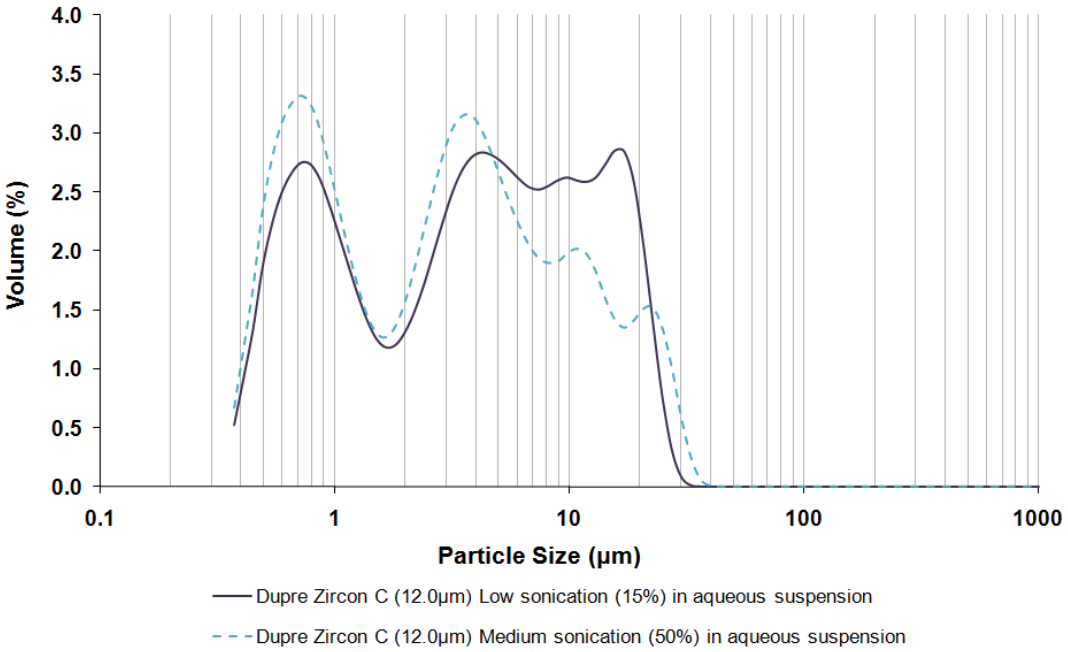

Figure A.9 Laser diffraction particle size analysis of the Dupré Zircon 'C' (12 µm) grade zircon powder, using deionised water as the suspending medium. The graph displays peak intensity according to volume% of the particles against particle size. Displays lower channel diameters, analysed using Mie theory.

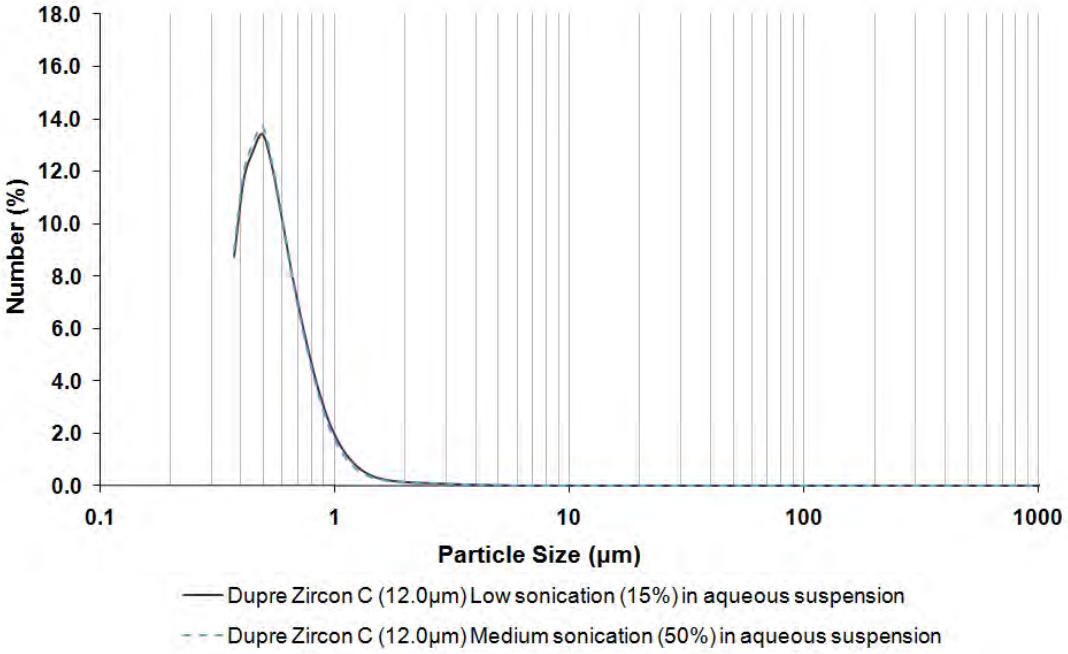

Figure A.10 Laser diffraction particle size analysis of the Dupré Zircon 'A' (2 µm) grade zircon powder, using deionised water as the suspending medium. The graph displays peak intensity according to number% of the particles against particle size. Displays lower channel diameters, analysed using Mie theory.

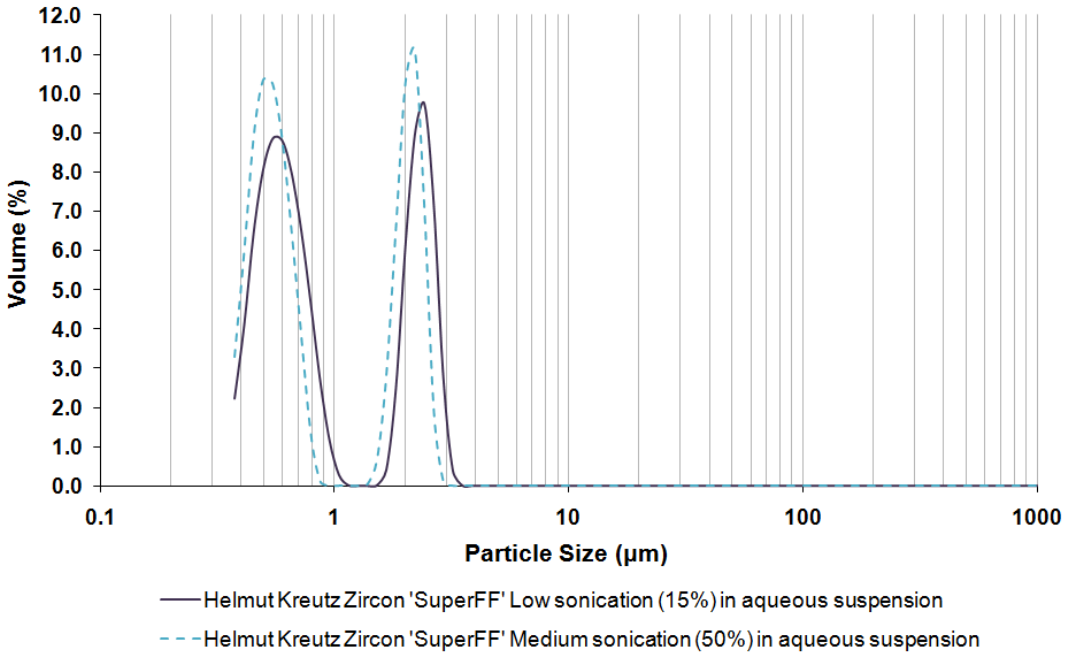

Figure A.11 Laser diffraction particle size analysis of the Helmut Kreutz 'Super FF' grade zircon powder, using deionised water as the suspending medium. The graph displays peak intensity according to volume% of the particles against particle size. Displays lower channel diameters, analysed using Mie theory.

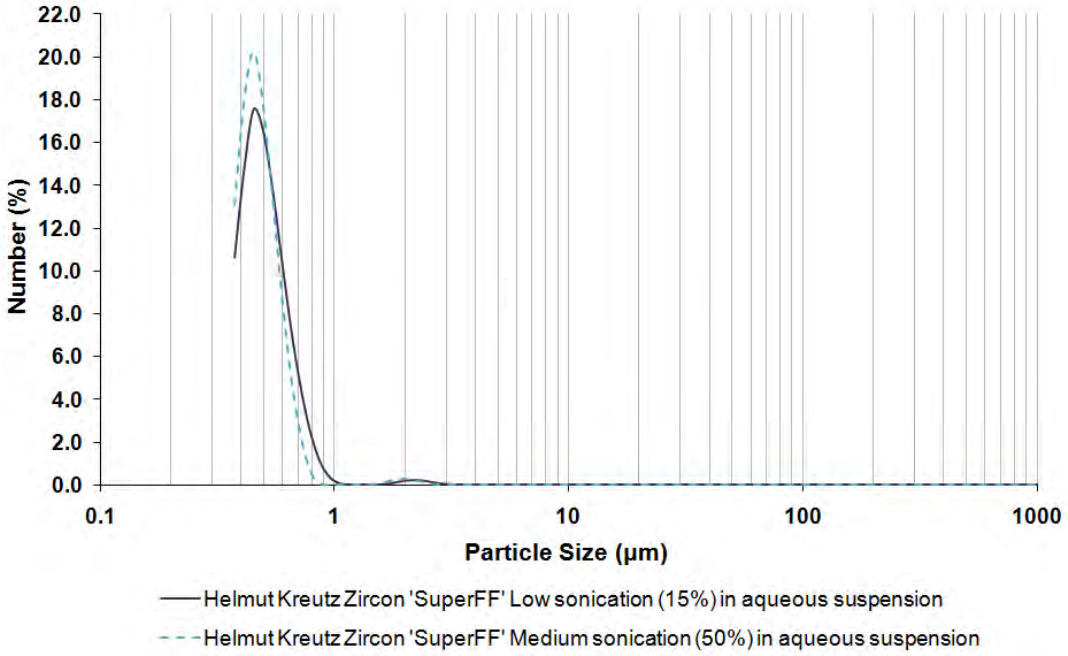

Figure A.12 Laser diffraction particle size analysis of the Helmut Kreutz 'Super FF' grade zircon powder, using deionised water as the suspending medium. The graph displays peak intensity according to volume% of the particles against particle size. Displays lower channel diameters, analysed using Mie theory.

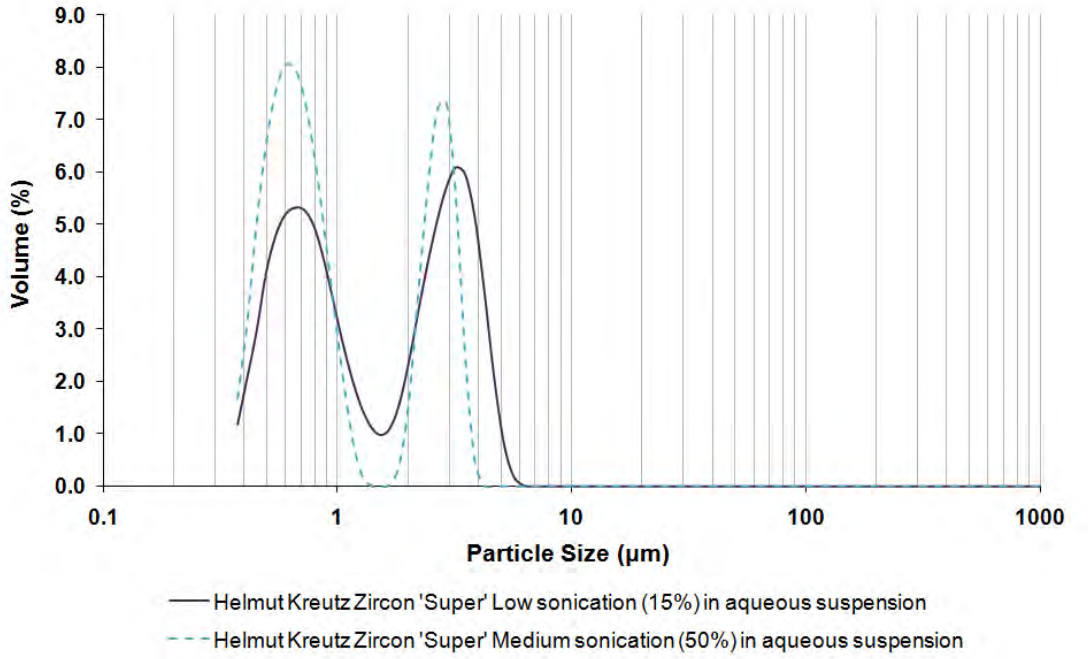

Figure A.13 Laser diffraction particle size analysis of the Helmut Kreutz 'Super' grade zircon powder, using deionised water as the suspending medium. The graph displays peak intensity according to volume% of the particles against particle size. Displays lower channel diameters, analysed using Mie theory.

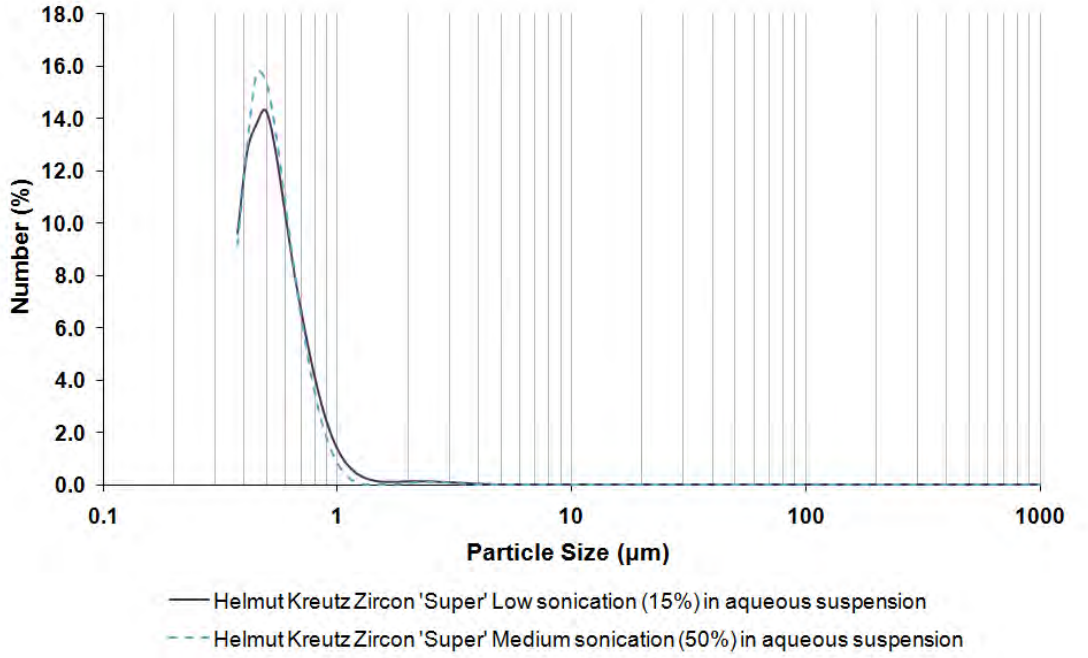

Figure A.14 Laser diffraction particle size analysis of the Helmut Kreutz 'Super' grade zircon powder, using deionised water as the suspending medium. The graph displays peak intensity according to volume% of the particles against particle size. Displays lower channel diameters, analysed using Mie theory.

Appendix B – Viscoelasticity and Oscillatory Rheometry

B.1 Introduction to Viscoelasticity and Oscillatory Testing

B.1.1 Solid and Liquid Behaviour

One can visually distinguish between solids and liquids by their different response to low stresses (usually determined by gravitational forces) over easily observable timeframes (ranging between seconds and minutes). The property that dominates, however, can depend principally upon the magnitude of the applied stress and the stress duration, as changing these conditions can affect material parameters like the shear modulus and viscosity.

Application of a very wide range of stresses over a wide spectrum of timeframes, can lead to observations of liquid-like behaviour in solids and solid-like behaviour in liquids. The particular response of a material sample in a given experiment depends on the timescale of the experiment in relation to the natural time-scale of the material's response to the external stimulus. The value of the Deborah number (D_e), as shown in Equation [B.1], can be used to define liquid and solid-like behaviour, taking into account timescales.

$$D_e = \lambda/t \qquad [B.1]$$

λ is the time of relaxation and t is the time of observation. The relaxation time (the t value) is infinite for a Hookean elastic solid and zero for a Newtonian viscous liquid. High D_e numbers therefore correspond to solid-like behaviour, whilst low D_e numbers correspond to liquid-like behaviour (Barnes, 1997).

B.1.2 Models describing Linear Viscoelasticity

Viscoelastic shear behaviour is based on the combination of viscous and elastic behaviour components, as shown in Table B.1. Viscoelastic behaviour can be described as 'linear', when the response (i.e. the strain) at any time is directly proportional to the value of the initiating signal (i.e. the stress). In the linear theory of viscoelasticity, the differential equations are linear, and the coefficients of the time differentials are constant. These constants are material parameters, such as viscosity and shear modulus, and are not allowed to change with changes in such variables as strain and strain rate. In this section, two simple models used to describe linear viscoelastic behaviour are shown.

Table B.1 Overview of different kinds of rheological behaviour (Mezger, 2006)

	SOLIDS		**LIQUIDS**	
Behaviour	(Ideal-) elastic deformation behaviour	Viscoelastic deformation behaviour	Viscoelastic flow behaviour	(Ideal-) viscous flow behaviour
Model Used	Hooke's Law	Kelvin/Voigt's law	Maxwell's Law	Newton's Law
Equations	[6.1], [A.2]	[A.4], [A.5]	[A.8], [A.9], [A.10]	[A.3], [6.4]
Diagram		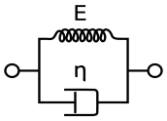	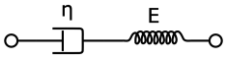	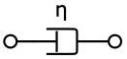
Mechanical Model	Spring	Spring and Dashpot in Parallel	Spring and Dashpot in Series	Dashpot

Mechanical models provide a method of describing linear viscoelastic behaviour without going into the mathematics of differential equations. These one dimensional models

consist of a series of springs and dashpots, arranged in a way so that the overall system behaves analogously to the real material. Hookean (ideal elastic) deformation is represented by a spring, which is an element where the force is proportional to the extension, whilst Newtonian (ideal viscous) flow is represented by a dashpot, which is an element where the force is proportional to the rate of extension. Hookean and Newtonian deformation behaviours are described more fully in Sections 6.2 and 6.3, respectively. Strains versus time curves for each of the models shown in Table B.1 are depicted in Figure B.1.

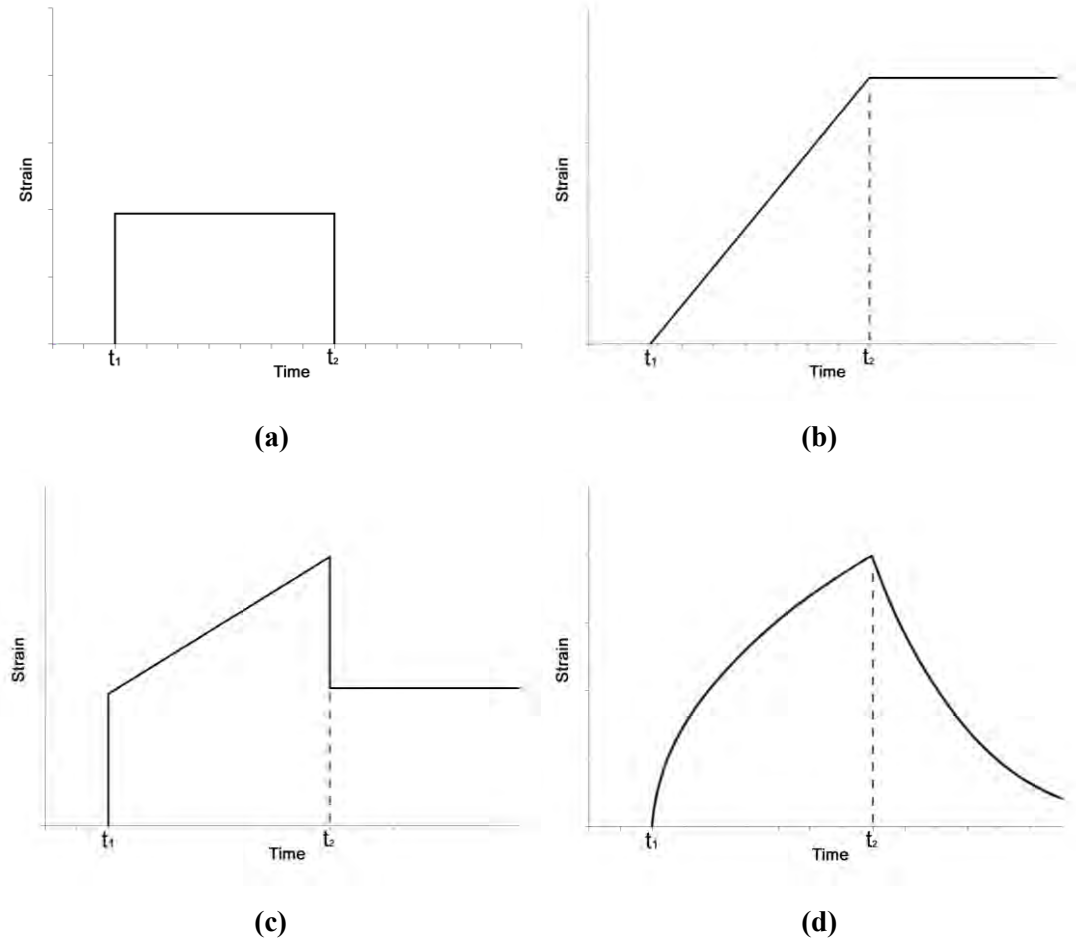

Figure B.1 Graphs showing plots of strain (ε) versus time (t) for **(a)** a Hookean solid; **(b)** a Newtonian liquid; **(c)** the Maxwell model of viscoelasticity; and **(d)** the Kelvin/Voigt model of viscoelasticity**.** A constant extensional stress is applied to the model sample at time t_1 and released at time t_2.

Equations [B.2] and [B.3] can be used to describe the behaviour of the spring and dashpot respectively. The behaviour of more complicated materials can be described by connecting these basic elements in series and/or in parallel.

$$\tau = G\gamma \qquad [B.2]$$

$$\tau = \eta\dot{\gamma} \qquad [B.3]$$

γ is the strain and G is the shear modulus (Pa) of the material. The shear rate $\dot{\gamma}$ (s^{-1}) is defined as the velocity gradient perpendicular to the direction of shear, and is proportional to the applied shear stress τ (Pa), η is the viscosity (Pa.s), and is a measure of a fluid's "lack of slipperiness" or resistance to flow. The Kelvin/Voigt model can be applied to viscoelastic solids. It uses a mechanical model where the spring and dashpot are combined in parallel, as shown in Table B.1. In interpreting these diagrams, the vertical connectors remain parallel at all times, and so the extension in both the string and dashpot is equal at all times. For a parallel set-up, the total stress τ is equal to the sum of the stresses in each element, as shown in Equation [B.4]:

$$\tau = \tau_E + \tau_V \qquad [B.4]$$

τ_E and τ_V are the stresses in the elastic and viscous elements respectively. Using Equations [B.2] and [B.3], we arrive at the Kelvin/Voigt model which is a simple expression for viscoelastic deformation, as shown in Equation [B.5]:

$$\tau = G\gamma + \eta\dot{\gamma} \qquad [B.5]$$

If a constant stress $\bar{\tau}$ is suddenly applied at t = 0 and held at a constant level after that, we can arrive at the following equation for t > 0:

$$\gamma = \left(\frac{\bar{\tau}}{G}\right)\left[1 - \exp(-t/\tau_K)\right] \qquad [B.6]$$

$$\tau_K = \eta/G \qquad [B.7]$$

Following the sudden application of shear stress $\bar{\tau}$, the value of τ_K controls the rate of growth of strain. The spring will eventually reach the strain given by $\bar{\tau}/G$, but the dashpot in the mechanical model retards the growth of the strain, which would be 'instantaneous' in a Hookean model.

The Maxwell model for viscoelastic liquids uses a mechanical model where a spring and dashpot are combined in series. In this case, the strains (or equally strain rates) are additive and the total strain rate $\dot{\gamma}$ is the sum of the rates of shear for the spring and dashpot elements, as shown in Equation [B.8]:

$$\dot{\gamma} = \dot{\gamma}_E + \dot{\gamma}_V \qquad [B.8]$$

$\dot{\gamma}_E$ and $\dot{\gamma}_V$ are the strain rates for the elastic and viscous elements respectively. Using Equations [B.2] and [B.3], we arrive at the Maxwell model which is a simple expression for viscoelastic flow shown in Equation [B.10] (a rearrangement of Equation [B.9]).

$$\dot{\gamma} = \frac{\dot{\sigma}}{G} + \frac{\sigma}{\eta} \qquad [B.9]$$

$$\tau + \frac{\eta}{G}\dot{\sigma} = \eta\dot{\gamma} \qquad [B.10]$$

If strain rate $\bar{\gamma}$ is suddenly applied at t = 0 and held at that value, the Maxwell model shows us that, for t > 0:

$$\tau = \eta\bar{\gamma}\left[1 - \exp(-t/\tau_M)\right] \quad [B.11]$$

$$\tau_M = \eta/G \quad [B.12]$$

This implies that on the start up of shear, the stress growth is delayed. The time constant in this case is τ_M, which controls the rate of growth of stress. If a strain rate which has had a constant value of $\bar{\gamma}$ for t < 0 is suddenly removed at t = 0, we can show that, for $t \geq 0$:

$$\tau = \eta\bar{\gamma}\left[\exp(-t/\tau_M)\right] \quad [B.13]$$

There are a number of more complex models for linear viscoelasticity, where an increasing number of parameters within the general differential equation for linear viscoelasticity are given non-zero values. For example, Jeffrey's model uses the results from a parallel spring and dashpot with a dashpot in series and Burger's model uses the results from a parallel spring and dashpot with a spring and dashpot in series (Mezger 2006).

Elastic and viscous behaviour has so far been described using Hookean and Newtonian models. These are linear models, where there is direct proportionality between stress and strain for the elastic models, and stress and strain rate for the viscous models. As viscoelastic models can be described using viscous and elastic components, they should therefore possess linear properties like their modelling elements.

B.1.3 Oscillatory Rheometry

Behaviour in the linear viscoelastic region is defined in Section B.1.2. To measure the change in the viscoelastic behaviour of a material over a range of temperatures, the material must exhibit linear viscoelastic behaviour as a liquid. A number of variables can be modified to place the liquid material in the linear viscoelastic region, and so oscillatory rheology testing is used to ascertain a suitable value for each variable.

Visco-elastic tests can be carried out with either oscillating stress (τ) or oscillating strain (γ). When oscillating stress is used, Equation [B.14] applies, and when oscillating strain is used, Equation [B.15] applies:

$$\tau = \tau_0.\sin(\omega t) \qquad [B.14]$$

$$\gamma = \gamma_0.\sin(\omega t) \qquad [B.15]$$

τ_0 is the stress amplitude, γ_0 is the strain amplitude, ω is the angular frequency of oscillation and t is the time. Visco-elastic tests provide data on the viscosity and elasticity related to the time-response of the material, and relates the angular frequency to the resulting oscillating strain. The viscoelastic behaviour observed lies between what is described in Kelvin-Voigt models and Maxwell models, which are discussed in further detail in Section 6.7. For a Kelvin-Voigt viscoelastic solid, the stress obtained is in phase with the stress, whilst for a Maxwell viscoelastic liquid, the stress obtained is 90° out of phase. The response of any visco-elastic fluid lies between these two extremes, as shown in Equation [B.16].

$$\tau = \tau_0.\sin(\omega t+\delta) \qquad [B.16]$$

Where δ is the phase angle, defined in such a way that if:

$\delta = 0$, the sample is defined as elastic

$\delta = 90°$, the sample is defined as viscous

$0 < \delta < 90$, the sample is defined as visco-elastic

When viscoelastic tests are carried out in an oscillating stress mode [B.14], the value of the oscillatory shear stress variable and oscillatory frequency variable determines whether the liquid material exists in the linear viscoelastic region. To obtain a value for the oscillatory shear stress variable, an oscillatory stress sweep is carried out on the material at a temperature above the sample melting point. A suitable stress variable value exists in the stress region where parameters G*, G', G", η', η" and η* present little change. These parameters are defined below:

- G* is the complex shear modulus, and is defined as τ_0 / γ_0, which represents the total resistance to the applied strain.
- G' is the elastic (or storage) modulus, which represents the stress energy temporarily stored during testing which is subsequently recovered.
- G" is the viscous (or loss) modulus, which is the stress energy used to initiate flow. It is 'lost' as it is transformed into shear heat.
- η' is the dynamic (absolute) viscosity, and describes the resistance to dynamic shear.
- η" is the storage viscosity, which is the ratio of the storage modulus to the angular frequency.
- η* is the complex viscosity, which is a frequency-dependent viscosity function. It is equal to the difference between the dynamic viscosity and storage viscosity

An oscillatory frequency sweep is used to ascertain a value for the oscillatory frequency variable. Linear viscoelastic behaviour is observed for oscillatory frequency values where G" is greater than G'. As the oscillatory shear stress influences the frequency regions where the material is linearly viscoelastic, the stress variable value obtained in the stress sweep experiment for the tested material must be used as a constant within the oscillatory frequency sweep.

Using the oscillatory shear stress and frequency values, oscillating stress mode tests can be carried out with temperature as a controlled variable. The loss (or damping) factor, tan(δ), can be defined as the quotient of the lost and stored deformation energies, as shown in Equation [B.17]:

$$\tan(\delta) = G''/G' \qquad [B.17]$$

The sol/gel transition occurs when tan(δ) = 1, when the loss modulus and storage modulus are equal. Liquid behaviour holds when tan(δ) > 1 (G" > G'), and solid behaviour holds when tan(δ) < 1 ((G" > G'). By carrying out an oscillating stress mode test over a temperature range, it is possible to obtain a sol/gel transition temperature for the material, using Equation [B.17].

B.2 Oscillatory Rheometry Testing of Waxes: Experimental Procedures

B.2.1 Introduction

The experiments of Section B.2.2 and Section B.2.3 were carried out to determine the stress and frequency parameters required to place the wax sample in the linear visco-elastic region at 80 °C. Linear viscoelastic behaviour is defined in Section B.1.2. The parameters and variables described within the oscillatory rheometry experiments of this section are defined in Section B.1.3.

For all the oscillatory tests, the same sample melting and setup procedures as those described in the flow curve experiments were used. A plate-plate separation distance of 300 μm was used, and a wax testing temperature of 80°C was chosen, as all graphite-filled wax samples were liquid at this temperature according to the temperature ramp experiments of Section 10.3.2.

B.2.2 Oscillatory Stress Testing

Within oscillatory stress testing, after the molten sample was positioned in the rotational rheometer set-up, the oscillating frequency was then set to 1 Hz, which was a figure drawn up from preliminary experiments. The first experiment for each composition was carried out over the AR500 operational oscillatory stress range (0.07938 – 3900 Pa), and data from this was used to carry out a second stress sweep on a new sample. In the second sweep, a smaller range of oscillatory stress values were studied, and corresponded to the stress region in the first experiment where the G', G" and |G*| curves formed a plateau region. This procedure was used to pinpoint a value that would be used as a constant within frequency sweep experiments.

B.2.3 Oscillatory Frequency Testing

Both G* and δ are also frequency dependent, and so oscillatory frequency testing (frequency sweeps) could determine whether the material's behaviour is changing from elastic to viscous, or visa-versa. Using a new wax sample, a frequency sweep was carried out. The oscillating stress constant was chosen according to the results of Section B.2.2, and the frequency sweep range ran from 0.0025 to 40 Hz.

G" and G' values were plotted graphically against oscillating frequency. Regions on the graph where G" is greater than G' can be described as linearly viscoelastic, and so frequencies within these ranges, at the constant oscillating stress stated, could be used within future temperature sweep experiments described in Section B.2.4. If there was no region on the graph where G" is greater than G', or if the transition points were not well defined, the stress sweep would be repeated, using an alternative oscillating frequency value (one which is not the original 1 Hz). A value within this stress plateau region would then be used within further oscillating frequency tests, and this process was repeated until a clearly defined viscoelastic window within oscillating frequency tests was found.

B.2.4 Temperature-related Oscillatory Behaviour

Oscillatory experiments with variable temperature (temperature sweeps) can be used to determine such parameters such as the sol/gel transition temperature, where the material behaviour changes from that of a viscous liquid to an elastic solid on cooling.

Temperature sweep experiments were carried out using a new wax sample. The oscillating stress and oscillating frequency values were chosen according to the results of the sweeps carried out in Section B.2.2 and Section B.2.3. The temperature was set on a ramp

going from 80°C to 55°C using a temperature ramp of 1°C.min^{-1}. This was then followed by a second ramp going from 55°C back up to 80°C. This ramp range was chosen as is should cover the solidification/melting processes of the wax matrices used, as stated in the manufacturer information given in Section 8.2.1.

B.3 Oscillatory Rheometry Testing of Waxes: Analysis and Evaluation

B.3.1 Introduction

The purpose of oscillatory testing is to find the position of the linear viscoelastic region, as defined in Section B.1.2. To measure changes in the viscoelastic behaviour of a material over a range of temperatures, one must first ensure that the testing parameters used place the liquid material within the linear viscoelastic region. These parameters are oscillatory shear stress and oscillatory frequency, and one must carry out tests on each of these over a range of parameter values, to find the regions where the material displays linearly viscoelastic character. As the value of one parameter has an influence of the linear viscoelastic region of the other, a series of experiments can be carried out, so that the interplay between stress and frequency can be taken into account.

B.3.2 Oscillatory Testing of Base Waxes

The procedures used for carrying out oscillatory stress sweeps and oscillatory frequency sweeps are described in Section B.2.2 and B.2.3 respectively. They were initially carried out at 70 °C, as both unfilled materials obeys AFE behaviour for a liquid at this temperature, as shown in Section 15.2.3. However, when oscillatory tests were carried out on filled samples, and more specifically carbon black-filled samples, the materials did not display viscoelastic behaviour over a wide range of tested oscillatory stress and oscillatory frequency values.

The oscillatory testing procedure is described in Section B.2.4, whereby oscillatory stress sweeps and oscillatory frequency sweeps are carried out to find stress and frequency values that place the material (at 80 °C), in the linear viscoelastic region. The graphs for these tests for the A7-7808 base wax are shown in Figure B.2, B.3 and B.4. The complex shear modulus (|G*|), phase angle (δ), storage modulus (G') and loss modulus (G") were plotted graphically against the oscillatory stress, with terms defined in Section B.1.3. In the first stress sweep (Figure B.2), the stress region where the plotted curves presented little change was used as the experimental range for the second stress sweep (Figure B.3), and from this graph, a suitable oscillatory stress value was taken for use in oscillatory frequency sweeps (Figure B.4). Within frequency sweeps, a suitable frequency value was chosen from a region on the graph where G" > G'. The graphs for these tests for the A7-TC2/e base wax are shown in Figure B.5, B.6 and B.7.

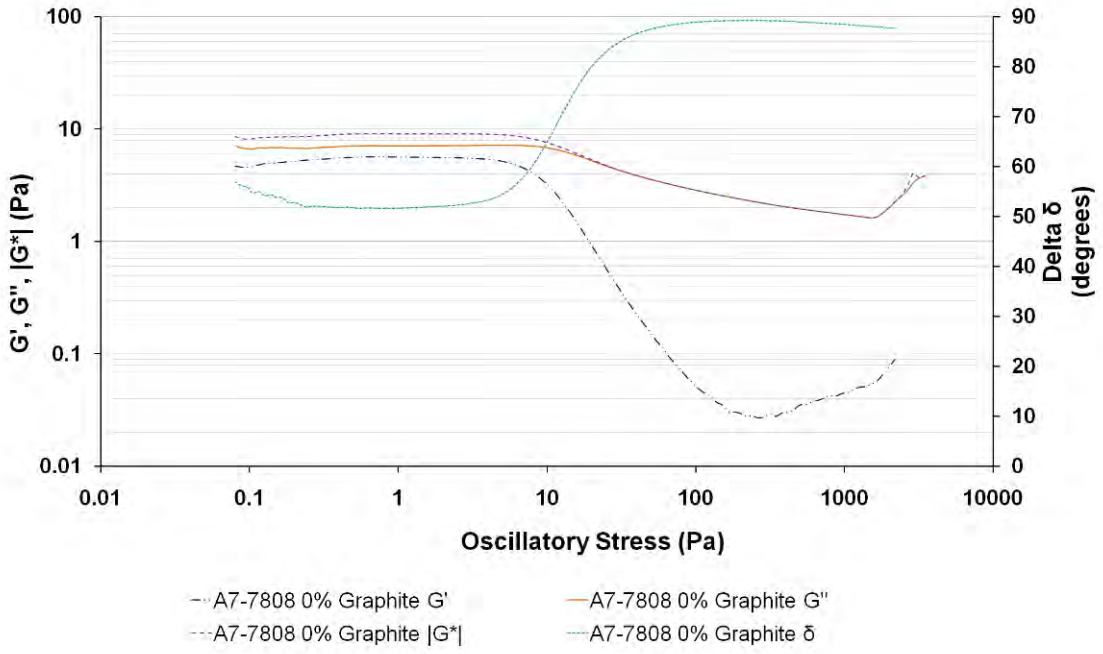

Figure B.2 Graph showing the change in G', G", |G*| and δ across a range of oscillatory stress values (0.07958 – 3500 Pa) for the A7-7808 base wax in a rotational rheometer. Oscillatory frequency was set to 1.0 Hz. Temperature was set to 80 °C.

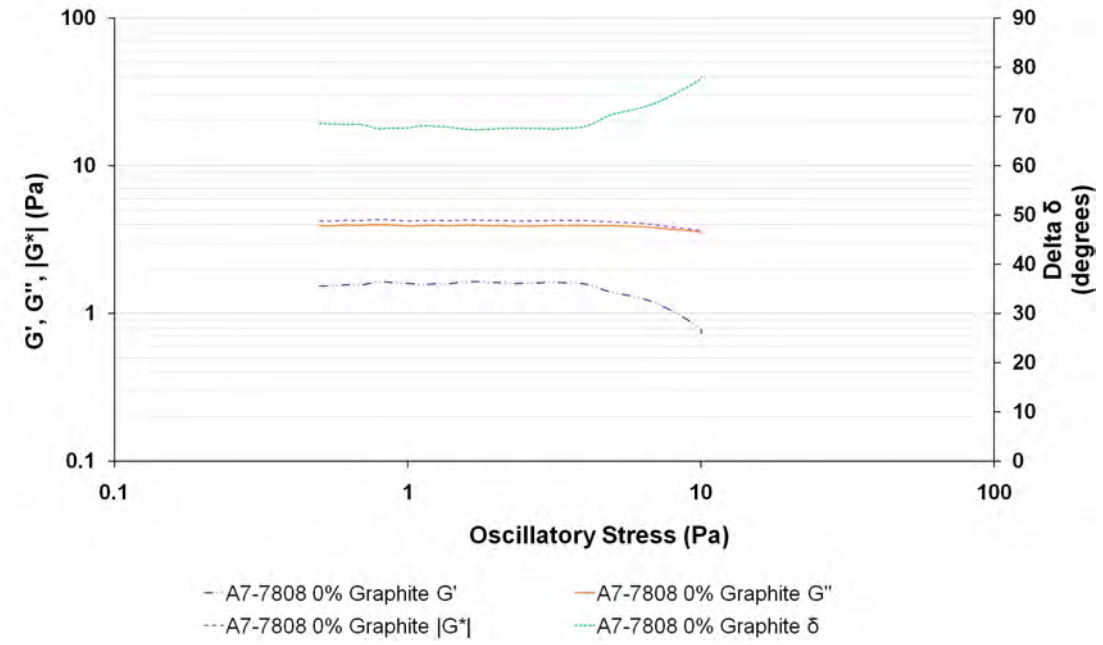

Figure B.3 Graph showing the change in G', G'', |G*| and δ across a range of oscillatory stress values (0.5 – 10.0 Pa) for the A7-7808 base wax in a rotational rheometer. Oscillatory frequency was set to 1.0 Hz. Temperature was set to 80 °C.

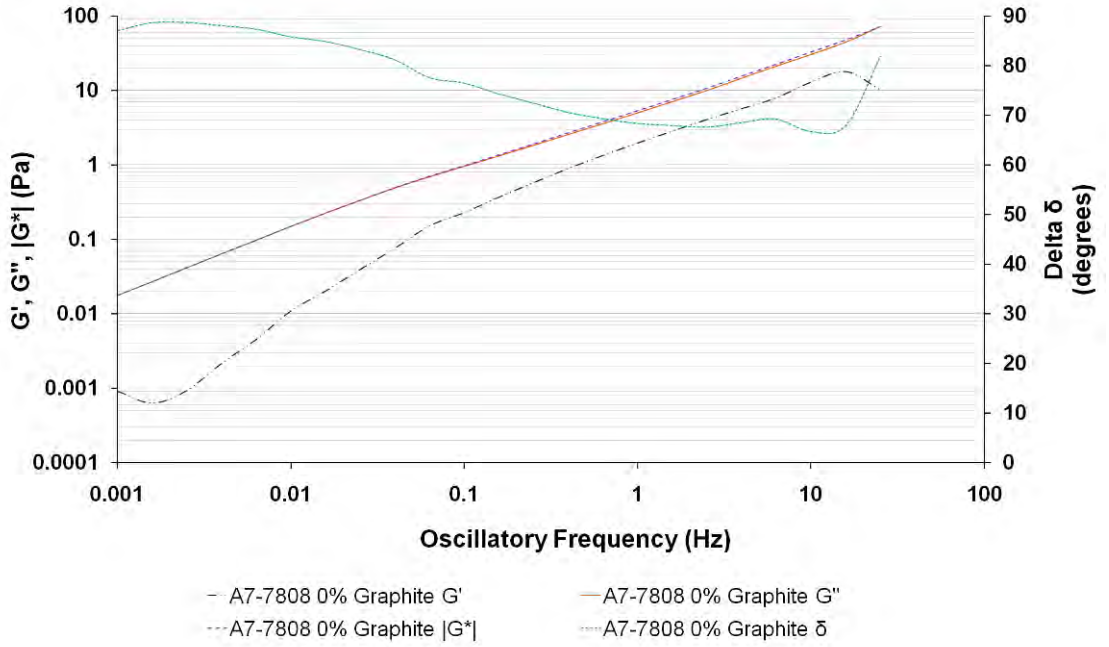

Figure B.4 Graph showing the change in G', G'', |G*| and δ across a range of oscillatory frequency values (0.001 to 40 Hz) for the A7-7808 base wax in a rotational rheometer. Oscillatory stress was set to 2.0 Pa. Temperature was set to 80 °C.

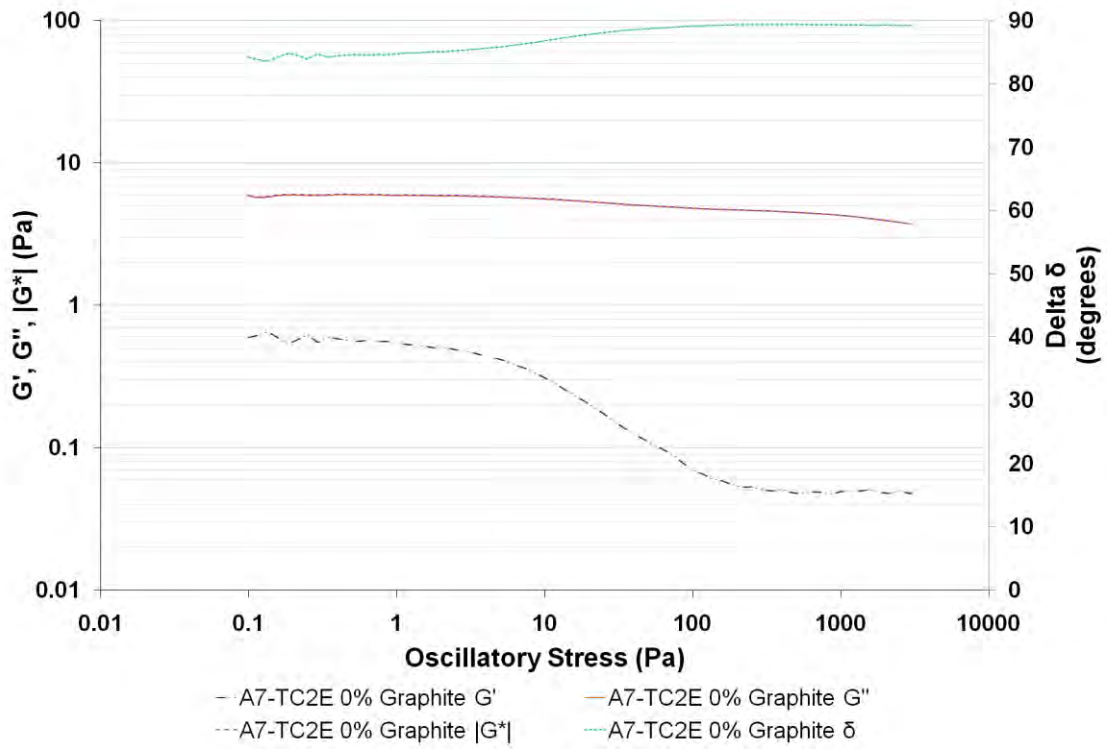

Figure B.5 Graph showing the change in G', G'', |G*| and δ across a range of oscillatory stress values (0.1 – 3500 Pa) for unfilled A7-TC2/e wax in a rotational rheometer. Oscillatory frequency was set to 1.0 Hz. Temperature was set to 80 °C.

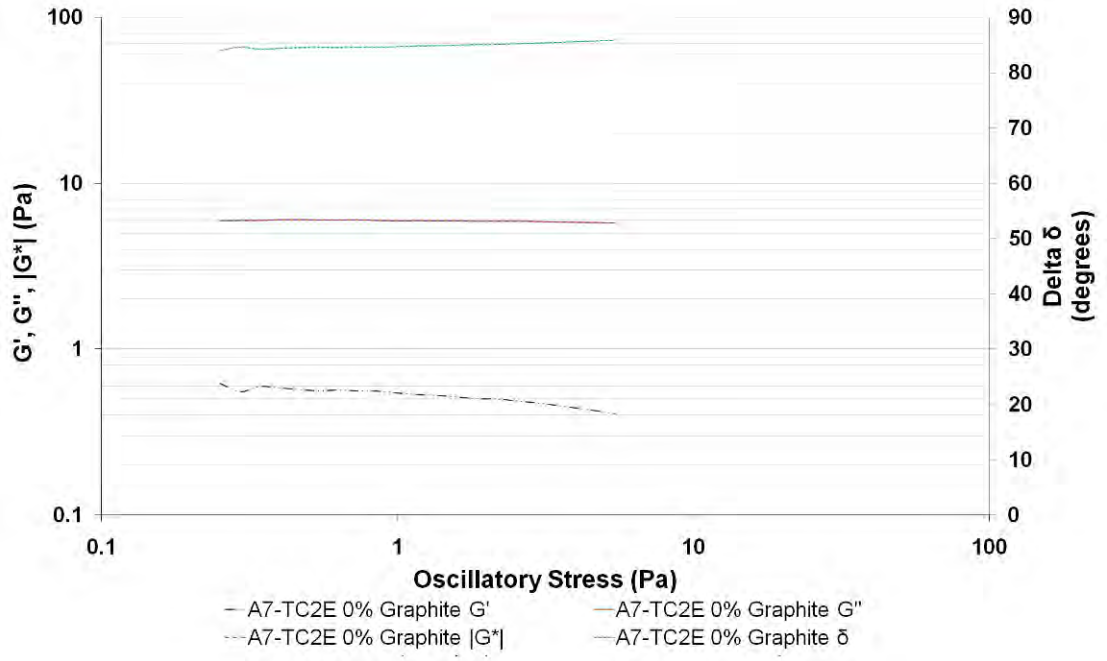

Figure B.6 Graph showing the change in G', G'', |G*| and δ across a range of oscillatory stress values (0.25 – 5.0 Pa) for unfilled A7-TC2/e wax in a rotational rheometer. Oscillatory frequency was set to 1.0 Hz. Temperature was set to 80 °C.

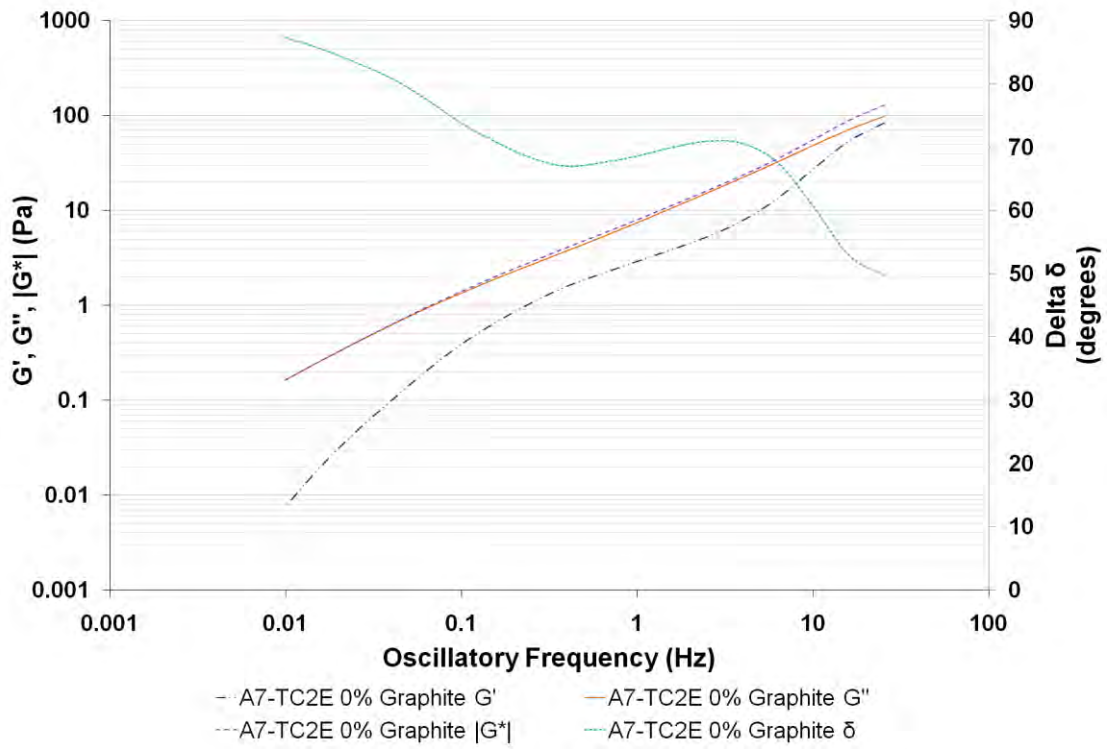

Figure B.7 Graph showing the change in G', G'', |G*| and δ across a range of oscillatory frequency values (0.01 to 40 Hz) for unfilled A7-TC2/e wax in a rotational rheometer. Oscillatory stress was set to 0.5 Pa. Temperature was set to 80 °C.

For the A7-7808 base wax, stress and frequency parameters of 2.0 Pa and 1.0 Hz were chosen, respectively, for use within oscillatory sweeps across a temperature range, as shown in Figure B.8 and B.9. The procedure used is described in Section B.2.4. For the A7-7808 grade cooling curve in Figure B.8, the gradient of the G', G'' and |G*| curves follow AFE liquid behaviour at temperatures above 71.5 °C. The magnitude of δ, as described in Section B.1.3, shows us whether the material is predominantly viscous (δ → 90°) or predominantly elastic (δ → 0°) in nature. In the cooling curve, the material behaves in a viscous manner in a plateau region where δ ≈ 87°. When the temperature drops below 71.5 °C, the gradients of the G', G'' and |G*| curves increase in magnitude, with the G'' and G' curves intersecting at 67.5 °C. Below 71.5 °C, the gradient of the δ curve rapidly increases in magnitude, and reaches a lower plateau region at 66 °C, where δ lies between 12.5 and 20.0°.

For the A7-7808 heating curve, shown in Figure B.9, a number of differences are present. As the temperature is increased, elastic behaviour is a dominant, and the δ value increases steadily from 12° at 62 °C to 24.5° at 65 °C. The intersection point between G' and G" curves occurs at approximately 66.5 °C (which is close to the value ascertained in the down sweep), although a region from 68 °C to 72 °C exists where the G' and G" curve paths do not diverge from one another. The δ curve at these temperatures forms a plateau, with 62.5° < δ < 70°. Between 77 and 80 °C, the behaviour of G', G", |G*| and δ is very similar to that observed at these temperatures within the cooling sweep, which suggests that linear viscoelastic behaviour holds for semi-solid and solid regions (Cirre Torres, 2004).

For the A7-TC2/e base wax, stress and frequency parameters of 0.5 Pa and 1.0 Hz were used, with temperature sweeps for this grade shown in Figure B.10 and B.11. For the A7-TC2/e base wax cooling graph, as shown in Figure B.10, the gradient of the G', G" and |G*| curves follow AFE behaviour at temperatures above 70 °C, where δ ≈ 86.7°. Like with the A7-7808 grade, the G', G" and |G*| curve gradients increase in magnitude below this temperature, and the G" and G' curves intersect at 67.0 °C. The gradient of the δ curve rapidly increases in magnitude at temperatures below 70 °C, so that δ = 10° at 65 °C.

Unlike for the A7-7808 grade, the shape G', G", |G*| and δ curves are not drastically changed in the heating (up) sweep in Figure B.11. The position of these curves in the temperature range is, however, altered. On heating, δ does not start to increase from a value approximately 19° until a temperature of 69 °C is reached, and the G'/G" intersection occurs at 72.3 °C.

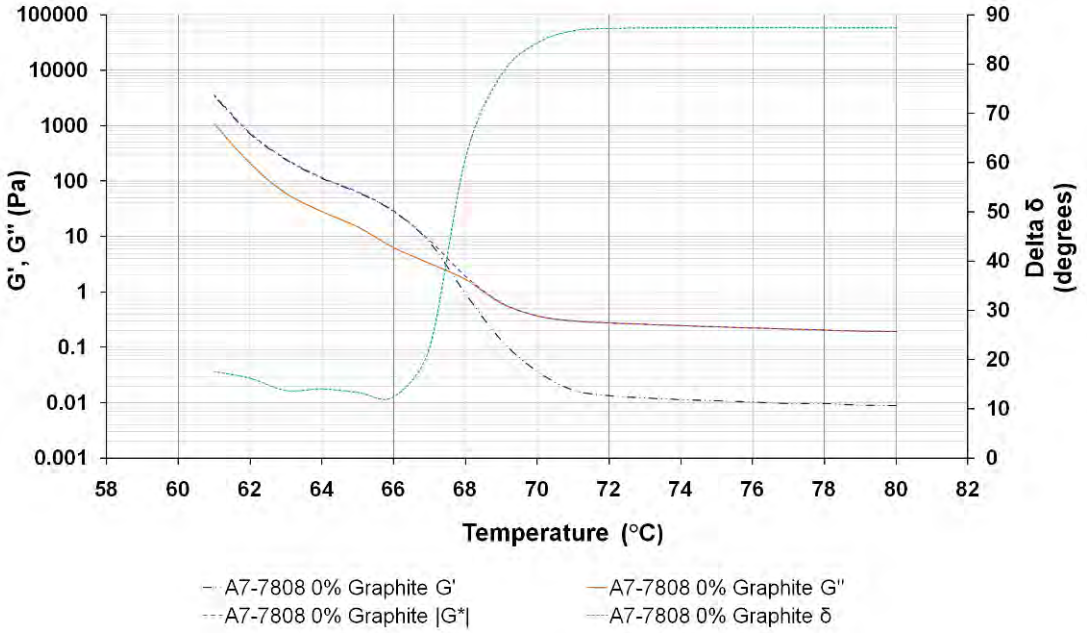

Figure B.8 Graph showing the change in G', G", |G*| and δ across a range of temperatures (cooling sweep from 80 °C to 60 °C) for unfilled A7-7808 wax in a rotational rheometer. Oscillatory stress was set to 2.0 Pa. Oscillatory frequency was set to 1 Hz.

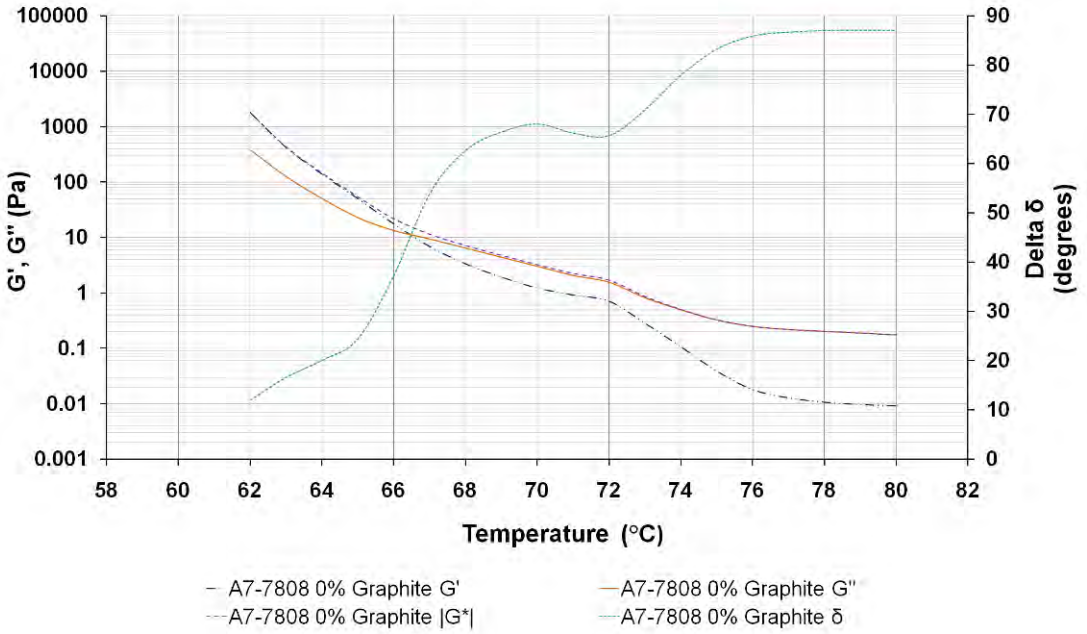

Figure B.9 Graph showing the change in G', G", |G*| and δ across a range of temperatures (heating sweep from 60 °C to 80 °C) for unfilled A7-7808 wax in a rotational rheometer. Oscillatory stress was set to 2.0 Pa. Oscillatory frequency was set to 1 Hz.

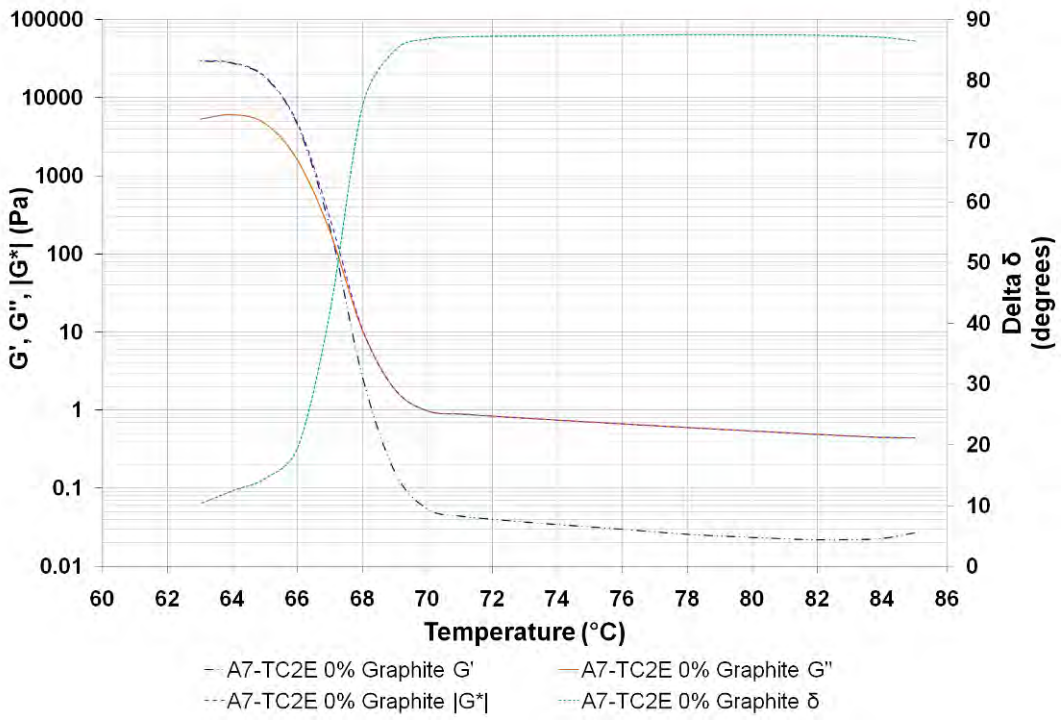

Figure B.10 Graph showing the change in G', G", |G*| and δ across a range of temperatures (cooling sweep from 85 °C to 60 °C) for unfilled A7-7808 wax in a rotational rheometer. Oscillatory stress was set to 0.5 Pa. Oscillatory frequency was set to 1 Hz.

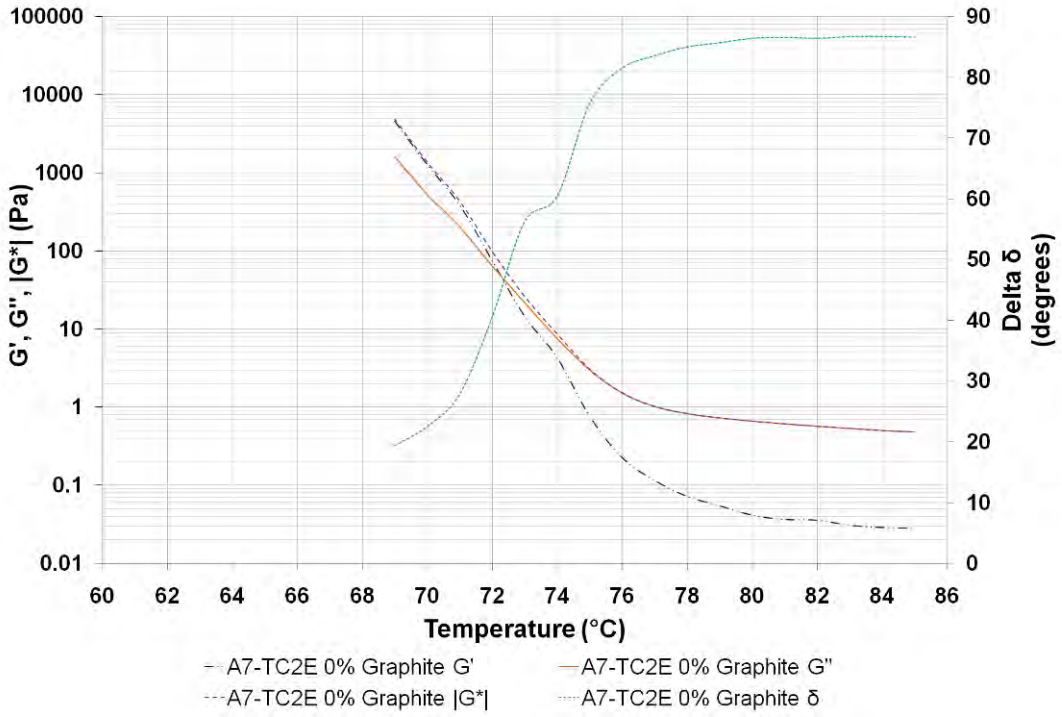

Figure B.11 Graph showing the change in G', G", |G*| and δ across a range of temperatures (heating sweep from 60 °C to 85 °C) for unfilled A7-7808 wax in a rotational rheometer. Oscillatory stress was set to 0.5 Pa. Oscillatory frequency was set to 1 Hz.

The gradients of the heating sweep curves are shallower than those in the cooling sweep. As with the temperature ramp experimental results discussed in Section 15.2.3, the differences between heating and cooling curves can be attributed to the composition of the wax. Even though the composition of the A7-7808 wax is unknown, it is proposed that it is a blend that contains both wax and resin components. Resins tend to have higher melting points than waxes, and as the wax cools from high temperatures, the motion of the rheometer ensures a homogenous distribution of components.

When the wax blend is heated, the wax tends to melt first, and leaves the resin component as solid particles in suspension until the resin melts. The presence of solid particles in suspension raises the value of G', G" and |G*|, and additionally lowers the δ value of the material at a given temperature (i.e. it has greater elastic character). Within the temperature region from 68 °C to 72 °C, solid resin particles are thought to be present.

B.3.3 Oscillatory Testing of Conductive Particle-Filled Waxes

For graphite and carbon black-filled waxes, the same oscillatory stress and frequency sweep procedures were carried out as for the base grades, using methods described in Section B.2. For graphite-filled A7-7808 and A7-TC2/e samples, G', G", |G*| and δ curves formed a plateau within oscillatory stress experiments that could be used to arrive at a stress parameter value. It was important to note the position of the G' and G" curves in the stress sweep. G" values in the plateau region should be greater than G', as the material's behaviour under those conditions can be described as linearly viscoelastic. This was the case for the unfilled waxes, although the effects of filler modification made the process of selecting of stress and frequency parameter values a more complicated one.

The use of a constant 1.0 Hz frequency in the stress sweep for the carbon black–filled waxes and high concentration graphite-filled waxes resulted in sweep curves where G' was greater than G" in the plateau region. The 18 vol% graphite-filled A7-TC2/e wax composition, whose stress and frequency sweeps are shown in Figures B.12 to B.14, is used as an example. In these cases, an oscillatory frequency sweep was carried out as shown in Figure B.13, and a frequency value was taken from a place where G" > G'. This frequency parameter was then used within a second stress sweep experiment, as shown in Figure B.14, and a suitable stress parameter value was determined from this before the usual testing order was resumed.

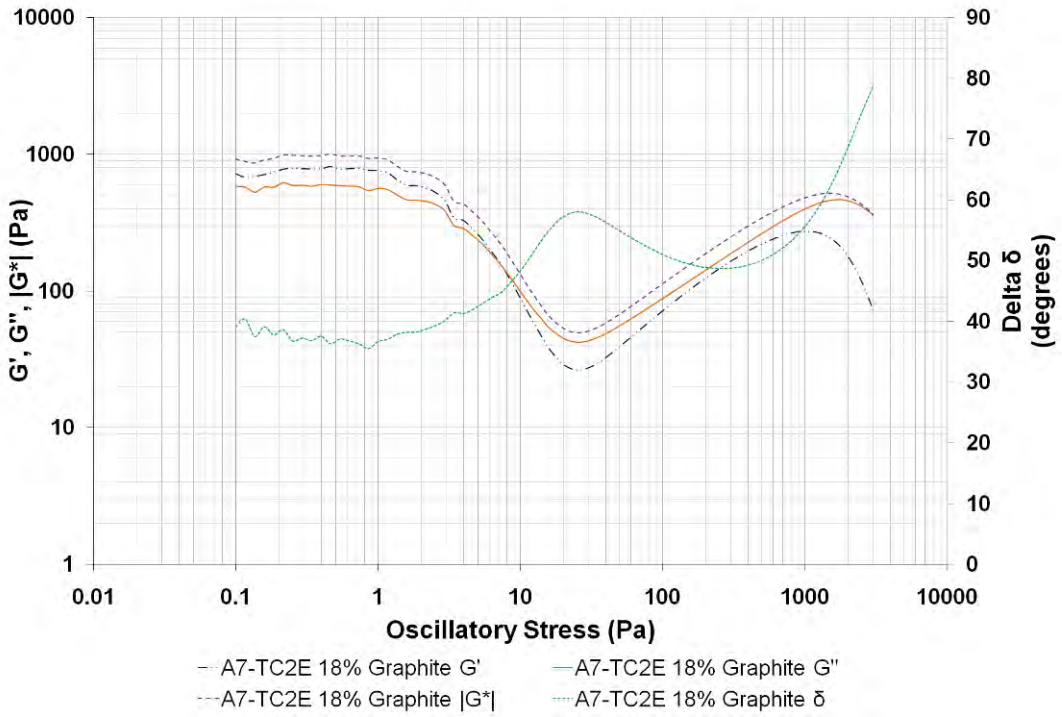

Figure B.12 Graph showing the change in G', G", |G*| and δ across a range of oscillatory stress values (0.1 – 3500 Pa) for 18 vol% graphite-filled A7-TC2/e wax in a rotational rheometer. Oscillatory frequency was set to 1.0 Hz. Temperature was set to 80 °C.

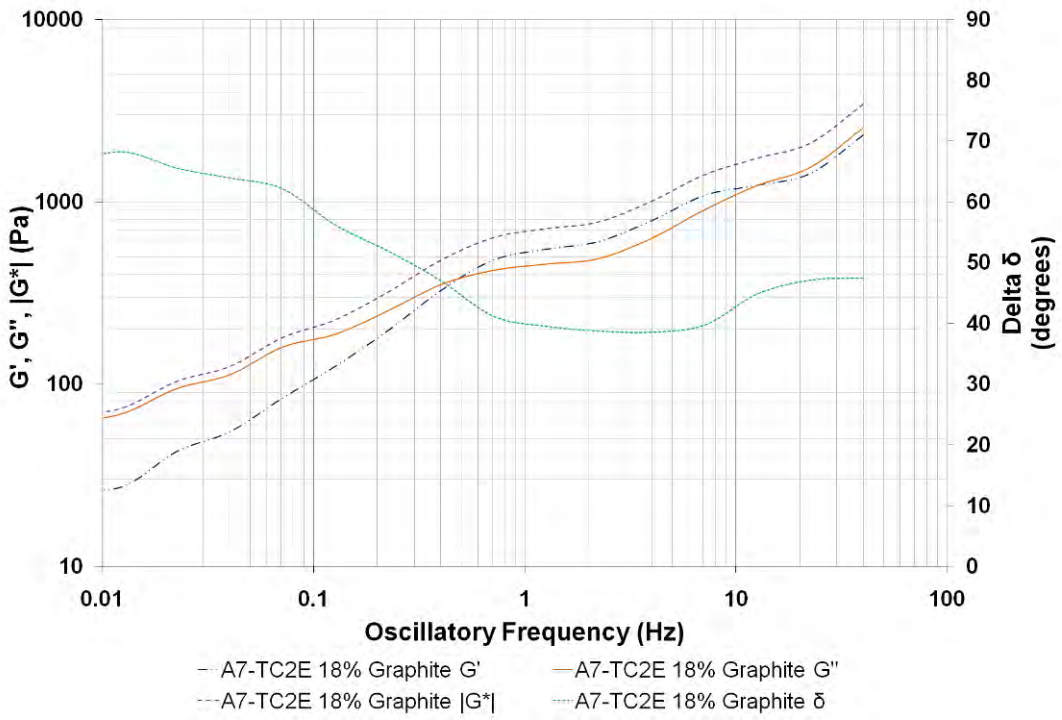

Figure B.13 Graph showing the change in G', G", |G*| and δ across a range of oscillatory frequency values (0.01 to 40 Hz) for 18 vol% graphite-filled A7-TC2/e wax in a rotational rheometer. Oscillatory stress was set to 0.5 Pa. Temperature was set to 80 °C.

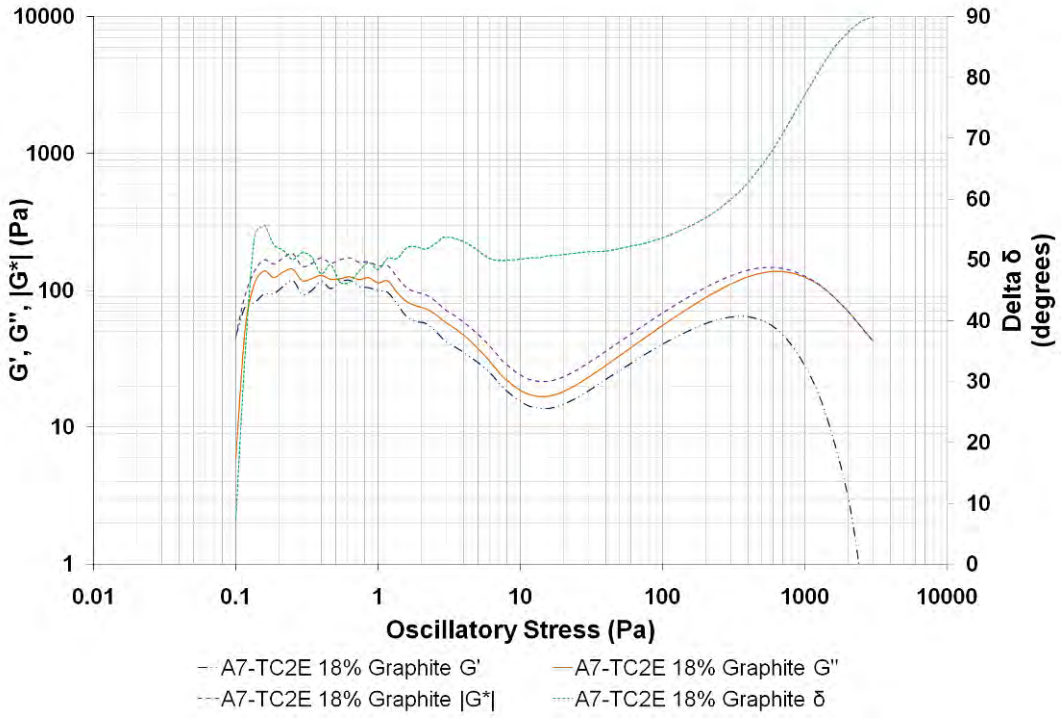

Figure B.14 Graph showing the change in G', G", |G*| and δ across a range of oscillatory stress values (0.1 – 3500 Pa) for 18 vol% graphite-filled A7-TC2/e wax in a rotational rheometer. Oscillatory frequency was set to 0.1 Hz. Temperature was set to 80 °C.

Stress and frequency parameters derived from oscillatory stress and frequency sweeps, for use within temperature sweeps, are shown in Table B.2 and Table B.3. From these tables, one can see how filler addition alters the position of parameter values. As the filler content is increased, the required frequency is generally shifted to lower values, as G' is greater than G" at medium to high frequencies for high filler concentration samples.

Table B.2 Oscillatory testing parameters derived from stress and frequency sweeps for graphite-filled A7-7808 and A7-TC2/e waxes

A7-7808 Wax	**vol% micronised graphite filler**				
	0.0	**6.0**	**10.0**	**14.0**	**18.0**
Oscillatory Stress (Pa)	2.0	0.5	0.8	0.3	0.6
Oscillatory Frequency (Hz)	1.0	1.59	1.59	0.1	0.1
A7-TC2/e Wax	**vol% micronised graphite filler**				
Oscillatory Stress (Pa)	0.5	0.5	0.35	0.35	0.2
Oscillatory Frequency (Hz)	1.0	1.0	0.1	0.1	0.1

Table B.3 Oscillatory testing parameters derived from stress and frequency sweeps for carbon black-filled A7-7808 and A7-TC2/e waxes

A7-7808 Wax	**vol% Vulcan carbon black filler**			
Parameters	0.0	6.9	11.4	15.9
Oscillatory Stress (Pa)	2.0	1.0	10.0	-*
Oscillatory Frequency (Hz)	1.0	0.05	0.05	-*
A7-TC2/e Wax	**vol% Vulcan carbon black filler**			
Oscillatory Stress (Pa)	0.5	10.0	10.0	-*
Oscillatory Frequency (Hz)	1.0	0.1	0.05	-*

* At 15.9 vol% carbon black, no values for stress and frequency could be given where G" > G'

Within the present work, the change in δ with sample temperature is plotted for each composition, and the position of the G'/G" intersection point for each composition is shown in Table B.4 and Table B.5. For micronised graphite-filled A7-7808 wax, δ graphs are shown in Figure B.15. In the cooling sweep, the base wax changes from a highly viscous material at

temperatures above 70 °C to a highly elastic one below 66 °C, with a steep transition region between the two plateaus, as described in Section B.3.2.

The concentration of graphite filler addition is linked to a corresponding reduction in the value of δ in the upper plateau region, going from 87° at 0 vol% to 48° at 14 vol%. Additionally, the temperature when the gradient of the δ curve starts to increase in magnitude increases with filler content. For example, the 10 vol% graphite grade sees the δ curve gradient increase in magnitude below 74 °C. Whilst the gradient of the curve in the transition region is steep for the unfilled wax, the gradient becomes shallower as filler content is increased. Across the temperature range studied, increasing the filler concentration causes a shift in the position of these curves to higher G' and G" values. The shape of the G' and G" curves in the heating and cooling ramps in graphite-filled samples follows that displayed by the unfilled A7-7808 grade, as described in Section B.3.2.

In the cooling curve, the position of transition point where G' = G" (δ = 45°) occurs at increasing temperatures with filler addition, as shown in Table B.4. For the graphite-filled A7-7808 wax heating curves, the G" and G' curves do not diverge from one another for several degrees above the transition temperature (as described in Section B.3.2 for the base wax). The transition point, however, stays relatively constant with graphite filler addition.

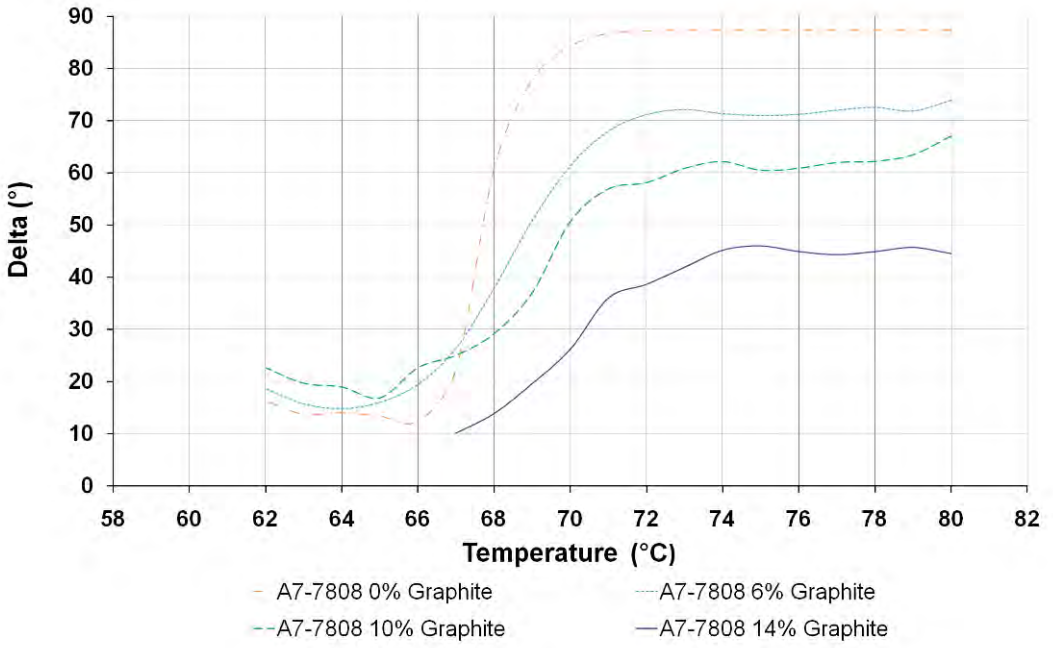

(a)

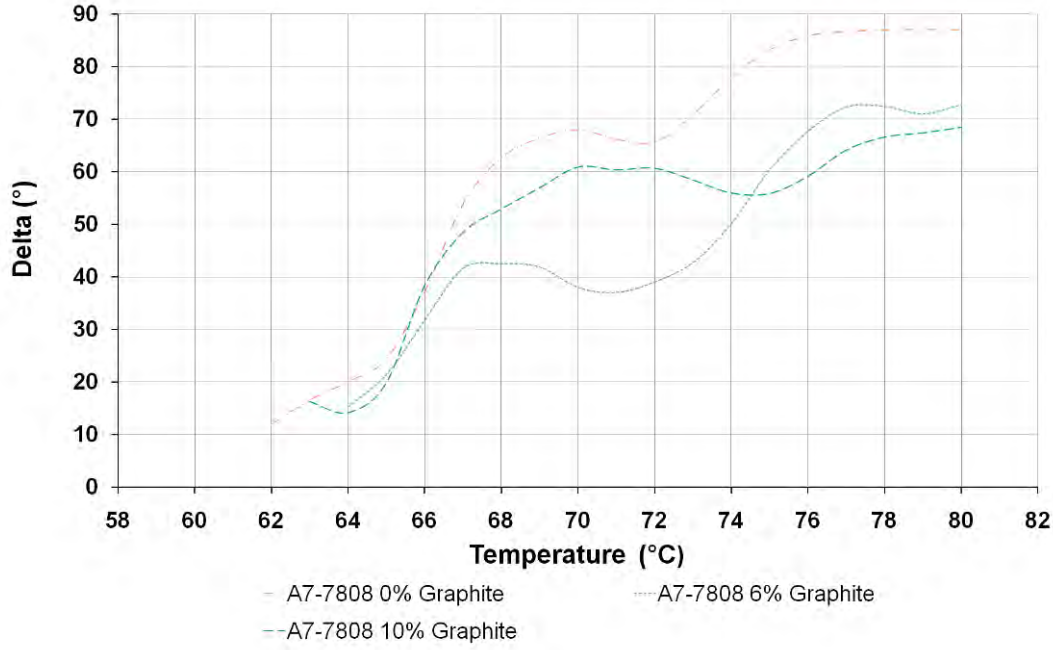

(b)

Figure B.15 Graph showing the change in δ across a range of temperatures for graphite filled A7-7808 waxes at differing concentrations in a rotational rheometer. Oscillatory stress and frequency parameters were set according to values in Table 15.11. Graph **(a)** is the cooling sweep (80 °C to 55 °C), whilst graph **(b)** is the heating sweep (55 °C to 80 °C)

The graphite-filled waxes displays similar behaviour to the unfilled A7-TC2/e counterpart in δ heating curves, which is described in Section B.3.2. Materials behave in a highly elastic manner (δ ≈ 10°) at low temperatures, and the curve gradient increases at about 70 – 71 °C. The gradient of the δ curve on heating is shallower than the ones formed on cooling, for all compositions. The change in the position of the G'/G" intersection point is shown in Table B.4. The main differences between the grades on the cooling sweep corresponds firstly to the gradient of the G' and G" curves as the material is cooled, which is far steeper for the both the A7-TC2/e grade and its graphite-filled derivatives. Secondly, the relationship between graphite concentration and the shift in G' and G" values at a given temperature is greater in the A7-7808 wax. For the heating sweep shown, the G' and G" curves shown in the cooling sweep undergo a transformation. The G'/G" transition and associated steep gradient region is shifted to higher temperatures, as shown in Table B.4. The point for each curve when the gradient becomes shallower at the temperatures is increased is also shifted to higher temperatures. The gradient of the curves in the heating sweep are shallower than those in the cooling sweep.

Table B.4 Results obtained from oscillatory testing, marking the temperature values when G' = G" (δ = 45°) for graphite-filled wax samples

A7-7808 Wax	vol% micronised graphite filler			
G' = G" Transition	0.0	6.0	10.0	14.0
Cooling Ramp Transition (°C)	67.6	68.6	69.6	73.7
Heating Ramp Transition (°C)	66.4	73.3* (67.4)	66.6	68.5
A7-TC2/e Wax	vol% micronised graphite filler			
Cooling Ramp Transition (°C)	67.1	67.7	68.5	69.5
Heating Ramp Transition (°C)	72.3	73.5	72.9	75.5

* The transition point for this composition was unclear, as the G' and G" curves were in very closely proximity from 67.4 to 73.3 °C.

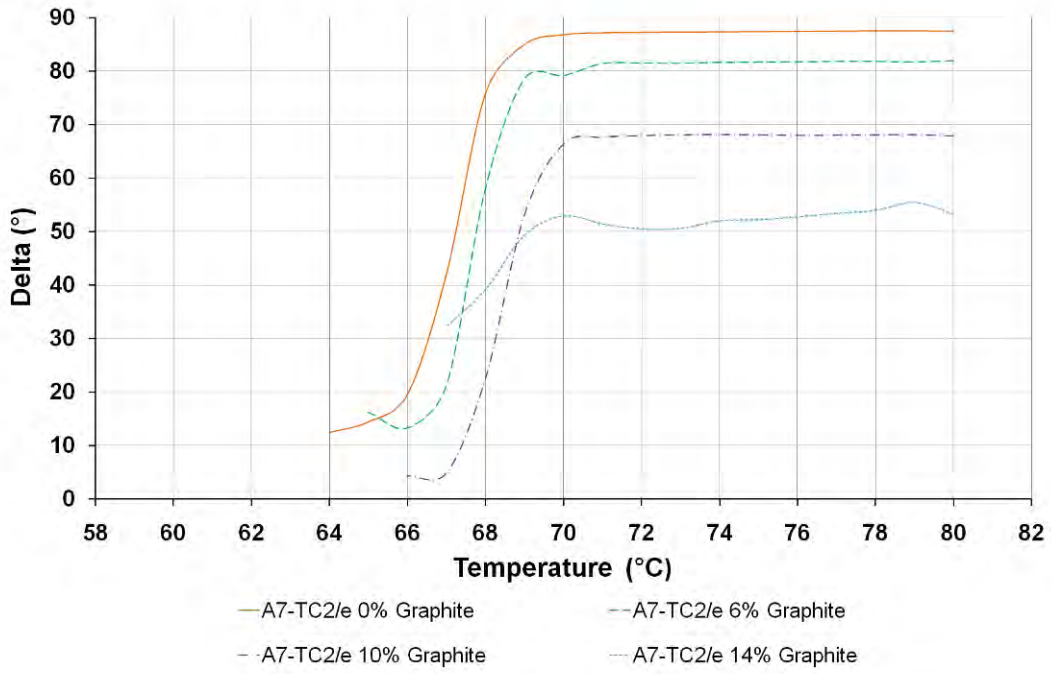

(a)

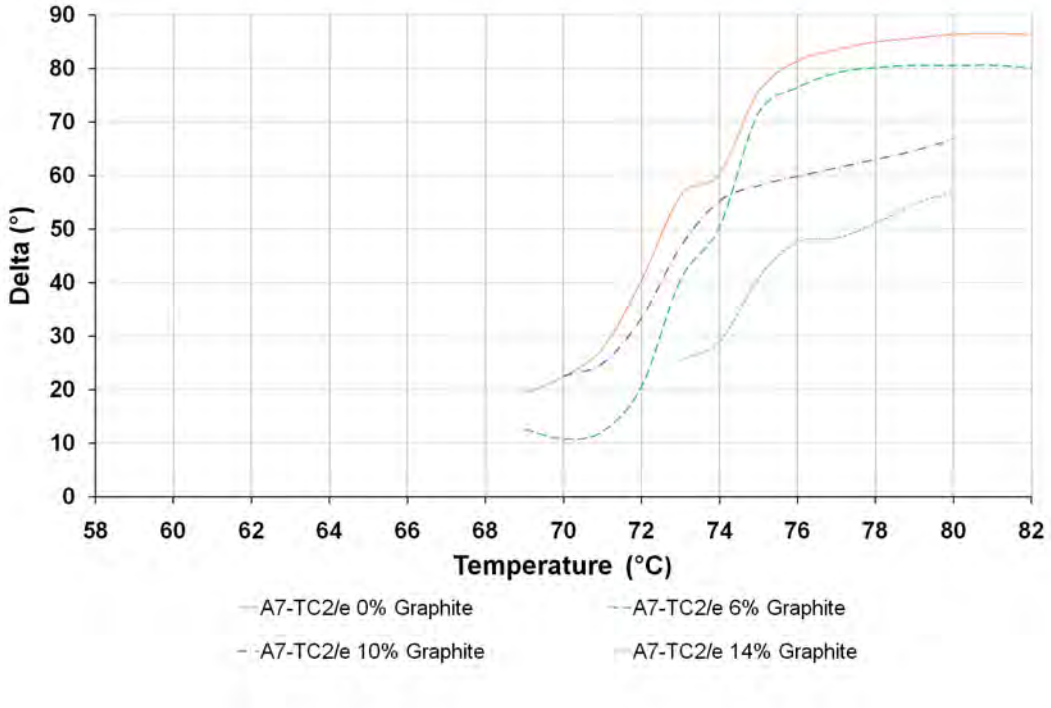

(b)

Figure B.16 Graph showing the change in δ across a range of temperatures for graphite filled A7-TC2/e waxes at differing concentrations in a rotational rheometer. Oscillatory stress and frequency parameters were set according to values in Table 15.11. Graph **(a)** is the cooling sweep (82 °C to 55 °C), whilst graph **(b)** is the heating sweep (55 °C to 82 °C)

For the carbon black filled samples, the number of temperature sweeps were more limited due to problems associated with anomalous results within each sweep, especially at lower temperatures. Additionally, the difference between the G' and G" curves at the highest studied temperatures was small, and so gauging the position of the intersection point was prone to error.

The changes in the value of δ with temperature for the cooling and heating sweeps are shown in Figure B.17. For the cooling sweep, a plateau region exists in both the 6.9 vol% and 11.4 vol% carbon black-filled wax samples at temperatures above 70 °C. The δ values were more variable in this region for the 11.4 vol% carbon black-filled wax, which can be attributed to the presence of particle clustering and therefore distributional inhomogeneities in the samples. In the heating (up) sweep, anomalous readings from multiple samples meant that only the 6.9 vol% carbon black-filled A7-TC2/e wax sweep could be plotted, and this sample exhibited gradient changes at the same temperatures as the unfilled base wax, all be it with a lowered maximum δ value of 50°.

In both the cooling and heating sweeps for carbon black-filled A7-TC2/e waxes, the G' and G" curves have a minimum value before the gradient increases again with temperature. The shift in the G"/G' transition temperature goes from 67.1 °C at 0 vol% to 69.4 °C at 6.9 vol% carbon black, as shown in Table B.5, although this position is disputable due to the shape of the G' and G" curves.

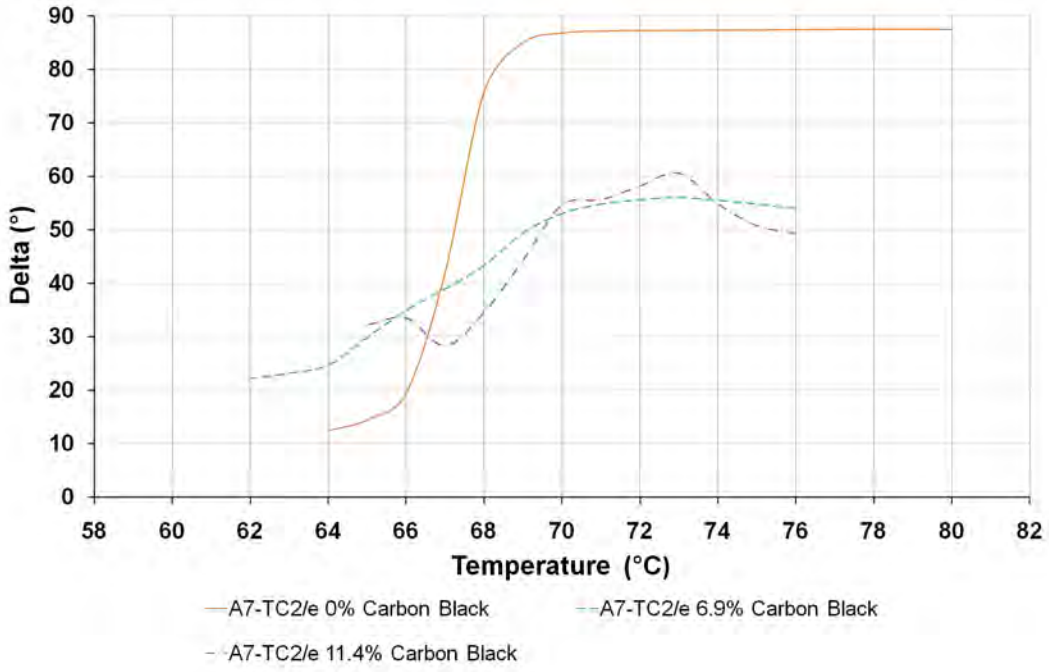

(a)

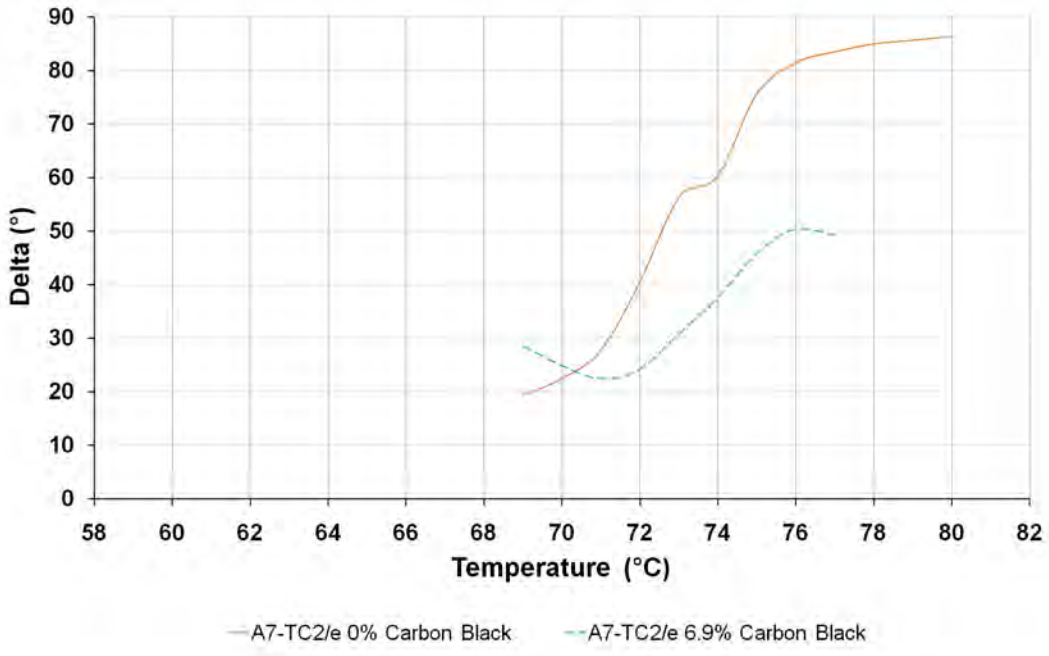

(b)

Figure B.17 Graph showing the change in δ across a range of temperatures for carbon black-filled A7-TC2/e waxes at differing concentrations in a rotational rheometer. Oscillatory stress and frequency parameters were set according to values in Table 15.12. Graph **(a)** is the cooling sweep (80 °C to 55 °C), whilst graph **(b)** is the heating sweep (55 °C to 80 °C)

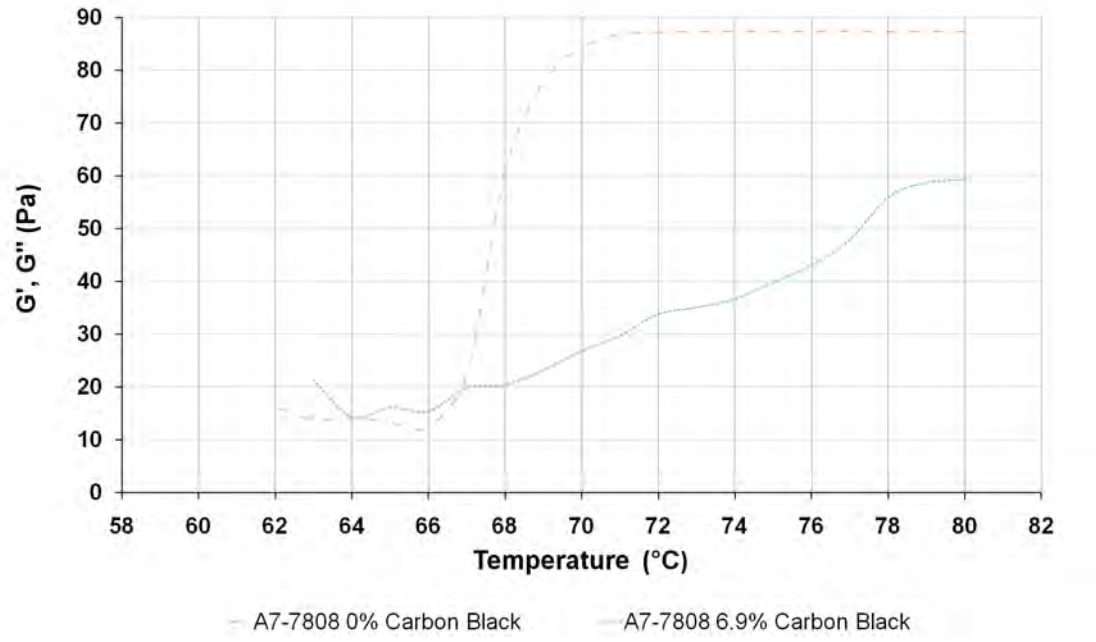

Figure B.18 Graph showing the change in δ across a range of temperatures for carbon black-filled A7-7808 waxes at differing concentrations in a rotational rheometer. Oscillatory stress and frequency parameters were set according to values in Table 15.11. The cooling sweep (80 °C to 55 °C) is shown.

The change in the shape of the delta (δ) curves with temperature for the carbon black-filled A7-7808 wax grade is shown in Figure B.18. The 6 vol% carbon black-filled A7-7808 wax displayed no upper plateau region of δ values, and instead displayed a shallow curve gradient, going from δ ≈ 58° at 80°C to δ ≈ 15° at 64°C. The initial δ value at the start of the sweep was comparable to that of the 14 vol% graphite-filled A7-7808 sample. The shift in the G"/G' transition temperature goes from 67.6 °C at 0 vol% to 76.2 °C at 6.9 vol% carbon black, as shown in Table B.5. The heating (up) ramp is not present within the present work, as anomalous readings from multiple samples meant that the sweep associated with the A7-TC2/e base wax was the only one that could be plotted.

Table B.5 Results obtained from oscillatory testing, marking the temperature values when G' = G" (δ = 45°) for carbon black-filled wax samples

A7-7808 Wax	vol% Vulcan carbon black filler			
G' = G" Transition	0.0	6.9	11.4	15.9
Cooling Ramp Transition (°C)	67.6	76.2	-*	-*
Heating Ramp Transition (°C)	66.4	-*	-*	-*
A7-TC2/e Wax	vol% Vulcan carbon black filler			
Cooling Ramp Transition (°C)	67.1	69.4	69.2	-*
Heating Ramp Transition (°C)	72.3	75.2	-*	-*

* With carbon black addition, anomalous results meant that G', G" and δ curves could not be plotted.

The viscoelastic behaviour of the A7-7808 and A7-TC2/e base waxes is described in Section B.3.2. When molten, both the base wax grades possess highly viscous behaviour, as the phase angle (δ) has a value near 90°. The addition of graphite filler decreases the value of δ in the molten sample, and the decrease is linked to the percentage of filler added. This increase in material elasticity with graphite filler addition is greater when the A7-7808 wax is used. This runs in line with the findings of Section 15.2.2, where the relative viscosity increase with graphite filler addition was greater for the A7-7808 wax. The effect that water-filler has in reducing the flow behaviour-modifying effect of graphite filler is not clear, and conclusions cannot be made until the effect of graphite filler addition on viscosity and viscoelastic behaviour for multiple wax grades is studied.

The use of carbon black filler acts in a similar way to the graphite, although its effect in reducing the δ value in the molten sample is far greater. Filler concentration is linked to an increase in the value of G' and G" at a specific temperature, and the presence of filler also smoothes the gradient of parameters over the solid/liquid transition region.

Appendix C – Additional Wax Properties

C.1 Wax Conductivity Measurements

C.1.1 Multimeter Conductivity Measurements for Waxes

C.1.1.1 Introduction and Methods

The initial experiments to determine the critical volume fraction for conductance, V_c, used a set-up described below, to study carbon black-filled and micronised graphite-filled A7-11 wax samples. A Fluke 83 multimeter was used to test the resistance between two parallel aluminium films that were 25 mm apart, mounted on a glass microscopy slide. The separation distance between them is bridged when a fixed volume of molten wax is placed on the glass slide so the wax makes contact with the top of each aluminium contact. The molten wax conductivity bridge is then sheared using a second glass slide, so that the wax sample has a thickness of 1 mm between plates. Any excess wax that is pushed to the edge of the slide gap on shearing is removed.

Resistance measurements can be taken across a wide range of filled wax compositions, as the more viscous forms could be compressed into a sheet of material by applying shear forces across the upper glass slide. The glass slides themselves were heated to wax mixing temperatures, to aid shear and prevent premature cooling.

C.1.1.2 Multimeter Measurement Results

Figure C.1 and Table C.1 show the results of these experiments graphically as plots of average sample resistance against the volume percent of conducting particle filler. As described in Section 5.4, the percolation threshold in this situation is defined as the

concentration when conductive particles in suspension form a continuous network. This is observable when the sample resistivity drops significantly from the value of the insulating matrix material. As described in Section 15.1.2, it is therefore only possible to estimate a value for V_c using the present set-up. In order to convert resistance to resistivity, the sample geometry has to be precisely defined and corrected for. The sample geometry and electrode tab positioning would make such calculations prone to error, and so only the resistance values across the sample are used here.

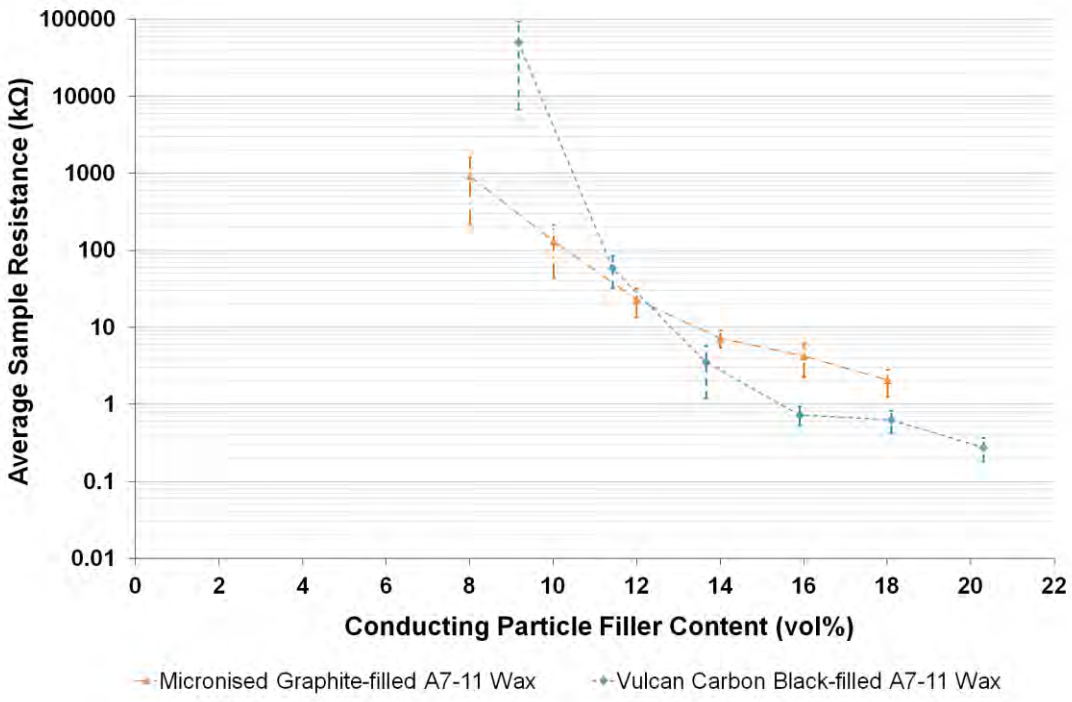

Figure C.1 Graph showing the relationship between the material samples' electrical resistance (kΩ) and the conductive filler content in A7-11 wax, according to the results from a set-up where the material is sheared to form a bridge between aluminium conductive tabs.

The difference in the shape of the two curves featured in Figure C.1 can be combined with observations made during sample formation, to explain the filler content-conductivity relationships. None of the graphite-filled A7-11 wax samples displayed resistance values when the filler concentration was 6 vol% (12.36 wt%) or lower, and the

relationship between filler content and 'bridge' resistance follows a roughly exponential reduction towards a finite resistance value. The carbon black-filled A7-11 wax samples displayed similar behaviour, and no resistance measurements were obtained from samples when the filler concentration was 6.9 vol% (12.36 wt%) or lower.

Table C.1 Tabulating the relationship between the material samples' electrical resistance (kΩ) and the conductive filler content in A7-11 wax, according to the results from a set-up where the material is sheared to form a bridge between aluminium conductive tabs.

Micronised Graphite-filled A7-11 Wax			
weight% Filler	**volume% Filler**	**Average Resistance (kΩ) (2 sf)**	**Standard Deviation (kΩ) (2 sf)**
0	0	NR	NR
8.43	4.0	NR	NR
12.36	6.0	NR	NR
16.11	8.0	920	702
19.71	10.0	130	86.99
23.15	12.0	23	9.32
26.45	14.0	7.3	1.83
29.61	16.0	4.3	1.96
32.65	18.0	2.1	0.79
Carbon Black-filled A7-11 Wax			
weight% Filler	**volume% Filler**	**Average Resistance (kΩ) (2 sf)**	**Standard Deviation (kΩ) (2 sf)**
0	0	NR	NR
8.43	4.6	NR	NR
12.36	6.9	NR	NR
16.11	9.2	51000	44000
19.71	11.4	59	26
23.15	13.7	3.5	2.3
26.45	15.9	0.73	0.20
29.61	18.09	0.62	0.20
32.65	20.3	0.28	0.09

Resistance measurements from carbon black-filled waxes at filler concentrations less than 13.7 vol% were greater than those of the graphite-filled samples, although carbon black-filled samples displayed a greater reduction in resistance as the concentration was increased. At the highest filler concentrations tested, the carbon black-filled A7-11 wax exhibited the lowest bridge resistance measurements; averaging 0.624 kΩ at 18.1 vol% (29.6 wt%). The reason for this behaviour can be attributed to the effects of particle interaction. The graphite and carbon black both consist of plate-like particles, although the level of agglomeration in the carbon black is far more prominent. High standard deviation values are evident at lower filler concentrations for both the carbon black and graphite-filled waxes, as shown in Table C.1. This is expected, as in the region just above the V_c for each material (with is undefined but assumed to be below 6 vol% for each sample), the material's conductivity, as defined by the measured resistance between two conductive plates (or probe points), is limited by the resistance across the network's least electrically-connected cross-section, which is higher when the number of conducting paths between the tested points is limited. Any inhomogeneities in the distribution of conducting particles within the wax at these concentrations have a large effect, therefore, on the resistance measurement results.

C.1.2 Four-point probe Results Tables

Within Section 15.1.2, a four-point probe resistance set-up was used to measure the resistivity of plate wax samples. Both the top and bottom surfaces of these circular plates were tested, to measure any local resistivity disparity due to filler settling. Both carbon black and micronised graphite powders described in Section 8.2.2 were used to fill A7-7808, A7-11 and A7-TC2/e wax grades, as described in Section 8.2.1. Table C.2, C.3 and C.4 show the results for conductive particle-filled A7-7808 waxes, A7-11 waxes and A7-TC2/e waxes, respectively.

Table C.2 Tabulating the relationship between the material samples' electrical resistivity (Ω.cm) and the conductive filler content in A7-7808 wax (vol%), according to the results from a set-up where circular material plates are tested using a four-point probe apparatus.

Carbon Black-filled A7-7808 Wax					
weight% Filler	**volume% Filler**	**Plate Side**	**Average Sample Resistance (kΩ) (2 sf)**	**Average Resistivity (Ω.cm) (2 sf)**	**Standard Deviation (Ω.cm) (2 sf)**
0	0	n/a	NR	NR	NR
12.36	6.9	Top	NR	NR	NR
12.36	6.9	Bottom	NR	NR	NR
19.71	11.4	Top	NR	NR	NR
19.71	11.4	Bottom	NR*	NR	NR
26.45	15.9	Top	1.7	990	200
26.45	15.9	Bottom	1.4	830	170
32.65	20.3	Top	0.071	42	11
32.65	20.3	Bottom	0.045	27	12
Graphite-filled A7-7808 Wax					
weight% Filler	**volume% Filler**	**Plate Side**	**Average Sample Resistance (kΩ) (2 sf)**	**Average Resistivity (Ω.cm) (2 sf)**	**Standard Deviation (Ω.cm) (2 sf)**
0	0	n/a	NR	NR	NR
12.36	6.0	Top	NR	NR	NR
12.36	6.0	Bottom	NR	NR	NR
19.71	10.0	Top	NR	NR	NR
19.71	10.0	Bottom	NR*	NR	NR
26.45	14.0	Top	11	6500	2800
26.45	14.0	Bottom	9.8	5900	2300
32.65	18.0	Top	2.9	1700	610
32.65	18.0	Bottom	1.6	980	560

* No results were plotted when more than 2/5ths of four-point probe placements led to no measurable resistance.

Table C.3 Tabulating the relationship between the material samples' electrical resistivity (Ω.cm) and the conductive filler content in A7-11 wax (vol%), according to the results from a set-up where circular material plates are tested using a four-point probe apparatus.

Carbon Black-filled A7-11 Wax					
weight% Filler	**volume% Filler**	**Plate Side**	**Average Sample Resistance (kΩ) (2 sf)**	**Average Resistivity (Ω.cm) (2 sf)**	**Standard Deviation (Ω.cm) (2 sf)**
0	0	n/a	NR	NR	NR
8.43	4.6	n/a	NR	NR	NR
12.36	6.9	n/a	NR	NR	NR
16.11	9.2	n/a	NR	NR	NR
19.71	11.4	Top	NR*	NR	NR
19.71	11.4	Bottom	20	12000	3700
23.15	13.7	Top	3.4	2100	580
23.15	13.7	Bottom	2.7	1600	624
26.45	15.9	Top	0.46	270	110
26.45	15.9	Bottom	0.35	210	69
29.61	18.09	Top	0.18	110	33
29.61	18.09	Bottom	0.14	80	28
32.65	20.3	Top	0.019	11	1.7
32.65	20.3	Bottom	0.014	8.1	1.3
Graphite-filled A7-11 Wax					
weight% Filler	**volume% Filler**	**Plate Side**	**Average Sample Resistance (kΩ) (2 sf)**	**Average Resistivity (Ω.cm) (2 sf)**	**Standard Deviation (Ω.cm) (2 sf)**
0	0	n/a	NR	NR	NR
12.36	6.0	n/a	NR	NR	NR
16.11	8.0	n/a	NR	NR	NR
19.71	10.0	Top	NR	NR	NR
19.71	10.0	Bottom	NR	NR	NR
23.15	12.0	Top	13	7700	950
23.15	12.0	Bottom	11	6700	2400
26.45	14.0	Top	5.8	3500	1300
26.45	14.0	Bottom	5.4	3300	950
29.61	16.0	Top	2.2	1300	400
29.61	16.0	Bottom	1.9	1100	460
32.65	18.0	Top	1.2	690	310
32.65	18.0	Bottom	0.61	360	170

* No results were plotted when more than 2/5ths of four-point probe placements led to no measurable resistance.

Table C.4 Tabulating the relationship between the material samples' electrical resistivity (Ω.cm) and the conductive filler content in A7-Tc2/e wax (vol%), according to the results from a set-up where circular material plates are tested using a four-point probe apparatus.

Carbon Black-filled A7-TC2/e Wax					
weight% Filler	**volume% Filler**	**Plate Side**	**Average Sample Resistance (kΩ) (2 sf)**	**Average Resistivity (Ω.cm) (2 sf)**	**Standard Deviation (Ω.cm) (2 sf)**
0	0	n/a	NR	NR	NR
12.36	6.9	Top	NR	NR	NR
12.36	6.9	Bottom	NR	NR	NR
19.71	11.4	Top	NR	NR	NR
19.71	11.4	Bottom	NR	NR	NR
26.45	15.9	Top	1.3	770	210
26.45	15.9	Bottom	1.1	640	170
32.65	20.3	Top	0.039	23	7.7
32.65	20.3	Bottom	0.020	12	3.7
Graphite-filled A7-TC2/e Wax					
weight% Filler	**volume% Filler**	**Plate Side**	**Average Sample Resistance (kΩ) (2 sf)**	**Average Resistivity (Ω.cm) (2 sf)**	**Standard Deviation (Ω.cm) (2 sf)**
0	0	n/a	NR	NR	NR
12.36	6.0	Top	NR	NR	NR
12.36	6.0	Bottom	NR	NR	NR
19.71	10.0	Top	NR	NR	NR
19.71	10.0	Bottom	NR	NR	NR
26.45	14.0	Top	7.9	4700	1100
26.45	14.0	Bottom	6.3	3800	1200
32.65	18.0	Top	1.4	850	240
32.65	18.0	Bottom	0.9	550	200

* No results were plotted when more than 2/5ths of four-point probe placements led to no measurable resistance.

C.2 Wax Rheology Flow Curves

In Section 15.2.2, wax samples were tested using controlled shear stress (CSS) flow ramps. Plotting shear rate against viscosity in Section 15.2.2 meant that the non-Newtonian behaviour of the wax samples could be described. Thixotropic and rheopectic behaviours are described both in Section 6.6 and Section 7.2.2. Within this Appendix Section, shear rate is plotted graphically against shear stress, so that the degree of thixotropy / rheopexy can be measured.

The shear stress and corresponding shear rate values obtained within the increasing shear (up) and decreasing shear (down) ramps were plotted graphically, on the y-axis and x-axis respectively. To measure the hysteresis area between the up and down flow curves, trend lines were fitted to each curve, and the associated trend-line equation was integrated between the minimum (0.779) and maximum (1500) stress values. This would lead to a good approximation for the total area under each curve; the hysteresis area was calculated by taking the area of the up curve from the area of the down curve.

These calculations would be invalid, however, if (1) the material undergoes non-recoverable degradation with time, or (2) the technique used leads to experimental errors that have an effect on the shape of the flow curves. To test this, the same sample was placed within the specimen gap, and tested three times with a relaxation time between each flow test, to see whether the viscosity or hysteresis behaviour changes as each successive cycle is carried out. To check whether the thixotropic behaviour shown in the flow curves were due to the properties of the material itself, or were a consequence of experimental design, the following experiments were carried out (Cirre Torres, 2004).

Samples of A7-7808 wax and A7-TC2/e wax were placed within a separation gap of 300 μm, and the first flow curve measurements was carried out up to a shear stress value of

750 Pa (Cycle 1). Without removing it from the geometry, the same sample then underwent a flow test with an increased maximum shear stress of 1600 Pa (Cycle 2). The same material was retested after a 5 minute rest period, when a flow test up to a maximum shear stress of 1600 Pa was carried out (Cycle 3). The results for the A7-7808 tests are shown in Figure C.2, and only slight differences were reported in the Cycle 1 for the up-curves and down-curves. The up-curves and down-curves of Cycle 2 follow more distinct paths, and in Cycle 3, the up-curve overlapped the down-curve of the previous cycle (Cycle 2). These results confirm that for the A7-7808-based samples, the apparent thixotropic behaviour is more likely to be an artefact of the experimental procedure than a measure of the reversible change in the structure of the non-filled wax. For the A7-TC2/e tests shown in Figure C.3, a similar behaviour was observed, although the material displays a smaller degree of thixotropy, and so overlapping of up-curves and down-curves between cycles was less distinct.

The ejection of wax from the plate separation gap could be observed during testing cycles, when the top parallel plate was rotated at high shear rates. A percentage of the wax would therefore be lost from the testing region between the viscometer plates, which would affect flow behaviour. As flow curve experiments have been carried out in CSS (controlled shear stress) mode, samples that are modified to a higher filler concentration do not reach such high shear rates, and so may not have material expelled to the same extent. However, there are other associated problems relating to the presence of filler; the most notable being phase separation and the formation of particle concentration gradients formed under shear, as described in Section 7.2.1 and in the work of Aramphongphun and Castro (2007).

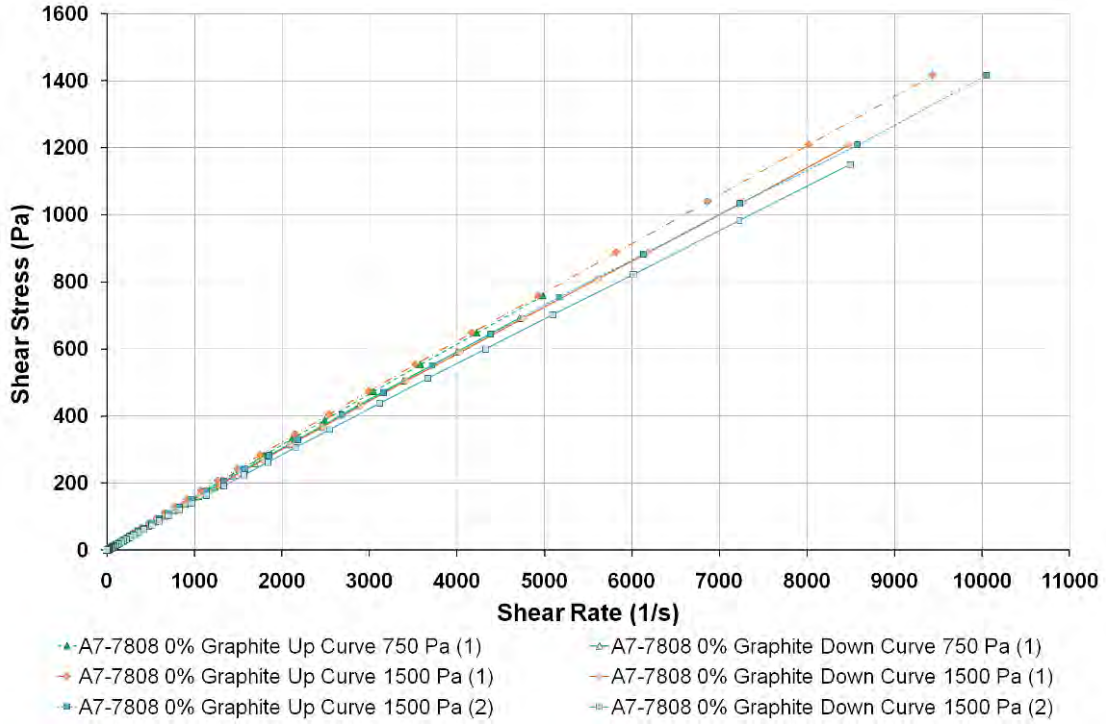

Figure C.2 Graph of shear stress as a function of shear rate, showing repeated flow curves, obtained from one sample of unfilled A7-7808 wax. Tests were carried out on a rotational rheometer at a temperature of 80 °C.

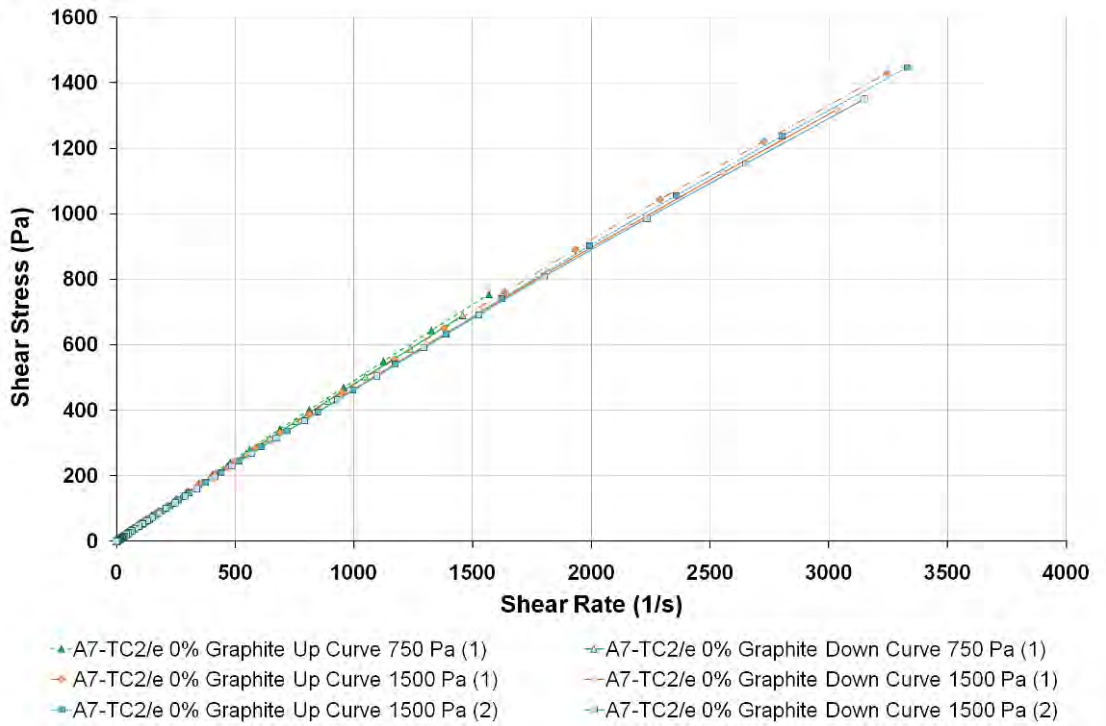

Figure C.3 Graph of shear stress as a function of shear rate, showing repeated flow curves, obtained from one sample of unfilled A7-TC2/e wax. Tests were carried out on a rotational rheometer at a temperature of 80 °C.

CSS flow curves for micronised graphite-filled A7-7808 are shown in Figure C.4 and Figure C.5. As the filler content is increased, the disparity between up-curve and down-curves increases. This increasingly ‘thixotropic character’ can be attributed to the effect of non-recoverable structural breakdown, as described in Section 6.6.2. As shown in Figure C.6, the A7-TC2/e base wax displays a lower level of ‘thixotropic character’ at 80 °C when compared to the A7-7808 grade base wax. In Figures C.6 and C.7, the addition of graphite is shown to increase the disparity between up and down flow curves for the A7-TC2/e wax grade, which can also be attributed to non-recoverable structural breakdown effects.

CSS flow curves for carbon black-filled A7-7808 wax are shown in Figure C.8 and Figure C.9. A low level addition of carbon black increases the difference between up-curve and down- curve, which both show ‘thixotropic character’. At higher concentrations, however, the curves display ‘rheopectic character’. Owing to structural breakdown effects, the material is not rheopectic under high shear, as at high shear, the filler particles agglomerate and lock together, inhibiting shear in a manner that is not fully reversible after relaxation.

The same behaviour is not, however, seen in the carbon black-filled A7-TC2/e wax samples. In Figure C.10 and C.11, the curves show an increasing degree of ‘thixotropic character’ as the filler content is increased. As shown in Section 15.2.4, there is evidence to suggest the presence of a threshold suspension concentration, at which the particle clusters go from being broken down at high shear to locking up; this threshold concentration level appears to be influenced by the matrix material.

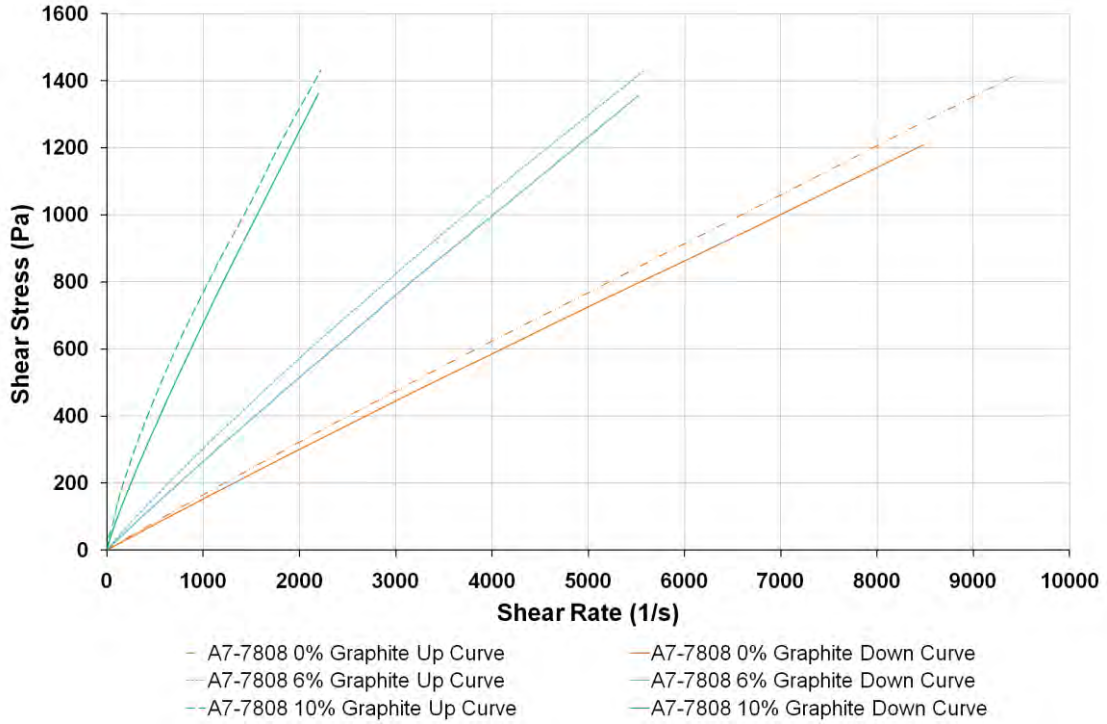

Figure C.4 Graph showing the relationship between shear stress and shear rate for controlled shear stress flow curves. Results are for graphite-filled A7-7808 wax at different loadings, carried out on a rotational rheometer at a temperature of 80 °C.

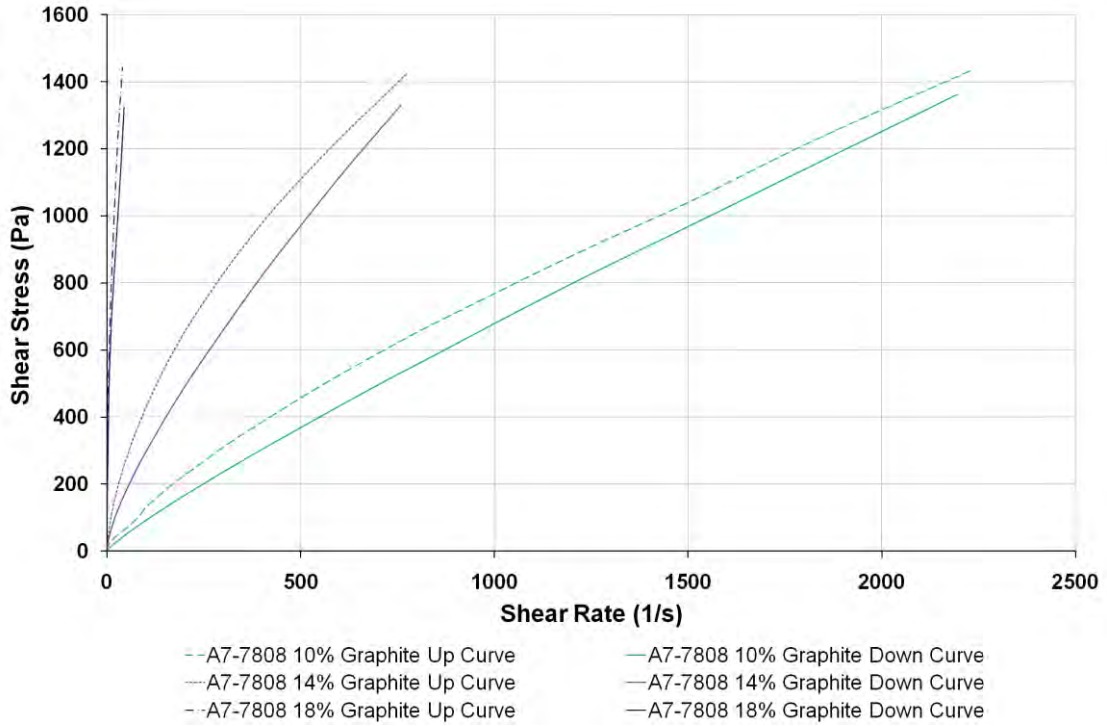

Figure C.5 Graph showing the relationship between shear stress and shear rate for controlled shear stress flow curves. Results are for graphite-filled A7-7808 wax at different loadings, carried out on a rotational rheometer at a temperature of 80 °C.

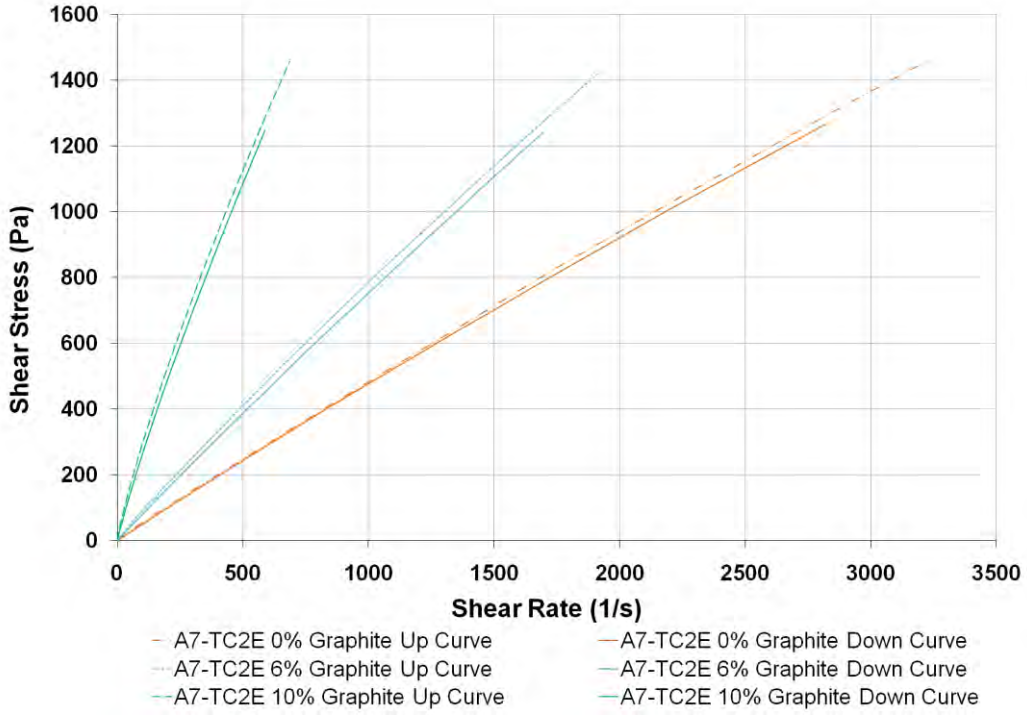

Figure C.6 Graph showing the relationship between shear stress and shear rate for controlled shear stress flow curves. Results are for graphite-filled A7-TC2/e wax at different loadings, carried out on a rotational rheometer at a temperature of 80 °C.

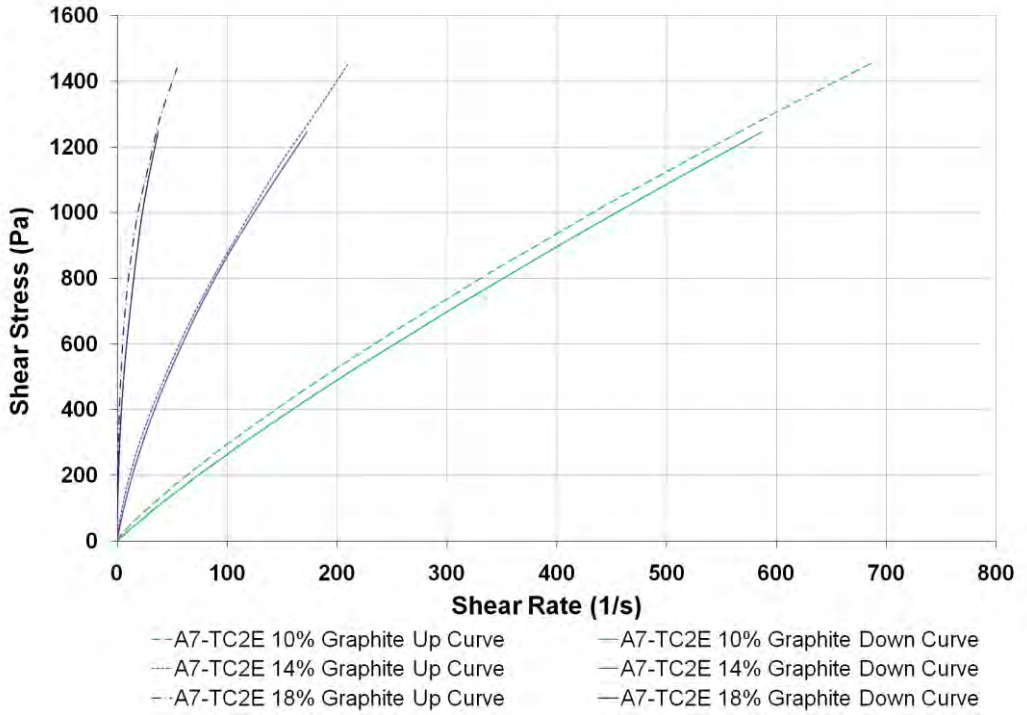

Figure C.7 Graph showing the relationship between shear stress and shear rate for controlled shear stress flow curves. Results are for graphite-filled A7-TC2/e wax at different loadings, carried out on a rotational rheometer at a temperature of 80 °C.

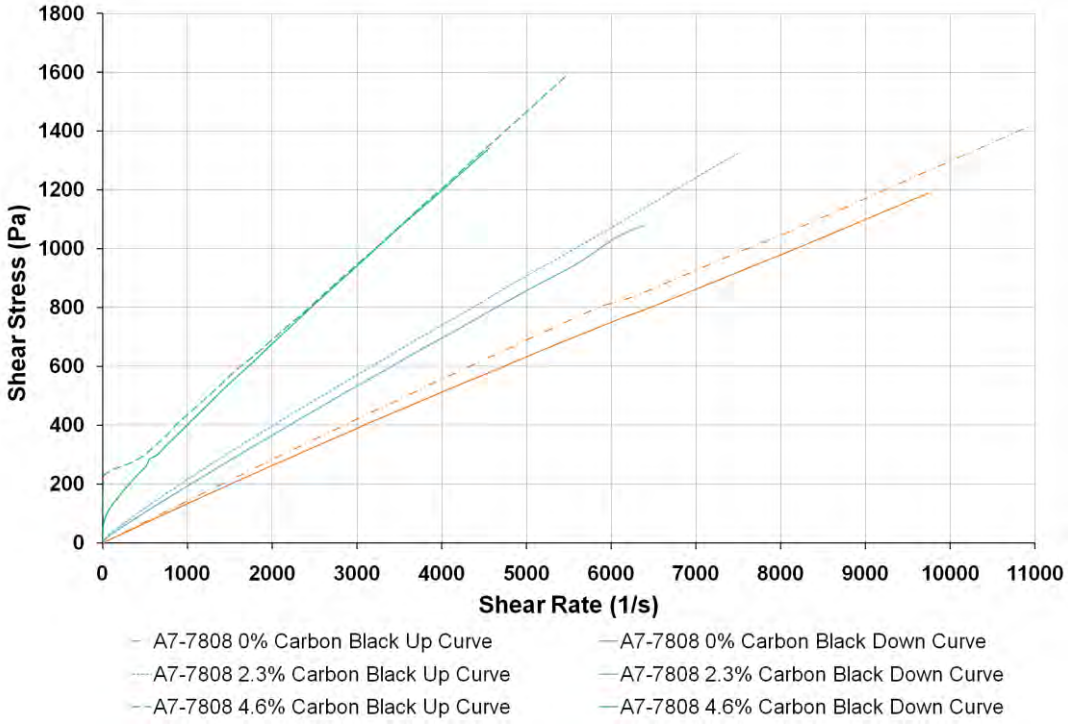

Figure C.8 Graph showing the relationship between shear stress and shear rate for controlled shear stress flow curves. Results are for carbon black-filled A7-7808 wax at different loadings, carried out on a rotational rheometer at a temperature of 80 °C.

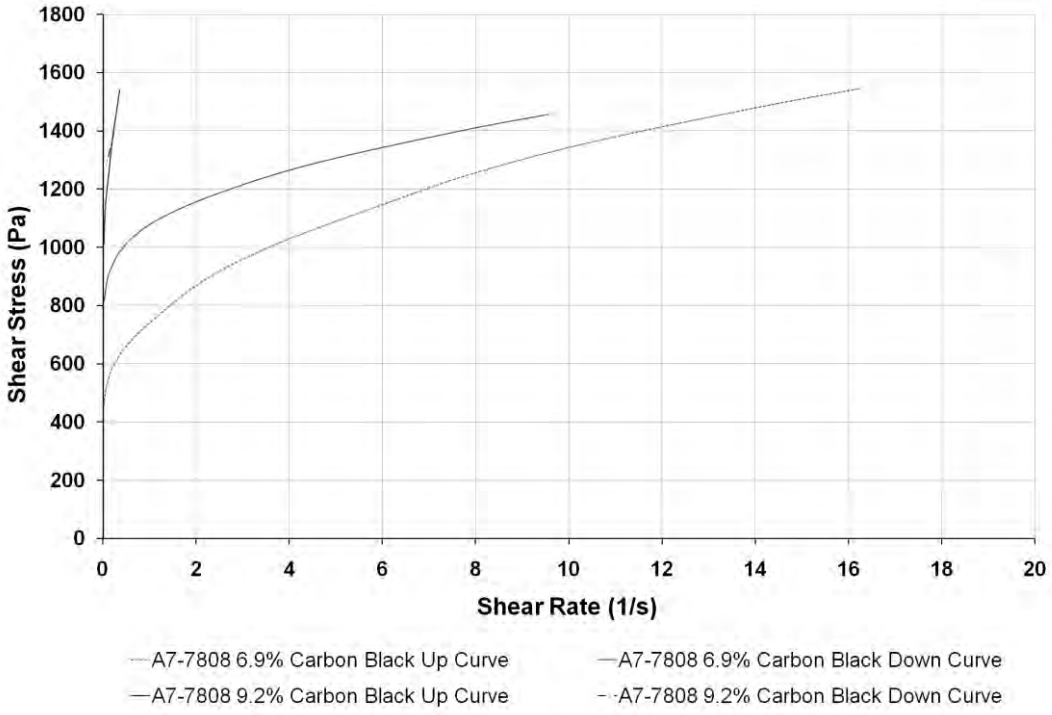

Figure C.9 Graph showing the relationship between shear stress and shear rate for controlled shear stress flow curves. Results are for carbon black-filled A7-7808 wax at different loadings, carried out on a rotational rheometer at a temperature of 80 °C.

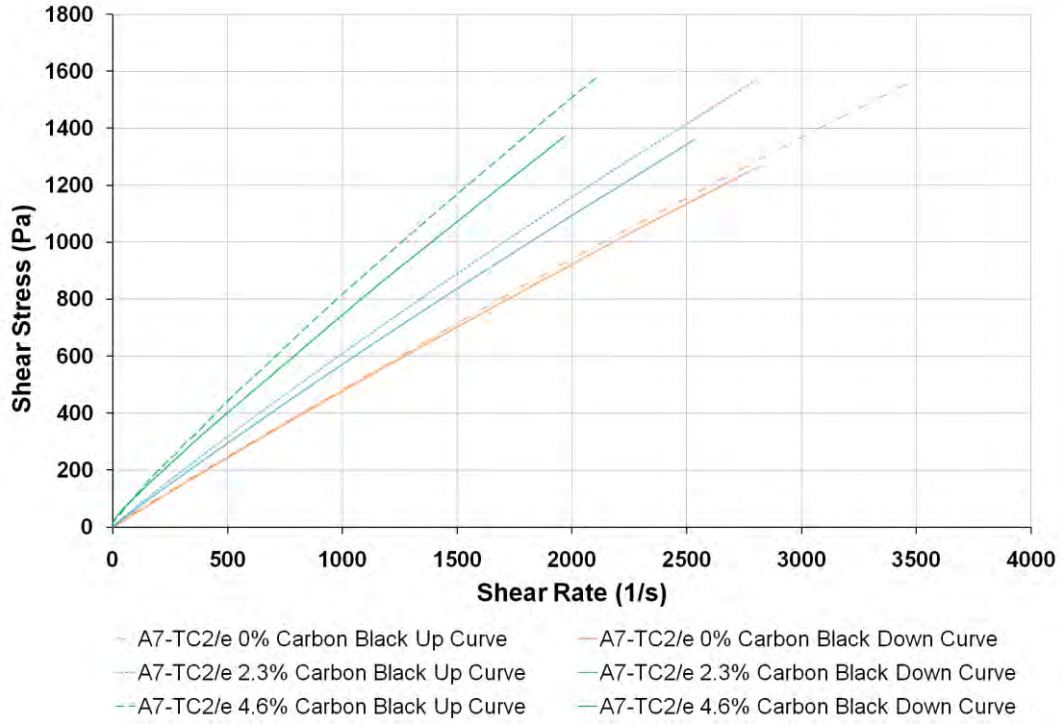

Figure C.10 Graph showing the relationship between shear stress and shear rate for controlled shear stress flow curves. Results are for carbon black-filled A7-TC2/e wax at different loadings, carried out on a rotational rheometer at a temperature of 80 °C.

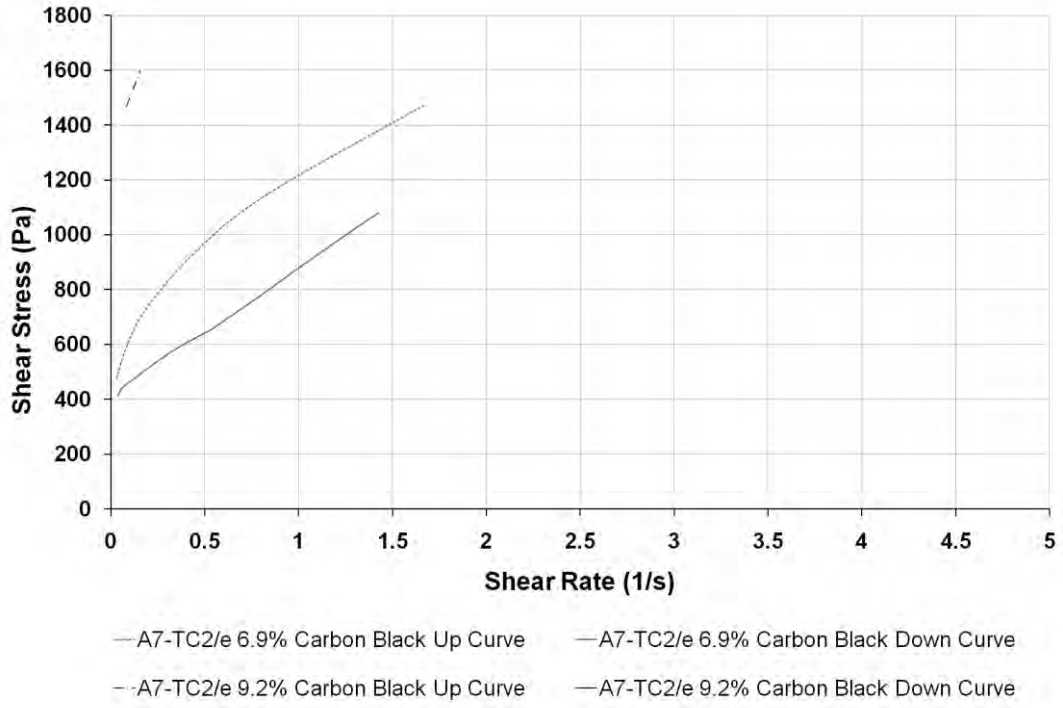

Figure C.11 Graph showing the relationship between shear stress and shear rate for controlled shear stress flow curves. Results are for carbon black-filled A7-TC2/e wax at different loadings, carried out on a rotational rheometer at a temperature of 80 °C.

C.3 Wax Density

C.3.1 Introduction and Methods

It is important to measure the wax density, as it gives an insight into the composition of the composite after the formation process. With the mass and density of constituent materials known, any discrepancy from a calculated material density can be explained by material loss in processing (for example, powder loss), as well as void entrapment, which can be observed in a qualitative way by examining sample cross-sections.

The wax composite density was measured using a hydrostatic weighing set-up, which measures density based on Archimedes' displacement principle (Paipetis, 2010). A&D instrument balance (GX-200), which is accurate to ±0.01 g, was used for mass measurements. Flat circular plate wax samples were used, with a plate diameter was 65.0 mm (± 0.2 mm). The plate thickness varied depending upon the filled wax composition, with dimensions measured using a digital calliper.

Each wax circular plate sample was weighed in air to give a value for m_m (g). A 500 cm^3 polymer container was filled with 400 cm^3 of water, and was placed on the instrument balance and the balance measurement was set to measure 0.00 grams. A 4 mm steel crocodile clip was then used to grip the plate sample edge, so that the sample could be fully immersed and not touch the sides of the container. The sample was placed in the water to a full immersion depth, with the end of the clip just breaking surface tension. The mass value, m_s, which corresponds to the mass measurement obtained when the material was immersed in water, was then measured. The density of the material was then calculated using Equation [C.1].

$$\text{Material Density } \rho_m = \frac{m_m}{(m_m - m_s)/\rho_w} \quad [C.1]$$

$$\text{Material Density } v_m = \frac{m_m}{\rho_m} \quad [C.2]$$

ρ_m is the experimentally derived density of the sample ($g.cm^{-3}$), m_m is the mass of the sample (g), m_s is the mass measurement obtained in water (g) and ρ_s is the density of water ($g.cm^{-3}$). As the volume of the sample could not be accurately determined by measuring the displacement volume in the water-filled container, it was calculated using Equation [C.2].

The measured sample density could then be compared with a theoretical density value, ρ_t (g/cm^3), which can be calculated using Equation [C.3]:

$$\text{Composite density } \rho_t = (V_f.\rho_f) + (V_m.\rho_m) \quad [C.3]$$

V_f is the filler volume fraction (at 20 ºC), V_m is the matrix volume fraction (at 20 ºC), ρ_f is the filler density at 20 ºC (g/cm^3) and ρ_m is the matrix density at 20 ºC (g/cm^3).

C.3.2 Wax Density Results and Analysis

Wax density experiments were carried out according to the procedures set out in Section C.3.1. As the filled samples were created according to weight% measurements, the 65.0 mm diameter circular plate samples were created with plate thicknesses that lay between 5.6 and 6.3 mm. For theoretical density calculations, matrix and filler density values were taken from manufacturer information. Cabot Vulcan XC605 had a density of 1.7 – 1.9 g/cm³ at 20°C, with a bulk density of 20 - 550 kg/m^3 (0.02 and 0.55 g/cm^3). A value of 1.9 g/cm^3 was used within this study for the wt% and vol% calculations. The micronised graphite had a density of

2.10 - 2.25 g/cm^3 at 20 ºC, with an unknown bulk density. A value of 2.2 g/cm^3 was used within this study. The wax density of all the base grades was taken to be 0.995 g/cm^3.

For these samples, the total mass of constituent elements for both unfilled and filled wax samples was 20.0 g. For an unfilled wax with zero porosity, 20.0 g of wax should occupy a volume of 19.90 cm^3. For an 18 vol% (32.65 wt%) graphite-filled sample, the sample was composed of ~ 6.5g graphite powder and ~ 13.5 g wax pellets. Again, if one can assume zero porosity and no material loss on mixing, this should occupy a volume of 16.50 cm^3. To calculate the theoretical density of each filled wax grade, the constituent vol% content was derived from wt% data in Table 8.2 and Table 8.3 of Section 8.3.

Table C.5 Sample density parameters as a function of micronized graphite filler content

Sample Density Parameters	**vol% micronised graphite filler**				
A7-7808 Wax	**0.0**	**6.0**	**10.0**	**14.0**	**18.0**
Calculated Sample Volume (cm^3)*	20.10	18.74	17.93	17.19	16.50
Submersion Sample Volume (cm^3)	19.75	19.15	18.74	17.88	17.85
Sample Mass (g)	19.74	19.76	19.68	19.40	19.46
Sample Density (g/cm^3)	0.998	1.032	1.050	1.085	1.090
Theoretical Density (g/cm^3)*	0.995	1.067	1.116	1.164	1.212
A7-TC2/e Wax					
Calculated Sample Volume (cm^3)*	20.10	18.74	17.93	17.19	16.50
Submersion Sample Volume (cm^3)	20.50	19.89	19.58	18.86	18.33
Sample Mass (g)	19.70	19.65	19.56	19.35	19.38
Sample Density (g/cm^3)	0.961	0.988	0.999	1.026	1.057
Theoretical Density (g/cm^3)*	0.995	1.067	1.116	1.164	1.212

* Graphite density taken to be 2.2 g/cm^3, wax density taken to be 0.995 g/cm^3

Table C.6 Sample density parameters as a function of Vulcan carbon black filler content

Sample Density Parameters	**vol% Vulcan carbon black filler**				
A7-7808 Wax	**0.0**	**6.9**	**11.4**	**15.9**	**20.3**
Calculated Sample Volume (cm^3)*	20.10	18.92	18.21	17.57	16.97
Submersion Sample Volume (cm^3)	19.78	18.86	18.36	17.66	17.63
Sample Mass (g)	19.74	19.65	19.39	19.06	18.99
Sample Density (g/cm^3)	0.998	1.042	1.056	1.079	1.077
Theoretical Density (g/cm^3)*	0.995	1.057	1.098	1.139	1.179
A7-TC2/e Wax					
Calculated Sample Volume (cm^3)*	20.10	18.92	18.21	17.57	16.97
Submersion Sample Volume (cm^3)	20.50	20.16	19.14	18.02	17.64
Sample Mass (g)	19.70	19.74	19.43	18.85	18.67
Sample Density (g/cm^3)	0.961	0.979	1.015	1.046	10.58
Theoretical Density (g/cm^3)*	0.995	1.057	1.098	1.139	1.179

* Carbon black density taken to be 1.9 g/cm^3, wax density taken to be 0.995 g/cm^3

Table C.5 and Table C.6 tabulate the test sample density parameters as a function of micronized graphite filler content and Vulcan carbon black filler content, respectively. The theoretical values quoted are based on the samples' constituent masses and manufacturer quoted densities. There are a number of contributing reasons that can be linked to the disparity between the submerged volumes and calculated volumes.

For the both the filled and unfilled wax grades, there are factors within the wax processing procedure that account for the measured mass being lower than the calculated mass. During the wax plate formation process, material is lost systematically, as both the magnetic stirring bar and PTFE stirring rod collected a small amount of material that could not be returned to the molten sample. The mass discrepancy increases with filler content, and this can be related to the higher thermal conductivity of the filled waxes. Particle-filled waxes cooled more readily on the magnetic stirrer and PTFE spatula, and were more difficult to remove so as to incorporate the material back into the liquid sample. Additionally, a small

amount of wax flash formed between the male and female parts due to the flexibility of the silicone moulds, and was lost as the cast wax was removed. The formation of this flash was more evident in the lower viscosity unfilled samples.

For filled-waxes, powder assimilation into the liquid wax was carried out in a fume cupboard, where the conductive powders were gradually fed into the magnetically stirred liquid. A small mass of powder would end up not being incorporated into the wax, as it either coated the mould wall, or was carried away by the airflow. This would also lower the density of the resulting wax plate, as the more dense filler particle content in the plate was lower than the amount originally weighed out as a constituent. The A7-TC2/e wax samples suffered a slightly higher mass loss than the A7-7808 grade, due to the loss of small quantities of water filler during the mixing and homogenisation cycle that took place at temperature between 80 and 85 ºC. Despite using the temperatures stipulated by the wax manufacturer during both the magnetic and manual stirring operations employed when forming these samples, hotspots above 85 °C may have existed that caused much higher levels of liquid filler evaporation than anticipated when heating then wax to between 80°C and 85 °C.

Air or gas entrapment during melting and mixing operations would be the principal plate sample volume-increasing factor, making the actual volume larger than the volume calculated from the material mass and density, although voids were not commonly found within the examined cross-sections of unfilled wax samples. Filler particles, and in particular agglomerates, produced greater temperature inhomogeneities within the wax. Examination of cross-sections of the wax samples, showed that presence of void formation also increased as the filler content was increased, in both wax grades. When processing unfilled waxes at a fixed mixing temperature, their lower viscosity (compared to the viscosity of the filled waxes at the same mixing temperature) decreased the likelihood of bubble entrapment during mixing. The presence of particle clusters would increase the mixing viscosity of the sample,

and so inhibit the removal of air bubbles from the resulting composite. Additionally, particle clusters would possibly aid air entrapment when added as a powder, as interstitial voids would exist between particles that cannot be filled by the molten wax.

Density values are shown in Table C.5 and Table C.6, and the disparity between values can be attributed to the reasons stated above. Additionally, the manufacturer's data often gave a range of density values of their product, although for the present work, a specific value within this range had to be chosen for calculations. If the chosen density value did not accurately represents that of the material used, the calculated density value would not accurately represent that of the composite material.

APPENDIX D – Suspension Stability Experiments

D.1 PZC Measurements to Find Regions of pH Stability

D.1.1 Experimental Techniques used in the Literature

The point of zero charge (PZC) corresponds to the pH value when the particle's surface charge is zero, and measurements are ascertained on the assumption that protons and hydroxyl groups are the potential determining ions. The colloid surface charge is defined by the number of $M–O^-$ and $M–OH_2^+$ sites, and the concentration of these sites is ruled by H^+ concentration in solution (Hsu 1999).

Potentiometric titration is a method used by Yopps et al. (1964) to ascertain the pH_{pzc} in their experiments. In this method, a voltage is put across the electrolyte, and the potential difference is measured as the pH is altered. The adsorption isotherms of the potential-determining H^+ and OH^- ions can then be determined by measuring the ion concentration of the colloidal suspension titration against that of a background electrolyte titration (Mao 1994). A set of suspensions are modified with supporting electrolytes over a range of molarities, as the oxide surface charge increases with increasing electrolyte strength to give different resultant titration curves. According to Yopps (1964), "there is no surface charge (at the PZC) and the adsorption of H^+ and OH^- will be nil". The position of the PZC is therefore defined as the pH where the series of titration curves intersect, because the point corresponding to zero adsorption is independent of ionic concentration.

In oxide suspensions, strong buffering effects are observed at pH values around the PZC, and so called 'batch equilibration' methods use this observation to ascertain the pH_{pzc}. To measure the buffering effect, a number of suspensions are formed using solutions with a range of pH values. The solution pH values are measured both prior to oxide particle addition

(pH_i) and after powder equilibration in suspension (pH_f). The position of the PZC can be determined by finding the region where the solution pH does not significantly change with powder addition ($pH_i - pH_f \approx 0$), for reasons described below.

The oxide surface becomes protonated when pH_i is below the PZC, and the solution from which the protons are removed becomes more basic (raising the pH). Surface deprotonisation above the PZC, in turn, makes the solution more acidic. As the solution pH is shifted to a value close to the apparent PZC, surface charge neutrality prevents further solution pH change.

In the research by Milonjic et al. (2007), samples of constant ionic strength KCl solution had their initial pH (pH_i) varied across a range of pH values (2 – 11). Silica was then added and the pH was allowed to equilibrate over 24 hours. The results were presented as pH values of filtered solutions (pH_f) (after their equilibration with SiO_2) as a function of initial solution pH (pH_i). The plateau, and not the pH_{pzc}, is mentioned in Milonjic's work, since variables such as the difference between ionisation constants (DpK) can cause these values to deviate from one another (Feltes). According to Kosmulski (2001), this method is in fact a modified potentiometric titration (called the drift method here), without correction factors in place.

D.1.2 Batch equilibrium Methods to Ascertain the PZC

The measurement technique used to ascertain the position of the PZC within the present work was a batch equilibrium method. A colloidal oxide protonates or deprotonates the supporting medium into which it is dispersed, and so alters the solution pH upon addition. This brings the pH towards a plateau region where the PZC is situated. At high solids loading, the pH change is more pronounced, which more clearly defines the pH position of the plateau region.

The method employed to form the suspensions used in the batch equilibrium experiment was similar in many ways to the one described within Section 12.3, and any differences are described below. Suspensions with an initial deionised water volume of 30cm^3 were used, with a zircon addition of 0.138 g (0.46 wt%). Due to the low concentration of zircon in suspension, the concentration of Dolapix CE64 dispersant was altered accordingly, so that the two tested concentrations were 0 mg/g and 20 mg/g. These two concentrations were used to observe the effect that an anionic dispersant had on the PZC of zircon in aqueous suspension.

After dispersant modification, the pH of each suspension was altered, using diluted HCl for solutions in the acidic (pH < 7) range and diluted TMAH for solutions in the alkaline (pH > 7) range. The pH was measured both before (pH_i) and after (pH_f) zircon addition. Milonjic et al. (2007) stated that the equilibrium position of H^+ and OH^- ion adsorption was reached after about 4 hours (240 minutes) for their silica suspensions, although they used a 24 hour equilibration time for convenience. Contescu (1994), however, stated that an equilibration time of only 10 minutes should be used, as it minimised the level of oxide dissolution that would otherwise lead to extraneous reactions. In the present work, to monitor the change in pH after powder addition to aqueous suspension, the initial pH (pH_i) was plotted against the final pH (pH_f), which was the suspension pH after a 230 minute roll mixing cycle.

D.1.3 Experimental Results and Discussion

Determining the position of the apparent PZC for these colloidal species enabled the identification of pH regions associated with suspension dispersion stability, so that electrophoretic deposits can be formed from suspensions of high colloidal stability, to confirm the findings of the zeta-potential experiments. Knowing where the zeta potential and surface

charge, as determined from the position of the IEP and PZC, respectively, are positive and negative for a specific colloidal powder will be of use in heterocoagulation studies for multi-component suspensions. Whilst the information could ultimately be important, heterocoagulation studies are beyond the scope of this study for reasons of time.

The procedures used for the experiments of this section are shown in Section D.1.2. In Figure D.1 and Figure D.2, suspensions with increasingly extreme acidic (i.e. low) and alkaline (i.e. high) pH_i values showed only small changes in pH during equilibration, and are not plotted, as the position of the apparent PZC, and the pH region surrounding it, is of greatest importance. For dispersant-free zircon suspensions in Figure D.1, both the Helmut Kreutz 'Super FF' and Dupré 'A' grades exhibited similar behaviour near an apparent PZC of pH ~ 5.6, although the 'Super FF' grade exhibited lower pH equilibration shifts when the suspension's pH_i was further from the pH_{pzc}.

For the dispersant-modified suspension results shown in Figure D.2, the Helmut Kreutz 'Super FF' and Dupré 'A' grades exhibited similar pH equilibration behaviour across the whole pH_i range, as shown on the graph. For both zircon grades, the addition of Dolapix CE64 dispersant to a concentration of 20 mg/g shifts the apparent PZC of suspensions from pH_i ~ 5.6 to ~ 6.5.

The positions of the PZC and the IEP for zircon suspensions, both with and without Dolapix CE64 dispersant, are compared in Section D.2.3. PZC and IEP results for a number of colloidal systems in the literature are also used to evaluate the findings of the present work in this Section.

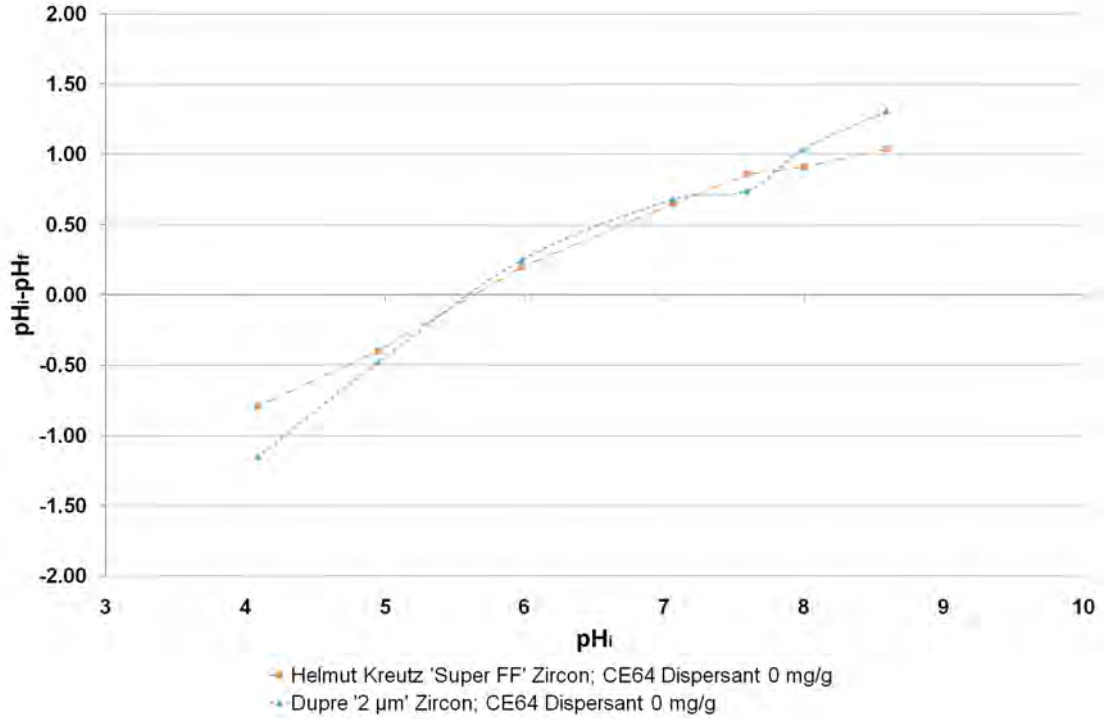

Figure D.1 Graph showing the difference between initial and final suspension pH values plotted against the initial pH of suspension (pH_i) as a function of zircon powder grade, for CE64 dispersant-free zircon suspensions.

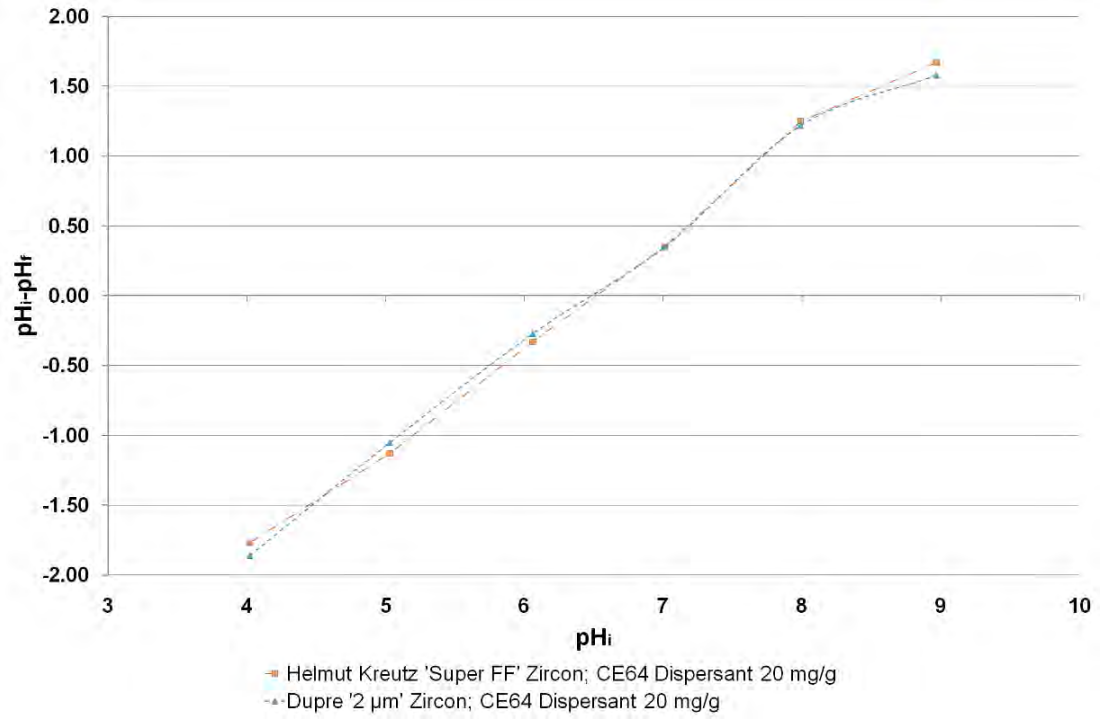

Figure D.2 Graph showing the difference between initial and final suspension pH values plotted against the initial pH of suspension (pH_i) as a function of zircon powder grade, for CE64 dispersant-modified zircon suspensions.

D.2 Ascertaining the Position of the IEP for Particles in Suspension

D.2.1 Methods used in the Literature

The pH_{iep} is usually determined by methods that measure the electrokinetic potential, and the IEP corresponds to the solution pH when the calculated zeta potential is zero. Zeta potential (ζ) can be linked to the particles' electrophoretic mobility (μ_e) using equations [3.2], [3.3] or [3.4], as described in Section 3.2.

In the electrophoresis method, the application of an electric field across the dispersion causes the migration of charged particles towards the electrode of opposite charge. The electrophoresis method can employ the use of a laser doppler anemometer to measure the velocity of particles in a suspension. The relationship between the particle velocity and the electric field strength can give a value for the electrophoretic mobility, and therefore the zeta potential, using either equation [3.2] or a more complex model.

Laser Doppler Anemometry is based upon the measurement of laser light scattered by particles as they pass through a series of interference fringes. This scattered laser light oscillates with a specific frequency that is related to the velocity of the particles (Boeker, 1999). The prepared suspensions that can utilise this piece of equipment have to have a low solids loading (~ 0.05 vol% (Costa, 1999)), since laser light can only permeate through dilute suspensions. This is a limiting factor, since the effect of additives within systems with a specifically high colloid concentration cannot be measured using this method.

Electroacoustic effects can also be used to determine zeta potentials, and two different measurement processes are derived from the phenomena. When sonic waves propagate through a colloidal system with differing particle and liquid densities, the amplitude and phase of the resultant particle movement differs from that of the liquid. The normally spherical electrical double-layer of counter-ions around the particle becomes

distorted, and a dipole is formed as the charged particle and counter-charged double layer are drawn away from one another. The alternating nature of the motion thus turns each of the individual particle sites into an oscillating dipole. This produces a macroscopic voltage called the ultrasonic vibration potential (UVP), which depends upon the sound wave frequency and electrode spacing. The UVP can be used to calculate the zeta potential, if variables related to liquid viscosity, as well as particle and liquid densities, conductivities and volume fractions, are known (Ozawa, 2006).

The opposite effect is also observed when there is a density difference between the particles and the suspending medium. A sound wave, called the electrokinetic sonic amplitude (ESA), is generated when an alternating electric field is applied across a colloidal suspension. The charged particles oscillate back and forth at the same frequency under the influence of an electric field, which effectively turns each particle into an acoustic dipole. These dipoles cancel out one another in the bulk of suspension, although in the region close to the electrodes, this does not happen, and a sound wave is generated.

Since the applied field and the response occur at the same frequency, a transducer can measure the amplitude and phase angle of this sound wave as a function of the transmitted signal. A mobility spectrum can be generated from this information, which is used to give both the zeta potential and particle size (Greenwood, 2003). Since sound can permeate through concentrated suspensions in the way that light cannot, both UVP and ESA techniques can measure the zeta potential of high solids loading suspensions and slurries.

D.2.2 Zeta Potential Analysis to Find the Position of the IEP

Zeta potential can be described as the effective charge of the particle in suspension, with the scientific principles behind charge formation discussed in Section 3.2. A high zeta potential magnitude increases both the electrophoretic mobility and the interparticle repulsion term. This inhibits particle agglomeration and so reduces the level of gravitational settling. By measuring the zeta potential across the pH range, it is possible to find the regions where particles are most stable in suspension.

Dolapix CE64 dispersant addition affects the zeta potential of the zircon particles in suspension throughout the pH range studied. As described in Section D.3.1, the curve plotting zeta potential against pH_i is shifted due to the presence of dispersant. In the present work, two dispersant concentrations of 0 mg/g and 20 mg/g were chosen, in accordance with the dispersant optimisation work of Appendix D.3. A more comprehensive study unconstrained by time would use a large number of dispersant concentrations, so that the shift in the zeta potential / pH_i curve could be measured as a function of dispersant content. A value for the optimum dispersant content could then be attained using zeta-potential analysis, as it occurs when the magnitude of the shift reaches a finite value.

Helmut Kreutz zircon ('Super FF') and Dupré zircon ('A' 2 μm) grades were both tested using zeta-potential analysis. The two different manufacturer grades exhibited vastly different deposition behaviour during the EPD experiments, and so the zeta potential / pH relationship for both dispersant–modified suspensions and dispersant–free suspension had to be investigated, to see whether the zeta potential differences could be accountable.

In the present work, the method used to obtain zeta-potential values across the pH range was laser Doppler anemometry, using a Delsa™Nano Zeta Potential and Submicron Particle Size Analyzer (Beckman Coulter), as shown in Figure D.3. This equipment utilises

electrophoretic light scattering (ELS) effects, which determines electrophoretic movement of charged particles under an applied electric field from the Doppler shift of scattered light. This information can then be used to determine the zeta potential.

The concentration had to lie within a specific range to be accurately analysed by the Delsa™NanoC apparatus. The zircon grades used within zeta potential analysis are Helmut Kreutz Kreutzonit 'Super FF' zircon powder (D50 ~ 1 μm) and Dupré Minerals Zircon A zircon powder (D50 ~ 2 μm). Preliminary experiments found that an aqueous zircon suspension concentration of 0.46 wt% could be directly injected into the flow cell for analysis without further dilution. The suspensions used within batch equilibrium study of Section D.1.2 were additionally used within the zeta potential experiments of this section, and so an identical suspension formation procedure was used.

It is important to note that the Delsa™NanoC has a 7 μm upper size limit for zeta potential measurements. The particle size distributions of the two zircon grades used within this experiment meant that this limitation would not have significant bearings on the work. A flow assembly cell for low concentration samples was used to house the tested suspensions for analysis, and Terumo 2ml syringes were used to pump the suspension into this cell, as shown in Figure D.3(b).

A syringe containing approximately 1.5 cm^3 of the suspension was attached to the first of the flow cell ports. A second syringe with a depressed plunger was placed in the second port, and the entire suspension volume was transferred through the cell and into the second syringe by depressing the first syringe fully. As deionised water is present within the flow cell prior to suspension injection, this is pushed through into the second syringe and replaced by the zircon suspension for analysis.

(a) **(b)**

Figure D.3 Photographs showing **(a)** the Delsa™Nano Analyser and **(b)** the flow assembly cell, containing two Terumo 2ml syringes used to flush the suspension into the testing volume.

Suspensions both with and without dispersant addition for both zircon grades were made up with pH_i values between pH 2.5 and 10.5. Samples in this range were each separated by 1.0 pH unit, apart from within in the alkaline region, where the spacing was set to 0.5 pH units. This was done due to increased interest in the zone where EPD experiments take place. The Smoluchowski criteria, which are appropriate for the analysis of aqueous suspensions, were used to calculate a value for the particle's zeta potential from its mobility, whereas the Hückel criteria are used when organic suspensions are studied. The Delsa™NanoC analyser used for the zeta potential measurements additionally takes into account electroosmotic effects when electrophoresis occurring, and so, arrives at more accurate values for both the particle mobility and zeta potential (Beckman Coulter, 2010).

For each tested sample, the values recorded for the zeta potential (mV), electrophoretic mobility (cm^2/Vs) and electric field (V/cm) were the peak values, calculated after measurements at 5 different cell positions (-0.7, -0.3, 0.0, 0.35, 0.7) were taken, to eliminate the effects of Brownian motion. These positions were stipulated for experiments using the flow cell by the manufacturer (Beckman Coulter, 2010). The data were analysed

using a Lorentzian fit with 1 peak, as all particles in single-component suspensions possess the same particle mobility. Each suspension was tested two times, using a new suspension sample for each. A third sample would be tested if the zeta potential against cell position curve differed noticeably in the initial two tests. The zeta potential ascertained for each sample was plotted against pH_i. The point where the best-fit curve linking the results crosses the x-axis (where the zeta potential is zero) was taken to be the position of the IEP.

D.2.3 Results and Discussion

The procedure used for zeta potential experiments is described in Section D.2.2. For most suspensions tested, the peak-value zeta potential recorded per test differed by between 1% and 5%. Graphs plotting peak value zeta potential (mV) against initial suspension pH (pH_i) are shown in Figure D.4 and Figure D.5, for CE64 dispersant-modified and dispersant-free suspensions, respectively.

For dispersant-free suspensions in Figure D.4, the 'Super FF' grade displayed slightly higher zeta potential values than the Dupré 'A' (2 μm) counterpart when the alkaline pH range is focussed upon. The zeta potential values go from high and positive at low pH to high and negative at high pH, and give the Duper zircon 'A' and Helmut Kreutz 'Super FF' grades IEP values of pH 4.5 and 4.6, respectively.

Both zircon grades tested possessed a zeta potential 'local dip' in the alkaline region, where the relationship between zeta potential magnitude and pH_i is reversed. As shown in Figure D.4, the Helmut Kreutz 'Super FF' grade displayed a dip minimum at a suspension pH_i of ~ 8.6. The Dupré 'A' (2 μm) grade displayed a similar dip minimum when the suspension pH_i was ~ 7.6.

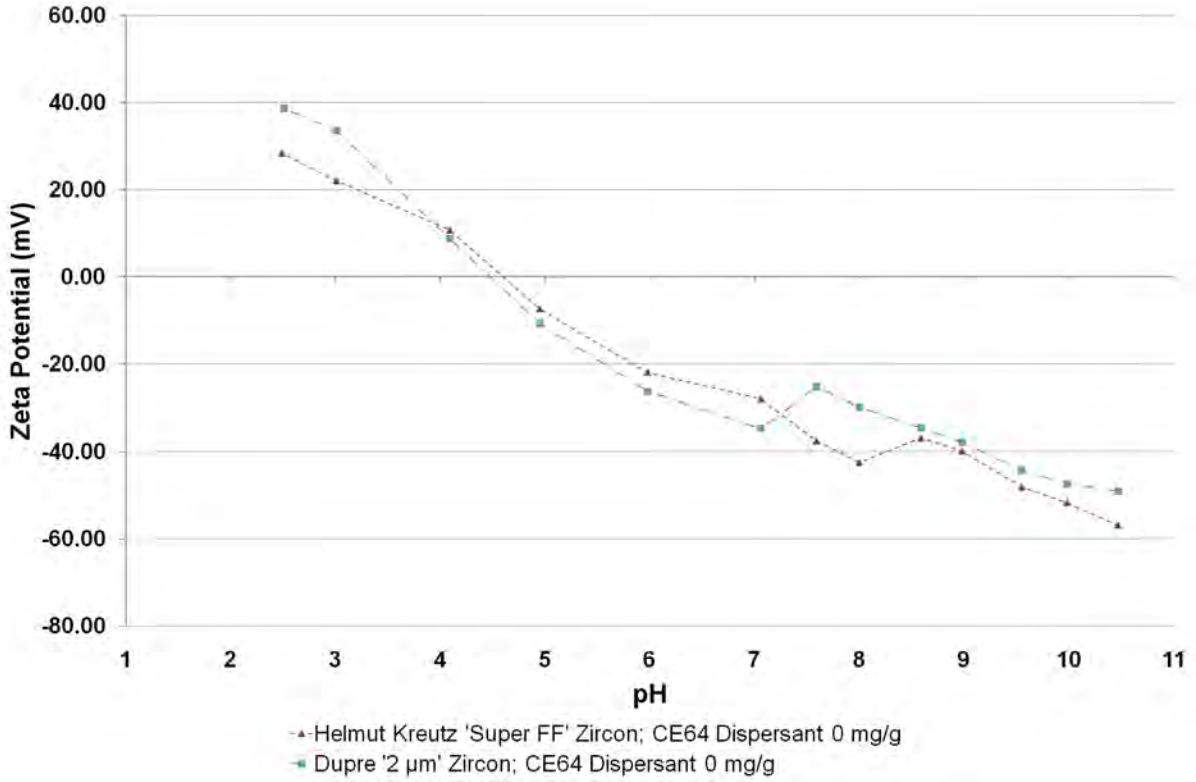

Figure D.4 Measured zeta potential (mV) as a function of zircon suspension initial pH (pH_i) and zircon powder grade, for dispersant-free suspensions.

For dispersant-free zircon suspensions, the experimentally derived positions of the IEP and PZC were compared against the results given by Mao et al. (1994), who obtained values for the pH_{iep} and pH_{pzc} for two zircon grades in aqueous suspension (being a commercial grade supplied by Westralian Sands Limited, and a natural grade from Mudd Tank, Australia).

In the present work, zeta potential analysis was used to give the Dupré and Helmut Kreutz zircon grades pH_{iep} values of 4.5 and 4.6, respectively. These values were lower than those measured by Mao et al. (1994), who obtained pH_{iep} values of 5.5 and 5.7, for the natural and commercial studied zircon grades, respectively. Mao, however, stated that zircon IEP values were highly grade specific, as zircon pH_{iep} values between 3.7 and 7.4 were obtained in the literature. Garrido (2001), for example, obtained a pH_{iep} of 5.0 for a Mahlwerke Kreutz zircon grade.

Within the batch equilibrium experiments of Appendix D.1, apparent pH_{pzc} values of 5.6 and 5.6 were obtained for the Dupré grade and Helmut Kreutz grade, respectively. These values were slightly lower than those measured by Mao et al. (1994), who obtained pH_{pzc} values of 5.9 and 6.1 for the natural grade and commercial studied grade, respectively.

The position of the PZC and IEP should roughly be equivalent in the absence of specifically adsorbing polyelectrolytes (of which anionic dispersants are an example), and so any disparity between the two values for can be used to indicate the level of sample purity. Mao (1994) attributed this PZC / IEP disparity in their grades to ions that may have been dissolved from the zircon surface during the conditioning stage and then been readsorbed as an anionic species. This disparity is greater for zircon grades in the present work, and this could be attributed to the presence of a greater number of readsorbed anionic species, since the zircon powders were not cleaned by any pre-processing technique before testing.

The addition of Dolapix CE64 dispersant at a concentration greater than the optimum (according to the sedimentation experiments of Appendix D.3) shifted the position of the IEP to a lower pH, i.e. to a more acidic pH value, as shown in Figure D.5. The point where the curve intersects the zeta potential = 0 line was never met, because consistent measurements could not be made below pH 3.0. Rao et al. (2007), who encountered the same issue when studying the zeta potential of zirconia, attributed the lack of results at low pH to particles either moving randomly, or not moving at all, when subjected to the electric field of the Delsa™NanoC apparatus during testing.

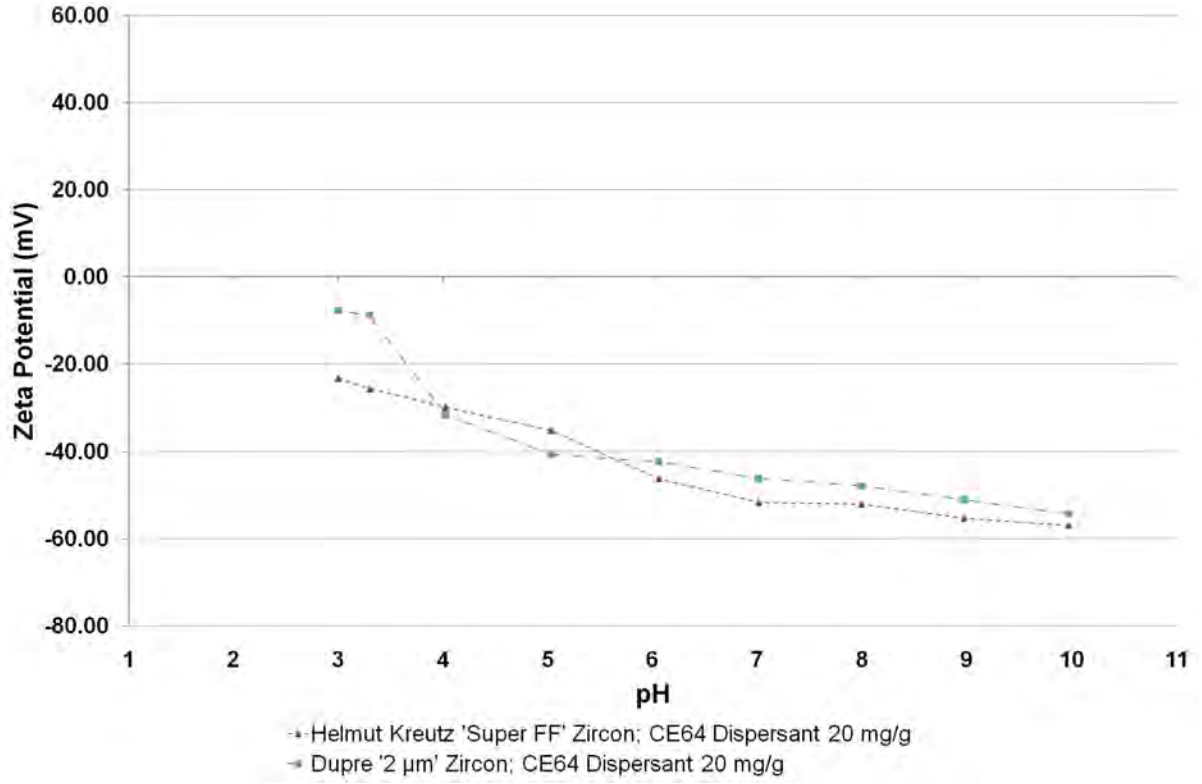

Figure D.5 Measured zeta potential (mV) as a function of zircon suspension initial pH (pH_i) and zircon powder grade, for CE64 dispersant-modified suspensions.

If one extrapolates the experimental curve to zero zeta potential, the pH_{iep} would be placed at about pH 1 – 2 for the Helmut Kreutz 'Super FF' zircon and pH 2 – 3 for the Dupré 'A' (2 µm) zircon, respectively, although the uncertainty of the results measured at low pH make curve extrapolation difficult. In addition to shifting the position of the zeta-potential curve through the addition of anionic dispersant, the gradient of the zeta-potential versus pH curve is flattened, so that the two curves would meet or cross at pH_i 10.5 to 11, as shown for the 'Super FF' grade in Figure D.6. The zeta-potential 'local dips' present in dispersant free suspensions also disappeared.

The IEP shift for both zircon grades with dispersant addition is in agreement with studies in the literature, although different anionic polyelectrolyte / ceramic species combinations were used in these instances. In a study by Rao et al (2007), the use of an optimum concentration of Dolapix CE64 shifted the pH_{iep} of zirconia from 5.4 to 3.3. Garrido

et al. (2001) showed that the presence of a polyacrylate dispersant changed the IEP of a zircon suspension from pH 5 to 3.5.

To explain this behaviour, one can describe the effect that the suspension pH has on the Dolapix CE64 dispersant. According to Albano and Garrido (2006), Dolapix CE64 is a carbonic acid ($O=C(OH)_2$ i.e. H_2CO_3)-based polyelectrolyte dispersant that starts ionising around pH 3.5, and does so to an increasing degree as the pH rises. It becomes completely dissociated above pH 8.5. Owing to the lack of experimental results in the region where the zeta potential of the dispersant modified zircon is positive (below the pH_{iep}), the explanation is assumed to follow that given by Rao et al. (2007), who studied the effect of Dolapix CE64 on zirconia aqueous suspensions. They stated that the particle surface was positively charged below the dispersant modified suspension IEP, although the magnitude of this charge was lower than that attained by dispersant-free suspensions. This could have been due to some possible weak interaction between the undissociated Dolapix CE64 and the surface of the particles through hydrogen bonding, which is a potential reason for any reduction in the observed zeta-potential magnitude.

Between the IEP of the dispersant-modified suspension (pH < 3) and the IEP of the dispersant-free suspension (~ pH 4.5), the Dolapix CE64 dispersant would start to ionise and adsorption takes place due to electrostatic attraction between the positively charged surface of the zircon particles and the negatively charged functional groups of the dispersant. The zeta-potential charge reversal and increase in electronegativity is dependent on the concentration of the dispersant (Rao, 2007). When the pH is increased beyond the IEP of the dispersant-free suspension, the surface consists of complexes which undergo specific interactions with the carboxylic groups of the dispersant and lead to an overall increase in surface charge. This increase in surface charge is associated with an increase in zeta potential, which, as explained

in Section 4.2.4, is the charge at the plane of shear, at a distance from the zircon particle surface.

When the results from this section and the results of Section D.1.3 are compared, the position of the experimental IEP and PZC are shifted in opposite pH directions when Dolapix CE64 was added to the system. Dolapix CE64 is an example of an anionic polyelectrolyte and according to Kallay (2000), the specific adsorption of anions shifts the PZC of a material to higher pH and the IEP to lower pH, to support these pH_{pzc} findings.

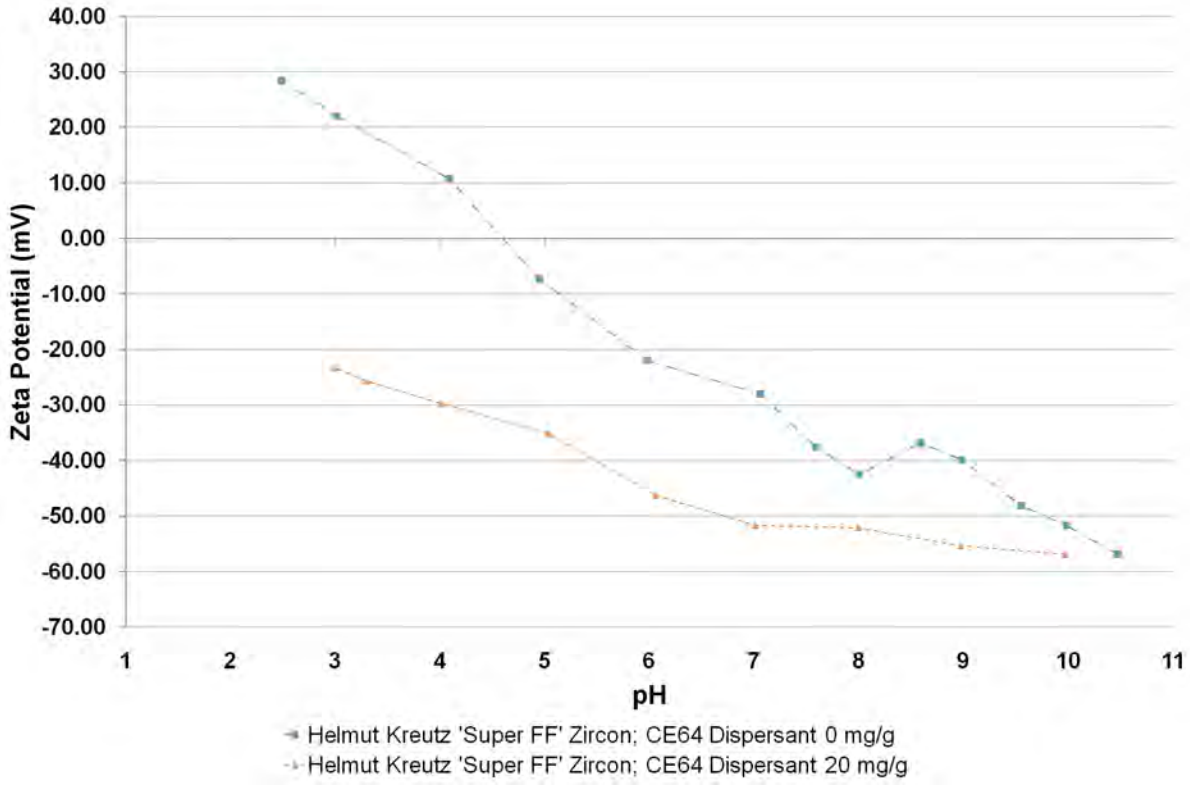

Figure D.6 Measured zeta potential (mV) as a function of zircon suspension initial pH (pH_i) and zircon powder grade, comparing Dolapix CE64 dispersant-modified and dispersant-free Helmut Kreutz 'Super FF' zircon suspensions.

D.3 Determination of the Optimum Dispersant Concentration

D.3.1 Experimental Techniques used in the Literature

Owing to the principal mechanisms by which dispersants stabilise the ceramic particles in suspension, an optimum polyelectrolyte concentration exists, as described in Section 4.2.3.2. Zeta potential analysis, sedimentation experiments, rheological analysis and capillary suction experiments can be employed to ascertain this optimum value (Rao, 2007), with each method described in this section.

The presence of polyelectrolyte dispersant in a colloidal suspension alters the particles' zeta potential across the pH range due to surface site interactions. When an anionic polyelectrolyte is present, for example, the particles' zeta potential shifts towards a more positive charge. In contrast, a shift towards a more negative charge is observed when a cationic polyelectrolyte is added to suspension. The magnitude of the shift is related to the dispersant concentration, which plateaus above the optimum concentration. For a given working pH, it is possible to obtain a value for the optimum concentration by plotting concentration against zeta potential, where the optimum dispersant concentration lies when the zeta potential shift begins to plateau (Ferrari, 1997) (Greenwood, 2003). In the work of Gaydardzhiev et al. (2006), however, the position of optimum dispersant concentration was said to lie where the inflection points lay on the curves of dispersant concentration against zeta potential and dispersant concentration against streaming current.

Methods used to measure the zeta potential are described in Section D.2.1, although specific cases in the literature are given below. Rao et al. (2007) studied the effect of adding an anionic dispersant (Dolapix CE64) to zirconia in aqueous suspension, and used a Zeta-Meter 3.0+ (Zeta-Meter Inc.) set-up for zeta-potential studies, which uses optical techniques to measure the electrophoretic mobility of particles in an electric field. As sample obscurity

limits analysis of suspensions with higher particle concentrations, 0.3 wt% zirconia suspensions were especially prepared for analysis. In contrast, Gaydardzhiev et al (2006) were able to use spectrometry techniques to arrive at zeta potential values, and so did not have to create low concentration suspensions specifically for charge analysis.

It is important to note that zeta potential measurements to find the optimum dispersant concentration only take into account the effect that the dispersant has on the magnitude of the electrostatic repulsive force between particles. As described in Section 4.2.3.2, dispersants also stabilise particles in suspension by forming on the particle surface and sterically inhibiting the close approach of particles that may otherwise lead to agglomeration. A number of other experimental methods can be carried out to measure the effect of dispersant on suspension stability as a whole, which takes into account both mechanisms, and therefore provides a more complete view on the dispersant's effect on suspension properties.

Sedimentation experiments are commonly utilised within work where suspension stability is an issue. Settling tests link sediment height with dispersant dosage, as destabilising mechanisms exist on either side of the optimum dispersant concentration, as described in Section 4.2.3.2. Gaydadzhiev (2006) stated that this technique could not be utilised within their work, as the suspension studied contained very fine particles that would not settle out over experimental timeframes.

Rheological studies can measure the change is suspension stability, and can therefore be used to ascertain the position of the optimum dispersant concentration. The theory behind the rheology (flow behaviour) of suspensions is described in Section 6.8, and states that particle agglomeration acts to increase the viscosity of dispersions. A viscosity minimum should exist for suspensions when the dispersant is present at an optimum

concentration, as destabilising mechanisms exist on either side of this concentration, as described in 4.2.3.2.

In Rao's work (2007), 40 wt% zirconia suspensions were considered to be most suitable for rheology studies, as viscosity differences were very small when low concentration suspensions (such as those suitable for EPD) were tested. For dispersant unmodified suspensions, the viscosity was high at low shear rates, although it rapidly decreased with increasing shear rate. When the optimum dispersant level was used, however, the peak corresponding to the initial resistance to flow did not exist and the suspension flowed easily. Within this study, no increase in viscosity was observed when dispersant was added at above the optimum concentration, as the effect of destabilising depletion flocculation was minimal within the experimental range.

Capillary suction experiments measure the level of flocculation in suspension, and a capillary suction timer (CST) determines the filterability of the suspension by measuring the filtration rate of water between two electrodes through a standard filter paper. For a flocculated sample, the CST (measured in seconds) should be low since water flows quickly through the bed of particles while for a well dispersed sample, the CST should be high. This gives a quick and reliable method for determining the dispersability of colloidal suspensions. Concentrated suspensions are, however, required to ascertain an accurate position for the dispersability maximum.

D.3.2 Choice of Experimental Method and Experimental Range

Methods in the literature used to determine the optimum dispersant concentration are described in Section D.3.1, and were drawn upon as the basis for this work. The optimum dispersant concentration occurs when the particle surface has become saturated with the

polyelectrolyte, and so the optimum concentration should be given as a surface area value (mg/m^2), so that the effect of dispersant content on grades with different specific surface areas can be compared.

Taking into account the range of Dolapix CE64 concentrations used within literature research (Greenwood 2003) (Gaydardzhiev 2006) (Rao 2007) (Ferrari 1997), the dispersant concentration was varied between 0.10 mg/m^2 and 10 mg/m^2 for these optimisation experiments. The surface area of Helmut Kreutz 'Super FF' zircon grade was stated as being 4.5 m^2/g, and so when this grade was tested, these dispersant concentrations can be converted to mass-related values between 0.45 mg/g and 45 mg/g.

Of the methods described in Section D.3.1, particle sedimentation experiments were decided upon as the technique used to ascertain the optimum Dolapix CE64 dispersant concentration. As described in Section D.3.1, sedimentation experiments take into account both the electrostatic and steric stabilising mechanisms when the optimum dispersant concentration is determined, whilst zeta-potential analysis only measures the effect that the dispersant has on the electrostatic repulsion term.

D.3.3 Particle Sedimentation Experiments

Sedimentation experiments were carried out to gauge the effect of Dolapix CE64 dispersant on stability, and three distinct experiments were carried out. Suspension preparation for the optimisation experiments closely followed the procedure described in Section 12.3, although each aqueous suspension was made up using a deionised water volume of 97.5 cm^3, and zircon addition of 2.50 g (~ 2.5 wt%).

The first experiment was associated with measuring settled zircon thicknesses from dispersant unmodified suspensions across a range of pH values. Deionised water solutions

were modified using either the 0.31 wt% HCl solution or the 0.51 wt% TMAH solution, using the equipment and technique described in Section 12.3. pH_i refers to the solution pH prior to zircon addition, and each suspension was modified to a different degree so that the range of studied pH_i values lay between 3 and 10, with suspensions spaced at 0.5 pH unit increments. 2.50 g of Helmut Kreutz 'Super FF' zircon was added to each suspension, and each suspension then underwent the roller mixer homogenisation and sonication steps set out in Section 13.3.3. The 'final pH' (pH_f) was recorded for each suspension, and three 20cm^3 samples from each homogenised suspension were transferred into 28 ml cylinders for settling. These cylinders were kept in laboratory conditions, with no agitation mechanisms in place. In addition to this, no noticeable vibrations were present from any nearby laboratory set-up. After 24 hours, the sediment height was measured after careful removal of liquid from the vessel.

The second experiment was carried out to ascertain the optimum level of Dolapix CE64 dispersant for Helmut Kreutz 'Super FF' zircon suspensions with a pH_i of 8.6. Seven suspensions were formed for this experiment, using the procedure described for the first experiment, all be it with a additional stage prior to pH modification when Dolapix CE64 was added to solution. Using Helmut Kreutz 'Super FF' as the zircon grade, with an average particle size of 1.1 μm and B.E.T specific surface area of 4.5 m^2/g, the dispersant concentration was varied between 0.10 mg/m^2 and 10 mg/m^2 (0.45 mg/g and 45 mg/g). 0.6 wt%, 3 wt% and 15 wt% Dolapix CE64 solutions were used for these additions, and were added using a graduated 5 ml pipette (±0.05 ml) with pipette pump. The lower end of additions equated to 0.190 cm^3 of the 0.6 wt% Dolapix solution, and the upper end equated to 0.720 cm^3 of the 15 wt% Dolapix solution. The pH of each tested solution was then modified using TMAH to reach a consistent pH_i value of 8.6, although TMAH addition varied from

suspension to suspension due to the buffering effect of the dispersant. The experimental procedure described in the first experiment of this section was then followed.

The third experiment was associated with measuring settled zircon thicknesses from dispersant modified suspensions across a range of pH_i values (pH 3 - 10). The procedure used in the first experiment of this section was used here, although a constant level of Dolapix CE64 dispersant was added to each solution prior to pH modification. The Dolapix CE64 addition was set to 4.4 mg/m^2 (20.0 mg/g), which was greater than the optimum concentration attained in the second experiment of this section. This level was chosen as the effect of depletion flocculation above the optimum dispersant level was less pronounced than that of bridging flocculation below it in destabilising the suspension, and so ensured that the dispersant would totally coat the zircon particles across the pH range.

D.3.4 Experimental Results and Discussion

Particle sedimentation experiments were one of a number of techniques carried out on zircon suspensions in order to find the conditions where the particles in suspension were stable. Methods used to increase suspension stability include pH modification and polyelectrolyte addition. Batch equilibrium measurements and zeta potential analysis were carried for similar reasons, as shown in Sections D.1 and D.2 respectively. The particle sedimentation study was carried out according to the procedures set out in Section D.3.3.

According to Appendix D.1.3, batch equilibrium methods gave the Helmut Kreutz 'Super FF' zircon an apparent pH_{pzc} of 5.10. In sedimentation experiments, the zircon showed aggregation behaviour in suspensions with pH_i values close to this value. Samples close to the apparent PZC settled out at a quicker rate than those away from it. Additionally, high stability was observed in the pH_i 3 and 3.5 samples. This finding supports the 'rule of thumb' set out

by Greenwood et al. (2003), stating that suspension particles approximately 2 - 3 pH units away from the IEP (or PZC in the absence of specifically adsorbing ions) can generate a high enough zeta-potential for suspension stability.

As shown in Figure D.7, the addition of 20mg/g Dolapix CE64 dispersant to zircon suspension samples changes the pH_i region around which the greatest settling effects occur,. Additionally, for all pH values, the settled mass and visible level of suspension depletion in the near-surface volume of each sample is reduced when anionic dispersant is added in excess to suspension. This can be attributed to the electrosterically stabilising actions of the polyelectrolyte, as described in Section 4.2.3.2. Whilst the region of instability in the dispersant-free suspensions existed between pH 4 and 7, for the dispersant modified suspensions, this instability region was evident at pH 4.5 and below. This shift on the addition of anionic dispersant correlates with the change in the IEP as determined both in Section D.2.3 and reported in the literature by Gaydardzhiev (2006) and by Rao (2007). The use of optimum and above-optimum concentrations of Dolapix CE64 both stabilise the zircon suspensions and shift the pH regions of instability away from more alkaline pH values, where EPD would take place.

For the second experiment, as described in Section D.3.3, the pH_i of Helmut Kreutz 'Super FF' zircon (2.5 wt%) suspensions was fixed at 8.6, and the Dolapix CE64 concentration was varied between 0 and 45 mg/g. The results are shown in Figure D.8. The settled depth decreases as the dispersant concentration is increased above, with the settled depth decreasing markedly for dispersant concentrations between 2 mg/g and 10 mg/g. However, at a dispersant concentration above 10 mg/g there is a slight increase in the settled depth that appears to plateau at dispersant concentrations of 10 mg/g and above; this minimum settled depth is approximately one third that observed in the dispersant-free unmodified suspensions at the same pH of 8.6.

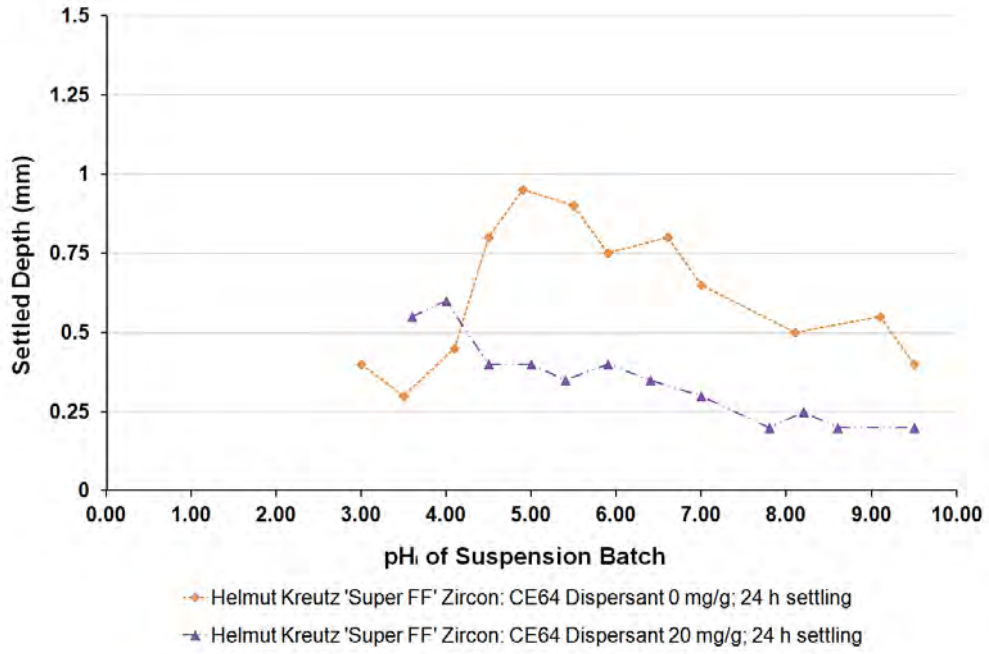

Figure D.7 Graph of settled zircon particle depth in suspension as a function of the initial zircon suspension pH (pH_i), 24 hours after suspension agitation was ceased, for 20 cm^3 samples of dispersant modified and dispersant-free Helmut Kreutz 'Super FF' zircon (2.5 wt%) in aqueous suspension.

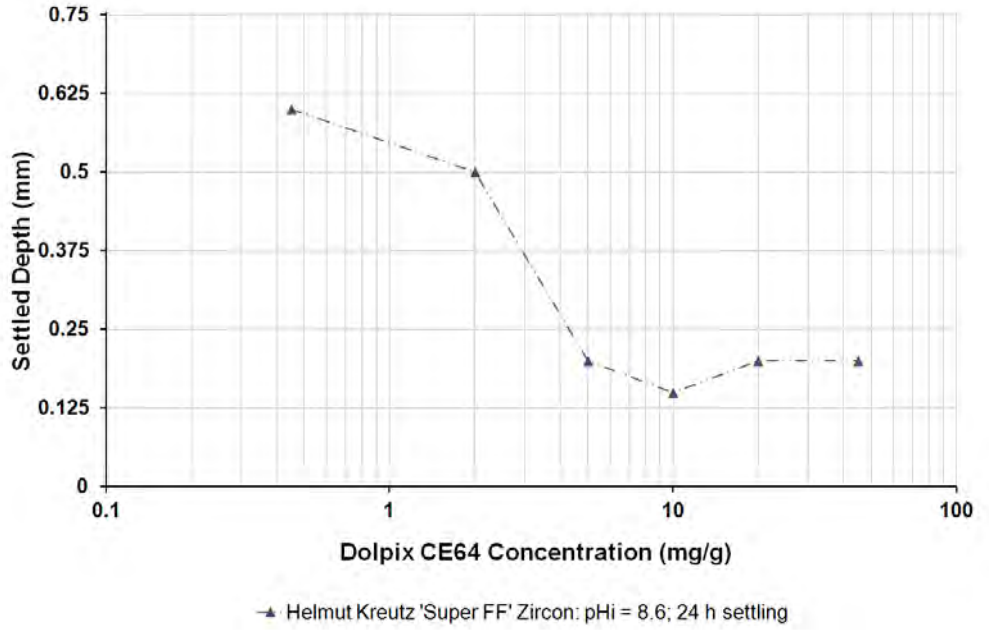

Figure D.8 Graph of settled zircon particle depth in suspension as a function of the Dolpix CE64 concentration (in mg/g), 24 hours after suspension agitation was ceased, for samples of Helmut Kreutz 'Super FF' zircon (2.5 wt%) in aqueous suspension at pH_i 8.6.

Although the calliper used to carry out measurements had an accuracy of ±0.05mm, the precision of settled depth measurement should have been carried out to a tolerance of 0.1 - 0.2 mm, owing to the fact that the settled depth itself could only be measured through the glass of the container. Additionally, although the suspension prior to settled thickness measurement was removed from the container using a syringe, there was uncertainty with regard to the position where the loosely flocculated settled deposit ended for the unstable suspensions. In retrospect, the use of both mass measurement and settled depth measurement would build up a more accurate picture of settling behaviour across the pH range, since settled depth values do not take into account the density and degree of loose flocculation that changes with suspension stability. Additionally, testing a greater number of dispersant concentrations tested would lead to a more accurate estimate of the optimum dispersant concentration in 'Super FF' zircon aqueous suspensions.

REFERENCES

Agafonov A V, Zakharov A G. (2010) Electrorheological fluids. *Russian Journal of General Chemistry 80 [3] pg. 567 – 575*

Albano M P, Garrido L B. (2006) Aqueous tape casting of yttria stabilized zirconia. *Materials Science and Engineering: A 420 [1-2] pg. 171 – 178*

Anné G, Vanmeensel K, Vleugels J, Beist O Van der. (2004) Influence of the suspension composition on the electric field and deposition rate during electrophoretic deposition. *Colloids and Surfaces A: Physicochem. Eng. Aspects 245 pg. 35–39*

Aramphongphun C, Castro J M. (2007) Microfluidics and rheology of dilute carbon black suspensions for in-mould coating (IMC) applications. *Modelling Simul. Mater. Sci. Eng. 15 157*

Asthana R, Kumar A, Dahotre N B. (2006) Materials processing and manufacturing science. *Butterworth-Heinemann, pg. 73*

ASTM (2011) Test Method for Ash Content in Plastics. *ASTM Volume 08.03, July 2011 Plastics (III): ASTM D5630 - 06*

Balberg I. (1987) Tunneling and nonuniversal conductivity in composite materials. *Physical Review Letters 59 [12] pg. 1305 – 1308*

Barnes H A, Hutton J F, Walters K. (1997) An introduction to rheology. vol. 3. *Elsevier*

Barnes H A. (1981) Dispersion Rheology 1980, a Survey of Industrial Problems and Academic Progress. *R. Soc. Chem. pg. 31*

Basu R N, Randall C A, Mayo M J. (2001) Fabrication of dense zirconia electrolyte films for tubular solid oxide fuel cells by electrophoretic deposition. *J Am Ceram Soc 84 [1] pg. 33 – 40*

Beckman Coulter (2010) [online] Delsa™Nano Series Zeta Potential and Submicron Particle Size Analyzer Brochure. https://www.beckmancoulter.com/wsrportal/bibliography?docname=BR-11313B%20DelsaNano%20Brochure.pdf (Accessed 28th September 2011)

Berg J C. (2009) An introduction to interfaces & colloids: the bridge to nanoscience. *World Scientific pg. 547*

Besra L, Compson C, Lui M. (2007) Electrophoretic deposition on non-conducting substrates: The case of YSZ film on NiO–YSZ composite substrates for solid oxide fuel cell application. *Journal of Power Sources 173 pg. 130 – 136*

Besra L, Liu, M. (2007) A review on fundamentals and applications of electrophoretic deposition (EPD). *Progress in Materials Science 52 pg. 1 – 61*

Besra L, Uchikoshi T, Suzuki T S, Sakka Y. (2009) Application of constant current pulse to suppress bubble incorporation and control deposit morphology during aqueous electrophoretic deposition (EPD). *Journal of the European Ceramic Society 29 [10] pg. 1837 – 1845*

Biest O Van der, Vandeperre L J. (1999) Electrophoretic deposition of materials. *Annu. Rev. Mater. Sci. 29 pg. 327 – 352*

Biest O Van der, Put S, Anné G, Vleugels J. (2004) Electrophoretic deposition for coatings and free standing objects. *Journal of Materials Science 39 pg. 779– 785*

Boeker E, Grondelle R van. (1999) Environmental Physics - Second Edition. *John Wiley, Chichester*

Brosseau C, Boulic F, Queffelec P, Bourbigot1 C, Le Mest1 Y, Loaec1 J, Beroual A. (1997) Dielectric and microstructure properties of polymer carbon black composites. *J. Appl. Phys. 81 pg. 882*

BSI (2003) Methods of testing refractory materials - Part 10: investment casting shell mould systems - Section 10.2: Determination of permeability and standard air flow capacity at elevated temperatures. *Incorporating Technical Corrigendum No. 1 BS 1902-10.2:1994*

Chan C-M, Cheng C-L, Yuen M M F. (1997) Electrical properties of polymer composites prepared by sintering a mixture of carbon black and ultra-high molecular weight polyethylene powder. *Polymer Engineering & Science 37 [7], pg. 1127 – 1136*

Chakrabarty R K, Bardhan K K, Basu A. (1991) Nonlinear I-V characteristics near the percolation threshold. *Physical Review B. 44 [13] pg. 6773 – 6779*

Chen C C, Chou Y C. (1985) Electrical-conductivity fluctuations near the percolation threshold. *Physical Review Letters 54 [23] pg. 2529 – 2532*

Chen F, Lui M. (2001) Preparation of yttria-stabilized zirconia (YSZ) films on $La_{0.85}Sr_{0.15}MnO_3$ (LSM) and LSM±YSZ substrates using an electrophoretic deposition (EPD) process. *Journal of the European Ceramic Society 21 pg. 127 – 134*

Chen G H, Wu D J, Weng W G, He B, Yan W L. (2001) Preparation of polystyrene-graphite conducting nanocomposites via intercalation polymerisation. *Polymer International 50 pg. 980 – 985*

Chiteme C, McLachlan D S. (2003) AC and DC conductivity, magnetoresistance, and scaling in cellular percolation systems. *Physical Review B 67, 024206*

Cirre Torres J. (2004) Thermo physical properties of investment casting waxes. *PhD thesis, University of Birmingham, UK*

Clarke, B. (1967) Rheology of coarse settling suspensions. *Chemical Engineering Research and Design 45a pg. 251 - 256*

Clegg A J. (1991) Precision casting processes. *Pergamon Press*

Contescu C, Contescu A, Schwarz J A. (1994) Thermodynamics of Proton Binding at the Alumina/Aqueous Solution Interface: A Phenomenological Approach. *J. Phys. Chem. 98 pg. 4327-4335*

Cortright E C. (2009) [online] Microfluidics of DNA Suspensions http://etd.ohiolink.edu/view.cgi/Cortright%20Emily.pdf?osu1242236618 (accessed on 28th September 2011)

Costa A L, Galassi C, Greenwood R. (1999) α-Alumina–H_2O Interface Analysis by Electroacoustic Measurements. *Journal of Colloid and Interface Science 212 pg. 350 – 356*

Coussot P. (2005) Rheometry of Pastes, Suspensions, and Granular Materials: Applications in Industry and Environment. *John Wiley & Sons, Inc.*

Dannenberg E M. (1977) Vanderbilt Rubber Handbook, 12th edition. *R.T. Vanderbilt Co.: New York*

De D, Nicholson P S. (1999) Role of Ionic Depletion in Deposition during Electrophoretic Deposition. *Journal of the American Ceramic Society 82 [11] pg. 3031 – 3036*

DeGarmo E P, Black J T, Kohser R A. (2003) Materials and Processes in Manufacturing. *John Wiley & Sons, Inc.*

Derjaguin B V, Landau L (1941) A theory of the stability of strongly charged lyophobic sols and the coalescence of strongly charged particles in electrolytic solution. *Acta Physicochim. USSR, 14 pg. 633 – 652*

Dijk N van, Fletcher S, Madden C E, Marken F. (2001) Nanocomposite electrodes made of carbon nanofibers and black wax. Anodic stripping voltammetry of zinc and lead. *Analyst 126 pg. 1878 – 1881*

Dobias B. (1993) Coagulation and Flocculation: Theory and Applications. *Marcel Dekker pg. 112-113*

Elias H-G. (2003) An introduction to plastics. *Wiley-VCH pg. 136*

Elsenbaumer R L, Jen K Y, Oboodi R. (1986) Processible and Environmentally Stable Conducting Polymers. *Synth. Met. 15 [2-3] pg. 169 – 174*

Feltes T, Timmons M, Regalbuto J. [online] A Simple Procedure to Determine Surface Charging Parameters in Aqueous Solutions http://www.uic.edu/labs/AMReL/NSFREU02/Final%20Reports%202002/Final%20Report.TFeltes.&.MTimmons.pdf (accessed on 26th August 2008)

Ferrari B, Moreno R. (1997) Electrophoretic deposition of aqueous alumina slips. *Journal of the European Ceramic Society 17 [4] pg. 549 – 556*

Fritz G, Schädler V,Willenbacher N, Wagner N J. (2002) Electrosteric Stabilization of Colloidal Dispersions. *Langmuir 18 (16) pg. 6381 – 6390*

Garrido L B, Aglietti E F. (2001) Zircon based ceramics by colloidal processing. *Ceramics International 27 [5] pg. 491-499*

Gaydardzhiev S, Ay P. (2006) Characterisation of aqueous suspensions of fumed aluminium oxide in presence of two Dolapix dispersants. *Journal of Materials Science 41 pg. 5257 – 5262*

Gere J M. (2001) Mechanics of Materials: 5th SI Edition. *Nelson Thornes*

Girotto E M, Santos I A. (2002) Medidas de resistividade elétrica DC em sólidos: como efetuálas corretamente. *Quím. Nova 25 [4]*

Greenwood R. (2003) Review of the measurement of zeta potentials in concentrated aqueous suspensions using electroacoustics. *Advances in Colloid and Interface Science 106 pg. 55 – 81*

Grimmett G. (1989) Percolation. *New York ; London : Springer-Verlag*

Hamaker H C, Verwey E J W. (1940) Part II.—(C) Colloid stability. The role of the forces between the particles in electrodeposition and other phenomena. *Trans. Faraday Soc. 35 pg. 180 – 185*

Hamagami J, Kanamura K, Umegaki T, Fujiwara N, Ito M, Hirata S. (2002) Direct Electrophoretic Deposition of Alumina Particles onto Porous Ceramics for Membrane Filter Application. *Trans. Mater. Res. Soc. Jpn. 27[1] pg.77 – 80*

Henry D C. (1930) The Cataphoresis of Suspended Particles. Part I. The Equation of Cataphoresis. *Proceeding of the Royal Society London A vol. 133 no. 821 pg. 106 –* 129

Horton R A. (1988) Investment casting. ASM Handbook: vol 15 Casting. *ASM International pg. 253 – 269*

Hsu J-P. (1999) Interfacial Forces and Fields: Theory and Application. *CRC Press, pg. 154*

Hu C C, Chu C-H. (2001) Electrochemical impedance characterization of polyaniline-coated graphite electrodes for electrochemical capacitors — effects of film coverage/thickness and anions. *Journal of Electroanalytical Chemistry 503 pg. 105 – 116*

ICBA: Users Guide **(2006)** [online] http://www.carbon-black.org/user_guide.html (accessed 30th July 2011)

Inagaki M. (1989) Applications of graphite-intercalation compounds. *Journal of Materials Research 4 [6] pg. 1560 – 1568*

ISI Images Scientific Instruments – Four Point Electrical Probe [online] http://www.imagesco.com/articles/superconductors/four-point-electrical-probe.html (accessed 29th August 2008)

Jones S, Yuan C. (2003) Advances in shell moulding for investment casting. *Journal of Materials Processing Technology 135 (2-3) pg 258 – 265*

Jones S. (2009) Investment Casting Process, *US Patent: 7,594,529 B2*

Kallay N. (2000) Interfacial Dynamics. *CRC Press pg. 205*

Kawaguchi M, Okuno M, Kato T. (2001) Rheological properties of carbon black suspensions in a silicone oil. *Langmuir 17 pg. 6041 – 6044*

Kerkar A V, Rice R W, Spotnitz R M. (1993) Manufacture of optical ferrules by electrophoretic deposition. *US Patent 5194129*

King J A, Johnson B A, Via M D, Ciarkowski C J. (2009) Electrical conductivity of carbon-filled polypropylene-based resins. *Journal of Applied Polymer Science 112 [1] pg. 425 – 433*

Koelmans H. (1955) Suspensions in non aqueous media, *Philips Res. Rep. 10 pg. 161 – 193*

Koenig M. (1978) Method of Electroforming. *US patent 4098652*

Kosmulski M. (2001) Chemical Properties of Material Surfaces. *CRC Press, pg. 65*

Kurlandsky S. (1955) Electrically conducting wax compositions. *US patent 2702756*

Kusy R P. (1977) Influence of the particle size on the continuity of aggregates. *Journal of Applied Physics 48 [12] pg. 5301 – 5306*

Kusy A. (1977) Chains of conducting particles that determine the resistivity of thick resistive films *Thin Solid Films 43 [3] pg. 243 – 250*

Lewis J A, Matsuyama H, Kirby G, Morissette S, Young J F. (2000) Polyelectrolyte effects on the rheological properties of concentrated cement suspensions. *Journal of the American Ceramic Society 83 [8] pg. 1905 – 1913*

Li S Z, Cao Y, Xue Z J. (1987) Soluble polyaniline. *Synthetic Metals 20 [2] pg. 141 – 149*

Lozano K, Bonilla-Rios J, Barrera E V. (2001) A study on nanofiber-reinforced thermoplastic composites (II): Investigation of the mixing rheology and conduction properties. *Journal of Applied Polymer Science 80 pg. 1162 – 1172*

Lyklema J. (1984) Points of zero charge in the presence of specific adsorption. *Journal of Colloid and Interface Science 99 (1) pg. 109 – 117*

Lyklema J. (2003) Electrokinetics after Smoluchowski. *Colloids and Surfaces A: Physicochemical and Engineering Aspects vol 222 [1-3] pg. 5 – 14*

Mao M, Fornasiero D, Ralston J, Smart R S C, Sobieraj S. (1994) Electrochemistry of the zircon-water interface. *Colloids and Surfaces A: Phpsicochemical and Engineering Aspects. 85 pg. 31 – 49*

Marken F, Gerrard M L, Mellor I M, et al. (2001) Voltammetry at carbon nanofiber electrodes. *Electrochemistry Communications 3 pg. 177 – 180*

Mezger T G. (2006) The rheology handbook: for users of rotational and oscillatory rheometers. *Vincentz Network GmbH & Co KG*

Microlab Berkeley – Chapter 8.01: Four-Point Probe Resistivity Measurement [online] http://microlab.berkeley.edu/labmanual/chap8/8.01.html (accessed 16th August 2008)

Mills A, Farid M, Selman J R, Al-Hallaj S. (2006) Thermal conductivity of phase change materials using a graphite matrix. *Applied Thermal Engineering 26 pg. 1652 – 1661*

Milonjić S K, Čerović L S, Čokeša D M, Zec S. (2007) The influence of cationic impurities in silica on its crystallization and point of zero charge. *Journal of Colloid and Interface Science 309 pg. 155–159*

Moon H. (2006) Crack Interactions and Thermal Shock Properties of Ceramic Laminates. *Proquest Dissertations & Theses. ISBN: 9780542855955 pg. 143*

Moreno R, Ferrari B. (2000) Effect of the slurry properties on the homogeneity of alumina deposits obtained by aqueous electrophoretic deposition. *Materials Research Bulletin 35 pg. 887 – 897*

Mullins W M, Averbach B L. (1988) Surface propertes of silicon and aluminium oxide powders. *Surface Science 206 pg. 41 – 51*

Munson B R, Young D F, Okiishi T H, Huebsch W W. (2008) Fundamentals of Fluid Mechanics. *Wiley*

Ozawa M, Hattori M. (2006) Ultrasonic vibration potential and point of zero charge of some rare earth oxides in water. *Journal of Alloys and Compounds 408–412 pg. 560 – 562*

Paipetis S A, Ceccarelli M. (2010) The Genius of Archimedes -- 23 Centuries of Influence on Mathematics. *Springer*

Pal R, Bhattacharya1 S N, Rhodes E. (1986) Flow behaviour of oil-in-water emulsions. *The Canadian Journal of Chemical Engineering 64 [1] pg. 3 – 10*

Pinto G, López-gonzález C, Jiménez-martín A. (1999) Polymer composites prepared by compression molding of a mixture of carbon black and nylon 6 powder. *Polymer Composites 20 [6] pg. 804 – 808*

Power D C. (1995) Palladium alloy pinning wires for gas turbine blade investment casting. *Platinum Metals Review 39 (3) pg. 117 – 126*

Powers R W. (1975) The electrophoretic forming of beta-alumina ceramic. *J. Electrochem. Soc.122 pg. 482 – 486*

Rahaman M N. (2003). Ceramic Processing and Sintering. *CRC Press. ISBN: 0824756150 pg. 314*

Rao P S, Tripathy S S, Raichur A M. (2007) Dispersion studies of sub-micron zirconia using Dolapix CE 64. *Colloids and Surfaces A: Physicochemical and Engineering Aspects 302 [1-3] pg. 553 – 558*

Rodriguez M R, Chambers A, Baker R T K. (1995) Catalytic engineering of carbon nanostructures. *Langmuir 11 pg. 3862 – 3866*

Rwei S P, Ku F-H, Cheng K C. (2002) Dispersion of carbon black in a continuous phase: Electrical, rheological, and morphological studies. *Colloid & Polymer Science 280 [12] pg. 1110 – 1115*

Sakka S. (2004) Handbook of Sol-Gel Science and Technology – Processing, Characterization and Applications. *Springer Chapter 23 pg. 462*

Sarkar P, Huang X, Nicholson P S. (1993) Zirconia/Alumina Functionally Gradiented Composites by Electrophoretic Deposition Techniques. *Journal of the American Ceramic Society 76 [4] pg 1055 – 1056*

Sarkar P, Nicholson P S. (1996) Electrophoretic deposition (EPD): mechanisms, kinetics and application to ceramics. *Journal of the American Ceramic Society 79 [8] pg. 1987 – 2002*

Sarkar P, De D, Rho H. (2004) Synthesis and microstructural manipulation of ceramics by electrophoretic deposition. *Journal of Materials Science 39 pg. 819 – 823*

Scarisbrick R M. (1973) Electrically conducting mixtures. *Journal of Physics D: Applied Physics 6 pg. 2098*

Sennett P, Olivier J P. (1965) Colloidal dispersions, electrokinetic effects and the concept of zeta potential. *Chemistry and physics of interfaces. Am Chem Soc pg. 73 – 93*

Shirakawa H, Louis E J, MacDiarmid A G, Chiang C K, Heeger A J. (1977) Synthesis of Electrically-Conducting Organic Polymers: Halogen Derivatives of Polyacetylene, (CH)(X). *J Chem Soc Chem Commun 578 pg. 578 – 580*

Strauss E, McBain D, Thompson J. (2001) Optimization of In-Mold Coating Injection Molded Thermoplastic Substrates. *US Patent: 6793861*

Su B, Ponton C B, Button T W. (2001) Hydrothermal and electrophoretic deposition of lead zirconate titanate (PZT) films. *Journal of the European Ceramics Society 21 pg. 1539 – 1542*

Suzdal'tsev E I, Kharitonov D V. (2004) Methods for the electrophoretic shaping of ceramic products from aqueous slips or inorganic materials (a review). *Refractories and Industrial Ceramics Vol. 45 [1]*

Swartzendruber L J. (1964) [online] Correction factor tables for four-point probe resistivity measurements on thin, circular semiconductor samples. *National Bureau of Standards Technical Note 199.* http://www.four-point-probes.com/nbs.pdf (accessed 16th August 2008)

Tabellion J, Clasen R. (2004) Electrophoretic deposition from aqueous suspensions for near-shape manufacturing of advanced ceramics and glasses – applications. *Journal of Materials Science 39 pg. 803 – 811*

Takamiya N, Kunimitsu Y, Adachi K, Mori K, Noda I, Wakabayashi A. (2000) Transparent conductive film, low-reflectivity transparent conductive film, and display device. *US Patent: 6143418*

Tassel J J Van, Randall C A. (2006) Mechanisms of Electrophoretic Deposition. *Key Engineering Materials 314 pg. 167 – 174*

Topsoe H. (1968) [online] Geometric Factors in Four Point Resistivity Measurement. http://www.fourpointprobes.com/haldor.html#hal (accessed 15th August 2009)

Tüken T. (2006) Polypyrrole films on stainless steel. *Surface & Coatings Technology 200 pg. 4713 – 4719*

Uchikoshi T, Furumi S, Shirahata N, Suzuki T S, Sakka Y. (2008) Conductive Polymer Coating on Nonconductive Ceramic Substrates for Use in the Electrophoretic Deposition Process. *Journal of the American Ceramic Society 91 [5] pg. 1674 – 1677*

Wallace G G, Dastoor P C, Officer D L, Too C O. (2000) Conjugated polymers: New materials for photovoltaics. *Chemical Innovation 30 [1] pg.14 – 22*

Wang K-c, Hu C-m. (2003) Carbon black coating for CRT display screen with uniform light absorption. *US Patent: 6623662*

Wolz S. (2009) Process for producing articles from ceramic or metal by electrophoretic free forming. *US Patent Application: 20090255813*

Yopps J A, Fuerstenau D W. (1964) The zero point of charge of alpha-alumina. *Journal of Colloid Science 19 pg. 61 – 71*

Zallen R. (1983) The Physics of Amorphous Solids. *Wiley, New York*

Zhitomirsky I, Gal-Or L. (1997) Electrophoretic deposition of hydroxyapatite. *J. Mater. Sci. Mater. Med. 8 pg. 213 – 219*

Zhitomirsky I. (2000) Ceramic Films Using Cathodic Electrodeposition**.** Journal of the Minerals, Metals & Materials Society JOM-e, 52 (1)